Hunting the ppK^-: A kinematic refit for the exclusive analysis of the reaction $pp \rightarrow pK^+\Lambda$

Diplomarbeit
von
Dominik Maximilian Pleiner

May 6, 2012

Technische Universität München - Physik Department
Exzellenz Cluster ‘Origin and Structure of the Universe’

Zusammenfassung

Innerhalb des letzten Jahrzehnts führten theoretische Modelle, basierend auf einem attraktiven Potential zwischen K^- und Nukleonen, zur Vorhersage tiefgebundener kaonischer Cluster [YA02]. Mehrere Kollaborationen berichteten über die mögliche Entdeckung des leichtesten kaonischen Clusters ppK^- [FIN05; Y+10].

Zur Untersuchung dieser hypothetischen Zustände wurde 2009 am ‘Helmholtzzentrum für Schwerionenforschung’ (GSI) ein Experiment mit dem Fixed-Target Spektrometer FOPI durchgeführt, bei dem Protonen bei einer Energie von 3.1 GeV zur Kollision gebracht wurden. Das Ziel dieses Experiments, welches in der folgenden Arbeit als ‘pp Experiment’ bezeichnet wird, ist die Rekonstruktion von ppK^- über ihren Zerfall in p und Λ.

Im Rahmen dieser Arbeit wird die Entwicklung eines kinematischen Refits für die exklusive Analyse der Reaktion $pp \rightarrow pK^+\Lambda$ präsentiert, welcher eine Reihe von physikalischen Zwangsbedingungen mit und ohne Berücksichtigung von Vertices beinhaltet. Kinematische Refits haben sich in der Analyse von elementaren Teilchenreaktionen als bewährtes Hilfsmittel etabliert, um die Massenauflösungen von kurzlebigen zerfallenen Teilchen zu verbessern, welche mittels “Invariant Mass” oder “Missing Mass” Methode rekonstruiert werden. Zudem kann mit ihrer Hilfe der Anteil von Untergrundreaktionen reduziert werden. In dieser Arbeit werden sowohl die theoretischen Grundlagen, als auch die Anwendung des kinematischen Refits auf verschiedene Simulationen unter Verwendung unterschiedlicher Kombinationen von Zwangsbedingungen beschrieben. Des Weiteren wird eine systematische Analyse der Auswirkungen des Refits auf Untergrundreaktionen, sowie erste Ergebnisse der Anwendung des kinematischen Refits auf experimentelle Daten, vorgestellt.

Zusätzlich zur Untersuchung der $pK^+\Lambda$ Reaktion wird die Analyse elastischer pp Kollisionen präsentiert. Der kinematische Refit wird hierbei auf die Daten angewendet um den Anteil von Untergrundreaktionen effizient zu reduzieren. Mit Hilfe der identifizierten elastischen Protonen können verschiedene Detektoreffizienzen berechnet, sowie die Orientierung des Protonenstrahls überprüft werden.

Abstract

During the last decade, the existence of an attractive potential between K^- and nucleons lead to the prediction of deeply bound kaonic nuclear clusters [YA02]. Experimental results on the search for the lightest representative ppK^- were reported by various collaborations [FIN05; Y+10].

In order to contribute to the investigation of the possible existence of this predicted state, an experiment measuring $p + p$ reactions at 3.1 GeV with the fixed target spectrometer FOPI at the 'Helmholtzzentrum für Schwerionenforschung' (GSI) in Darmstadt was performed in 2009. The goal of this experiment, which is referred to as 'pp experiment' throughout this thesis, is the analysis of ppK^- via its decay into p and Λ.

This work presents the development of a kinematic refit for the exclusive analysis of the reaction $pp \rightarrow pK^+\Lambda$, providing various vertex and non-vertex constraints. Kinematic fitting is a well-established tool in the analysis of elementary particle reactions to improve the mass resolutions of intermediate particles reconstructed via the invariant or missing mass technique and to reduce background reactions. The theoretical principles as well as the effect of its application to various simulations using different constraint conditions are discussed in this thesis. Furthermore, a systematic study of the behavior of refitted background is performed and first results of the application to experimental data are presented.

Additionally to the investigation of the $pK^+\Lambda$ reaction, the analysis of elastic $p + p$ reactions is shown. For an effective background reduction, the kinematic refit is applied to the data. The selected elastic protons are exploited to determine the detector efficiencies and to validate the beam alignment.

Contents

1 Theory

The universe reveals its innermost structure and coherence through fundamental symmetries, that govern the laws of nature. Connected to the concept of conserved quantities via the Noether's theorem, most of modern physics is based upon the implications of symmetry transformations acting on its underlying equations.

The interaction between the constituents of hadronic matter, quarks and gluons, mediated by the strong force, is described within the theoretical framework of quantum chromodynamics (QCD). It is based on the non-abelian gauge group $SU(3)_C$, associated with the color charges of strong interaction. The non-abelian character of this gauge theory leads to interesting effects, such as gluon-gluon interaction, color confinement and asymptotic freedom. However, due to the increasing of the strong coupling constant α_S with decreasing transferred momentum, perturbative QCD is limited to the high energy regime. For the description of low energy effects like hadronization, non-perturbative methods as lattice QCD or chiral perturbation theory (ChPT) have been applied with great success.

Turning towards very high energies, asymptotic freedom implies that at high temperatures or densities, the relevant degrees of freedom are quarks and gluons rather than hadrons. The transition from confined hadrons to a deconfined phase, the so called quark gluon plasma, was confirmed by lattice QCD calculations [FH11]. This extreme state of matter, which composed the universe for a short time after the big bang, might exclusively occur under very special conditions in nature (e.g. in the center of neutron stars or during supernovae) and has to be produced in heavy ion collisions in the laboratory.

In order to achieve a fundamental understanding of these effects, and therefore finally of the matter that constitutes our nature, the phase diagram of nuclear matter (Figure 1.1) has been investigated extensively during the last decades. Its properties are quantitatively described by the equation of state (EOS) of nuclear matter, which determines the physical evolution of the system[1] by relating the state variables temperature T, density ρ and energy per baryon $\frac{\varepsilon}{A}$ [Uhl03].

With energies of 2 AGeV, that are achieved with the SIS18 synchrotron, the experiments at the GSI contribute to this research at moderate temperatures and densities.

---

[1] The recent measurement of a 2 solar mass neutron star sets narrow constraints on the EOS of strong interacting matter, rejecting most of the theoretical models which predict exotic non-nucleonic matter in the center of neutron stars [DPR$^+$10; Röt11].

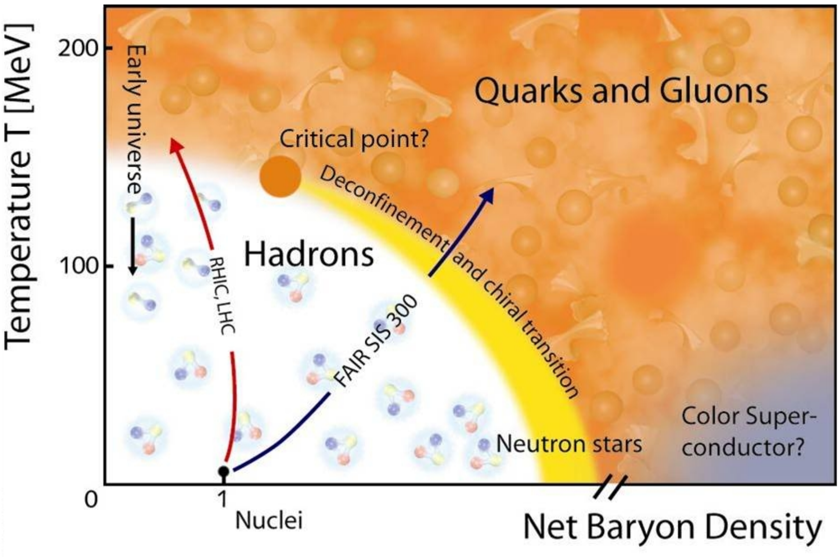

Figure 1.1: Phase diagram of the QCD. The phase boundary between confined hadronic matter and the quark gluon plasma is illustrated by the yellow band. Analog to the phase diagram of water, a critical point exists, beyond which the phase boundary disappears and the transition happens continuously [Lor08].

1.1 In-medium modification of hadrons

A further topic of research in this field is the modification of hadron masses in hot and dense nuclear matter [BR91; CRW96; SBMJ97; PSSG99].
Due to the small masses of up- and down-quarks, an approximate $SU(2)_F$ symmetry is realized in QCD, which mixes the two quark flavors. The corresponding Lagrangian contains left- and right-handed terms of the quark fields, which transform independently under $SU(2)_F$. At low temperatures, this so called chiral symmetry is spontaneously broken by the chiral quark condensate $\langle q\bar{q}\rangle$, a suprafluid phase of quark-antiquark pairs constituting the QCD vacuum [PS95]. The associated Goldstone bosons are the three pions with finite masses of around 140 GeV/c^2, caused by explicit chiral symmetry breaking due to the small up- and down-quark masses[2]. The pion mass is related to the quark masses m_u and m_d and to the expectation value of the chiral condensate via the Gell-Mann-Oakes-Renner relation [Koc96]

$$m_\pi^2 = -\frac{m_u + m_d}{2f_\pi^2}\,\langle 0|u\bar{u} + d\bar{d}|0\rangle \tag{1.1}$$

where f_π is the pion decay constant. According to this equation, the pion mass directly depends on the explicit and spontaneous breaking of chiral symmetry.

---

[2] In case of an approximate $SU(3)_F$ symmetry including the strange-quark, the associated Goldstone bosons are pions and kaons. The latter possess higher masses of approximately 500 GeV/c^2, due to the higher mass of the strange-quark.

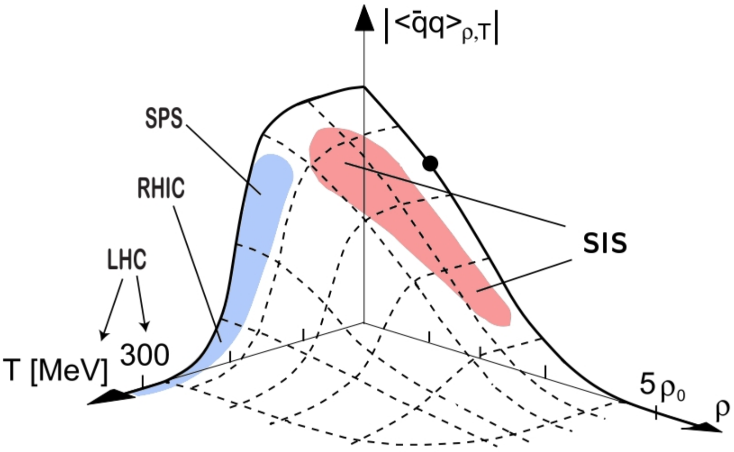

Figure 1.2: Chiral condensate as a function of the baryon density ρ and the temperature T. The black dot indicates the position of normal nuclear matter. The colored fields mark the regions, where the matter is investigated by different experiments [Nöh98; LKW92].

At high temperatures and densities, the chiral symmetry is expected to be restored [Mic06], leading to a vanishing chiral condensate $\langle q\bar{q}\rangle$. This situation is illustrated in figure 1.2, where the chiral condensate is shown as a function of the temperature T and the baryon density ρ [LKW92]. Different theoretical models predict a close relation between the chiral condensate and the in-medium properties of hadrons, such as the masses[3] or spectral functions [BR91; HL92]. Therefore, even though the quark condensate itself is not directly accessible in the experiment, the observation of changes in these observables could be an indirect method to explore the restoration of chiral symmetry [Nöh98].

Other theoretical models based on chiral symmetry frameworks predict a mass modification for charged kaons in the medium [SBMJ97; Cha01]. As illustrated in figure 1.3, according to these predictions, K^- feel an attractive potential in the nuclear environment, whereas the K^+ potential is slightly repulsive. The strength of the effects increases with the baryon density ρ. The change of the kaon masses in the nuclear medium should result in modified production probabilities for K^- and K^+. Indeed, several experimental results point towards a kaon modification based on in-medium potentials [Cro98; HOA03]. However, additional investigations are necessary in order to evaluate the properties of these potentials, especially the K^-N potential. The difficulties for K^- arise from the presence of further production mechanisms below the KN threshold, in particular the so called strangeness exchange

---

[3] The predicted effect of chiral symmetry restoration on the pole masses of light vector mesons (especially the ρ meson with its strong coupling to the $\pi^+\pi^-$ channel) is criticized in [CRW96] due to the possibility of modifications of the pion propagation in a hot and dense environment. Indeed, experimental results of the NA60 experiment contradict the mass shift of the ρ meson, whereas the broadening of its spectral function is confirmed [D$^+$07; NA609].

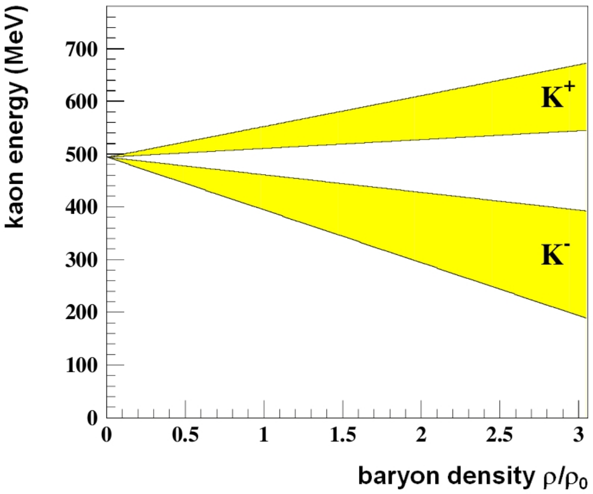

Figure 1.3: Effective mass of K^+ and K^- as a function of the baryon density ρ. The colored regions summarize the results of various theoretical calculations [Stu01; SBMJ97].

channel [FS⁺09; Sch08].

$$\pi\, Y \longrightarrow K^- N \tag{1.2}$$

Here, Y stands for the hyperons Λ and Σ.
Another problematic issue results from the fact that the invariant mass spectroscopy of hadrons in nuclear matter delivers the respective energy states, suffering from collisional shifts and broadening, rather than the scalar masses themselves [YA99]. A recent method to overcome this problem is the production of deeply bound states containing the respective hadron. From the measured binding energy, the hadron-nucleon potential and therefore the scalar hadron mass can be deduced subsequently [YA02]. A first successful application of this method was the estimation of the π^- mass shift in ^{205}Pb and ^{207}Pb via the measurement of narrow $1s$ and $2p$ states [Y⁺96; Y⁺98; WBW97; I⁺00; G⁺02].

1.2 The $\Lambda(1405)$

The existence of an attractive potential between K^- and nucleons implicates the possible formation of K^-N bound states. Indeed the well-known $\Lambda(1405)$ resonance is associated with a bound K^-p system. Its properties are listed in table 1.1 [Par10]. It

Mass	*Width*	*Strangeness*	*Spin*	*Isopin*	*Parity*
1406 MeV/c^2	50 MeV/c^2	-1	$\frac{1}{2}$	0	–

Table 1.1: Properties of the $\Lambda(1405)$.

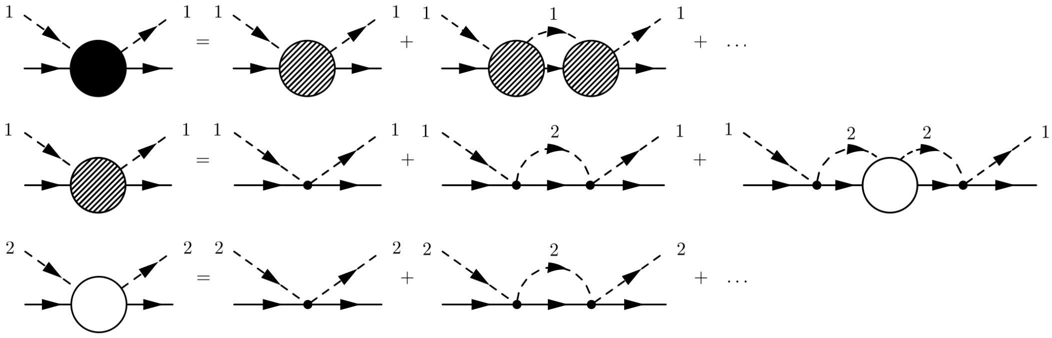

Figure 1.4: Illustration of the coupled channels dynamics with two channels 1 and 2. Baryons are represented by solid, mesons by dashed lines. The black sphere stands for $T^{eff} = T_{11}$, shaded spheres represent V^{eff} and white spheres denote the single channel scattering matrix T_{22}^{single}. The effective scattering matrix $T^{eff} = T_{11}$ is shown by the upper row. The dynamics of channel 2, mediated via T_{22}^{single}, is absorbed into the effective interaction V^{eff}, which only acts in channel 1 (middle row). Hence, the effect of channel 1 on the dynamics of channel 2 is neglected (no channel 1 loops appear in T_{22}^{single}) [HW08].

is located around 30 MeV/c^2 below the $\bar{K}N$ and 75 MeV/c^2 above the $\pi\Sigma$ threshold. Therefore, the $\Lambda(1405)$ can only be directly observed via its decay into $\pi\Sigma$.
In general, the dynamics of hadrons at low energies can be successfully described within the framework of chiral perturbation theory. ChPT is an example of an effective field theory, where the symmetries and symmetry breaking mechanisms of the QCD are incorporated [BNW05]. However, its perturbative application fails in the vicinity of resonances due to rescattering effects [OM01]. Hence, the dynamics of the K^-p channel cannot be studied with ChPT due to the existence of the $\Lambda(1405)$ right below threshold. Instead, the $\Lambda(1405)$ is described to be dynamically generated as an $I = 0$ K^-p quasi-bound state embedded in a strongly interacting $\pi\Sigma$ continuum [HW08]. The theoretical method is based on the combination of $SU(3)$ ChPT with non-perturbative coupled channels techniques [BNW05; KSW95; OR98]. In the coupled channels approach, the meson-baryon scattering matrix[4] T_{ij} is calculated via the self-consistent Bethe-Salpeter equation

$$T_{ij}(\sqrt{s}) = V_{ij}(\sqrt{s}) + V_{il}(\sqrt{s})G_l(\sqrt{s})T_{lj}(\sqrt{s}) \tag{1.3}$$

where $G_l(\sqrt{s})$ is a diagonal matrix collecting the loop integrals in each meson-baryon channel and $V_{ij}(\sqrt{s})$ is the model dependent scattering amplitude derived from the $SU(3)$ effective Lagrangian. It depends on the explicit interaction terms taken into account in the meson-baryon Lagrangian. The effect of different choices for $V_{ij}(\sqrt{s})$ is discussed in [BNW05]. In case of two contributing channels (e.g. $\bar{K}N$ and $\pi\Sigma$),

---

[4] The absolute value of the scattering matrix is directly connected to the differential cross section via Fermi's golden rule: $\frac{d\sigma_{ij}}{d\Omega} \propto |T_{ij}|^2$.

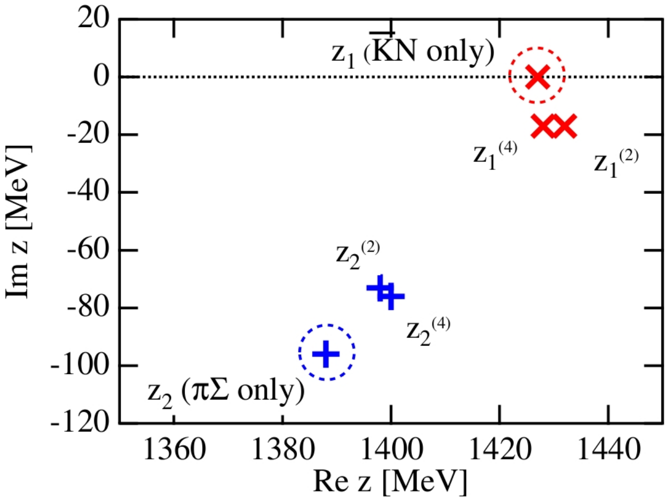

Figure 1.5: Pole positions of the $\bar{K}N$ scattering matrix $T^{eff}(\sqrt{s})$ for single channel, double channel (2) and full channel (4) (i.e. including non-diagonal $\bar{K}N \leftrightarrow \Sigma\pi$ couplings) models in the complex $\sqrt{s}$ plane [HW08].

equation 1.3 is solved by incorporating the dynamics of channel 2 into an effective interaction V^{eff}, which exclusively acts in channel 1. The contributions to the effective scattering matrix T^{eff} are illustrated in figure 1.4.

In [OM01] and [JOO^{+}03] it is argued that the $\Lambda(1405)$ is a superposition of two nearby poles with equal quantum numbers in the complex $\sqrt{s}$ plane[5]. The pole positions of the $\Lambda(1405)$ for different coupled channels models are shown in figure 1.5. According to the calculations, the two poles couple with different strengths to the $\bar{K}N$ and $\pi\Sigma$ channels. Whereas the pole close to the real axis z_1 strongly couples to the $\bar{K}N$ channel, the second pole z_2, which is associated with the $\pi\Sigma$ channel, has a large imaginary part, resulting in a large width Γ_R. Hence, the $\Lambda(1405)$ is described as a K^-p bound state embedded in a $\pi\Sigma$ continuum.

Due to the different coupling strengths of the two poles, the $\Lambda(1405)$ peak position in the invariant mass (π^-, Σ^+) spectrum depends on the initial reaction. As illustrated in figure 1.6, the $\Lambda(1405)$ peak is located at the nominal value of 1405 MeV/c^2 for the $\pi\Sigma \rightarrow \pi\Sigma$ channel (dashed line) but sits at 1420 MeV/c^2 for the $\bar{K}N$ initiated reaction (solid line) [JSI^{+}10]. Therefore, the resonance structure of the invariant mass (π^-, Σ^+) spectrum cannot be associated with the $\Lambda(1405)$ as a K^-p bound state by implication [HW08].

Since the direct decay of the $\Lambda(1405)$ into the K^-p state cannot be measured, the $\bar{K}N$ spectral function has to be determined by indirect procedures, such as multiple fits to scattering data above threshold [BNW05] or the measurement of the energy shift and

---

[5] In general, resonances are expressed as poles in the scattering matrix, where the real and imaginary part correspond to the mass m_R and the half width $\Gamma_R/2$ of the resonance, respectively [HJ12].

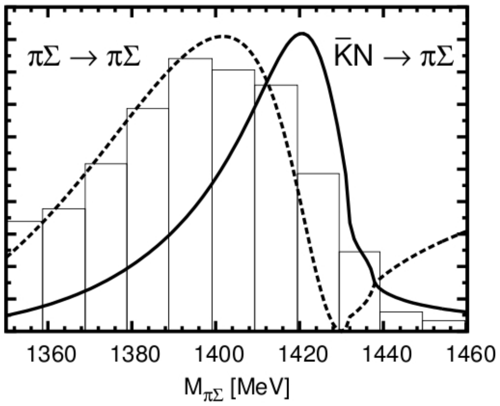

Figure 1.6: Invariant mass (π^-, Σ^+) spectrum from [Hem84] with fitted spectral functions of the channels $\bar{K}N \to \pi\Sigma$ (solid line) and $\pi\Sigma \to \pi\Sigma$ (dashed line) [JSI+10].

broadening of atomic states in kaonic hydrogen [Z+05; O+12]. These measurements at threshold and above set constraints for the extrapolation of the $\bar{K}N$ spectral function into the sub-threshold region.
Recently, the $\Lambda(1405)$ was investigated in elementary $p + p$ reactions via its decay into the neutral $\pi^0\Sigma^0$ channel [FE10; Epp09] and for the first time into the charged $\pi\Sigma$ channels [S+11; Sie10] with the HADES spectrometer at the GSI.

1.3 Kaonic nuclear cluster

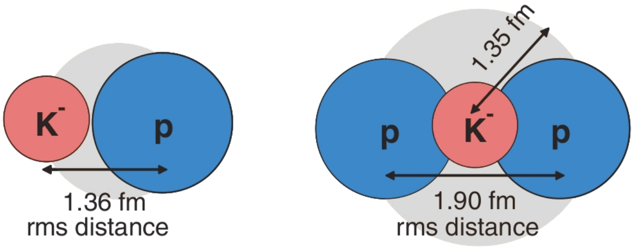

Figure 1.7: Predicted structure of K^-p and K^-pp according to [YA02].

According to the theoretical predictions, the $\Lambda(1405)$ is dominated by the z_1 pole coupling to the K^-p channel [HW08]. Therefore, this K^-p state could act as a doorway for the production of kaonic nuclear cluster by catching additional nucleons. The lightest representative of kaonic nuclear clusters, the ppK^-, was predicted 2002 in [YA02] with a binding energy of 48 MeV. The structure of the ppK^- emerges from a $\bar{K}N$ interaction, which is deduced in a semi-empirical model such to reproduce the binding energy $B_{\Lambda(1405)} = 27\,\text{MeV}$ and width $\Gamma_{\Lambda(1405)} = 40\,\text{MeV}$ of the $\Lambda(1405)$. Figure 1.7 illustrates the predicted structures of $\Lambda(1405)$ and ppK^- with the corresponding rms distances.

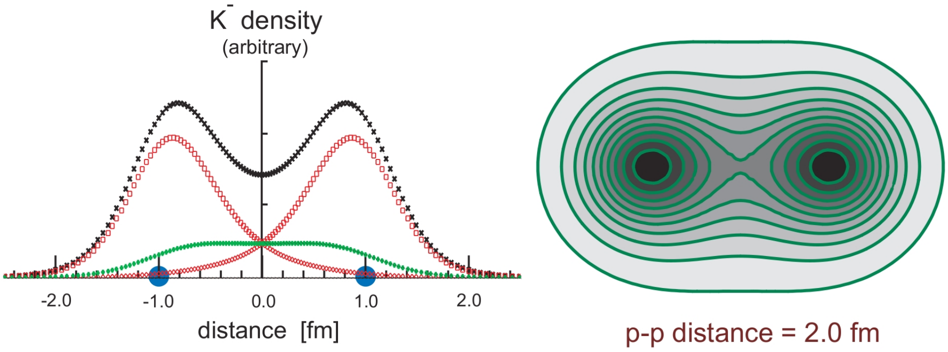

Figure 1.8: Molecular structure of the ppK^-. Left: Projected density distributions of K^- in the ppK^-. The "atomic" part is shown by the red, the "exchange" part by the green distributions. The protons are indicated by the blue dots with a fixed distance of 2 fm. Right: Corresponding K^- contour distribution [YA07].

This simple model assumes a single pole character of the $\Lambda(1405)$, neglecting the $\pi\Sigma \rightarrow \pi\Sigma$ coupling predicted by the coupled channels approach. In [HW08], this phenomenological model is criticized, since within the full framework of chiral dynamics, the K^-p amplitude of the $\Lambda(1405)$ has a maximum at $\sqrt{s} \approx 1420\,\mathrm{MeV/c^2}$ with an associated binding energy of 12 MeV (see figure 1.6). This value is supported by very recent calculations based on realistic NN potentials and sub-threshold energy dependent chiral $\bar{K}N$ interactions, discussed in [BGL12].

However, in [YAOW10] it is argued that the z_2 pole coupling to the $\pi\Sigma$ amplitude is irrelevant to any peak structure in the mass region between the $\pi\Sigma$ and $\bar{K}N$ thresholds. Therefore, an effective single pole nature of the $\Lambda(1405)$ associated with the K^-p bound state is concluded.

Besides this phenomenological ansatz, an independent approach based on three-body $\bar{K}NN - \pi\Sigma N$ coupled channel Fadeev calculations predicts a ppK^- with very similar properties [SGM07].

An interesting feature of the predicted ppK^- is that the K^-p substructure, though modified, persists in the nuclear bound system. This situation resembles a molecular type binding, similar to the hydrogen molecule, where the K^- traverses between the two protons producing "strong covalency" through the strongly attractive $\bar{K}N$ interaction [YA07]. This situation is illustrated in figure 1.8. The left picture shows the projected density distributions of K^- in K^-pp for a fixed p-p distance. The K^- distribution, which is centered around the two protons, is composed of an "atomic" part (red) and an "exchange" part (green), analog to the Heitler-London mechanism of molecular binding. The right picture shows the corresponding contour distribution of K^-.

1.3.1 Experimental results

Experimental results on the existence of kaonic bound states were published by the FINUDA collaboration [FIN05]. In the experiment, K^- from the decay of Φ mesons,

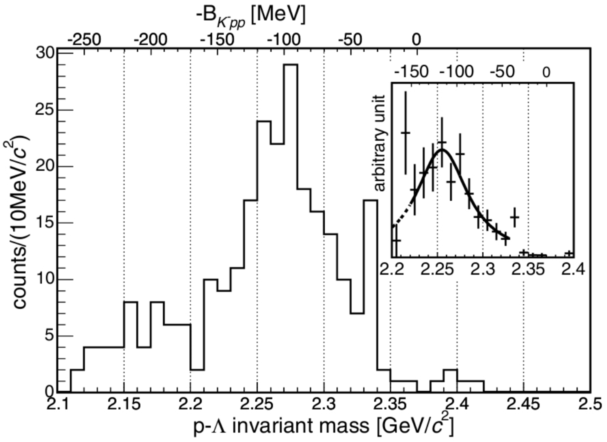

Figure 1.9: FINUDA data showing the invariant mass (p, Λ) spectrum. The distribution associated with the ppK^- is located between 2210 MeV/c^2 and 2320 MeV/c^2 with a peak at 2256 MeV/c^2. The inset shows the acceptance corrected spectrum [FIN05].

which were produced in e^+ e^- collisions at the DAΦNE accelerator, were stopped in different nuclear targets (^{6}Li, ^{7}Li, ^{12}C, ^{27}Al and ^{51}V). The underlying reaction reads as follows.

$$K^- + {}^{A}\mathrm{Z} \longrightarrow {}^{A-2}(\mathrm{Z}-2) + \Lambda + p \tag{1.4}$$

Figure 1.9 shows the invariant mass distribution of the Λ and the p produced in the stopping reactions after the subtraction of background. The spectrum has a peak at 2256 MeV/c^2 which was associated with the ppK^- via its decay into Λ and p (see section 1.3.2). However, this interpretation was criticized in [MORT06], where based

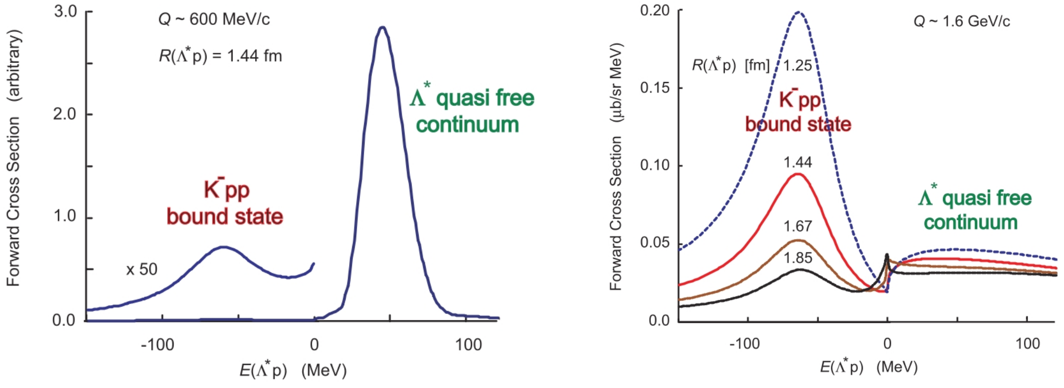

(a) (b)

Figure 1.10: Cross sections for the formation of ppK^- in strangeness transfer reactions (a) and in pp collisions (b) [YA07]. In these pictures, Λ^* denotes the $\Lambda(1405)$.

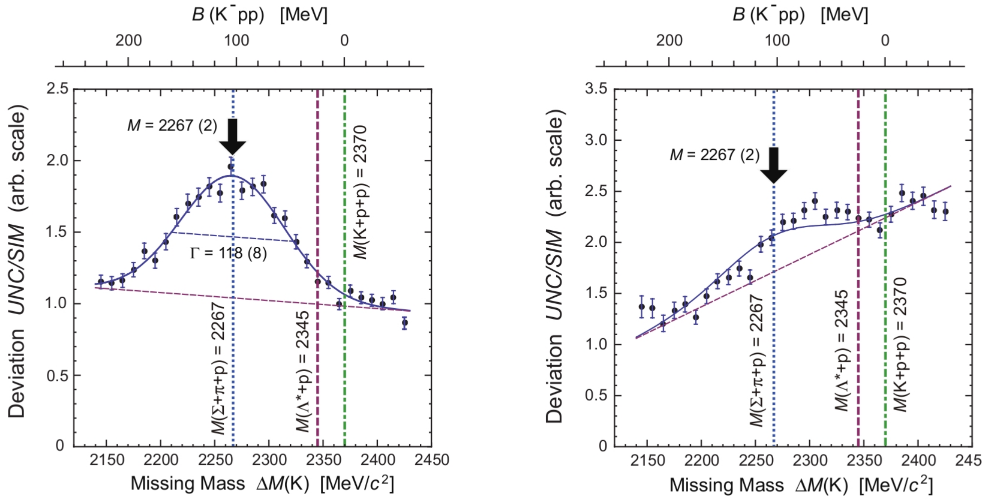

(a) **(b)**

Figure 1.11: DISTO missing mass K^+ deviation spectra for large angle (a) and small angle (b) protons [Y+10].

on simulations the structure was explained as a consequence of final state interaction of the particles produced in nuclear K^- absorption. In [YA07] the possible formation of the ppK^- is explained via a strangeness transfer reaction (equation 1.4 with a $\Lambda(1405)$ instead of a Λ) and the subsequent fusion of the $\Lambda(1405)$ and the proton. Figure 1.10a shows a typical cross section for the formation of ppK^- in strangeness transfer reactions. Due to the small momentum transferred in this reaction[6], the production of ppK^- is suppressed compared to the quasi-free production of a $\Lambda(1405)$ together with a proton.

Another possibility to produce kaonic nuclear cluster is the formation in proton-proton collisions via the following reaction.

$$p + p \longrightarrow ppK^- + K^+ \tag{R.1}$$

Exploiting this production mechanism at a beam energy of 2.85 GeV, the DISTO collaboration reported on the possible discovery of the ppK^- in their missing mass K^+ and invariant mass (p, Λ) spectra [Y+10; Y+11]. Figure 1.11 shows the deviation spectra of the missing mass K^- distribution for large proton angles (a) and small proton angles (b). The observed resonance has a mass of 2265 MeV/c^2 with a corresponding binding energy of 105 MeV/c^2.

The production of ppK^- in pp collisions is predicted to be accompanied by a large momentum transfer [YA07]. Therefore, the probability of a fusion of $\Lambda(1405)$ and p

---

[6] A small momentum transfer causes the produced particles $\Lambda(1405)$ and p to be emitted with a large opening angle. Hence, the probability of a subsequent ppK^- formation is small.

is larger compared to the strangeness transfer reaction. This is illustrated by figure 1.10b, where a dominance of ppK^- formation compared to the quasi-free production in the cross section is visible. Hence, pp collisions are well suited for the investigation of the possible formation of kaonic nuclear clusters.
Recently, the HADES experiment measured pp reactions at a beam energy of 3.5 GeV, motivating an ongoing investigation of the production of ppK^- [SB12].

1.3.2 Kinematics of the pp reaction

In [YA07], kinematical calculations based on reaction R.1 with a beam energy of 3 GeV were performed. At this energy, the production cross section for ppK^- has a maximum value, whereas it is expected to be small for background reactions, according to [IKMW08]. Figure 1.12 shows the kinematical distributions of K^+ and ppK^- for a simulation of reaction R.1. The pictures show that the K^+ are emitted under polar angles θ_{Klab} smaller than 50° in the laboratory frame. The heavier ppK^- are emitted in a narrow forward cone of $\theta_{Xlab} < 10°$.
According to [IKMW08], the ppK^- decays into the following three channels.

$$p + p \longrightarrow ppK^- + K^+$$

$$\hookrightarrow \Lambda + p \qquad 50\% \tag{R.2}$$

$$\hookrightarrow p + \pi^- \qquad 63.8\%$$

$$\hookrightarrow \Sigma^0 + p \tag{R.3}$$

$$\hookrightarrow \Lambda + \gamma$$

$$\hookrightarrow p + \pi^-$$

$$\hookrightarrow \Sigma^+ + n \tag{R.4}$$

$$\hookrightarrow \pi^+ + n + n$$

The analysis in context of the pp experiment performed with the FOPI spectrometer concentrates on the investigation of the ppK^- via its decay into Λ and p (B.R. = 50 %), where the Λ subsequently decays into p and π^- (B.R. = 63.8 %) with a mean free path of $c\tau_\Lambda \approx 7\,\text{cm}$ (reaction R.2). Since this final state only contains charged particles (p,K^+,p,π^-), the intermediate Λ and finally the ppK^- can be reconstructed via the invariant or missing mass technique (see section 2.7.3).
Due to the predicted high laboratory momenta of the ppK^- ($p_{ppK^-} \approx 3\,\text{MeV/c}$), the decay products Λ and p are emitted in forward direction, with corresponding polar angles of around 14° with respect to the ppK^- direction. Hence, the analysis of reaction R.2 requires an identification of protons and pions in forward direction

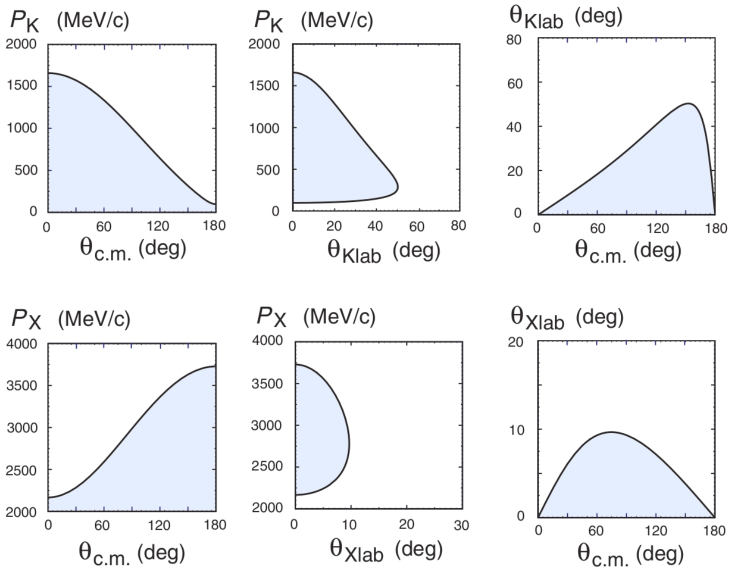

Figure 1.12: Kinematic plots for K^+ and ppK^- (here denoted as X) produced in reaction R.1 at a beam energy of 3 GeV [YA07].

($\theta_{lab} < 30°$), whereas the primary K^+ are measured at larger angles $\theta_{Klab} < 50°$. Due to these requirements, the pp experiment was performed with the FOPI spectrometer at the GSI. It is capable of measuring particles at small polar angles with an azimuthal acceptance of 4π and enables an excellent kaon identification within polar angles of $30 - 50°$ with its MMRPC detector (see chapter 2). Moreover, the SIS18 accelerator of the GSI facility delivers proton beams with the necessary energy of more than 3 GeV.

1.4 N^* resonances

Besides the investigation of the predicted ppK^-, the study of the $pK^+\Lambda$ final state can additionally deliver information about other possible production mechanisms in elementary particle reactions. In case of the reaction

$$p + p \longrightarrow p + K^+ + \Lambda \tag{R.5}$$

three different production mechanisms are possible, which are illustrated in figure 1.13. The two left pictures show the production of the $pK^+\Lambda$ final state via non-resonant meson exchange[7], whereas the right picture illustrates the situation, where an intermediate N^* resonance, e.g. in the $\pi^0 p$ system, is produced, which subsequently

---

[7] In principle, resonances could also be involved in the first K exchange mechanism, however, up to now no resonant states in the K^+p system are known [SW+10].

decays into Λ and K^+. Since the sub-reaction $\pi^0 p \rightarrow K^+\Lambda$ has a high cross section for intermediate N^* production[8], this reaction mechanism is likely to be of major importance for proton-proton induced hyperon production [SW+10; SPM08].

Indeed, experimental results published by the COSY-TOF collaboration indicate a significant contribution of $N(1650)$, $N(1710)$ and $N(1720)$ resonances to reaction R.5 at beam energies of around 2.8 GeV [E+10; SW+10]. By comparing the different resonance strengths at various beam energies, an energy dependence of the single N^* contribution strengths can be deduced. This dependence is shown in figure 1.14. The red diamonds represent the $N(1650)$ strengths, the combined strengths of $N(1710)$ and $N(1720)$ are shown by the blue squares. The dashed curves indicate the fits to the data points and the colored bands visualize the 3σ error bands of the fits to the contribution strengths [E+10]. The plot shows a diminishing of the relative $N(1650)$ contribution with increasing beam energy, whereas the influence of the $N(1710)$ and $N(1720)$ resonances increases.

Extrapolating to the beam energies of the pp experiment predicts a dominant contribution of the $N(1710)$ and $N(1720)$ resonances to the production of the $pK^+\Lambda$ final state compared to the $N(1650)$, which is likely to play a minor role. However, also resonances with higher masses such as the $N(1900)$ could be produced at these energies. Since the occurrence of intermediate N^* resonances has a considerable impact on the angular, momentum and mass distributions of the $pK^+\Lambda$ tracks, the investigation of the ppK^- inevitably requires a basic understanding of the underlying reaction processes. However, also besides their role in the ppK^- analysis, the study of intermediate N^* resonances in the $pK^+\Lambda$ channel could provide further information about the fundamental mechanisms, which govern elementary particle reactions.

---

[8] The production of intermediate Δ^* resonances in this reaction is forbidden due to isospin conservation.

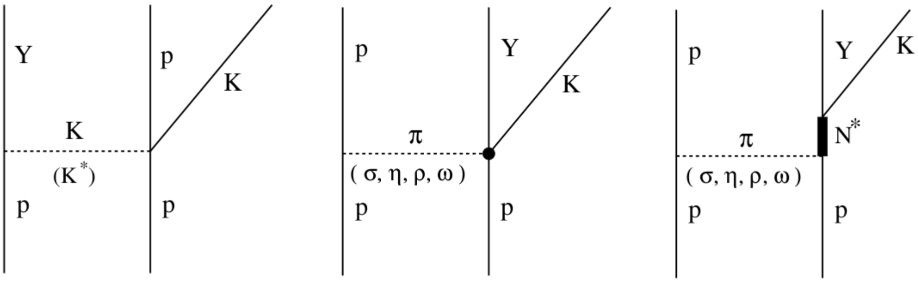

Figure 1.13: Production mechanisms for the $pK^+\Lambda$ final state including non-resonant strange (left) and non-strange (middle) meson exchange. The right picture illustrates the resonant production via an intermediate N^* resonance. The Λ hyperon is denoted by Y [SW+10].

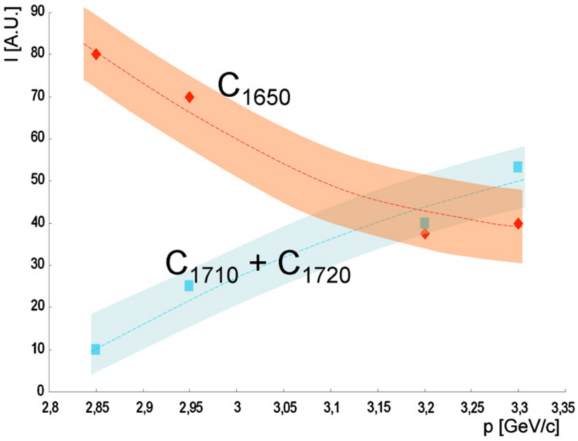

Figure 1.14: Contribution of the $N(1650)$ resonance compared to the sum of $N(1710)$ and $N(1720)$ as a function of the beam momentum [E+10].

2 The FOPI Experiment at GSI

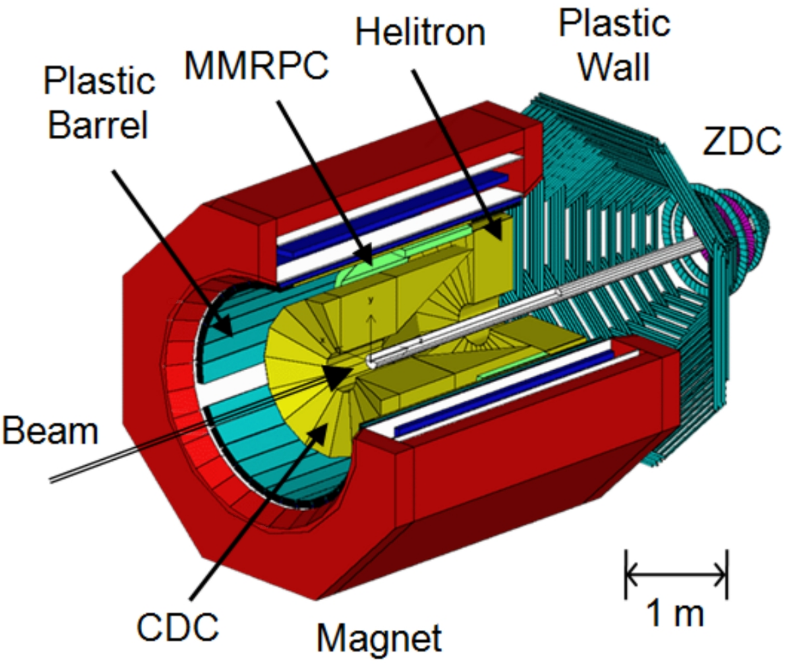

Figure 2.1: Schematic view of the FOPI spectrometer with its sub-detector systems [RHK11].

The FOPI detector system is a fixed target experiment located at the 'Schwerionensynchrotron' SIS18 of the 'Helmholtzzentrum für Schwerionenforschung' GSI in Darmstadt [Ryu09]. It is used to study the properties of nuclear matter at moderate temperatures and baryon densities [RHK11]. The name FOPI is an acronym for **FO**ur **Pi**, which indicates the spectrometers capability of detecting charged particles within a solid angle of almost 4π.

The SIS18 synchrotron has a circumference of 213 m and a magnetic rigidity of 18 Tm. It can deliver heavy ion beams with energies up to 2 AGeV and proton beams with 4.5 GeV maximum energy, corresponding to a momentum of 5.4 GeV/c. The accelerated particles are led to the experiment, where they collide with a target.

In order to investigate the properties of the created nuclear matter, it is necessary to measure the particles which are produced in the reaction process and their decay products [Mün08; Ber09]. At the same time, it is not only important to identify the particles, but also to detect their characteristics as e.g. momentum, energy or phase space distribution. For this purpose, the FOPI spectrometer is constructed in a modular design (Figure 2.1), where the different sub-detectors specifically measure certain particle observables [Rit95]. The tracks of charged particles are reconstructed by the two drift chambers CDC and HELITRON. Together with a homogeneous magnetic field of 0.6 T, which is produced by the large superconducting solenoid magnet surrounding the drift detectors, the momentum and the charge polarity of the particles can be calculated [Kim04]. Combining the particles trajectories with the information delivered by the time-of-flight (TOF) detectors, which are located inside the solenoid magnet (Barrel and RPC) and downstream (PLAWA and ZDC), allows to determine the velocity.

2.1 Tracking detectors

FOPI uses drift chambers as tracking detectors. Drift chambers resemble ordinary **M**ulti**W**ire **P**roportional **C**hambers (MWPC), which consist of alterning planes of parallel proportional wires, placed in a gas volume between two cathodes. Charged particles traversing the gas ionize the gas atoms, creating electron-ion pairs. The electrons drift towards the anode wires, accelerated by an electric field, which is established by the negatively charged cathodes and the positively charged anode wires. Due to the large field gradient in the vicinity of the wires, the electrons gain enough energy to further ionize the gas, resulting in a local charge avalanche. The charges created in this avalanche induce a signal on the neighboring signal wires, which is proportional to the energy of the detected particle.

In drift chambers, additionally the drift time of the primary electrons in the gas volume is measured, to determine the spatial position of the particle, leading to an improved spatial resolution and a reduced number of readout channels due to a larger wire spacing. This requires a well known relation between the distance of the created electrons and the drift time, which is guaranteed by additional field wires in order to avoid regions of low electric field [Leo94; Ket10].

2.1.1 CDC

The cylindrical shaped **C**entral **D**rift **C**hamber (CDC) is the main tracking detector of the FOPI spectrometer. Its outer cylinder has a length of 2 m and a diameter of 1.8 m. The length of the inner cylinder is 80 cm with a diameter of 30 cm, leading to conical end caps on both sides (see Figure 2.2) [Ryu09; Kut99].

In the xy plane, the CDC is divided into 16 sectors, each of them separated by 252 cathode wires (125 µm diameter) and containing 61 field wires[1] (125 µm diameter) and 60 signal wires[2] (20 µm diameter), all of which are aligned parallel to the beam axis [Kim04; Ben07].

The gas composition of 88% Argon, 10% Isobuthane and 2% Methane leads to an electron drift velocity of 4 cm/µs, nearly independent of the drift field and to a

---

[1] Also referred to as potential wires.

[2] Also referred to as sense wires.

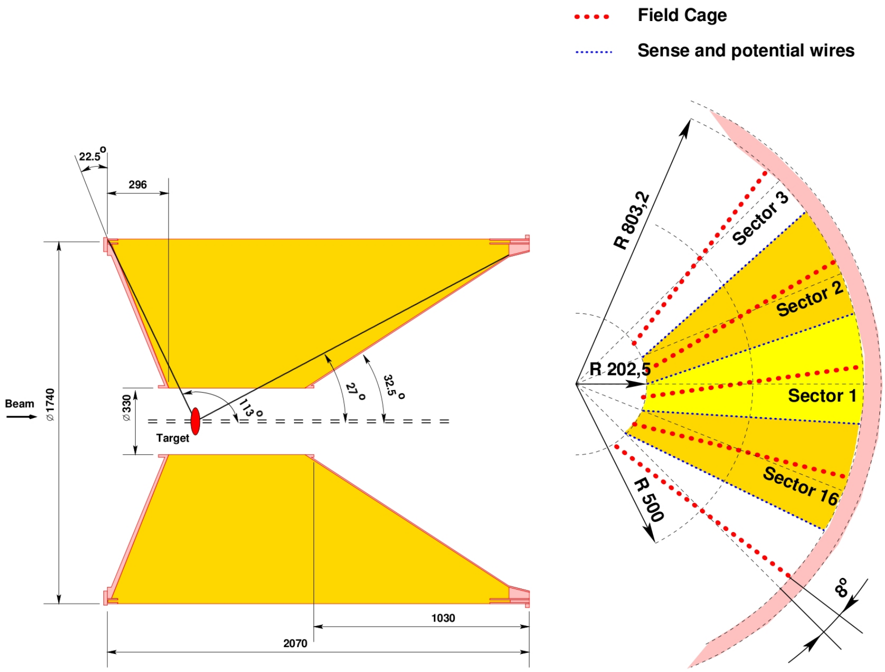

Figure 2.2: Cross sections of the CDC [Ber09].

momentum resolution of 7% to 12% [Ben07; Mün08]. Applying a voltage of −15 kV to the cathode wires generates a drift electric field of about 800 V/cm, which accelerates the primary electrons generated by an incident charged particle towards the signal wires, where the avalanche formation occurs and where the charges are collected. In order to provide an electric field with a $\frac{1}{r}$ behavior around the grounded signal wires, a voltage of −1275 V is applied to the field wires [Ben07].

The flight path of the traversing particle is characterized by various hitpoints in the CDC. The position of the hitpoints in the xy plane is determined by the location of the sense wires and the drift time of the electrons. The z component can be reconstructed with the charge division method[3] by reading out both ends of the signal wires, which have a resistivity of 500 Ω/m [Rit95].

Drift chambers measure surfaces of constant drift time around the signal wires, which introduces a left-right ambiguity with respect to the wires within a readout plane. Each hitpoint has a mirror hit on the other side of the wire plane. In order to avoid those ambiguities, the wire planes are tilted by 8°. The mirror tracks can be identified and the corresponding hit points discarded, since they do not originate from the target. In addition, the wires are alternately staggered by ±200 µm to further improve the identification of mirror tracks and to maintain electrical stability

---

[3] The ratio of the charges collected on the left and right ends of the signal wire Q_L and Q_R is given by $\frac{Q_L}{Q_R} = \frac{z}{L-z}$, where L is the wire length and z the distance of the hit to the left end along the wire [Kim04].

[Rit95; Kre97].

The CDC has a spatial secondary vertex resolution of 0.5 cm in the xy plane and 2 cm in the z direction. It covers a polar angle of 27°< Θ <113° and an azimuthal angle of 2π [Ber09].

2.1.2 HELITRON

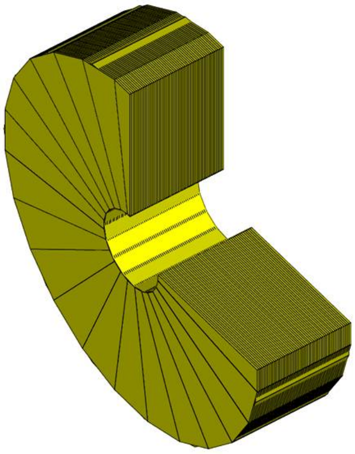

Figure 2.3: Sketch of the HELITRON drift chamber [Har03].

The second drift chamber of the FOPI spectrometer for the tracking of charged particles in forward direction is the HELITRON (Figure 2.3) [Ryu09]. It is cylindrical shaped with an inner diameter of 42 cm, an outer diameter of 198 cm and 60 cm length, covering polar angles of 4.5°< Θ <27° with full azimuthal acceptance [Kre97; Mün08]. The name HELITRON originates from the helix trajectory of charged particles in the solenoidal magnetic field [4].

The drift chamber is divided into 24 sectors, where each sector contains 54 field wires (125 µm diameter) for field shaping and 53 signal wires (50 µm diameter) for charge collection [Ryu09]. In contrast to the CDC the field and signal wires are orientated perpendicularly to the beam axis, running radially outward, to accommodate the helix shaped flight path of the measured particles. The homogeneous drift field of 750 V/cm is generated by a drift voltage of −12.3 kV and a voltage of −1.6 kV applied to the field wires [Har03]. Analogous to the CDC, the signal wires are staggered for the identification of mirror tracks and read out at both ends, to provide the radial spatial component of the hits via charge division with a resistivity of 1 kΩ/m [Ryu09; Har03]. The gas mixture of 88% Argon, 10% Isobuthane and 2% Methane is the same as in the CDC. The momentum resolution of the HELITRON is around 7% [Mün08].

Normally the HELITRON cannot be used for the reconstruction of secondary vertices,

---

[4] The HELITRON is placed at the end of the solenoid magnet where the magnetic field starts to become inhomogeneous [Kre97].

due to the large distance of the detector to the target. In this experiment, an additional hitpoint close to the target is delivered by the silicon based Λ-Trigger SiΛVio (see section 2.5), which enables the reconstruction of secondary vertices in the forward direction [Ber09].

2.2 Time of flight detectors

The FOPI spectrometer includes several detectors for the measurement of the flight time of the particles traversing the drift chambers. The flight time is given by the difference of a stop signal, delivered by the time of flight detectors, which are placed behind the drift chambers, and a start signal, provided by a start counter, placed right inside the beam in front of the target (see section 2.3.1). Together with the reconstructed flight path length and the momentum, this information can be used to identify the particles (see section 2.7.2) [Ber09].

Furthermore, since they are very fast, the time of flight detectors are used to create a trigger signal (LVL1), which starts the data acquisition during the experiment (see section 2.6). The centrality of the collision can be determined via the hit multiplicity [Mün08].

2.2.1 Plastic Barrel

The Plastic Barrel detector surrounds the CDC and consists of 180 plastic scintillator strips, aligned parallel to the beam axis with a length of 2.4 m. 6 single strips are combined to one module, respectively [Har03]. The Barrel covers a polar angle of $50° < \Theta < 117°$ and the full azimuthal angle, except for two holes of 11° due to the mounting structure of the CDC [Ber09].

Charged particles crossing the plastic scintillator, excite the organic material, which deexcites through the emission of luminescent light. Via total reflexion, this light is guided through the scintillator, which is transparent for its own emitted radiation[5]. The scintillators are read out on both ends via photomultipliers, which convert the photons into an electric current. Additional to the time of flight information (in combination with the start signal), the plastic strips deliver an extra hit, whose z component is defined by the time difference between the two photomultipliers [Ryu09].

In the pp experiment, the time resolution of the Plastic Barrel varies between 300 ps and 400 ps, dependent on the position of the strip and the light yield [Ber09].

2.2.2 MMRPC

The MMRPC (**M**ulti Gap **M**ulti Strip **R**esistive **P**late **C**hamber) barrel is a gaseous detector for precise time of flight measurements within polar angles of $27° < \Theta < 50°$

---

[5] In some cases, the scintillator contains several wavelength shifters, which absorb the light and reemit it with a smaller wavelength. This method can be necessary, if the photo detectors are sensitive to a certain wavelength interval.

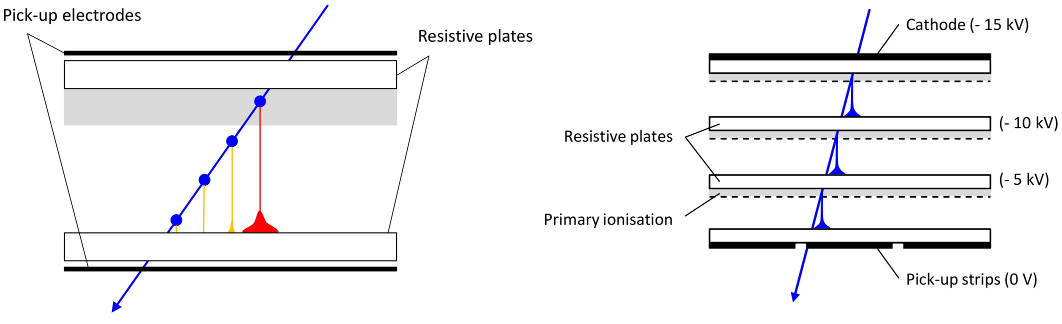

(a) (b)

Figure 2.4: (a): Avalanche formation in a Single Gap RPC. Only primary ionization which occurs within the region close to the cathode (gray area) leads to a detectable signal (red avalanche). (b): Schematic view of a Multiple Gap RPC.

(see Figure 2.1).
MMRPCs are advancements of ordinary RPCs, which consist of two gas enclosing layers of high-ohmic material (e.g. glass), coated with copper on the outside. A voltage difference, applied to the two electrodes, produces an electric field, which accelerates the primary electrons, created by a traversing particle, towards the anode, where the avalanche formation takes place. Primary ionization happens only within a small region since only avalanches that originate close to the cathode grow big enough to result in a detectable signal (Figure 2.4a) [ZCH+96]. The avalanches induce signals on the anodes, which can be read out on both ends, to reconstruct the spatial position of the hit. Finally, the charges are neutralized in the resistive layers in front of the electrodes [Ber09]. The variation of the position of the initial clusters, produced in the primary ionization region, introduces a time jitter, which limits the time resolution of the RPCs [ZCH+96].
MMRPCs have been developed, in order to improve the timing by decreasing the primary ionization and the avalanche growth region. This is achieved by subdividing the gas volume into multiple gaps (Figure 2.4b). In addition, the anodes are segmented, to enhance the spatial resolution.
The FOPI MMRPC barrel consists of 30 super-modules, surrounding the CDC, each containing 5 single MMRPCs, which are mounted alternately staggered in two layers, to avoid acceptance holes [Sch04]. It has an intrinsic time resolution of less than 65 ps [Kiš10]. Together with the start detector for the pp experiment (see section 2.3.1), which is the limiting factor, the overall time resolution is around 180 ps. Analogous to the Plastic Barrel, the mounting structure of the CDC is reflected in two acceptance holes of approximately 11°. The gas mixture is composed of 88% R134a[6], 15% SF_6 and 5% Isobuthane. The high drift field of 110 kV/cm is generated by a drift voltage of 9.6 kV, which is applied to the cathode [Kiš10].

---

[6] Also referred to as tetrafluorethan.

2.2.3 PLAWA

The PLAWA (**Pla**stic **Wa**ll) is the time of flight detector of the forward system, covering polar angles of 7°< Θ <30°. It consists of 8 radial sectors, each containing 64 plastic scintillators [Ryu09]. The strips, whose length range from 45 cm for small to 165 cm for large polar angles, are read out on both ends for the position measurement of the hit [Har03]. The intrinsic time resolution varies between 80 ps to 120 ps, corresponding to a spatial resolution of 1.2 cm to 2 cm [Ryu09]. The total time of flight resolution together with the start detector is around 400 ps.

2.2.4 ZDC

The flight time of particles with small polar angles between 1° and 7° is measured with the **Z**ero **D**egree **C**ounter (ZDC). It forms the inner part of the forward wall and is made of 252 plastic scintillator strips, which are arranged in 7 concentric rings around the beam axis [Ryu09]. In contrast to the other scintillator detectors, the strips are read out on one side, which is turned away from the beam. The ZDC has an intrinsic time resolution of 230 ps to 340 ps [Ber09].

2.3 Beam detectors

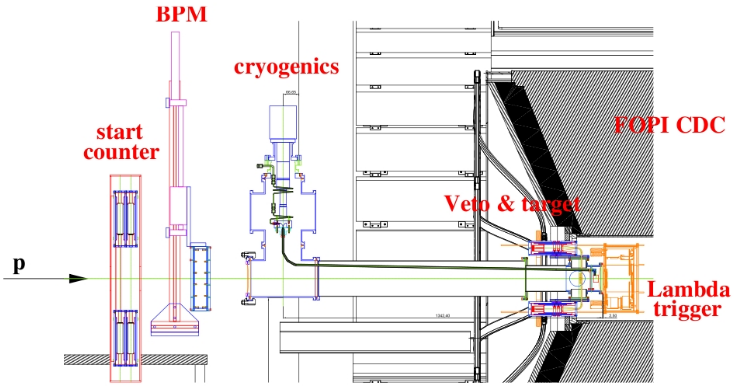

Figure 2.5: Location of the beam detectors, target system and Λ trigger [BHS$^+$09].

2.3.1 Start detector

The start signal for the time of flight measurement is delivered by a start detector, which is placed directly inside the beam in front of the target (Figure 2.5). It is composed of 5 vertically arranged, 1 cm thick and 2 mm wide scintillator strips [BHS$^+$09]. The segments are read out on both ends with photomultiplier tubes (PMTs), which are magnetically shielded and equipped with power supply boosters, to maintain the high gain at high rates up to $2 \cdot 10^6$ 1/s. The start detector achieves an intrinsic time resolution of around 130 ps [BHS$^+$09].

2.3.2 Veto detector

Besides the interaction with the target, the beam particles can furthermore interact mutually before hitting the target and attain to the detectors [Ber09]. In order to suppress those events, a veto detector is placed between start detector and target (Figure 2.5). It consists of 2 half-divided 5 mm scintillators with a hole in the center, which limits the usable target size in the xy plane to a circle with a diameter of 1 cm (Figure 2.6). Because of the magnetic field of 0.6 T close to the target, fine-mesh PMTs are used for the read out, since they are capable of operating even within strong magnetic fields [BHS+09]. Particles, scattered off the beam axis due to reactions before target interaction, are detected by the veto detector, which creates a trigger signal. This signal is fed into the general trigger logic, stopping the data acquisition, if such an event occurs.

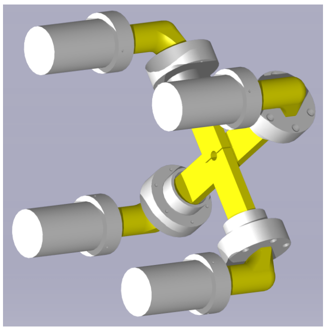

Figure 2.6: Sketch of the veto detector: The scintillators are indicated in yellow, the PMTs in gray [Ber09].

2.4 Target

For the pp experiment, a liquid hydrogen LH_2 target was used, consisting of a cryogenic cooler and a cylindrical target volume with 1.5 cm diameter and 2 cm width [BHS+09]. The cooler is located outside of the beam pipe (Figure 2.5) and is connected to the target volume via a thin synthetic pipe, through which the liquid hydrogen flows due to gravity. The evaporated hydrogen flows back into the cryostat via a aluminum pipe, which surrounds the synthetic tube. This procedure affords a final temperature of approximately 12 K [Ber09].

The luminosity $\mathcal{L}$ for fixed target collisions is defined by the following relation

$$\mathcal{L} = n_t \cdot L_t \cdot \dot{N}_b \tag{2.1}$$

where n_t is the target particle density, L_t the width of the target volume and $\dot{N}_b$ the beam rate.

The target particle density is calculated via the Avogadro constant N_A, the density and the molar mass of LH_2 as follows.

$$n_t = \rho_{LH_2} \frac{N_A}{\frac{1}{2} M_{mol,LH_2}} = 70.8 \frac{kg}{m^3} \frac{2 \cdot 6.022 \cdot 10^{26} \frac{1}{kmol}}{2 \frac{kg}{kmol}} = 4.12 \cdot 10^{28} \frac{1}{m^3} \tag{2.2}$$

Together with the number of around 10^7 beam protons per 10 seconds total spill length and the target width of $L_t = 0.02$ m, the luminosity for the pp experiment calculates as

$$\mathcal{L} = 4.12 \cdot 10^{28} \frac{1}{m^3} \cdot 0.02m \cdot \frac{10^7}{10s} = 82.4 \frac{1}{mb\ s} \tag{2.3}$$

Finally, the luminosity multiplied with the total cross section for pp reactions at 3 GeV beam energy $\sigma_{pp} = 44\,\text{mb}$ determines the target reaction rate of the experiment.

$$R_{pp} = \mathcal{L} \cdot \sigma_{pp} = 82.4 \frac{1}{mb\ s} \cdot 44mb = 3.63kHz \tag{2.4}$$

This reaction rate is 6 times higher than the recording rate of the FOPI DAQ system of 0.6 kHz, which is limited mainly due to the dead times of the drift chambers [Mün08; Mün12]. Therefore, a number of different trigger conditions is used to reduce the data rate (see section 2.6).

2.5 Λ Trigger SiΛVio

The Λ Trigger SiΛVio (**Si**licon for Λ-**V**ertexing and **I**dentification **O**nline) has been developed especially for the pp experiment, to generate a trigger signal on the decay signature of Λ hyperons. Additionally to the enhancement of events containing Λ's, SiΛVio improves the tracking capability of the FOPI spectrometer for particles emitted in forward direction.

The Λ hyperons produced in the decay of kaonic bound states partially (B.R. = 63.8%) decay with a mean free path of $c\tau_{\Lambda} \approx 7\,\text{cm}$ into a proton and a negatively charged pion, which are mainly emitted into the forward direction (see section 1.3.2) and therefore detected by the HELITRON drift chamber and the PLAWA. Due to the large distance of the HELITRON to the Λ decay vertex, the detector is not well suited for secondary vertex reconstruction. By providing an additional hitpoint close to the target, SiΛVio enables the reconstruction of the Λ decay vertex.

The SiΛVio trigger is placed right after the target inside the CDC (Figure 2.5) and consists of two layers of silicon detectors: SiΛVio-A and SiΛVio-B.

SiΛVio-A is an annular silicon detector with an inner diameter of 14 mm and an outer diameter of 47 mm, which is divided into 32 sectors. It covers full azimuthal acceptance and polar angles of $10° < \Theta < 25°$ [Mün12]. The silicon is read out on only one side, since it is exclusively used for the trigger generation.

The second layer SiΛVio-B contains 8 single rectangular silicon detectors with an active area of 40x60 mm^2. Each detector is read out on both sides and divided into 40[7] and 60 1 mm thick strips respectively, which are orientated perpendicularly [Fab10]. The position of the hitpoints can be reconstructed by combining the signals of both sides.

The distances between the target and SiΛVio-A of 3 cm and between the two silicon layers of 12.5 cm are adjusted according to the mean free path of the Λ hyperons, rendering 60% of the Λ's decay between SiΛVio-A and SiΛVio-B (Figure 2.7) [MFBH10]. The neutral Λ's traverse the first layer unobserved, while the primary kaons and protons are detected. The protons and the pions, which are produced in the Λ decay, are measured afterwards in the second silicon together with the two primary particles.

---

[7] For read out reasons, the 40 strips are grouped to 16 strips.

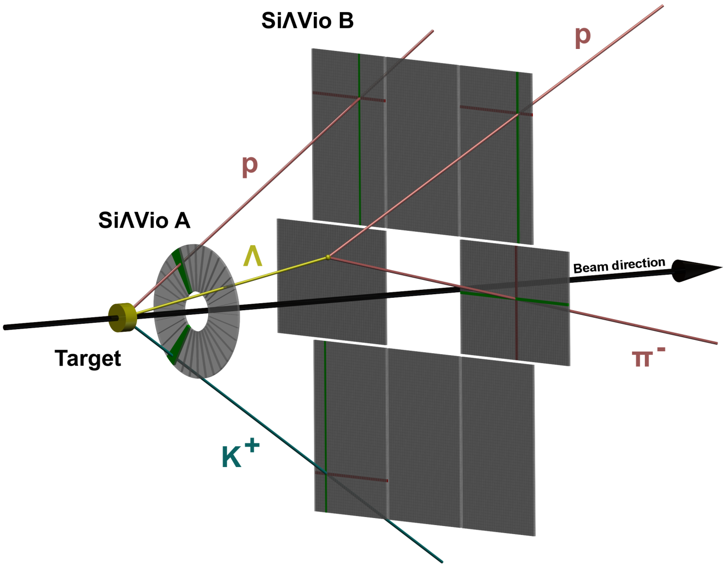

Figure 2.7: Scheme of the trigger concept of SiΛVio: The kaon and the proton are detected in the first layer, while the neutral Λ is traverses unobserved. Subsequently, the lambda decays into a proton and a pion, which are measured in the second silicon layer together with the two primary particles. The increase of the multiplicity in SiΛVio-B with respect to SiΛVio-A defines the trigger pattern.

This difference in multiplicities of the two silicon layers defines the Λ-trigger condition for the SiΛVio detector (see section 2.6).
For the pp experiment, the trigger condition was set such, to have at least 1 particle detected in SiΛVio-A and minimum 2 particles measured by SiΛVio-B. Based on simulations, this condition is optimized to record Λ-trigger events with a maximum efficiency[8] and to simultaneously guarantee a high Λ enhancement capability [MFBH10].

2.6 Trigger conditions

Like any high energy experiment, the FOPI spectrometer uses several trigger conditions to select interesting events to be recorded for the later analysis. Due to the limited DAQ rate, a first selection has to be made online. Generally, the most fundamental trigger condition is based on the multiplicity in the time of flight detectors, which indicates, that a real reaction took place. In combination with a start detector and a veto detector to reject pre-target reactions, the LVL1 trigger is defined. The explicit conditions, which were used for the pp experiment, are listed in the following.

---

[8] If the DAQ rate exceeds the trigger rate, Λ-trigger events can get lost due to dead time.

- LVL1 trigger
    - ≥ 1 hit in the start detector
    - < 1 hit in the veto detector
    - ≤ 1 hit in the ZDC
    - ≥ 1 hit in the PLAWA
    - ≥ 1 hit in the MMRPC or Plastic Barrel
- Λ trigger
    - ≥ 1 hit in SiΛVio-A
    - ≥ 2 hits in SiΛVio-B
- LVL2 trigger
    - LVL1 and Λ trigger

As explained in the previous section, the SiΛVio detector delivers a Λ-trigger, based on the difference in multiplicities of the two silicon layers SiΛVio-A and SiΛVio-B. Together with the LVL1 trigger, this condition constitutes the LVL2 trigger.
Depending on the special requirements of the analysis, the different trigger conditions can be combined in each possible way.

2.7 Particle identification with the FOPI spectrometer

In order to study the properties of nuclear matter created in particle collisions, it is essential to identify the produced particles of interest by measuring their mass and charge polarity. Since it is not possible to measure the mass directly, it has to be reconstructed from other observables.
One of these observables is the momentum, which is measured with the drift chambers CDC and HELITRON. A non-neutral particle with charge q and velocity $\vec{v}$ moving inside of a magnetic field $\vec{B}$ is deflected from its original flight path due to the Lorentz force

$$\vec{F} = q\left(\vec{E} + \vec{v} \times \vec{B}\right) \tag{2.5}$$

which acts only, if the particles velocity has components, which are non-parallel to the magnetic field. Since the FOPI solenoid magnet generates a homogeneous field inside the CDC parallel to the beam axis, the trajectory of the particle is bent circularly in the xy plane, where the Lorentz force acts as centripetal force. Solving this relation for the transverse momentum component p_t delivers the following expression.

$$p_t = qB_z r \tag{2.6}$$

B_z is the z-component of the magnetic field $\vec{B} = (0{,}0{,}B_z)^T$. Thus, the transverse momentum of CDC tracks can be calculated by measuring the radius of the circular

track inside the magnetic field.
As mentioned before, the HELITRON is already located in the region, where the magnetic field starts to become inhomogeneous. Therefore, the method described before is not applicable. In this drift chamber, the momentum reconstruction is done via an interpolation with quintic B-splines in an iterative way [Ple99; Win74].
Another standard method for momentum reconstruction is the measurement of the tracks sagitta s, which is the deviation of the curved track from a straight line with length L. The sagitta is related to the magnitude of the particles transverse momentum p_t via the following equation [Gru93].

$$p_t = \frac{qB_zL^2}{8s} \tag{2.7}$$

Therefore, the transverse momentum of charged particles can be reconstructed by measuring the sagitta of their flight tracks with the tracking detectors. Since the sagitta decreases with increasing velocity, the relative error of p_t is proportional to the transverse momentum of the particle [PRCZ09].

$$\frac{dp_t}{p_t} \propto p_t \tag{2.8}$$

The total momentum can be calculated together with the polar angle $\varTheta$ of the track.

$$p = p_t sin(\varTheta) \tag{2.9}$$

Besides the momentum, additional observables are required in order to identify charged particles by determining their mass. The FOPI spectrometer offers 2 possibilities for this purpose.

2.7.1 Energy Loss

The first possibility is to measure the energy loss $\frac{dE}{dx}$ of charged particles in the detector material.
Charged particles passing through matter deposit energy mainly by undergoing inelastic collisions with electrons of the material. This process is characterized by the average energy loss per unit pathlength[9], which is given by the Bethe Bloch formula [Leo94].

$$\left\langle -\frac{dE}{dx} \right\rangle = \frac{4\pi}{(4\pi\varepsilon_0)^2} \frac{z^2e^4n_e}{m_ec^2\beta^2} \left[\frac{1}{2} ln \left(\frac{2m_ec^2\beta^2\gamma^2T_{max}}{I^2} \right) - \beta^2 - \frac{\delta}{2} \right] \tag{2.10}$$

with

- $z \cdot e$: charge of incident particle
- n_e: electron number density of material

---

[9] Also referred to as stopping power.

- m_e: electron mass
- $\beta = \frac{v}{c}$: velocity of incident particle
- γ: Lorentz factor
- T_{max}: maximum kinetic energy transferred to electron in single collision
- I: mean excitation energy
- δ: density correction factor

The average energy loss as a function of the momentum depends on the particle mass. This enables the identification of charged particles within a certain momentum interval, depending on the specific detector resolution (see Figure 2.8).

2.7.2 Time of flight

The second method uses the flight time Δt of the particle, which is measured with the time of flight detectors. Together with the length of the flight track L extracted from the drift chambers, the velocity $\beta c = \frac{L}{\Delta t}$ can be calculated, which defines, in combination with the momentum p, the mass m_0 of the particle according to the following relation [Mün08].

$$p = m \cdot v = m_0 \cdot \gamma \cdot \beta c \tag{2.11}$$

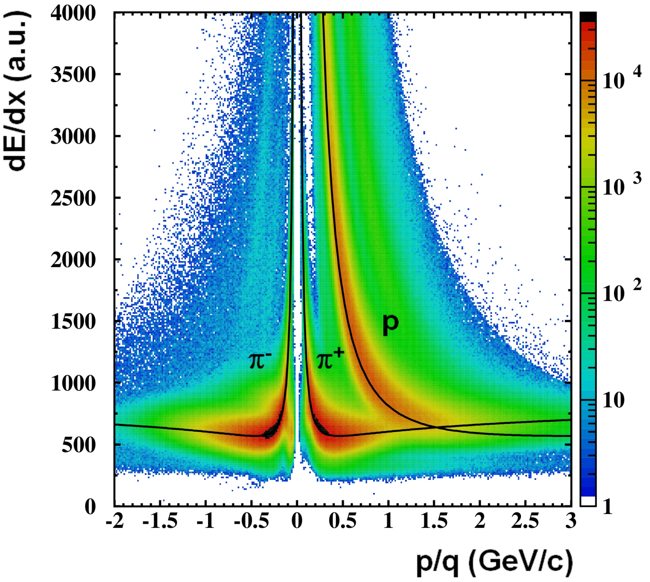

Figure 2.8: Particle identification via the energy loss of charged particles in the CDC drift chamber for the data taken during the pp experiment. The black curves indicate the theoretical positions of the different particle species according to the Bethe-Bloch equation (2.10).

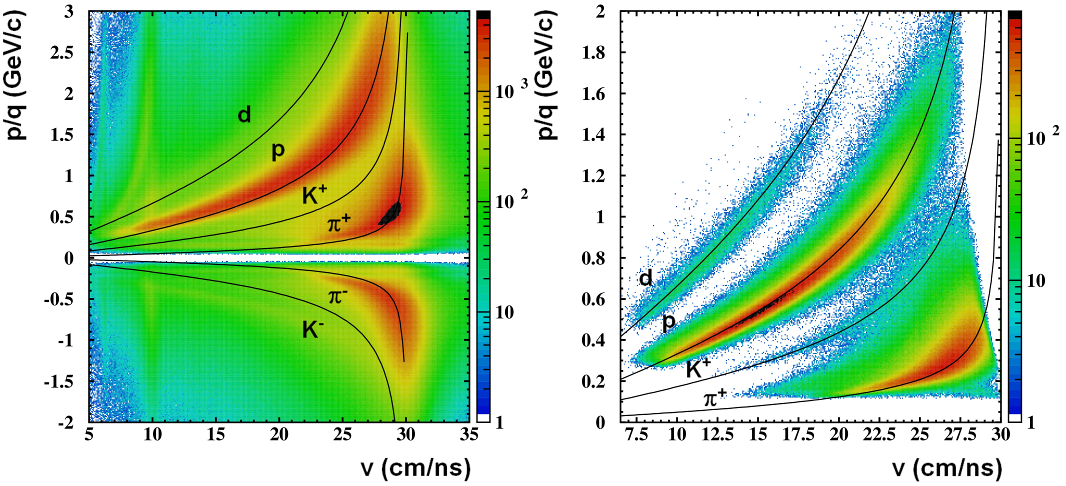

(a) PID with the PLAWA **(b)** PID with the MMRPC

Figure 2.9: Particle identification via the time of flight measurement for the data taken during the pp experiment. The black lines represent the positions of the different particle species according to equation 2.11. With the RPC, kaons can be separated from protons and pions, which is not possible with the PLAWA.

Figure 2.9 shows the momentum p per charge q plotted against the velocity v, where the time of flight is measured with the PLAWA (left) and the RPC (right). The data was recorded during the pp experiment. With the PLAWA detector, the separation of kaons from protons and pions is not possible due to its limited time resolution. In contrast, the excellent time resolution of the MMRPC enables the identification of kaons, which is necessary for the reconstruction of ppK^-, since its decay contains a K^+ in the final state.

2.7.3 Invariant mass and missing mass technique

The methods described above allow to identify charged particles, which are directly measured in the FOPI sub-detectors. However, in many reactions, particles with short lifetimes are produced, which cannot be measured directly, since they decay before reaching the detectors. Anyhow, under certain circumstances it is possible to reconstruct the decayed particles afterwards.

In the center of mass (CMS) reference frame of the daughter particles, the mother particle is at rest at the moment of the decay. Therefore, the sum of the 4-momenta $p_i^\mu = (E_i, \vec{p}_i)^T$ of the daughter particles is exclusively determined by the mass of the mother, referred to as the invariant mass. Since this sum is connected to the square of the mother particles 4-momentum, which is a Lorentz invariant scalar, this relation is valid in every reference frame. If now all n decay products of the mother particle are detected, its mass can be reconstructed via the invariant mass technique, using the following equation.

$$M_{inv} = \frac{1}{c^2}\sqrt{p^{\mu}_{mother}\, p_{\mu,mother}} = \frac{1}{c^2}\sqrt{\left(\sum_{i=1}^{n} E_i\right)^2 - \left(\sum_{i=1}^{n} \vec{p}_i\right)^2 c^2} \tag{2.12}$$

Another method to reconstruct the mass of a decayed particle exploits energy and momentum conservation. If the particle of interest is produced together with m other particles, which are measured in the detectors, it is possible to reconstruct the so called missing mass via the subsequent formula

$$\begin{aligned} M_{miss} &= \frac{1}{c^2}\sqrt{p^{\mu}_{mother}\, p_{\mu,mother}} \qquad (2.13) \\ &= \frac{1}{c^2}\sqrt{\left(E_{beam} + E_{target} - \sum_{j=1}^{m} E_j\right)^2 - \left(\vec{p}_{beam} + \vec{p}_{target} - \sum_{j=1}^{m} \vec{p}_j\right)^2 c^2} \end{aligned}$$

where $p^{\mu}_{beam} = (E_{beam}, \vec{p}_{beam})^T$ and $p^{\mu}_{target} = (E_{target}, \vec{p}_{target})^T$ are the 4-momenta of the beam and the target particle, respectively [Sie10].

If energy and momentum conservation are fulfilled, the invariant and the missing mass are equivalent.

3 The Kinematic Refit

Kinematic fitting is a well-established tool in the exclusive analysis of particle reactions to reduce background and to improve the mass resolution of intermediate particles, which are reconstructed via the invariant or missing mass technique [BLL10; Sie10]. For the analysis of the ppK^-, it is essential to have a good mass resolution and S/B ratio of the intermediate Λ, which itself has to be reconstructed. This is the motivation for the development of a kinematic refit for the analysis of the pp experiment. The refit algorithm is based on the work of Johannes Siebenson, described in [Sie10], the theoretical framework mainly relies on the write-ups of Paul Avery [Ave98].

3.1 Motivation and Theory

For the exclusive analysis of elementary particle reactions, the 4-momenta $p^\mu = (E, \vec{p})^T$ of all produced particles have to be determined. This is done in general with various specialized detectors, which are capable of measuring the momenta $\vec{p}$ of the particles and other observables, that allow for particle identification. After identifying the different particles, the masses are set to the nominal values, enabling, together with the momentum, the calculation of the energy E. Intermediate particles, that have a short lifetime and decay before being detected, can be reconstructed via the invariant or missing mass technique, applied to the particles, which are measured in the final state (see section 2.7).
The different particle tracks are completely characterized by the momentum $\vec{p}$, the energy E (or the mass m, respectively) and a space point $\vec{x}$, at which the momentum is evaluated, the so-called emission point. These observables are hereafter referred to as track parameters. However, these track parameters can only be determined within certain errors, since the detectors possess finite resolutions for the measurements. In many cases, the particle tracks of an exclusive reaction are measured with different detector systems and are independently fitted to the respective set of hit points. Therefore, the final state of an exclusive event will always deviate from the real event within uncertainties, that depend on the specific detectors involved in the measurements. Consequently, the mass resolution of intermediate particles, which are reconstructed via the invariant or missing mass technique, is also finite.

The scope of kinematic fitting is to improve the mass resolution of these intermediate particles and to reduce the amount of recorded background reactions, where the exclusive events are spuriously identified as such. The kinematic refit is a mathematical procedure, which uses physical laws that govern particle reactions to improve the measurement of the process [Ave98]. It forces the particle tracks to conform to external knowledge in terms of physical laws and geometrical relations by imposing certain constraint conditions. These constraints can be either fundamental principles as energy and momentum conservation or a fixed invariant or missing mass of reconstructed particles, or geometrical correlations such as common vertices and kinematics topology (e.g. back-to-back emission of particles in the CMS reference frame).

Each particle track i of an exclusive event is represented by a set of parameters[1], e.g. the momentum and the emission point $\vec{\alpha}_{0,i} = (p_{x,i}, p_{y,i}, p_{z,i}, x_i, y_i, z_i)^T$ in Cartesian coordinates. The kinematic refit calculates a new set of parameters $\vec{\alpha}_i$ for each particle, that fulfills the constraint conditions. The tracks are pulled away from their original positions within the uncertainties of the measurements, which have to be estimated previously and provided to the fit as input. At the same time, the kinematic refit ensures, that the new parameters stay as close as possible to the unconstrained ones.

3.1.1 General principles of constrained fitting

Mathematically, the kinematic refit is performed via the method of Lagrange multipliers by minimizing the following Lagrange equation with respect to $\vec{\alpha}$ and $\vec{\lambda}$.

$$L(\vec{\alpha},\vec{\lambda}) = (\vec{\alpha} - \vec{\alpha}_0)^T \, \mathbf{V}_{\vec{\alpha}_0}^{-1} \, (\vec{\alpha} - \vec{\alpha}_0) + 2\vec{\lambda}^T \vec{H}(\vec{\alpha}) \tag{3.1}$$

$\mathbf{V}_{\vec{\alpha}_0}^{-1}$ is the inverse of the measurement covariance matrix[2], $\vec{\alpha}$ contains the $6n$ refitted and $\vec{\alpha}_0$ the $6n$ unconstrained parameters of the n tracks.

$$\mathbf{V}_{\vec{\alpha}_0}^{-1} = \begin{pmatrix} \frac{1}{\sigma^2_{\alpha_1}} & 0 & \cdots & 0 \\ 0 & \frac{1}{\sigma^2_{\alpha_2}} & \cdots & 0 \\ \vdots & \vdots & \ddots & \vdots \\ 0 & 0 & \cdots & \frac{1}{\sigma^2_{\alpha_{6n}}} \end{pmatrix} \qquad \vec{\alpha} = \begin{pmatrix} \vec{\alpha}_1 \\ \vec{\alpha}_2 \\ \vdots \\ \vec{\alpha}_n \end{pmatrix} \qquad \vec{\alpha}_i = \begin{pmatrix} p_{x,i} \\ p_{y,i} \\ p_{z,i} \\ x_i \\ y_i \\ z_i \end{pmatrix}$$

$\vec{H}(\vec{\alpha})$ contains the m holonomic[3] constraint conditions and $\vec{\lambda}$ is the m-dimensional vector of Lagrange multipliers. The factor 2 simplifies the further calculations.

The first term of equation 3.1 ensures, that the refitted parameters $\vec{\alpha}$, which fulfill

---

[1] The parameters and their coordinate system can be chosen in different ways. For the kinematic refit, however, it is important, that the track representation completely describes the tracks and that it is physically meaningful, i.e. the errors of the parameters have to be Gaussian distributed.

[2] The covariance matrix $\mathbf{V}_{\vec{\alpha}_0}$ is a $(6n \times 6n)$-matrix containing the uncertainties of the measured unconstrained parameters $\vec{\alpha}_0$. The diagonal elements are the squares of the standard deviations of the parameters, the non-diagonal elements contain the correlated errors. For a full description of the measurement, these non-diagonal elements, e.g. originating from multiple scattering, have to be incorporated. In the following, however, they will be neglected.

[3] i.e. constraint equations of the form $\vec{H}(\vec{\alpha}) = \vec{0}$.

the constraints, stay as close as possible to the unconstrained parameters $\vec{\alpha}_0$. Coincidentally, the parameters are shifted only within the measurement uncertainties $\sigma^2_{\alpha_i}$, which are contained in the covariance matrix $\mathbf{V}_{\vec{\alpha}_0}$. The expression is defined via the well-known χ^2-statistics.

$$\chi^2 = (\vec{\alpha} - \vec{\alpha}_0)^T \, \mathbf{V}^{-1}_{\vec{\alpha}_0} \, (\vec{\alpha} - \vec{\alpha}_0) = \sum_l^{6n} \frac{(\alpha_l - \alpha_{0,l})^2}{\sigma^2_{\alpha_l}} \tag{3.2}$$

For the correct functioning of the kinematic refit, it is advantageous, that the errors are Gaussian distributed. From this follows, that the parameters obtained from the least squares method equal the values resulting from the maximum likelihood procedure[4]. Provided that the uncertainties have an expectation value of zero, the Gauss-Markov theorem assures, that the refitted parameters are unbiased[5] and have minimum variance $\sigma^2_{\alpha_i}$, i.e. the kinematic refit delivers the best possible set of parameters [FRB+00; Jam06].

The second term of equation 3.1 guarantees, that the refitted tracks exactly fulfill the constraint conditions. This is achieved via Lagrange multipliers, which will be explained in the following subsection.

Lagrange multipliers

The method of Lagrange multipliers is a standard tool for the task of minimizing or maximizing a function in consideration of constraint conditions.

The m constraint conditions for the kinematic refit are defined in a holonomic way.

$$\vec{H}(\vec{\alpha}) = 0 \tag{3.3}$$

Instead of substituting the m constraint equations into the function L (equation 3.1), a set of m new variables λ_i, the so called Lagrange multipliers, is introduced to the fit. The Lagrange multipliers are included in L as coefficients of a linear combination of the constraints.

For the following visualization, the $6n$-dimensional parameter space is without loss of generality reduced to 2 dimensions ($\vec{\alpha} = (\alpha_1, \alpha_2)^T$), with only one constraint condition. Then the two conditions for the kinematic refit read as follows.

(i) Minimize the function $\chi^2(\alpha_1,\alpha_2) = (\vec{\alpha} - \vec{\alpha}_0)^T \, \mathbf{V}^{-1}_{\vec{\alpha}_0} \, (\vec{\alpha} - \vec{\alpha}_0)$

(ii) Subject to $H(\alpha_1,\alpha_2) = \vec{0}$

Figure 3.1 depicts a visualization of the two conditions. Condition (ii) defines a contour $H(\alpha_1,\alpha_2) = 0$ of the function H, which is projected onto the function

---

[4] In case of Gaussian errors, the probability density function (pdf) for the parameters reads $g(\vec{\alpha}) = \prod_l (\sqrt{2\pi}\sigma_{\alpha_l})^{-1} exp\left[-\sum_l^{6n} \frac{(\alpha_l - \alpha_{0,l})^2}{2\sigma^2_{\alpha_l}}\right] = \prod_l (\sqrt{2\pi}\sigma_{\alpha_l})^{-1} exp\left(-\frac{\chi^2}{2}\right)$. Obviously, maximizing this pdf is equal to minimizing χ^2.

[5] i.e. the parameters converge to the true values if the experiment is repeated very often [Ave98].

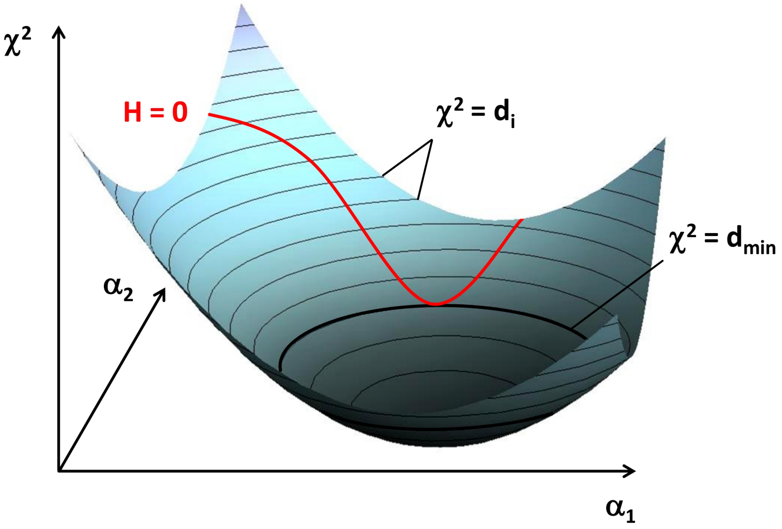

Figure 3.1: Illustration of the Lagrange multiplier method. The black lines are the contours of $\chi^2(\alpha_1,\alpha_2)$, the red line represents the holonomic constraint condition $H(\alpha_1,\alpha_2) = 0$, which is a contour of $H(\alpha_1,\alpha_2)$. The solution of the constrained minimization problem is obtained, if the contours touch tangentially. The minimum value of χ^2 is illustrated by the thick black contour $\chi^2 = d_{min}$.

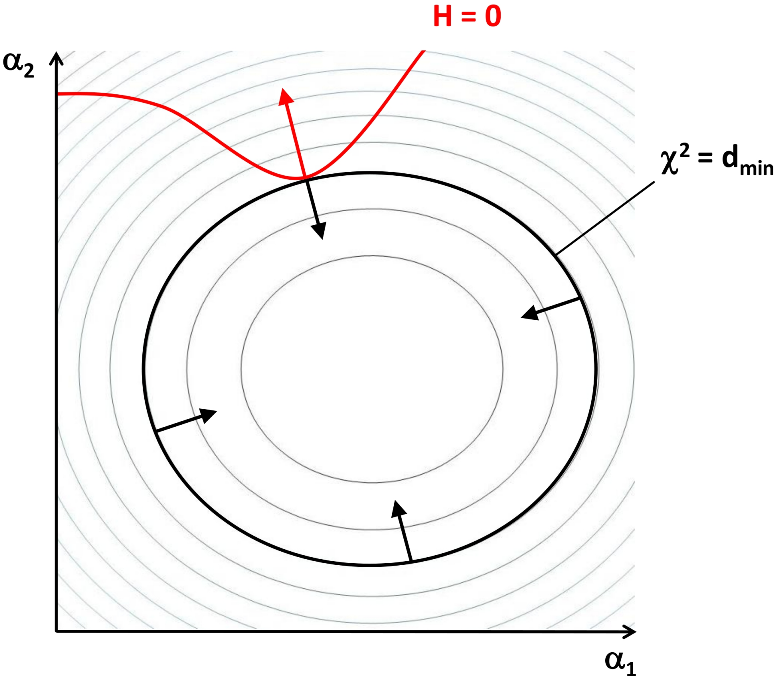

Figure 3.2: 2-dimensional projection of the contour map. The demand, that the two contours touch tangentially, is equivalent to the condition, that the gradients of H (red arrow) and χ^2 (black arrows) are parallel orientated. However, the two gradients do not have to posses the same magnitude.

to be minimized χ^2 (indicated by the red line), and which crosses its contours $\chi^2(\alpha_1,\alpha_2) = d_i$. Following the contour $H(\alpha_1,\alpha_2) = 0$, condition (i) requires the contour lines of H and χ^2 to contact tangentially, otherwise the value of χ^2 could be decreased by moving along $H(\alpha_1,\alpha_2) = 0$ in either direction. This is equivalent to the demand that the gradients of H and χ^2, which are always perpendicular to the respective contour lines, are parallel (Figure 3.2).

$$\vec{\nabla}_{\alpha_1,\alpha_2}\chi^2 = -\lambda\vec{\nabla}_{\alpha_1,\alpha_2}H \tag{3.4}$$

The Lagrange multiplier λ appears as a constant, since the two gradients are not restricted to have the same magnitude. These conditions are combined into the Lagrange equation.

$$L(\alpha_1,\alpha_2,\lambda) = \chi^2(\alpha_1,\alpha_2) + \lambda H(\alpha_1,\alpha_2) \tag{3.5}$$

The solution of the constrained minimization problem (equations 3.3 and 3.4) is now obtained by minimizing L with respect to $\vec{\alpha}$ and λ.

$$\frac{\partial L(\alpha_1,\alpha_2,\lambda)}{\partial\vec{\alpha}} = \vec{0}, \qquad \frac{\partial L(\alpha_1,\alpha_2,\lambda)}{\partial\lambda} = 0 \tag{3.6}$$

Figure 3.3 illustrates the effect of the kinematic refit on the track parameters. The constraint condition (red line) defines a hyperplane in the parameter space, on which the real parameters $\vec{\alpha}_{real}$ are located. The uncertainties of the measurement lead to parameters $\vec{\alpha}_0$, which, in the majority of cases, do not fulfill the constraint. The blue ellipsoid indicates the the area, within which the parameters are allowed to be shifted, defined by the errors of the measurement. The kinematic refit moves the parameters onto the constraint hyperplane, resulting in a new set of parameters $\vec{\alpha}$. Coincidently, the refit forces the parameters to be shifted by the minimum distance. In most of the cases, the new parameters $\vec{\alpha}$ will be closer to the real values than the unconstrained ones[6] [Sie10].

Linearization of the constraint equations

Returning to the general description, the minimization of equation 3.1 yields derivatives of the constraint equations $\vec{H}(\vec{\alpha})$, which can in principle be highly non-linear functions of the parameters $\vec{\alpha}$. Since no general procedure exists for solving these equations analytically, the constraint functions $\vec{H}(\vec{\alpha})$ have to be expanded around an approximate solution $\vec{\alpha}_A$[7].

$$\vec{H}(\vec{\alpha}) \approx \vec{H}(\vec{\alpha}_A) + \frac{\partial\vec{H}(\vec{\alpha}_A)}{\partial\vec{\alpha}}(\vec{\alpha} - \vec{\alpha}_A) \equiv \mathbf{D}\delta\vec{\alpha} + \vec{d} \tag{3.7}$$

---

[6] In fact, the refit does not guarantee explicitly, that the refitted parameters $\vec{\alpha}$ are closer to the real values $\vec{\alpha}_{real}$ than the unconstrained parameters $\vec{\alpha}_0$. Nevertheless, this situation is favored, since the new parameters fulfill the constraints, which is also the case in the real experiment.

[7] For convenience, e.g. the unconstrained parameters $\vec{\alpha}_0$ can be chosen as the approximate solution.

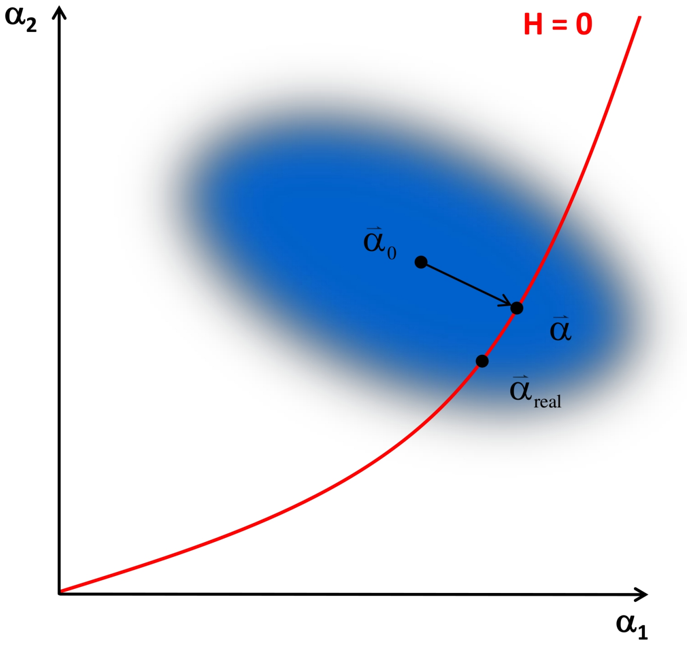

Figure 3.3: The kinematic refit shifts the parameters $\vec{\alpha}$ onto the constraint hyperplane (red line) within the measurement error band, indicated by the blue ellipsoid. With high probability, the new parameters $\vec{\alpha}$ are closer tho the real values $\vec{\alpha}_{real}$.

where $\delta\vec{\alpha} = \vec{\alpha} - \vec{\alpha}_A$ and

$$\mathbf{D} = \begin{pmatrix} \frac{\partial H_1(\vec{\alpha})}{\partial \alpha_1} & \frac{\partial H_1(\vec{\alpha})}{\partial \alpha_2} & \cdots & \frac{\partial H_1(\vec{\alpha})}{\partial \alpha_{6n}} \\ \frac{\partial H_2(\vec{\alpha})}{\partial \alpha_1} & \frac{\partial H_2(\vec{\alpha})}{\partial \alpha_2} & \cdots & \frac{\partial H_2(\vec{\alpha})}{\partial \alpha_{6n}} \\ \vdots & \vdots & \ddots & \vdots \\ \frac{\partial H_m(\vec{\alpha})}{\partial \alpha_1} & \frac{\partial H_m(\vec{\alpha})}{\partial \alpha_2} & \cdots & \frac{\partial H_m(\vec{\alpha})}{\partial \alpha_{6n}} \end{pmatrix} \qquad \vec{d} = \begin{pmatrix} H_1(\vec{\alpha}_A) \\ H_2(\vec{\alpha}_A) \\ \vdots \\ H_m(\vec{\alpha}_A) \end{pmatrix} \tag{3.8}$$

This simplification is justified, because the constraints vary slowly enough within the error bands of the parameters. Now equation 3.1 can be written as

$$L(\vec{\alpha},\vec{\lambda}) = (\vec{\alpha} - \vec{\alpha}_0)^T \, \mathbf{V}_{\vec{\alpha}_0}^{-1} \, (\vec{\alpha} - \vec{\alpha}_0) + 2\vec{\lambda}^T (\mathbf{D}\delta\vec{\alpha} + \vec{d}) \tag{3.9}$$

This linearized Lagrange equation can be minimized analytically with respect to $\vec{\alpha}$ and $\vec{\lambda}$. Solving the resulting formulas for the new parameters $\vec{\alpha}$ and the new covariance matrix $\mathbf{V}_{\vec{\alpha}}$ yields the following matrix equations.

$$\vec{\alpha} = \vec{\alpha}_0 - \mathbf{V}_{\vec{\alpha}_0}\mathbf{D}^T\mathbf{V}_D(\mathbf{D}\delta\vec{\alpha}_0 + \vec{d}) \tag{3.10}$$

$$\mathbf{V}_{\vec{\alpha}} = \mathbf{V}_{\vec{\alpha}_0} - \mathbf{V}_{\vec{\alpha}_0}\mathbf{D}^T\mathbf{V}_D\mathbf{D}\mathbf{V}_{\vec{\alpha}_0} \tag{3.11}$$

where the auxiliary matrix $\mathbf{V}_D$ is defined as

$$\mathbf{V}_D = (\mathbf{D}\mathbf{V}_{\vec{\alpha}_0}\mathbf{D}^T)^{-1} \tag{3.12}$$

Remarkably, only one single matrix has to be inverted, the $(m \times m)$ matrix V_D. The diagonal elements of the new covariance matrix $\mathbf{V}_{\vec{\alpha}}$ are reduced in size compared to $\mathbf{V}_{\vec{\alpha}_0}$, which is caused by the minus sign in equation 3.11. Finally, the χ^2 value of the fit is obtained via the following equation.

$$\chi^2 = (\mathbf{D}\delta\vec{\alpha}_0 + \vec{d})^T\mathbf{V}_D^{-1}(\mathbf{D}\delta\vec{\alpha}_0 + \vec{d}) \tag{3.13}$$

The expression for χ^2 is a sum of m distinct terms, so the number of degrees of freedom of the fit is equal to the number of constraint equations m.
In the rare cases, where the constraint conditions 3.3 are linear in $\vec{\alpha}$, the final result is already given by the equations 3.10-3.13. In the non-linear cases, the kinematic refit has to be applied iteratively, where the values obtained by 3.10-3.13 are used as input for the next iteration step: $\vec{\alpha}_A = \vec{\alpha}$. After solving the new Lagrange equation, improved values for $\vec{\alpha}$ and $\mathbf{V}_{\vec{\alpha}}$ are calculated, which fulfill the constraints better. This procedure, which is repeated until the solution converges, is illustrated by Figure 3.4. Since the constraints vary only slowly with respect to the parameters $\vec{\alpha}$, usually 4-6 iteration steps are sufficient.

3.1.2 Solving for unknown parameters

The constrained fitting technique, described in the sections above, can be expanded to the situation, where unknown parameters $\vec{z}$ are contained in the Lagrange equation L. In this case, the r unknown values z_i have to be calculated previously to the track parameters $\vec{\alpha}$. The modified Lagrange equation, which is additionally expanded around a convenient point $\vec{z}_A$, reads

$$L(\vec{\alpha},\vec{z},\vec{\lambda}) = (\vec{\alpha} - \vec{\alpha}_0)^T \, \mathbf{V}_{\vec{\alpha}_0}^{-1} \, (\vec{\alpha} - \vec{\alpha}_0) + 2\vec{\lambda}^T(\mathbf{D}\delta\vec{\alpha} + \mathbf{E}\delta\vec{z} + \vec{d}) \tag{3.14}$$

with $\delta\vec{z} = \vec{z} - \vec{z}_A$. The $(m \times r)$ matrix

$$\mathbf{E} = \begin{pmatrix} \frac{\partial H_1(\vec{\alpha},\vec{z})}{\partial z_1} & \frac{\partial H_1(\vec{\alpha},\vec{z})}{\partial z_2} & \cdots & \frac{\partial H_1(\vec{\alpha},\vec{z})}{\partial z_r} \\ \frac{\partial H_2(\vec{\alpha},\vec{z})}{\partial z_1} & \frac{\partial H_2(\vec{\alpha},\vec{z})}{\partial z_2} & \cdots & \frac{\partial H_2(\vec{\alpha},\vec{z})}{\partial z_r} \\ \vdots & \vdots & \ddots & \vdots \\ \frac{\partial H_m(\vec{\alpha},\vec{z})}{\partial z_1} & \frac{\partial H_m(\vec{\alpha},\vec{z})}{\partial z_2} & \cdots & \frac{\partial H_m(\vec{\alpha},\vec{z})}{\partial z_r} \end{pmatrix} \tag{3.15}$$

contains the derivatives of the constraints $\vec{H}(\vec{\alpha})$ with respect to the unknown parameters $\vec{z}$. The ndf of the fit is equal to the number of constraint equations m minus the number of unknown parameters r. The procedure to calculate the new values of $\vec{\alpha}$ and $\vec{z}$ is described in the next subsections.

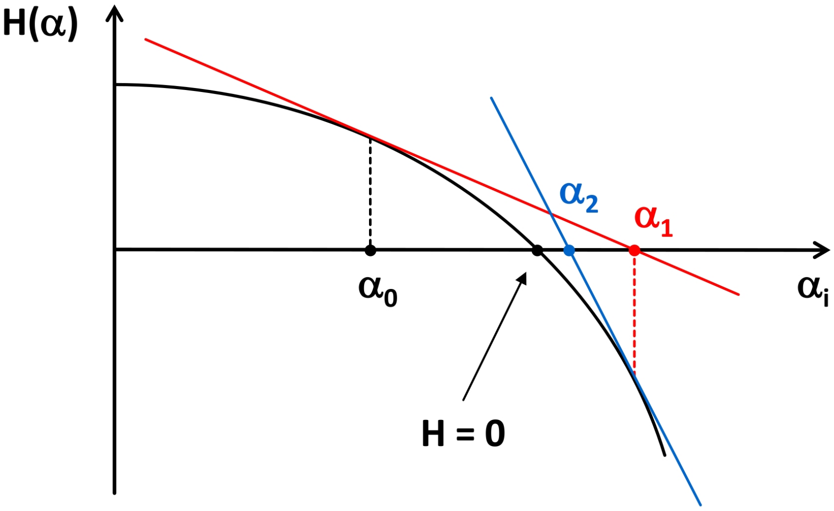

Figure 3.4: 1-dimensional visualization of the iteration procedure. The constraint condition (black line) is expanded around an approximate solution $\alpha_A = \alpha_0$. The new parameters α_1 are located at the zero of this linearized constraint (red line). In the second iteration step, the constraint function is expanded around the solution of the previous iteration step α_1 (blue line), resulting in a new parameter α_2. This illustration shows, that the parameters converge to the zero of the full constraint.

Vertex constraints

Equation 3.14 contains no prior covariance matrix for the parameters $\vec{z}$. If the n tracks are supposed to be forced to pass through a common space point $\vec{z}$, however, the covariance matrix $\mathbf{V}_{\vec{z}}$ of the vertex is possibly known in advance. Provided that this is the case, the errors of the vertex are accounted for by adding a second χ^2 term to the Lagrange equation.

$$L(\vec{\alpha},\vec{z},\vec{\lambda}) = (\vec{\alpha} - \vec{\alpha}_0)^T\, \mathbf{V}_{\vec{\alpha}_0}^{-1}\, (\vec{\alpha} - \vec{\alpha}_0) + (\vec{z} - \vec{z}_0)^T\, \mathbf{V}_{\vec{z}_0}^{-1}\, (\vec{z} - \vec{z}_0) \\ + 2\vec{\lambda}^T(\mathbf{D}\delta\vec{\alpha} + \mathbf{E}\delta\vec{z} + \vec{d}) \tag{3.16}$$

where $\vec{z}_0$ is the initial vertex and $\mathbf{V}_{\vec{z}_0}$ its respective covariance matrix. Minimizing this function with respect to $\vec{\alpha}$, $\vec{z}$ and $\vec{\lambda}$ yields the following matrix equations for the parameters.

$$\vec{z} = \vec{z}_0 - \mathbf{V}_{\vec{z}_0}\mathbf{E}^T(\mathbf{V}_D - \mathbf{V}_D\mathbf{E}\mathbf{V}_{\vec{z}}\mathbf{E}^T\mathbf{V}_D)(\mathbf{D}\delta\vec{\alpha}_0 + \mathbf{E}\delta\vec{z}_0 + \vec{d}) \tag{3.17}$$

$$\vec{\alpha} = \vec{\alpha}_0 - \mathbf{V}_{\vec{\alpha}_0}\mathbf{D}^T(\mathbf{V}_D - \mathbf{V}_D\mathbf{E}\mathbf{V}_{\vec{z}}\mathbf{E}^T\mathbf{V}_D)(\mathbf{D}\delta\vec{\alpha}_0 + \mathbf{E}\delta\vec{z}_0 + \vec{d}) \tag{3.18}$$

The auxiliary matrix $\mathbf{V}_D$ is defined in equation 3.12. The new covariance matrices are calculated as follows.

$$\mathbf{V}_{\vec{z}} = \left(\mathbf{V}_{\vec{z}_0}^{-1} + \mathbf{E}^T\mathbf{V}_D\mathbf{E}\right)^{-1} \tag{3.19}$$

$$\mathbf{V}_{\vec{\alpha}} = \mathbf{V}_{\vec{\alpha}_0} - \mathbf{V}_{\vec{\alpha}_0}\mathbf{D}^T\mathbf{V}_D\mathbf{D}\mathbf{V}_{\vec{\alpha}_0} + \mathbf{V}_{\vec{\alpha}_0}\mathbf{D}^T\mathbf{V}_D\mathbf{E}\mathbf{V}_{\vec{z}}\mathbf{E}^T\mathbf{V}_D\mathbf{D}\mathbf{V}_{\vec{\alpha}_0} \tag{3.20}$$

In contrast to the previous case, two additional matrices have to be inverted, the $(r \times r)$ matrices $\mathbf{V}_{\vec{z}_0}$ and $\mathbf{V}_{\vec{z}}$. The new vertex covariance matrix $\mathbf{V}_{\vec{z}}$ is the weighted average of the initial vertex error matrix $\mathbf{V}_{\vec{z}_0}$ and the errors determined from the tracks, contained in the definition of $\mathbf{V}_D$ (equation 3.12). The new covariance matrix of the track parameters $\mathbf{V}_{\vec{\alpha}}$ is decreased in comparison to the initial covariance matrix $\mathbf{V}_{\vec{\alpha}_0}$ due to the applied constraints. In the case of vertex constraints, however, the covariance matrix elements are increased by the last term of equation 3.20, which originates from the vertex fit itself. It is worth mentioning, that this last term is the only one, that contains track-track correlations trough the matrix $\mathbf{V}_{\vec{z}}$. This fact is reflected by the shape of the $(6n \times r)$ covariance matrix of the tracks and the unknowns.

$$cov(\vec{\alpha},\vec{z}) = -\mathbf{V}_{\vec{\alpha}_0}\mathbf{D}^T\mathbf{V}_D\mathbf{E}\mathbf{V}_{\vec{z}} \tag{3.21}$$

The matrices of the other term $\mathbf{V}_{\vec{\alpha}_0}$, $\mathbf{D}$ and $\mathbf{V}_D$ are block diagonal, so that the different tracks are not mixed, equivalent to fitting each track separately.
The expression for the χ^2 value is given by

$$\chi^2 = (\mathbf{D}\delta\vec{\alpha}_0 + \mathbf{E}\delta\vec{z}_0 + \vec{d})^T(\mathbf{V}_D - \mathbf{V}_D\mathbf{E}\mathbf{V}_{\vec{z}}\mathbf{E}^T\mathbf{V}_D)^T(\mathbf{D}\delta\vec{\alpha}_0 + \mathbf{E}\delta\vec{z}_0 + \vec{d}) \tag{3.22}$$

Fitting to an unknown vertex position

If the initial vertex position $\vec{z}_0$ is not known in advance, the refitted vertex has to be determined from the constraints. One way to achieve this, is to assign large values to the covariance matrix $\mathbf{V}_{\vec{z}_0}$. Consequently, the term

$$(\vec{z} - \vec{z}_0)^T\,\mathbf{V}_{\vec{z}_0}^{-1}\,(\vec{z} - \vec{z}_0) \tag{3.23}$$

can be neglected in equation 3.16 and the previous Lagrange equation 3.14 is obtained again. The criterion for the refit, to shift the new vertex as little as possible away from the initial position, does not hold anymore. Thus, the fitted vertex position is completely arbitrary and only determined by the other constraint conditions.
Again, the effective number of degrees of freedom for this type of fit is equal to number of constraint equations m minus the number of unknown parameters r. Now, the physical meaning of this relation can be understood. Because the errors of the vertex are very large, the fit forces the vertex parameters to move within an insignificant number of standard deviations. Since adding the term 3.23 with large errors to the Lagrange equation 3.14 does not change the results, the ndf is equal in both cases. Due to this equivalence, the equations 3.17-3.22, where large errors are assigned to $\mathbf{V}_{\vec{z}_0}$ (i.e. $(\mathbf{V}_{\vec{z}_0}^{-1})_{ij} = 0$), can be used to solve for unknown parameters in equation 3.14 and to calculate the new parameters $\vec{\alpha}$.

Fitting to a fixed vertex position

If the kinematic refit is supposed to fit the tracks through a fixed vertex, the equations 3.10-3.13 can be used. The same solution is obtained by setting $\delta\vec{z}_0 = \vec{0}$, $(\mathbf{E})_{ij} = 0$ and $(\mathbf{V}_{\vec{z}_0})_{ij} = 0$ in the equations 3.17-3.22. In this case, the tracks remain uncorrelated after the fit, i.e. the constraints could also be applied sequentially.

3.2 Quality criteria of the kinematic refit

The effect of the kinematic refit crucially depends on the correct input of the parameter covariance matrix $\mathbf{V}_{\vec{\alpha}_0}$. In some cases, this may be exactly known in advance, e.g. if a kalman filter is used for track fitting, but frequently the uncertainties have to be estimated. Hence, it is important to have a set of criteria which are a measure for the quality of the fit and that indicate the presence of misidentified events and whether the error input is correct.

3.2.1 χ^2 distribution and p-value

The kinematic fitting technique is based on the minimization of the χ^2 value, being represented by the first term of equation 3.1. Therefore, the final χ^2 distribution of the fit should be a good measure of its global performance quality.
The probability density function of the χ^2 values for correctly estimated and Gaussian distributed errors is given by the equation[8]

$$f_\nu(\chi^2) = \frac{1}{2^{\nu/2}\Gamma(\nu/2)}(\chi^2)^{\nu/2-1}e^{-\frac{1}{2}\chi^2} \tag{3.24}$$

with a mean value of

$$\langle\chi^2\rangle = \nu \tag{3.25}$$

where ν is the number of degrees of freedom of the fit and Γ the gamma function. Figure 3.5 shows the χ^2 distributions for different values of ν. A χ^2 distribution following the theoretical pdf roughly indicates that the global fit was performed correctly.
It is convenient to define a quantity, which gives the probability that the same fit, if repeated, will result in a χ^2 value as large as or larger than the value of the current fit χ^2_{fit}. The so called p-value is defined as

$$p - value = \int\limits_{\chi^2_{fit}}^{\infty} f_\nu(\chi^2) d\chi^2 \tag{3.26}$$

---

[8] This formula can be derived from the joint pdf of footnote 4 via a Jacobian transformation [FRB+00].

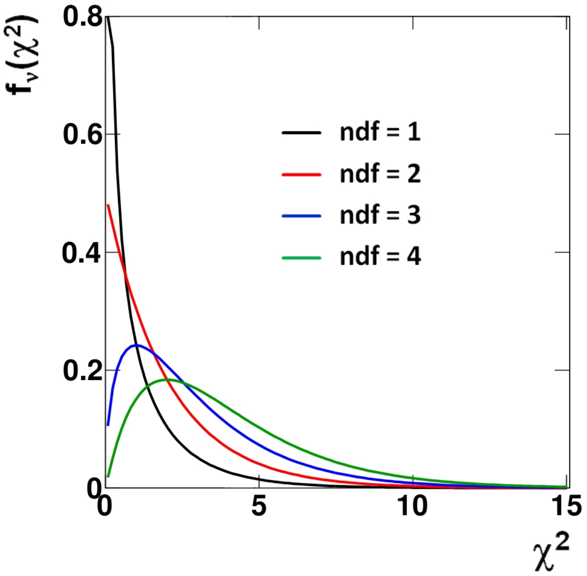

Figure 3.5: χ^2 distributions for different values of the ndf [Sie10]. The functions are shifted towards higher χ^2 values for an increasing ndf, since the fit has to move the parameters $\vec{\alpha}$ within a larger distance if more constraints are applied. In the limit of $\nu \rightarrow \infty$, the χ^2 distribution approaches a normal distribution. This follows from the central limit theorem.

Instead of looking at the χ^2 distribution, it is more descriptive to map the χ^2 to a flat distribution [Bau00]. If the error input is correct, the p-value is indeed evenly distributed between 0 and 1. Since high χ^2 values correspond to low p-values, misidentified events, the track parameters of which have to be shifted far away from $\vec{\alpha}_0$, are located at low p-values. Cutting on the p-value therefore enables the reduction of background[9] (see section 3.3.4).

---

[9] The p-value is not to be confused with the significance or the confidence level. Usually, one defines a significance level, which in statistics is also referred to as the $1 - \alpha$ quantile. χ^2 values larger than the significance level are rejected in the case of kinematic fitting, since they probably belong to misidentified events. The probability, that these values are wrongly rejected is equal to the area to the right of the significance level beneath the χ^2 distribution. This area is called the significance α. The area to the left of the significance level is called the confidence level and is defined as $1 - \alpha$. These values are fixed during the analysis and determine the conditions under which the refitted events are rejected. In contrast, the p-value is calculated for each event and is equal to the area to the right of χ^2_{fit}, which differs from fit to fit. The event is rejected, if the p-value is smaller than the defined significance α (and accordingly χ^2_{fit} is larger than the respective significance level). The probability to reject non-background events with $p - value < \alpha$ by mistake is called type I error α (since it usually equals the significance α). The probability to accept background events with $p - value > \alpha$ is referred to as type II error β and is mostly unknown.

3.2.2 Pull distributions

The χ^2 and p-value distributions are global criteria evaluating the overall quality of the fit. A quantity more sensitive to the single track parameters is the pull function $P(\alpha_i)$, which is defined for each single parameter α_i as

$$P(\alpha_i) = \frac{\alpha_{0,i} - \alpha_i}{\sqrt{\sigma^2_{\alpha_{0,i}} - \sigma^2_{\alpha_i}}} \tag{3.27}$$

where $\sigma^2_{\alpha_{0,i}}$ and $\sigma^2_{\alpha_i}$ are the errors of the unconstrained and the refitted parameters, respectively. This function, which is also referred to as reduced residual, is a measure of how much the particular parameter is shifted by the fit, normalized to the reduced error difference [She07]. As shown in the equations 3.11 and 3.20, the elements of the covariance matrix $\mathbf{V}_{\vec{\alpha}}$ are reduced compared to the values of $\mathbf{V}_{\vec{\alpha}_0}$. This is important for the definition of the pull functions concerning the square root in the denominator, which has to be a real value.

If the covariance matrix $\mathbf{V}_{\vec{\alpha}_0}$ is estimated correctly, the pull distributions for the single parameters are Gaussian distributed around 0 with a standard deviation of $\sigma = 1$. The effect of wrongly estimated uncertainties or systematic errors can directly be read out of the shape of the pull distributions (this is discussed in more detail in section 3.3.3). Hence, they are a very important and highly sensitive quality criterion for the kinematic refit. Indeed, if the covariance matrix is only roughly known in advance, the pull distributions can be used to tune the errors to the correct values afterwards.

3.3 The kinematic refit for the pp analysis

The kinematic refit algorithm for the analysis of the ppK^- is constructed in a modular and general way. In particular, it can be used with an arbitrary number of particle tracks and different track representations regarding the number of track parameters and the coordinate system. Three different track representations are included, $\vec{\alpha}_{car}$, $\vec{\alpha}_{sph}$ and $\vec{\alpha}_{mix}$, hereafter referred to as Cartesian, spherical and mixed track representation. They are defined in the following way.

$$\vec{\alpha}_{car,i} = \begin{pmatrix} p_{x,i} \\ p_{y,i} \\ p_{z,i} \\ x_{x,i} \\ x_{y,i} \\ x_{z,i} \end{pmatrix} \qquad \vec{\alpha}_{sph,i} = \begin{pmatrix} 1/p_i \\ \theta_i \\ \varphi_i \\ R_{\vec{x},i} \\ \theta_{\vec{x},i} \\ \varphi_{\vec{x},i} \end{pmatrix} \qquad \vec{\alpha}_{mix,i} = \begin{pmatrix} 1/p_i \\ \theta_i \\ \varphi_i \\ x_{x,i} \\ x_{y,i} \\ x_{z,i} \end{pmatrix} \tag{3.28}$$

p_x, p_y and p_z are the Cartesian, $1/p$, θ and φ the spherical coordinates of the momentum vector $\vec{p}$, where $1/p$ is the inverse magnitude[10] of $\vec{p}$. The lower three components parameterize the emission point $\vec{x}$ of the tracks in Cartesian (x_x, x_y, x_z) and spherical ($R_{\vec{x}}$, $\theta_{\vec{x}}$, $\varphi_{\vec{x}}$) coordinates. The energy does not appear as free parameter, since the masses of the particles are set to their nominal values after the identification.

Depending on the specific detector setup, the track representation has to be chosen such, that the parameters are uncorrelated and Gaussian distributed. In the case of the FOPI spectrometer, no preferable coordinate system for the momentum parameters exists. As described in section 2.7, the momentum of CDC tracks is determined via the circular deflection inside the homogeneous magnetic field of the solenoid. However, due to the inhomogeneity of the magnetic field, the momentum of HELITRON tracks is calculated via a complicated iterative procedure using spline interpolation. Since it is not possible to account for both reconstruction methods (especially for the HELITRON), spherical momentum coordinates are used for the kinematic refit in this analysis. The second silicon layer of the SiΛVio detector (see section 2.5) delivers a hitpoint, which is defined in Cartesian coordinates. Therefore, this coordinate system is also used for the emission point parameters of the kinematic refit. Together with the momentum coordinates, the mixed track representation $\vec{\alpha}_{mix}$ is used for the analysis.

Additionally, the track representations can be chosen to contain only the 3 momentum parameters. This is possible if only non-vertex constraints are used, since they do not alter the emission points of the particles.

The following subsections describe the different constraint conditions, that are implemented in the kinematic refit. Since it is designed in a modular way, every possible combination of the single constraints can be used.

The first step in the analysis of the ppK^- is the reconstruction of the intermediate Λ (see reaction R.2). In order to test the correct functioning of the different constraint conditions, the following reaction with a beam energy of 3.1 GeV is simulated with the PLUTO event generator ($4 \cdot 10^5$ events) [F+10].

$$\begin{aligned} p + p \longrightarrow\ & \Lambda + p_1 + K^+ \\ & \hookrightarrow p_2 + \pi^- \end{aligned} \tag{R.6}$$

In order to simulate the finite resolution of the FOPI detectors, the track parameters are manually Gaussian smeared around the simulated values. The errors are extracted

---

[10] The parameter is defined this way, because many experiments measure the momentum via the curvature of the tracks in a magnetic field, which is proportional to $1/p$ (see section 2.7). Therefore, $1/p$ is the quantity, that is Gaussian distributed.

from pull distributions, where the kinematic refit is applied to full scale simulations[11] with realistic measurement uncertainties (see chapter 4). Since the reaction contains 4 charged particles in the final state (p_1,K^+,p_2,π^-), the parameter vectors $\vec{\alpha}$ and $\vec{\alpha}_0$ are 24 dimensional $(4 \cdot 6)$ vectors and the covariance matrices are (24×24) matrices.

$$\vec{\alpha} = \begin{pmatrix} \vec{\alpha}_{p_1} \\ \vec{\alpha}_{K+} \\ \vec{\alpha}_{p_2} \\ \vec{\alpha}_{\pi^-} \end{pmatrix} \qquad \mathbf{V}_{\vec{\alpha}} = \begin{pmatrix} \sigma^2_{1/p,p_1} & 0 & \cdots & 0 & 0 \\ 0 & \sigma^2_{\theta,p_1} & \cdots & 0 & 0 \\ \vdots & \vdots & \ddots & \vdots & \vdots \\ 0 & 0 & \cdots & \sigma^2_{\theta_{\vec{x}},\pi^-} & 0 \\ 0 & 0 & \cdots & 0 & \sigma^2_{\varphi_{\vec{x}},\pi^-} \end{pmatrix} \tag{3.29}$$

Because the tracks are smeared manually with the same errors that are set in $\mathbf{V}_{\vec{\alpha}_0}$, the kinematic refit should deliver a flat p-value distribution and pull functions with $\sigma = 1$ centered around zero. In addition to the obvious tests, that the respective constraints are fulfilled, this is used to check, whether the refit works correctly. In the following chapters, 5 iteration steps are used for the kinematic refit.

3.3.1 Non-vertex constraints

Constraints that do not affect the exact position of the particle tracks in terms of common vertices are called non-vertex constraints. The corresponding equations do not contain the emission points of the particles, which are therefore unchanged by the refit. The kinematic refit for the pp analysis contains 3 non-vertex constraints, an invariant mass, a missing mass and an energy and momentum conservation constraint.

Invariant and missing mass constraint

This constraint forces the invariant mass of two or the missing mass of several particles to equal a fixed value by shifting the involved tracks correspondingly.
In case of the invariant mass constraint, only the parameters of the two particles are changed, the invariant mass of which is fixed by the refit. For the ppK^- analysis, this corresponds to the invariant mass of the p_2 and the π^-, which is set to the mass of the Λ mother particle: $M(p_2,\pi^-) = M_\Lambda = 1.116\,\mathrm{GeV/c^2}$. The holonomic constraint equation reads[12]

$$H = 0 = (E_{p_2} + E_{\pi^-})^2 - (\vec{p}_{p_2} + \vec{p}_{\pi^-})^2 - M_\Lambda^2 \tag{3.30}$$

---

[11] i.e. simulations where the particles created by an event generator (e.g. PLUTO) traverse simulated detectors with realistic uncertainties. The calculation of the trajectories within the detectors is usually done with the software GEANT [GEA]. Via so called digitizers, realistic detector output signals are simulated, which pass the whole analysis chain, including particle identification, etc.

[12] For convenience, the speed of light constant c is set to 1 hereafter.

where the energy of the particles with mass M_i is given by the relativistic energy-momentum relation.

$$E_i = \sqrt{M_i^2 + \vec{p}_i^2} \tag{3.31}$$

Since the track representation $\vec{\alpha}_{mix}$ is used, the 3-momenta of the particles are parameterized in spherical coordinates.

$$\vec{p}_i = p_i \begin{pmatrix} sin\theta_i \, cos\varphi_i \\ sin\theta_i \, sin\varphi_i \\ cos\theta_i \end{pmatrix} \tag{3.32}$$

The elements $(\mathbf{D})_{ij} = \frac{\partial H_i(\vec{\alpha})}{\partial \alpha_j}$ of the D-matrix (see 3.8) are listed in appendix A. Analog, the missing mass constraint can be used to set the missing mass of the two other particles in the final state, p_1 and K^+, to the nominal Λ mass: $MM(p_1{,}K^+) = M_\Lambda$. The missing mass constraint equation is given by

$$H = 0 = (E_{p_b} + E_{p_t} - E_{p_1} - E_{K^+})^2 - (\vec{p}_{p_b} + \vec{p}_{p_t} - \vec{p}_{p_1} - \vec{p}_{K^+})^2 - M_\Lambda^2 \tag{3.33}$$

In this case, only the parameters of the involved particles p_1 and K^+ are changed. The missing mass constraint is also useful for reactions containing non-charged particles, which cannot be measured by most detector systems (e.g. neutrons). Setting the missing mass of the other charged particles to the nominal value of the neutral one, increases the mass resolution of intermediate particles (see e.g. [Sie10]).

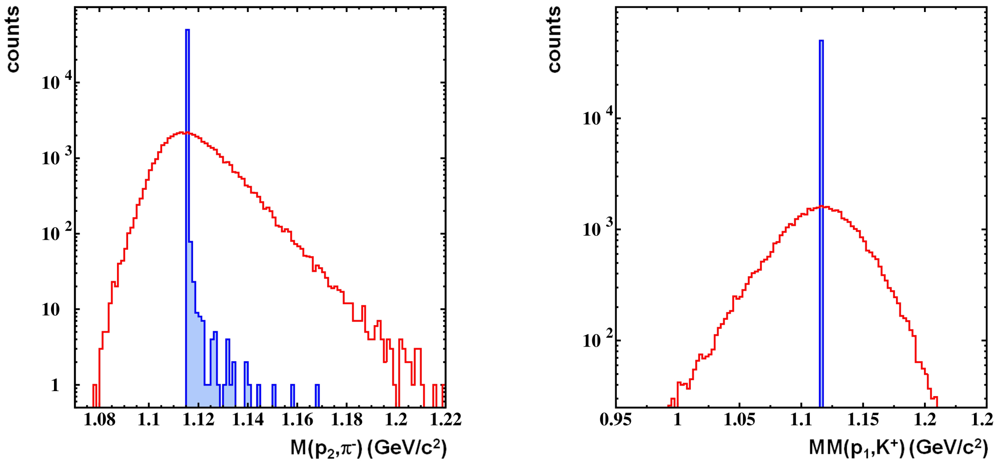

(a) (b)

Figure 3.6: Invariant mass of p_2 and π^- (a) and missing mass of p_1 and K^+ (b) before (red) and after (blue) the kinematic refit with invariant and missing mass constraint, respectively.

Figure 3.6 shows the invariant mass (p_2, π^-) and the missing mass (p_1, K^+) before (red) and after (blue) the kinematic refit. The large widths of the unrefitted (raw) spectra result from the smearing of the original tracks. The spectra of the refitted tracks show sharp peaks at the Λ mass $M_\Lambda = 1.116\,\mathrm{GeV/c^2}$. For the missing mass constraint, the kinematic refit clearly succeeds in shifting all tracks in order to exactly fulfill the constraint. However, in case of the invariant mass constraint, some refitted events have a mass slightly larger than the constraint mass, corresponding to the tail on the right side of the Λ peak in figure 3.6a. About 0.06 % of the refitted events have a mass which differs by more than $5\,\mathrm{MeV/c^2}$ from the nominal Λ mass. The reason for this effect could be the existence of local minima of the constraint condition, detaining the parameters $\vec{\alpha}$ from reaching the constraint mass. This hypothesis is supported by the fact, that the tail cannot be reduced by increasing the number of iterations in the fit. However, the tail diminishes if the smearing amplitude of the track parameters decreases. Indeed, the events contained in the tail correspond to a smearing amplitude within the 3σ quantile of the smearing normal distribution. If the errors are smaller, the parameters are less shifted by the fit and the probability of getting trapped by a local minimum is lower.

It is peculiar, that the tail in figure 3.6a only appears on the right side, i.e. at larger invariant masses. As illustrated in picture 3.4, the zeros of the linearized constraints are always located on either side of the full constraint condition. This corresponds to parameters, which are either to large or to small, depending on the particular constraint function. In case of the invariant mass constraint, the refitted masses are always slightly larger than the constraint mass. Certainly, the tracks approach the correct mass after a few iteration steps. However, if the parameters are trapped within a local minimum, the masses will stay at values, which are noticeably larger than the Λ mass.

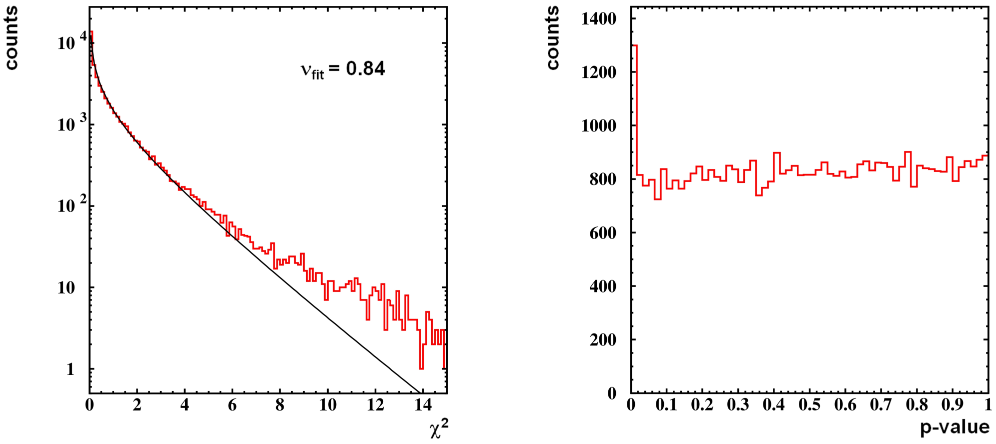

(a) (b)

Figure 3.7: χ^2 distribution (a) and p-value distribution (b) of the refit with invariant mass constraint.

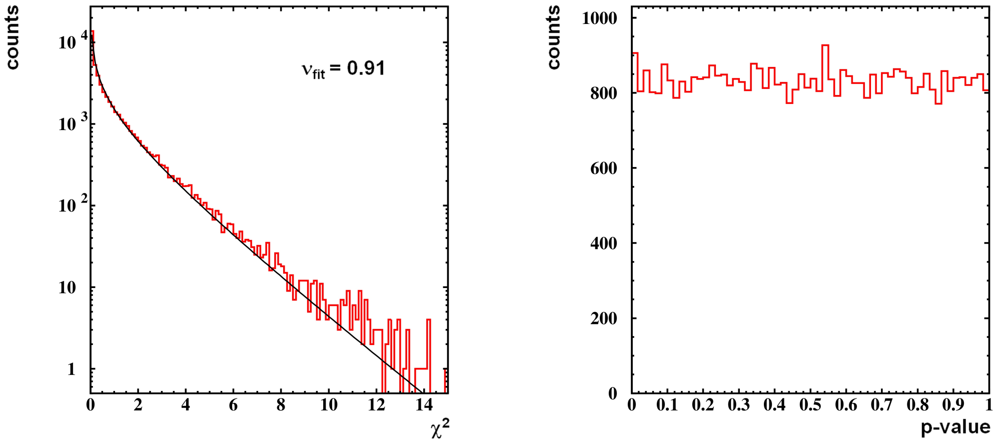

(a) (b)

Figure 3.8: χ^2 distribution (a) and p-value distribution (b) of the refit with missing mass constraint.

Figure 3.7a shows the χ^2 distribution for the fit with invariant mass constraint. Since both, invariant and missing mass constraint, contain only one constraint equation, the expected ndf of the fit is 1 (according to equation 3.13). The black curve indicates the fit of equation 3.24 to the spectrum, which delivers a value for the ndf of 0.84. The deviation from the fitted curve at large χ^2 values results from the events with the excessive invariant mass. In Figure 3.7b, the corresponding p-value distribution is plotted. It is evenly distributed between 0 and 1, which is expected due to the fact, that the covariance matrix $\mathbf{V}_{\vec{\alpha}_0}$ contains the correct errors.

Again, the tail of the invariant mass spectrum appears in the p-value distribution in the shape of a small peak at low p-values. Since in the further analysis a cut on small p-values is used to reduce the amount of background (see section 3.3.3), also

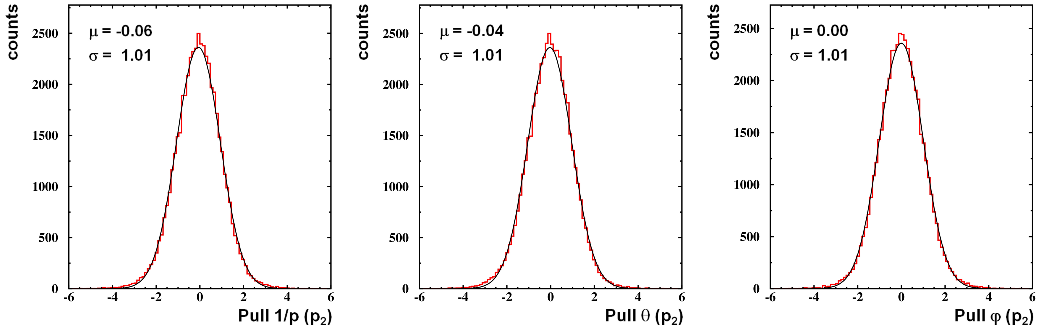

Figure 3.9: Pull distributions for 3 of totally 6 parameters after applying the kinematic refit with invariant mass constraint. The black lines indicate the fitted normal distributions, corresponding to the values in the upper right corners.

Particle	$\langle \Delta(dp/p) \rangle$	$\Delta(d\theta)$	$\Delta(d\varphi)$
Invariant mass constraint			
p_2	8.68%	-	-
π^-	21.9%	8.67%	-
Missing mass constraint			
p_1	21.6%	5.45%	0.79%
K^+	11.6%	5.25%	-

Table 3.1: Average improvement of the momentum, θ and φ resolution due to the kinematic refit with invariant and missing mass constraint.

these wrongly fitted events are removed.

The respective distributions for the missing mass constraint are shown in figure 3.8. The fitted value for the ndf is 0.91. In this case, the p-value distribution is completely flat, because the refitted missing mass spectrum (Figure 3.6b) shows no tail. This results from the different errors of the particles, involved in the missing mass constraint.

The correct error input arises also in the shape of the pull distributions (Figure 3.9), which have the demanded width of $\sigma = 1$ and an average of zero. The corresponding pull spectra for the missing mass constraint look analogous.

Since the kinematic refit partially restores the realistic event topology, not only the mass resolution of intermediate particles is improved, but moreover the momentum and angular resolution of the singe particles. The different values are listed in table 3.1. The momentum and angular resolution is determined by the difference of the measured values and the Monte Carlo truth values, which constitute normal distributions around zero (in the absence of systematic errors). The relative momentum resolution dp/p is calculated for different momentum bins. $\langle \Delta(dp/p) \rangle$ is the average of the differences in resolution with and without kinematic refit for the respective momentum bins. The single values are weighted by the propagated errors of the Gaussian fits.

Energy and momentum conservation constraint

This constraint exploits the most fundamental principles of physical processes to improve the measurements, the conservation of the total energy and momentum. It affects all measured particles and forces the tracks to fulfill 4-momentum conservation. With respect to reaction R.6, the four constraint equations are given by

$$H_1 = 0 = E_{p_b} + E_{p_t} - E_{p_1} - E_{K^+} - E_{p_2} - E_{\pi^-} \tag{3.34}$$

$$\vec{H}_{2,3,4} = \vec{0} = \vec{p}_{p_b} + \vec{p}_{p_t} - \vec{p}_{p_1} - \vec{p}_{K^+} - \vec{p}_{p_2} - \vec{p}_{\pi^-} \tag{3.35}$$

where $p_b^\mu = (E_b, \vec{p}_b)^T$ and $p_t^\mu = (E_t, \vec{p}_t)^T$ are the 4-momenta of the beam and the target particles, respectively. Equation 3.35 is a vector equation and contains the

momentum conservation constraints in x, y and z direction. The D-matrix elements are collected in appendix A.
If the final state does not contain photons[13], the energy and momentum conservation constraint is equal to setting the missing mass of all particles to zero. However, if photons occur in the particle reaction, the 4-momentum conservation constraint is not applicable. In this case, the missing mass constraint for all particles can be applied, since the rest mass of the photon is equal to zero. In principle, this method can be used to analyze the second decay channel of the ppK^- into a Σ^0 and a proton, where the Σ^0 further decays into Λ and γ (reaction R.3). Since the γ of the second channel cannot be detected by FOPI, both reactions end up in the same final state. The application of the energy and momentum conservation constraint inevitably rejects events containing the intermediate Σ^0. Fitting these events results in large χ^2 values, because the 4 charged particles alone do not fulfill 4-momentum conservation in reality. Though, the employment of the missing mass constraint would keep events belonging to this reaction.
Figure 3.10 shows the missing energy $\Delta E = E_{p_b} + E_{p_t} - E_{p_1} - E_{K^+} - E_{p_2} - E_{\pi^-}$ and the missing momentum in z direction $\Delta p_z = p_{z,p_b} + p_{z,p_t} - p_{z,p_1} - p_{z,K^+} - p_{z,p_2} - p_{z,\pi^-}$ before (red) and after (blue) applying the kinematic refit with 4-momentum conservation constraint. The refit clearly succeeds in shifting the missing energy and momentum

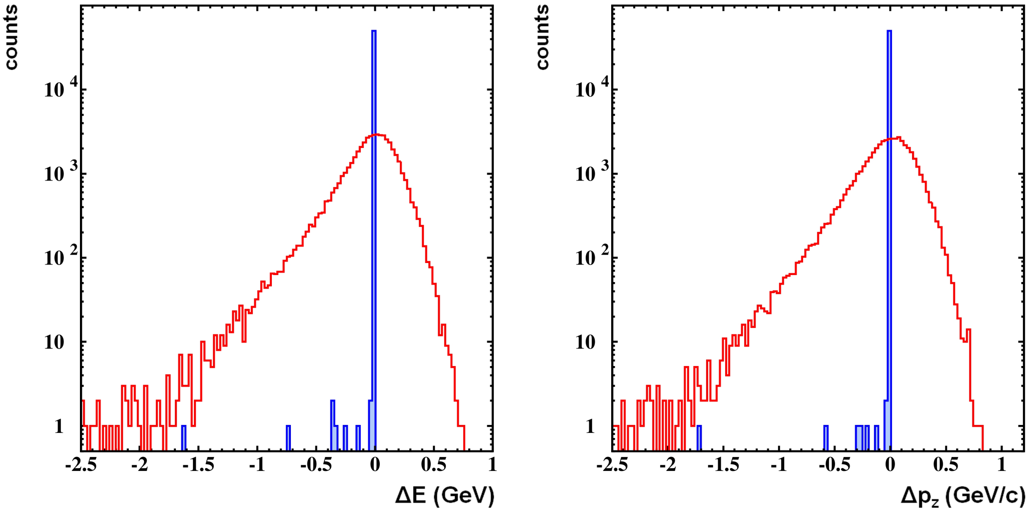

(a) (b)

Figure 3.10: (a): Energy conservation. The difference of the initial energy and the energy of the final particles is illustrated for raw (red) and refitted (blue) events. (b): Momentum conservation in z-direction. The plot shows the difference of initial and final z component of the momentum for raw (red) and refitted (blue) particles.

---

[13] The FOPI spectrometer is not capable of detecting photons.

to zero. Only in very rare cases, the constraint condition is not perfectly fulfilled after the fit, similar to the invariant mass constraint. For the energy conservation, these events are located on the left side of the zero peak, resulting from the particular definition of the constraint function. Even though the failed events are also exclusively located on the left side in the missing momentum spectrum (figure 3.10b), they can in principle occur on either side.

The χ^2 distribution with a ndf fit value of 3.99 is shown in figure 3.11a. The true ndf of the refit is 4, due to the four constraint equations (3.34-3.35). The corresponding p-value distribution (figure 3.11b) is evenly spread, with an excess at low values. This peak originates from the events where the 4-momentum conservation constraint is not accurately satisfied. Analog to the invariant mass constraint, the reason for these events could be local minima of the constraint condition.

A selection of the set of pull distributions is shown in figure 3.12. Again, the spectra have a width of $\sigma = 1$ and a mean value at $\mu = 0$ due to the known errors.

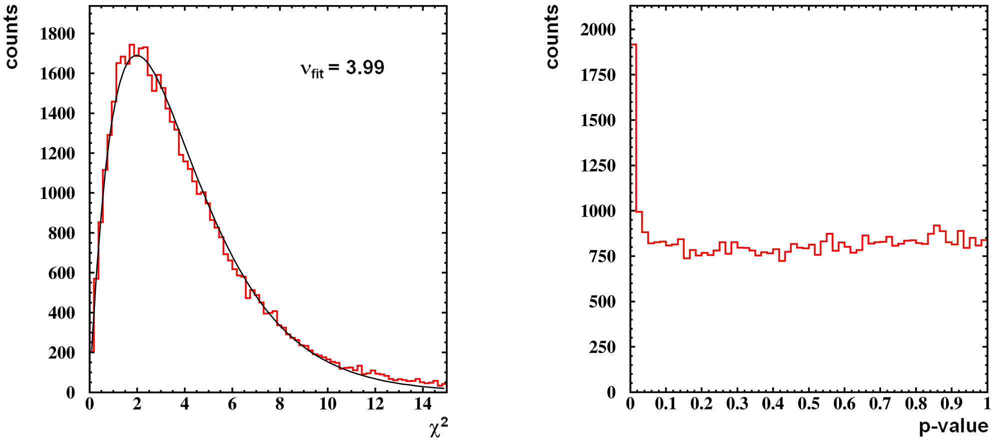

(a) (b)

Figure 3.11: χ^2 distribution with $ndf = 4$ (a) and p-value distribution (b) of the kinematic refit with energy and momentum conservation constraint. The black curve indicates the fit to the red χ^2 spectrum.

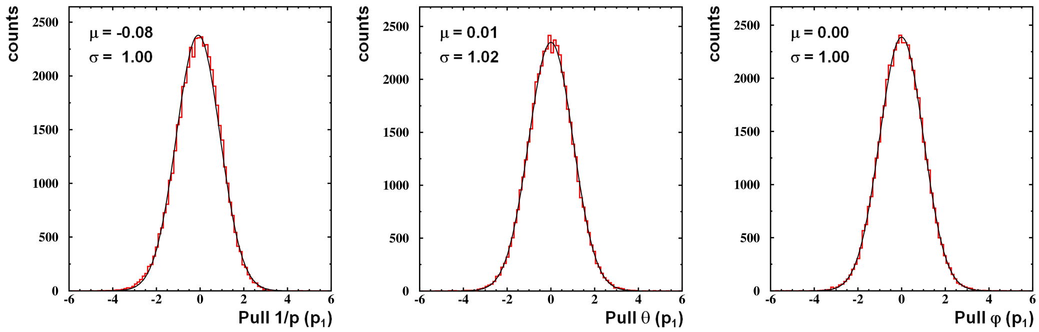

Figure 3.12: Kinematic refit with energy and momentum conservation constraint. Shown are the pull distributions for 3 of totally 12 parameters. The black curves represent the fitted Gauss functions.

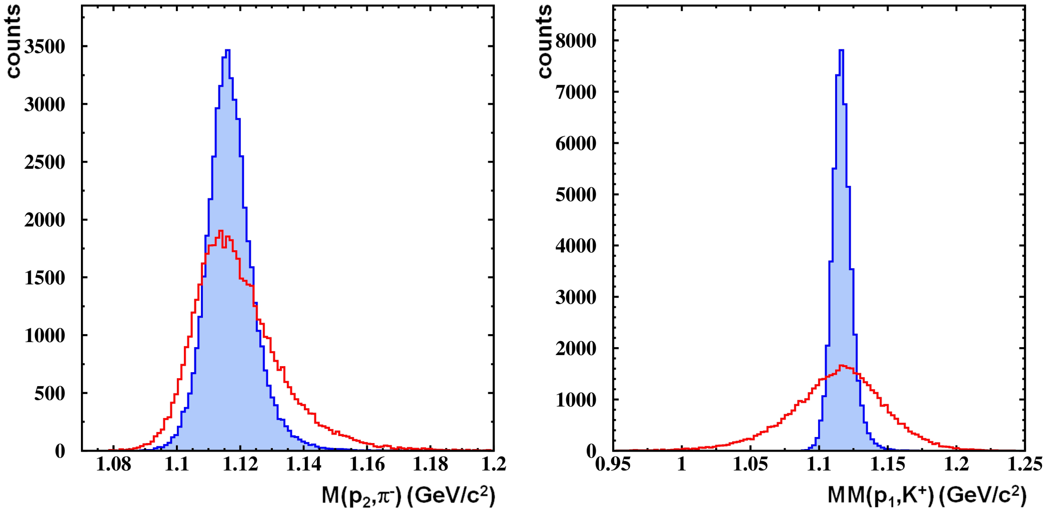

(a) (b)

Figure 3.13: Invariant mass of p_2 and π^- (a) and missing mass of p_1 and K^+ (b) before (red spectrum) and after (blue spectrum) the kinematic refit with energy and momentum conservation constraint.

With high probability, the refitted tracks that fulfill 4-momentum conservation, reflect the real process to a better extent than the raw tracks. Therefore, observables like the mass, momentum or angular resolution, should improve with the refit. This effect is illustrated in figure 3.13, where (a) shows the invariant mass spectrum of p_2 and π^- and (b) the missing mass distribution of p_1 and K^+ before (red) and after (blue) the kinematic refit. The width of the invariant mass spectrum decreases by 35 %, the missing mass resolution improves by 82 %. The initial width of the raw missing mass spectrum is larger compared to the invariant mass distribution due to the different measurement resolutions for the involved particles. After the refit, the two different

spectra have equal shape, because the 4-momenta are conserved (see section 2.7.3). Therefore, the improvement of the missing mass resolution exceeds the enhancement of the invariant mass resolution.
Table 3.2 contains the changes in momentum and angular resolution as a result of kinematic fitting with energy and momentum conservation constraint.

3.3.2 Vertex constraints

The procedure of solving for unknown parameters $\vec{z}$ in the constraint conditions was introduced in section 3.1.2. If $\vec{z}$ contains components of particle vertices, the respective constraints are called vertex constraints. In contrast to non-vertex constraints, the particle trajectories have to be fully determined, including the emission points of the tracks. Therefore, all six parameters $\vec{\alpha}_{mix,i} = (1/p_i, \theta_i, \varphi_i, x_{x,i}, x_{y,i}, x_{z,i})^T$ have to be included in the fit.
The kinematic refit for the pp analysis includes intersection constraints of two particles, respectively and a secondary vertex constraint, which is especially customized for the exclusive analysis of reaction R.6.

Intersection constraint

The intersection constraint forces the tracks of two particles to intersect at a common space point. This constraint vertex is parameterized by the vector of unknowns $\vec{z}$ in the Lagrange equation 3.14. As explained in section 3.1.2, the kinematic refit calculates a new set of parameters $\vec{\alpha}$ and a fitted vertex $\vec{z}$. In this respect, it can be chosen whether the tracks have to intersect at a fixed vertex, which has to be given as input in advance. The other possibility, which is going to be discussed in the following subsection, is to let the refit place the new vertex $\vec{z}$ within an error band around an initial vertex $\vec{z}_0$. The vertex covariance matrix $\mathbf{V}_{\vec{z}_0}$ determines the range of the error ellipsoid. If the errors are set to very large values, the vertex can be arbitrarily placed by the refit. The final position $\vec{z}$ will then be determined by the other constraints (e.g. energy and momentum conservation), which govern the shifts of the particle tracks. This type of vertex constraint is used in the pp analysis.
Concerning the underlying reaction R.6, the intersection constraint can be used to force the daughter particles p_2 and π^- of the Λ hyperon to intersect at a Λ vertex $\vec{z}_\Lambda$. The tracks are represented by their momentum $\vec{p}_i$ and an emission point $\vec{x}_i$, at which the momentum is evaluated. The emission points are the points of closest approach

Particle	$\langle \Delta(dp/p) \rangle$	$\Delta(d\theta)$	$\Delta(d\varphi)$
p	58.9%	12.3%	1.39%
K^+	19.1%	10.5%	12.7%
π^-	14.5%	16.4%	1.28%

Table 3.2: Average improvement of the momentum, θ and φ resolution due to the kinematic refit with energy and momentum conservation constraint.

(poca) to the beam axis (see Figure 3.14).
For reasons of simplification, the particle tracks are approximated as straight lines. This assumption is motivated by the short Λ decay length of $c\tau_\Lambda \approx 7\,\mathrm{cm}$. In order to check if the approximation is legitimate, the deviation of the straight tracks from real bended curves within the distance of 15.5 cm from the target to the SiΛVio-B plane was estimated using simulations. The polar angle deviation is completely negligible, whereas the maximum difference in the φ angle is 0.4° for protons and 1.8° for pions. This deviation is acceptable, in particular since around 67 % of the Λ's already decay within half the distance. The straight tracks are represented by the following vector equation.

$$\vec{r}_i = \vec{x}_i + \tau_i\,\vec{p}_i \tag{3.36}$$

where τ_i is a variable scalar. The condition, that the p_2 and π^- tracks intersect at a Λ vertex $\vec{z}_\Lambda$, reads

$$\vec{r}_{p_2}(\vec{z}_\Lambda) - \vec{r}_{\pi^-}(\vec{z}_\Lambda) = \vec{x}_{p_2} + \tau_{p_2}(\vec{z}_\Lambda)\,\vec{p}_{p_2} - \vec{x}_{\pi^-} - \tau_{\pi^-}(\vec{z}_\Lambda)\,\vec{p}_{\pi^-} = \vec{0} \tag{3.37}$$

The coefficients $\tau_i(\vec{z}_\Lambda)$ times the length of the momenta give the distance between the emission points of the particles and the Λ vertex.

$$\tau_i(\vec{z}_\Lambda) = \frac{|\vec{z}_\Lambda - \vec{x}_i|}{|\vec{p}_i|} \tag{3.38}$$

The full intersection constraint condition is a 3-component vector equation and is

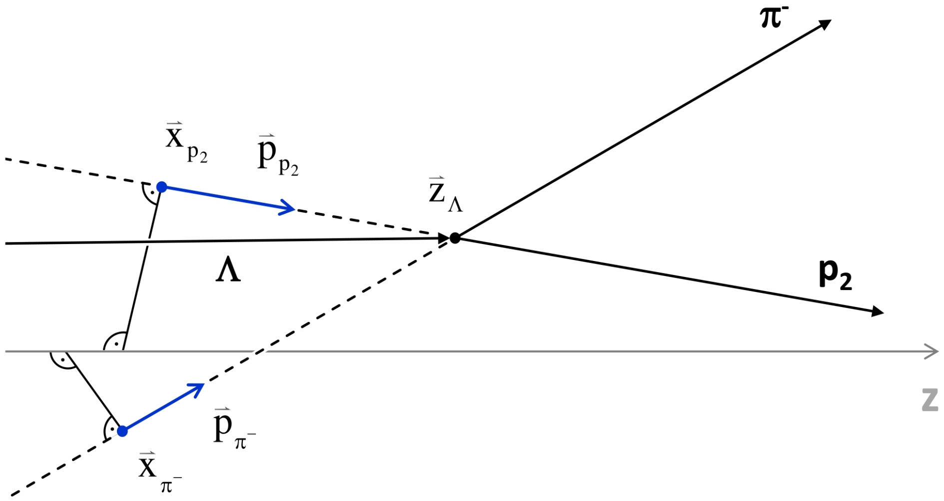

Figure 3.14: Scheme of the Λ decay into p_2 and π^-. The tracks are represented by straight lines, which are illustrated with the respective emission points $\vec{x}_i$ and direction vectors $\vec{p}_i$.

given by the following expression.

$$\vec{H}(\vec{\alpha},\vec{z}_\Lambda) = \vec{0} = \vec{x}_{p2} + C_{p2}\frac{|\vec{z}_\Lambda - \vec{x}_{p2}|}{|\vec{p}_{p2}|}\vec{p}_{p2} - \vec{x}_{\pi^-} - C_{\pi^-}\frac{|\vec{z}_\Lambda - \vec{x}_{\pi^-}|}{|\vec{p}_{\pi^-}|}\vec{p}_{\pi^-} \tag{3.39}$$

The coefficients C_i are defined in the following way.

$$C_i = \frac{z_{\Lambda,z} - x_{z,i}}{\sqrt{(z_{\Lambda,z} - x_{z,i})^2}} = \begin{cases} +1 & \text{if } x_{z,i} < z_{\Lambda,z} \\ -1 & \text{if } x_{z,i} > z_{\Lambda,z} \end{cases} \tag{3.40}$$

They are either 1 or -1, depending on if the z-component of the emission points $x_{z,i}$ is smaller or larger than the z-component of the Λ vertex $z_{\Lambda,z}$. These coefficients are necessary, since the leading signs in front of the factors $\tau_i(\vec{z}_\Lambda)$ have to change, if the emission points are located in front of or behind the Λ vertex with respect to the direction of the momentum $\vec{p}_i$. However, the terms $|\vec{z}_\Lambda - \vec{x}_i|$ themselves are independent of this relation, because the different signs are canceled by the squares. Including now the coefficients C_i enables the kinematic refit to change the leading signs in the constraint equations autonomously[14]. Since the C_i are constant, the derivatives of the constraints (D-matrix elements), which determine the new parameters $\vec{\alpha}$, are unchanged. The D-matrix elements are listed in appendix A.

The initial vertex position $\vec{z}_0$ is principally unknown in advance. Therefore, the kinematic refit reconstructs the center of the closest connection between the two tracks and defines this space point as initial vertex position. The corresponding calculations are shown in appendix B.

A criterion to check, whether the intersection constraint is in fact fulfilled after the kinematic refit, is the linear dependence of 3 vectors within a common plane, also referred to as coplanarity. If the tracks intersect, the two direction vectors $\vec{p}_{p2}$ and $\vec{p}_{\pi^-}$ and the difference vector of the two emission points $\vec{s} \equiv \vec{x}_{p2} - \vec{x}_{\pi^-}$ lie in a common plane (Figure 3.15). From this, it follows that one of the three vectors can be written as a linear combination of the two others, they are linear dependent. Mathematically, the determinant of a matrix containing linear dependent column vectors is zero. Therefore, the particle tracks are

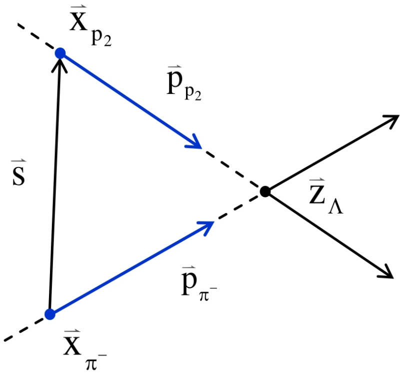

Figure 3.15: Linear dependence of 3 vectors within a common plane.

---

[14] It could for example be the case, that fulfilling all constraints would require the Λ vertex to move on the other side of the emission point of a certain particle with respect to its momentum vector. This would change the leading signs of the respective terms in the constraint equations. The coefficients C_i allow these signs to change freely during the refitting process.

coplanar if the determinant

$$D_{int} = \begin{vmatrix} p_{x,p_2} & p_{x,\pi^-} & s_x \\ p_{y,p_2} & p_{y,\pi^-} & s_y \\ p_{z,p_2} & p_{z,\pi^-} & s_z \end{vmatrix} \tag{3.41}$$

is equal to zero. Though, in principle the tracks could also be mutually parallel. This case can be excluded by calculating the angle between the two momentum vectors and rejecting values close to zero. Figure 3.16a shows the determinant D_{int} for unrefitted (red) end refitted (blue) tracks with angles unequal to zero. The peak at zero for refitted events clearly shows, that the two tracks indeed intersect after applying the kinematic refit. The p-value distribution (Figure 3.17b) is flat and the pull distributions have the expected shape (Figure 3.18). The pull distributions of the $1/p$ parameters are always zero, since the respecting D-matrix elements vanish. This originates from the fact, that the kinematic refit can shift the tracks in order to intersect by varying the track angles exclusively. A change in the magnitude of the particles momenta would not result in different track orientations. The expected ndf of the fit is the number of constraints minus the number of vertex parameters, as explained in section 3.1.2, which should be 0 in case of the intersection constraint. However, figure 3.17a shows the χ^2 distribution of the fit with a fitted ndf value of 0.79.
The distribution of the $\vec{z}_\Lambda$ vertex y-component is displayed in figure 3.16b. The Monte Carlo truth values are represented by the black curve, the spectra of the unrefitted and refitted events are indicated in red and blue, respectively. A clear broadening of the raw distribution due to the smearing is visible. However, the spectrum of refitted tracks is nearly identical. This means, that the kinematic refit forces the tracks to intersect at a new vertex, that is very close to the initial vertex position, which is determined by the center of closest distance between the two original tracks. Moreover, the intersection constraint has no noticeable effect on the other observables such as mass, momentum or angular resolutions either.

Secondary vertex constraint

The kinematic refit for the pp analysis additionally contains a secondary vertex constraint, which is designed exclusively for the underlying reaction R.6. Though, it can be principally used for every reaction with four particles in the final state, where two tracks stem from a common mother particle. The secondary vertex constraint contains 9 single constraint conditions, which are defined via the following equations.

$$\begin{aligned} \vec{H}_{1-3}(\vec{\alpha},\vec{z}_\Lambda) = \vec{0} = \vec{x}_{p_2} + C_{p_2}\frac{|\vec{z}_\Lambda - \vec{x}_{p_2}|}{|\vec{p}_{p_2}|}\vec{p}_{p_2} \\ - \vec{x}_{\pi^-} - C_{\pi^-}\frac{|\vec{z}_\Lambda - \vec{x}_{\pi^-}|}{|\vec{p}_{\pi^-}|}\vec{p}_{\pi^-} \end{aligned} \tag{3.42}$$

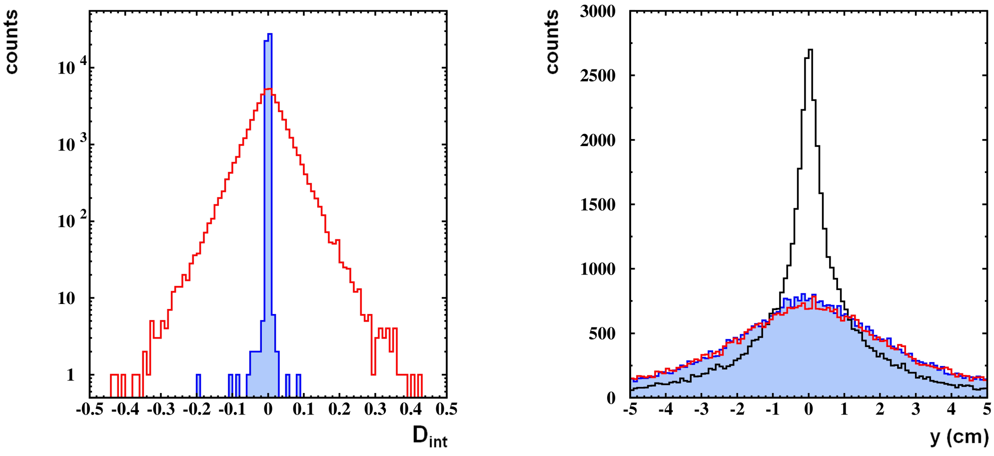

(a) (b)

Figure 3.16: (a): Intersection determinant D_{int} for raw (red) and refitted (blue) tracks, (b): y-component of the Λ vertex $\vec{z}_\Lambda$ for Monte Carlo truth values (black), raw (red) and refitted (blue) tracks.

$$\vec{H}_{4-6}(\vec{\alpha},\vec{z}_\Lambda,\vec{z}_{Prim}) = \vec{0} = \vec{x}_{p_1} + C_{p_1}\frac{|\vec{z}_{Prim} - \vec{x}_{p_1}|}{|\vec{p}_{p_1}|}\vec{p}_{p_1} - \vec{z}_\Lambda - C_\Lambda\frac{|\vec{z}_{Prim} - \vec{z}_\Lambda|}{|\vec{p}_{p_2} + \vec{p}_{\pi^-}|}(\vec{p}_{p_2} + \vec{p}_{\pi^-}) \tag{3.43}$$

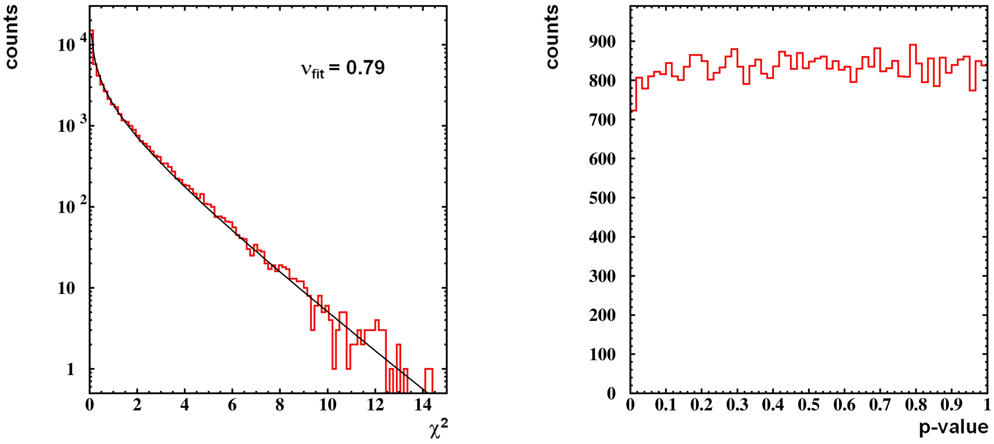

(a) (b)

Figure 3.17: χ^2 distribution (a) and p-value distribution (b) of the kinematic refit with intersection constraint.

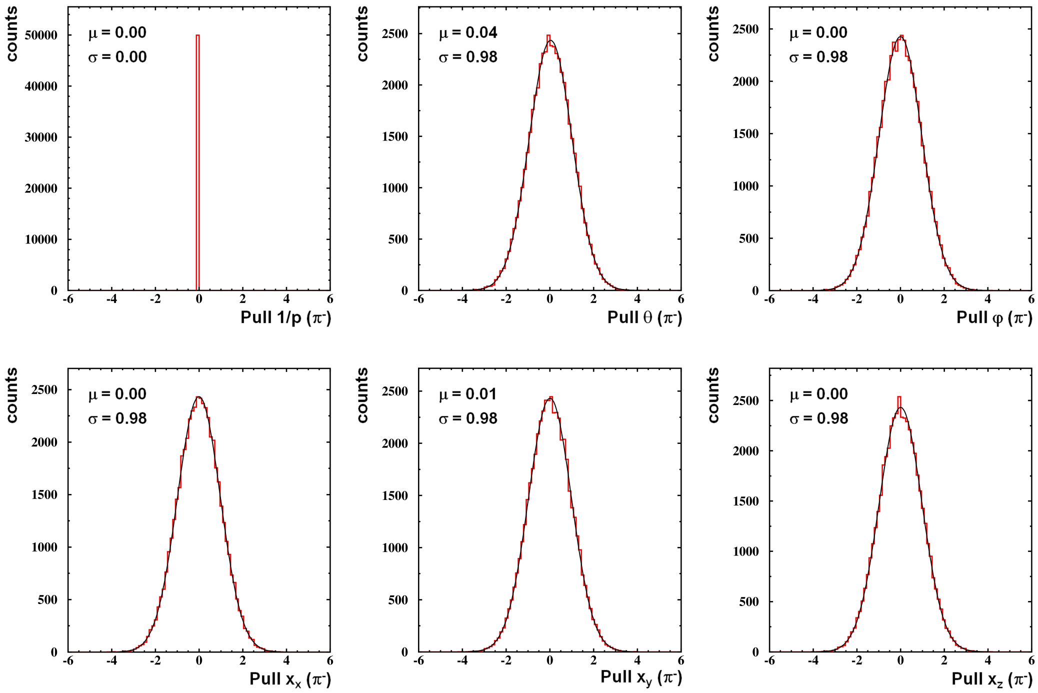

Figure 3.18: Kinematic refit with intersection constraint. The upper row shows the pull distributions for 3 momentum parameters. The distributions for the $1/p$ parameters vanish, since the corresponding D-matrix elements are equal to zero. The lower row shows the pull distributions for 3 emission point parameters. The black curves indicate the fitted Gauss functions.

$$\vec{H}_{7-9}(\vec{\alpha},\vec{z}_{\Lambda},\vec{z}_{Prim}) = \vec{0} = \vec{x}_{K^+} + C_{K^+}\frac{|\vec{z}_{Prim} - \vec{x}_{K^+}|}{|\vec{p}_{K^+}|}\vec{p}_{K^+} - \vec{z}_{\Lambda} - C_{\Lambda}\frac{|\vec{z}_{Prim} - \vec{z}_{\Lambda}|}{|\vec{p}_{p_2} + \vec{p}_{\pi^-}|}(\vec{p}_{p_2} + \vec{p}_{\pi^-}) \tag{3.44}$$

Analog to the other coefficients, C_{Λ} is defined as

$$C_{\Lambda} = \frac{z_{\Lambda,z} - z_{Prim,z}}{\sqrt{(z_{\Lambda,z} - z_{Prim,z})^2}} = \begin{cases} +1 & \text{if } z_{Prim,z} < z_{\Lambda,z} \\ -1 & \text{if } z_{Prim,z} > z_{\Lambda,z} \end{cases} \tag{3.45}$$

The constraint fitting procedure consists of three single steps. In the first step (equation 3.42), the p_2 and π^- are forced to intersect at a common Λ vertex $\vec{z}_{\Lambda}$ (equal to the single intersection constraint of the previous subsection). The Λ particle is reconstructed via vector addition from the daughter particles p_2 and π^-: $\vec{p}_{\Lambda} = \vec{p}_{p_2} + \vec{p}_{\pi^-}$. The emission point of the Λ is the secondary vertex $\vec{z}_{\Lambda}$. In the next two steps (equations 3.43 and 3.44), the reconstructed Λ is forced to intersect with the other two particles p_1 and K^+ at a primary vertex $\vec{z}_{Prim}$.

Since the constraint equations are essentially three single intersection constraints, the quality spectra are expected to have shapes analog to the single constraint. Indeed, the χ^2, p-value and pull distributions resemble the spectra of the single intersection constraint, however, they slightly deviate from the correct shape which cannot be traced back to a wrong error input (Figure 3.20). Also the determinants $D_{int,i}$ of all intersecting particle combinations peak at zero, so they in fact intersect (Figure 3.19 shows the intersection determinant for the reconstructed Λ and p_1). Hence, the obvious reason might be, that the number of constraint conditions is so large, that the kinematic refit starts to deviate from its expected behavior. Nevertheless, the discrepancies are small compared to the effect of wrong errors, which are discussed in the next subsection.

Figure 3.21 shows the spatial resolutions of the primary vertex, where the three particles p_1, K^+ and Λ intersect. The black curve represents the true Monte Carlo values, the raw and refitted spectra are illustrated in red and blue, respectively. Obviously, an improvement of the primary vertex resolutions is obtained by applying the secondary vertex constraint. The corresponding values are listed in table 3.3. Analog to the single intersection constraint, the secondary vertex constraint has no impact on momentum, mass, angular and secondary vertex resolutions.

3.3.3 Effect of wrong errors

In the previous cases, the errors of the kinematic refit were exactly known. Hence, the different fit quality distributions had the expected shape. However, in the real experiment, the uncertainties are never perfectly known and have to be estimated. Since the χ^2, p-value and pull distributions are sensitive to the correct error input, they can be used to optimize the uncertainties. In any case, the kinematic refit shifts the particle tracks in order to satisfy the constraints, even if the corresponding errors are not correct. If the uncertainties are underestimated, the parameters are

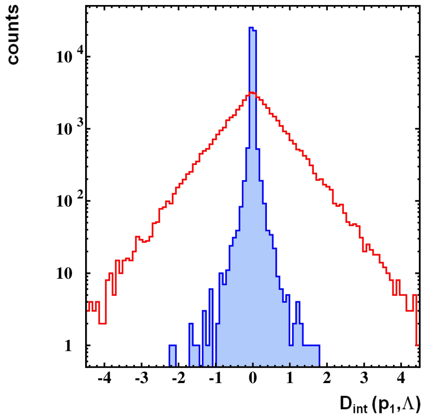

Figure 3.19: Kinematic refit with secondary vertex constraint. Intersection determinant of the reconstructed Λ and the p_1. After the fit (blue), the tracks clearly intersect. This is also valid for the other intersecting particle combinations.

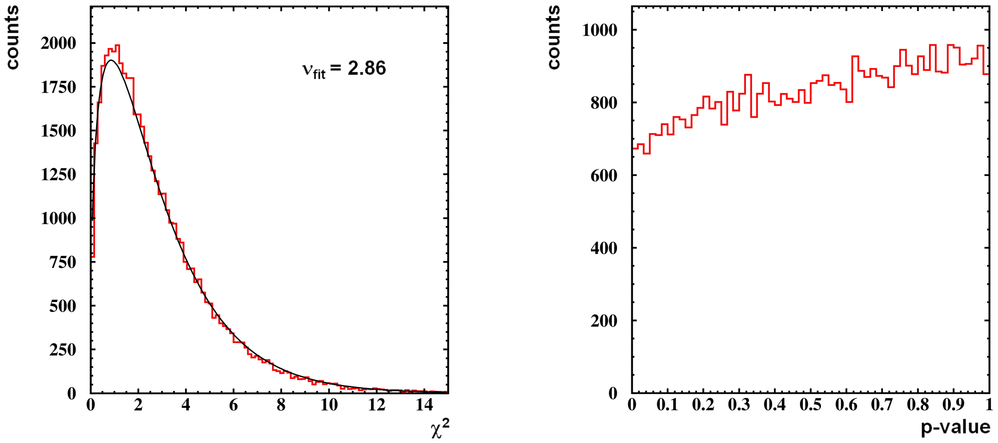

(a) (b)

Figure 3.20: χ^2 distribution (a) and p-value distribution (b) of the kinematic refit with secondary vertex constraint.

$\Delta\sigma_{Prim,x}$	$\Delta\sigma_{Prim,y}$	$\Delta\sigma_{Prim,z}$
13.8%	14.3%	10.6%

Table 3.3: Improvement of the primary vertex resolution due to the kinematic refit with secondary vertex constraint.

moved outside of their error band, causing a shift which is larger than the refit would

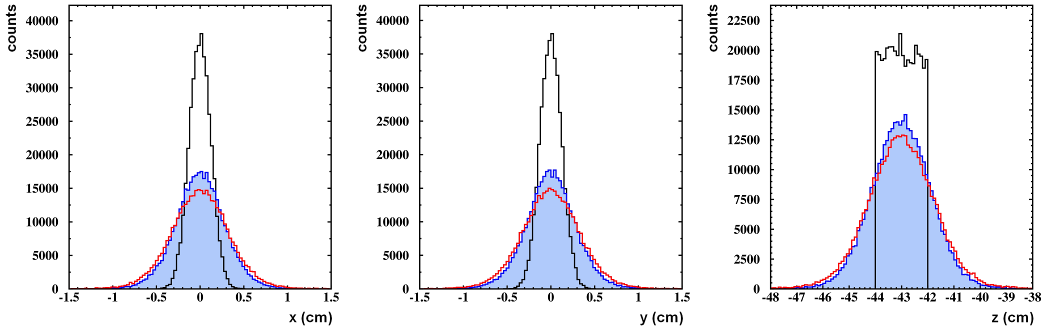

(a) (b) (c)

Figure 3.21: Kinematic refit with secondary vertex constraint. Shown are the primary vertex (p_1, K^+, Λ) distributions. The Monte Carlo truth values (black), the raw (red) and the refitted (blue) events are illustrated.

expect due to the covariance matrix. This generally results in larger χ^2 values[15] . The effect of manually increasing the errors of $1/p$ by 25 % compared to the true values is illustrated in figure 3.22a, where energy and momentum conservation is used as constraint. The shown χ^2 distribution resembles a distribution corresponding to a larger ndf. The ndf value of the fit is 4.84, however the distribution slightly deviates from the theoretical curve. The larger χ^2 leads to a lower p-value, the distribution of which is non-flat with a shift to the left side (figure 3.23a). The effect of underestimated errors on the pull distributions is a broadening ($\sigma > 1$), which is shown in figure 3.24a. Also the pull distributions of the angular parameters are broadened, even though only the $1/p$ error is wrong. This originates from the attempt of the kinematic refit to compensate the small error in $1/p$ direction by partially exceeding the changes of the other parameters. However, the pull functions are still centered around zero. An underestimation of the angular errors within a realistic range does not show any noticeable effect on the discussed distributions.
Figures 3.22b and 3.23b show the implications of overestimated errors. For this purpose, the errors of the $1/p$ parameters are scaled down by 25 %. In this case, the error bands of the tracks are larger than necessary, hence the refit shifts the parameters $\vec{\alpha}$ less than it is in principle allowed due to the covariance matrix. This results in smaller χ^2 values and larger p-values. The corresponding χ^2 distribution is shifted to smaller ndf, providing a fit value of 3.19. Again, the spectrum deviates from the theoretical pdf function. The effect on the pull distributions is contrary to the previous case of underestimated errors, causing a reduction of the width ($\sigma < 1$)

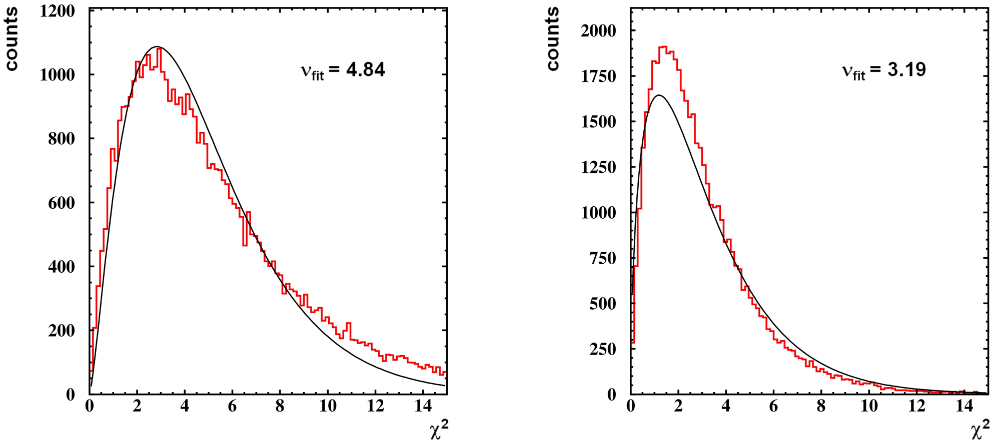

(a) (b)

Figure 3.22: χ^2 distributions for the kinematic refit with energy and momentum conservation constraint. (a): underestimation of errors by 25 % (b): overestimation of errors by 25 %. The black lines represent the fitted χ^2 curves.

---

[15] Notice, that the errors sit in the denominator of the χ^2 equation (3.2). Therefore, smaller errors result in larger χ^2 values, given the same change of parameters in the nominator.

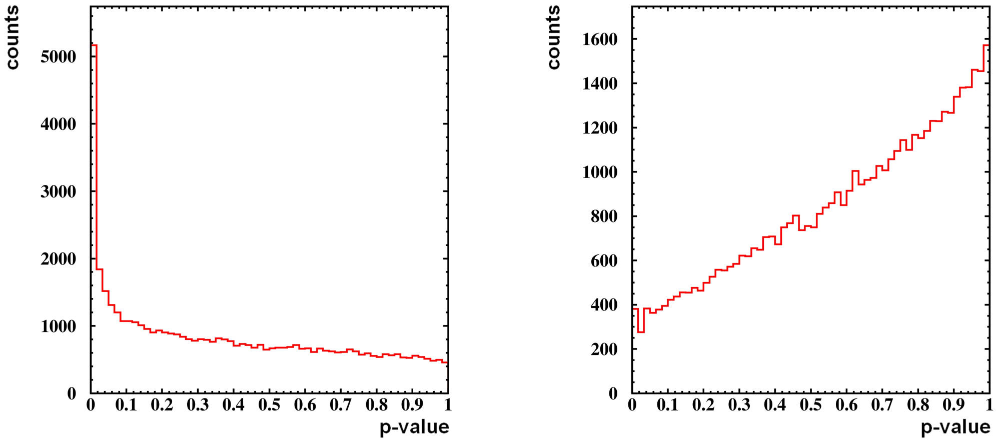

(a) **(b)**

Figure 3.23: p-value distributions for the kinematic refit with energy and momentum conservation constraint. (a): underestimation of errors by 25 % (b): overestimation of errors by 25 %.

(Figure 3.24b).
If the elements of the covariance matrix $\mathbf{V}_{\vec{\alpha}_0}$ are not completely Gaussian distributed but additionally include systematic errors, the pull distributions are shifted along the x-axis, whereas their width is unaffected. Figure 3.24c shows the pull distribution of the kaons $1/p$ parameter, where the $1/p$ parameters of all particles are systematically increased by 5 %. Also the χ^2 and p-value spectra (Figure 3.25) deviate from the theoretical curves. However, it is hardly possible to detect the presence of systematic errors by looking at these distributions alone. Only the pull distributions are sensitive

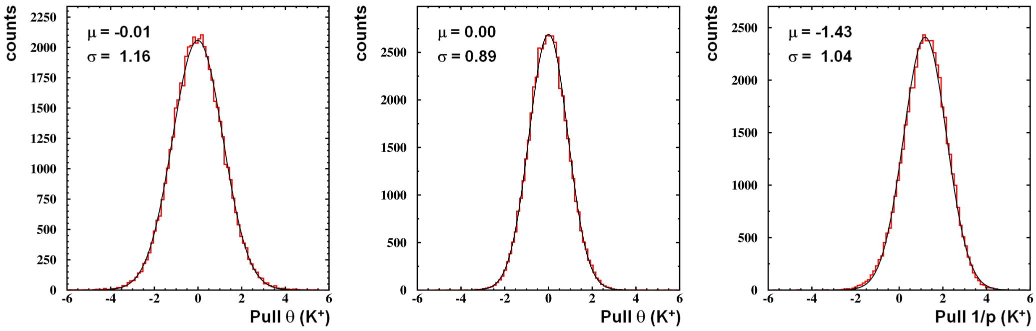

(a) **(b)** **(c)**

Figure 3.24: Pull distributions for the kinematic refit with energy and momentum conservation constraint. (a): underestimation of $1/p$ error by 25 % (b): overestimation of $1/p$ error by 25 % (c): systematic shift of $1/p$ parameter by 5 %. The fitted normal distributions are indicated by the black curves.

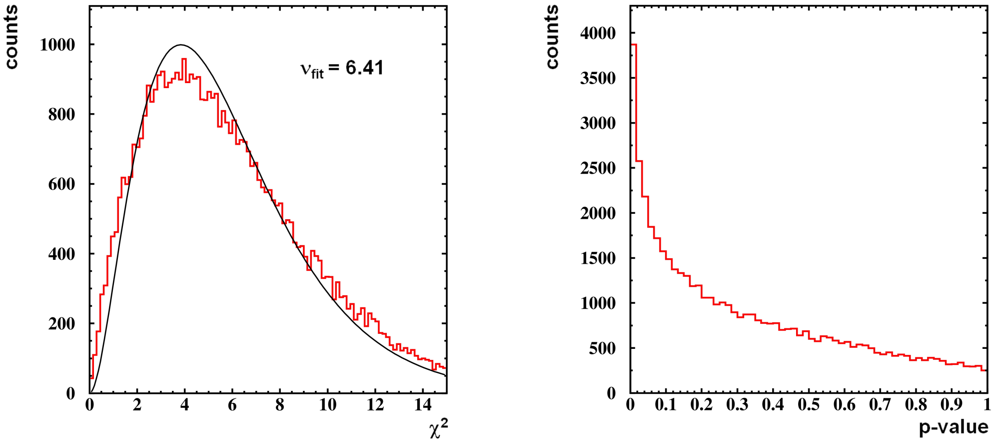

(a) (b)

Figure 3.25: Effect of a systematic shift by 5 % of the parameters $1/p$. χ^2 distribution (a) and p-value distribution (b) of the refit with energy and momentum conservation constraint.

to the statistic or systematic nature of the uncertainties. If the errors possess a systematic component, they are no longer centered around zero. Hence, the Gauss-Markov theorem is not valid anymore in the presence of systematic errors, which can lead to an unexpected behavior of the kinematic refit. In this case, the new parameters $\vec{\alpha}$ are not guaranteed to have minimum variance and to be unbiased.

3.3.4 Consequences of background

In the preceding examples, the kinematic refit was applied to events, that fulfilled the constraint conditions in the beginning, exclusively. However, in the real experiment, a certain amount of background will always be present. This background can for example be caused by events with misidentified particles. Of course, these events did not meet the different constraint conditions originally. Nevertheless, the kinematic refit also shifts the background events such, that the corresponding particles fulfill the constraints after the fit. Since the variation of the respective parameters will be larger than for the correct events in most of the cases, the refitted background will result in large χ^2 values. The corresponding p-value distribution has a peak at low values, similar to the spectrum shown in figure 3.23a. Due to the fraction of events, that are stronger shifted compared to the assumed errors, the pull distributions show larger tails. This leads to a non-Gaussian shape of the distributions.

In the real analysis, the kinematic refit will inevitably be applied to a certain fraction of background events. Usually, the background can be reduced by cutting on low p-values. For this purpose, a significance α is defined, which is the area to the right of the corresponding significance level beneath the χ^2 distribution (see footnote 9). The refitted events are rejected, if the p-value is smaller than the significance: $p - value < \alpha$. However, for this cut it is important to determine the covariance matrix $\mathbf{V}_{\vec{\alpha}_0}$ as careful as possible. If for instance the errors are too small, the p-value distribution is shifted to low values (see figure 3.23a). In this case, the cut on low p-values will reject a lot of non-background events as well. In contrast, if the errors are overestimated, the p-values cumulate at high values (see figure 3.23b), rendering the cut ineffective [Sie10].

The behavior of refitted background events using the example of full scale pp simulations is discussed in section 4.2.2.

4 Exclusive analysis of the reaction $pp \rightarrow pK^+\Lambda$

This chapter presents the exclusive analysis of the reaction $pp \rightarrow pK^+\Lambda$, measured at a beam energy of 3.1 GeV with the FOPI spectrometer. The main goal of the underlying analysis is the investigation of the predicted kaonic bound state ppK^-, exploiting its decay into Λ and p. The reaction of interest reads as follows.

$$\begin{array}{l} p + p \longrightarrow ppK^- + K^+ \\ \qquad\qquad\quad \hookrightarrow \Lambda + p \\ \qquad\qquad\qquad\quad \hookrightarrow p + \pi^- \end{array} \tag{R.2}$$

Before analyzing the ppK^-, the intermediate Λ hyperon has to be reconstructed, which decays into p and π^- with a branching ratio of 64 % (see section 1.3). As described in the previous chapter, the improvement of the Λ signal quality and the reduction of background are the main motivations for the development of the kinematic refit. After an introduction about the identification of $pK^+\Lambda$ events, the results of applying the kinematic refit to full scale simulations and to experimental data are discussed in the following sections.

4.1 Identification of $pK^+\Lambda$ events

The first step in the exclusive analysis of the reaction $pp \rightarrow pK^+\Lambda$ is the identification of all four charged particles in the final state (p_1, K^+, p_2, π^-). As described in section 2.7, the particles can be separated via the time of flight or energy loss information in combination with the momentum of the particles, delivered by the different sub-detectors of the FOPI spectrometer. For this purpose, 2-dimensional graphical cuts are used in order to select the different particle species.
Particles emitted in the HELITRON acceptance are identified via the time of flight information measured by the PLAWA[1]. Figure 4.1 shows the momentum divided by the charge as a function of the particle velocity v for experimental data. The black lines represent the graphical cuts, chosen to select the protons and the negatively charged pions. Particles whose velocity and momentum fall within these cuts are identified as protons or pions, respectively. Consequently, the measured masses

---

[1] A separation of the different particles using the energy loss in the HELITRON drift chamber is not possible due to the limited resolution.

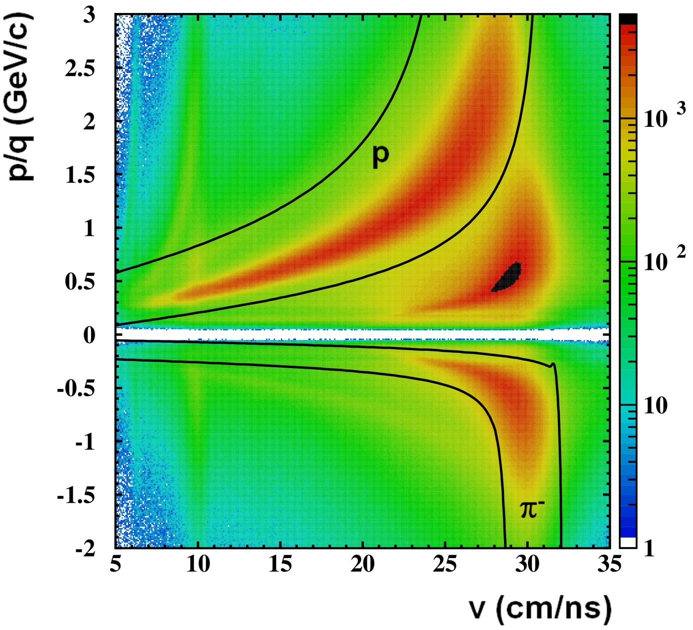

Figure 4.1: Identification of charged particles measured with the HELITRON and the PLAWA. The graphical cuts for the separation of protons and negatively charged pions are indicated by the black curves.

are set to the nominal values in order to determine the 4-momenta[2]. However, an identification of kaons using these observables is not possible due to the limited time resolution of the PLAWA and HELITRON detectors.

Particles which are emitted into the backward hemisphere are either identified via the energy loss in the CDC drift chamber or via the time of flight information delivered by the MMRPC. Figure 4.2a shows the energy loss as a function of the momentum per charge for particles measured with the CDC for experimental data. Again, the graphical cuts are indicated by the black lines. Even though the separation of p and π^- is more distinct than for HELITRON tracks (Figure 4.1), an identification of kaons is not possible. In contrast, the excellent time resolution of the MMRPC allows to separate kaons from protons and pions up to several hundreds of GeV. This is illustrated by figure 4.2b. The black lines show the theoretical positions of the different particle species, the graphical cut used for the kaon identification is indicated by the red curves. Since the particle identification with the RPC requires the measurement of the momentum with the CDC, a good matching capability of these two detectors is necessary. The investigation of the CDC-RPC matching efficiency with help of elastic proton events is discussed in section 5.4.1.

---

[2] At this point, unphysical background is introduced in case of misidentification, since the wrong energies are assigned to the respective particles.

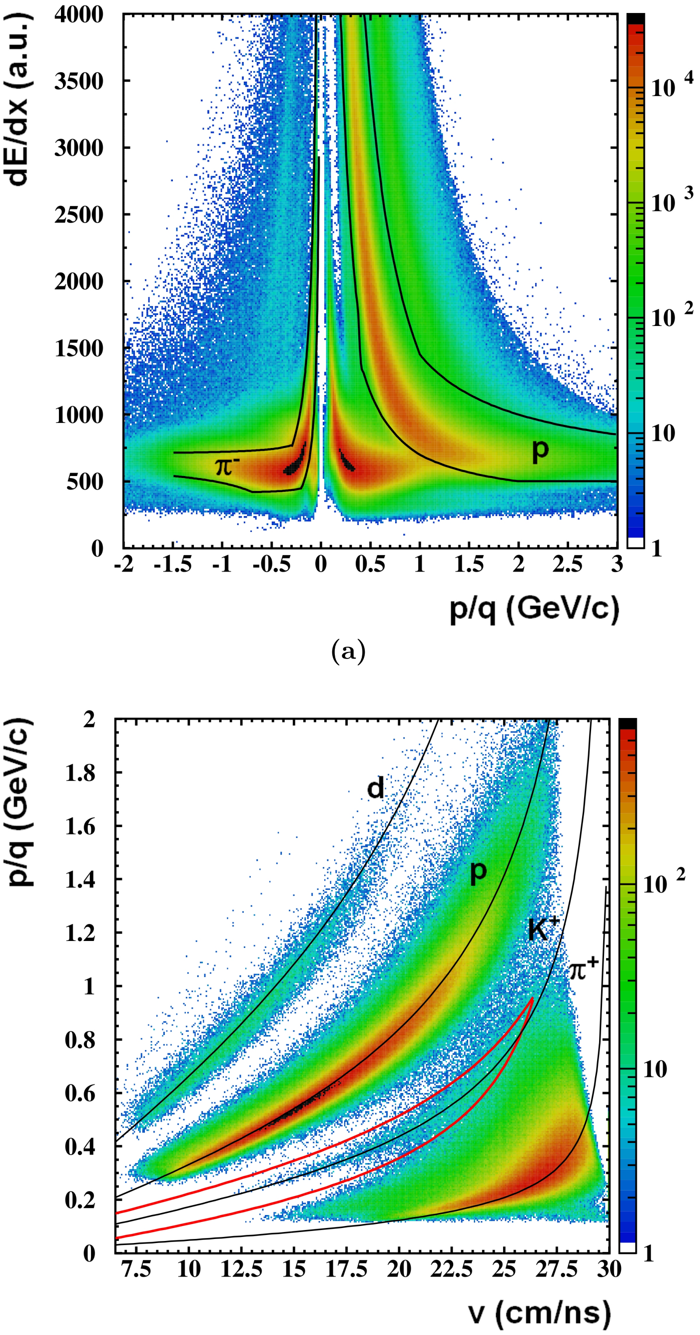

(a)

(b)

Figure 4.2: Identification of charged particles in the backward hemisphere of the FOPI spectrometer. (a): Energy loss dE/dx in the CDC vs. momentum per charge. The black curves represent the graphical cuts for the separation of protons and pions. (b): CDC momentum per charge as a function of the particle velocity v measured with the MMRPC. The theoretical positions of the different particles according to equation 2.11 are indicated by the black lines. The kaon cut is shown by the red curves. The cutoff at large velocities results from a cut on the mass differences between CDC and MMRPC in course of the matching.

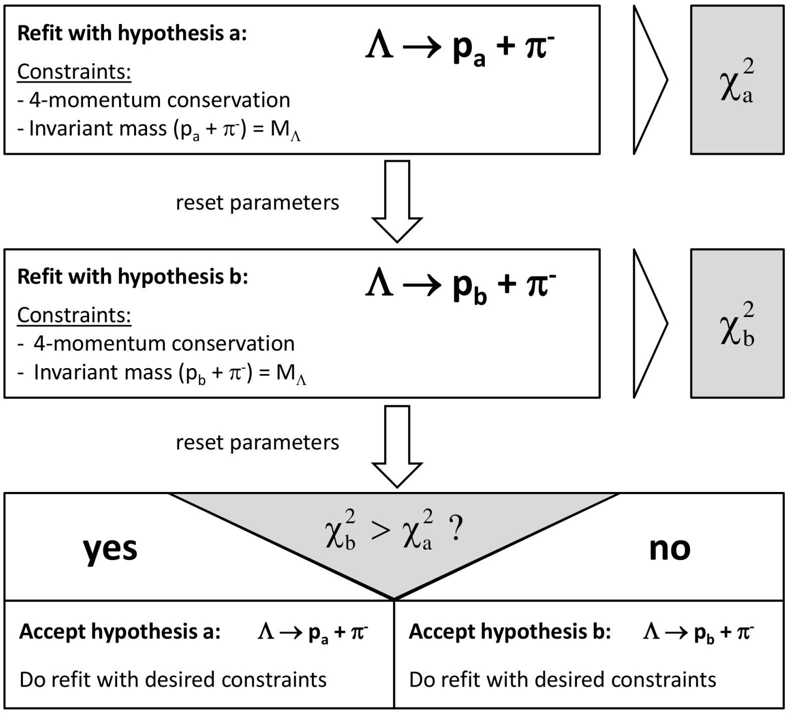

Figure 4.3: Scheme of the pre-selection process. The particle combination which results in the smaller χ^2 value is accepted and used for the actual refit.

The next step after the identification of the final state particles is the assigning of the right proton to the Λ decay. Since two protons occur in the final state of interest, it is not known in the first place, which proton originally stems from the decay of the intermediate Λ. For this purpose, a pre-selection method based on the repeated application of the kinematic refit is implemented. The scheme of the procedure is shown in figure 4.3. The two protons are referred to as p_a and p_b in this illustration. First, the kinematic refit is applied based on the hypothesis, that p_a stems from the Λ decay: $\Lambda \to p_a + \pi^-$. For the pre-selection, the energy and momentum conservation and the Λ invariant mass constraints are used. The invariant mass constraint is crucial, since it is sensitive to the correct combination of proton and pion. The refit calculates a χ^2_a value, which is stored for further comparison. The refitted parameters $\vec{\alpha}$ are discarded and reseted to the original values $\vec{\alpha}_0$. Second, the kinematic refit with the same constraint conditions is repeated with the hypothesis, that the other proton p_b was created in the Λ decay: $\Lambda \to p_b + \pi^-$. Again, a χ^2_b value is calculated, which is compared to the χ^2_a of the previous refit. Since one hypothesis is certainly wrong, the corresponding χ^2 value will be larger than the χ^2 of the refit with the right particle combination. Finally, the parameters are again reseted to the unrefitted values $\vec{\alpha}_0$ and the proton pion combination, which corresponds to the smaller χ^2, is chosen. This assignment of the final state particles is the input for the actual kinematic refit, which calculates the new set of parameters $\vec{\alpha}$ for the further analysis.

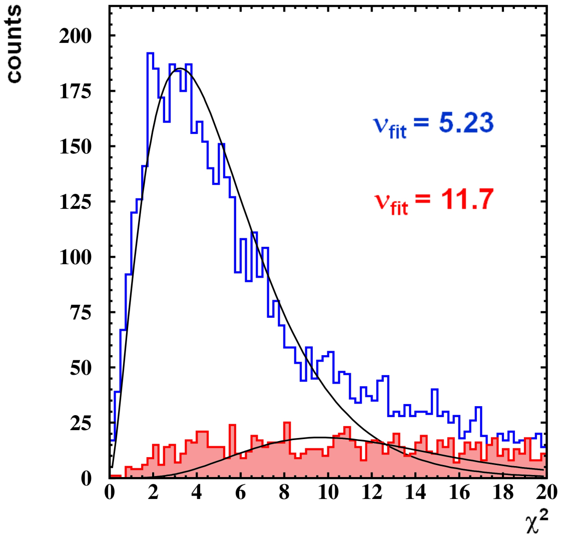

Figure 4.4: Preselection with kinematic refit for full scale $pK^+\Lambda$ simulations. The blue distribution corresponds to the fitted combinations of p and π^- with the smaller χ^2 value. The spectrum of the larger χ^2 values is shown in red. The black lines represent the fitted χ^2 curves to the spectra, yielding the ndf values in the upper right corner. The true ndf of the refit is equal to 5, due to the number of constraint equations.

The pre-selection procedure is tested with full-scale simulations of reaction R.6 (see section 4.2.1). Figure 4.4 shows the χ^2 distributions for all accepted (blue) and rejected (red) proton pion combinations. The distribution for the accepted combinations has the characteristic shape and corresponds to a fitted ndf value of 5.23. The true ndf of the fit is 5, since one invariant mass and four energy and momentum conservation constraint equations are applied. In contrast, the red spectrum, corresponding to the wrong combinations, is broadly distributed and hardly agrees with the theoretical shape of the χ^2 curve. The respective fitted ndf value is 11.7, reflecting the background character of this distribution.
Figure 4.4 clearly demonstrates, that an accurate distinction between the right and the wrong combination of p and π^- is achieved by the pre-selection procedure.

4.2 Application of the kinematic refit to full scale simulations

Before the kinematic refit is applied to the experimental data, it is tested with full scale simulations. First, the particles are created with an event generator (e.g. PLUTO or UrQMD) as straight lines, satisfying energy and momentum conservation. Subsequently, the generated particle tracks are further propagated through simulated detector material under consideration of the deflection in a magnetic field [F$^+$10; UrQ]. This is done with the software GEANT, which additionally simulates the energy loss of the particles in the detectors. The detector response to the simulated hit points is modeled with digitizers, which take into account realistic uncertainties and electronic

Particle	$\sigma(1/p)$	$\sigma(\theta)$	$\sigma(\varphi)$	$\sigma(x)$	$\sigma(y)$	$\sigma(z)$
CDC						
p	3.80 %	0.52°	0.40°	0.60 cm	0.60 cm	1.3 cm
K^+	3.40 %	0.57°	1.7°	0.40 cm	0.40 cm	1.2 cm
π^-	5.80 %	0.80°	0.92°	0.60 cm	0.60 cm	1.4 cm
HELITRON						
p	17.0 %	0.49°	0.57°	0.010 cm	0.010 cm	0.20 cm
π^-	13.4 %	2.6°	3.6°	0.20 cm	0.20 cm	1.0 cm

Table 4.1: Errors for the kinematic refit applied to full scale simulations. The values are extracted from pull distributions, where the kinematic refit with energy and momentum conservation constraint is applied to simulations of the reaction $pp \to pK^+\Lambda$.

noise [GEA; Sie10]. The signals, that are produced with this method, are treated in the same way as the real experimental signals, passing the whole analysis including particle identification. In the following analysis, all possible combinations of trigger settings are accepted (see section 2.6).

In contrast to the application of the kinematic refit to manually smeared tracks (see section 3.3), the covariance matrix $\mathbf{V}_{\vec{\alpha}_0}$ is not exactly known in advance in case of full-scale simulations. Therefore, the errors, which are listed in table 4.1, are extracted from the adjustment of pull distributions[3]. Nevertheless, the errors have always certain correlations, especially according to equation 2.9. Hence, it is impossible to adjust the uncertainties such, that all pull distributions have a variance of $\sigma = 1$. In fact, the errors are tuned in order to generate pull distributions with variances as close as possible to $\sigma = 1$ in average.

It is peculiar, that the spatial errors for HELITRON tracks are noticeably smaller than for CDC tracks. This results from HELITRON tracks that have a hit point in the SiΛVio detector, which has well determined spatial components.

Particle	$\langle\sigma(1/p)\rangle$	$\sigma(\theta)$	$\sigma(\varphi)$
CDC			
p	3.66 %	0.091°	0.83°
K^+	4.27 %	0.23°	0.26°
π^-	8.34 %	1.0°	2.0°
HELITRON			
p	15.3 %	0.24°	0.25°
π^-	14.3 %	1.3°	1.0°

Table 4.2: Errors of the momentum parameters extracted from simulations of the reaction $pp \to pK^+\Lambda$.

---

[3] In the following analysis, the non-diagonal elements of the covariance matrix are neglected.

The errors extracted from the pull distributions can be compared to the uncertainties that occur in the simulations and that can directly be estimated. The corresponding values for the momentum parameters are listed in table 4.2. The uncertainty in $1/p$ is calculated as the average of the errors $\sigma(1/p)$ for different momentum bins, weighted with the respective fitting errors. The angular errors are defined as the width of the differences between measured and simulated angles. Typically, the corresponding distributions should be Gaussian distributed around zero, however, the obtained spectra for the θ angles show deviations from normal distributions and systematic shifts. This is a clear indication for systematic errors in the θ parameters, which also propagate to the momentum parameters. Due to these effects, the errors extracted from the pull distributions (table 4.1) and directly from the simulations (table 4.2) slightly differ. Nevertheless, the uncertainties have the same order of magnitude.
Since the tests in the previous chapter showed, that the improvement of the mass, angular and momentum resolutions, achieved by applying the vertex constraints, is negligible, they are not included in the further analysis.

4.2.1 Simulation of the channel $pp \to pK^+\varLambda$

Analog to the tests in the previous chapter, the following reaction is simulated with the Monte Carlo based PLUTO event generator ($4 \cdot 10^5$ events) with a beam energy of 3.1 GeV [F+10].

$$\begin{array}{l} p + p \longrightarrow \varLambda + p_1 + K^+ \\ \qquad\qquad\quad \hookrightarrow p_2 + \pi^- \end{array} \tag{R.6}$$

Invariant mass constraint

The invariant mass constraint is important for the pre-selection, described in the previous section, since it is sensitive to the correct combination of proton and pion that stem from the decay of the intermediate $\varLambda$. Moreover, it can be used in the final step of the ppK^- analysis, where the invariant mass (p_1, $\varLambda$) and the missing mass of the K^+ is investigated. Setting the invariant mass (p_2, π^-) equal to the $\varLambda$ mass $M_\varLambda$ should improve the invariant mass, and in case of simultaneous application of energy and momentum conservation also the missing mass resolution, provided that the ppK^- is observed.
Figure 4.5a shows the invariant mass (p_2, π^-) for raw (red) and refitted (blue) events. Analog to picture 3.6a, the spectrum shows a tail on the right side of the $\varLambda$ mass peak. The corresponding events result in a peak at low p-values, which is shown in figure 4.6b. The origin of these events can be either the existence of local minima of the constraint equation or misidentified $p\ \pi^-$ combinations. A significance of $\alpha = 0.05$ (gray area beneath the p-value spectrum), defines a cut on low p-values, which nearly completely removes the tail in the invariant mass (p_2, π^-) spectrum (Figure 4.5b). The estimation of this value is described in section 4.2.2. At the same time, the constrained $\varLambda$ mass peak is not noticeably shrinked. This shows, that the p-value cut

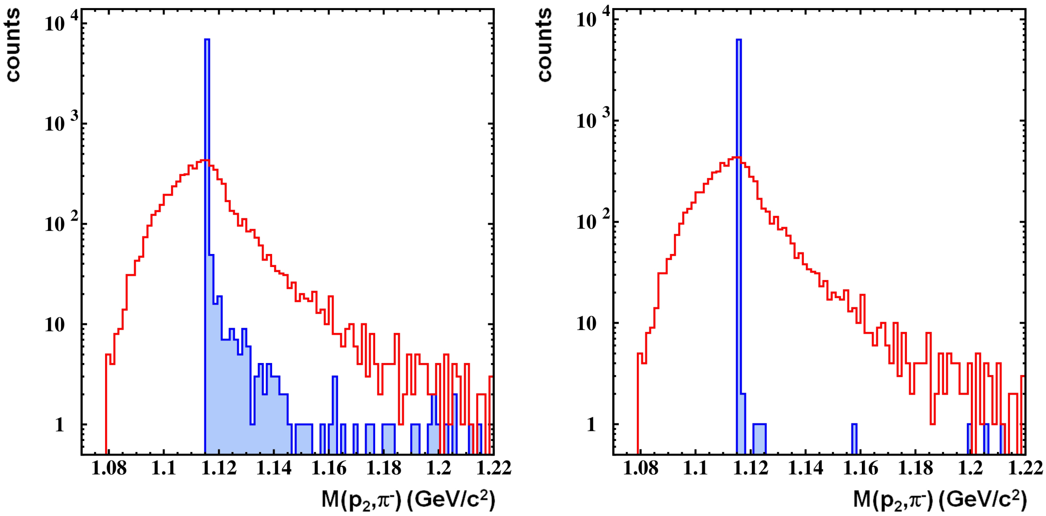

(a) (b)

Figure 4.5: Invariant mass of p_2 and π^- before (red) and after (blue) the kinematic refit with invariant mass constraint applied to $pK^+\Lambda$ simulations. Picture (b) shows the refitted spectrum (blue) after a cut on the p-value ($\alpha = 0.05$) is applied. The tail on the right side of the Λ peak is nearly completely removed, while the peak does not shrink noticeably.

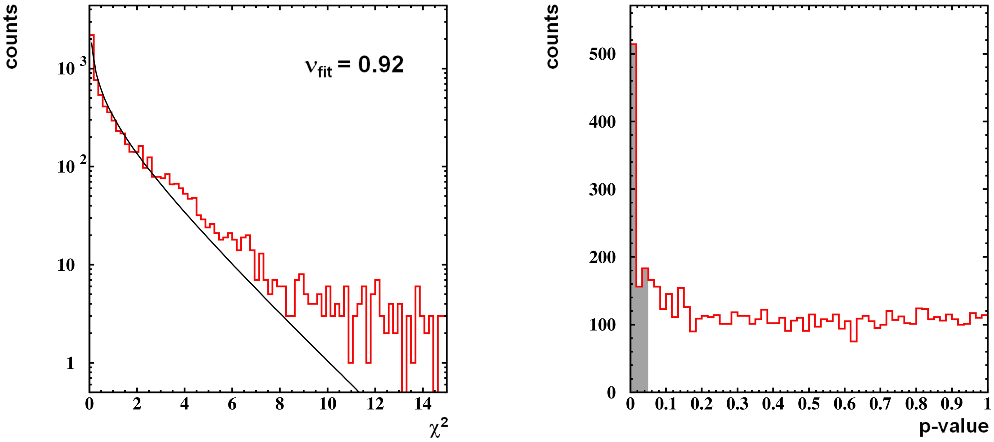

(a) (b)

Figure 4.6: Kinematic refit with invariant mass constraint applied to $pK^+\Lambda$ simulations. (a): χ^2 distribution with $ndf = 1$. The black curve represents the fit to the spectrum. (b): p-value distribution. The gray area indicates the significance of $\alpha = 0.05$, which is used as a cut on low p-values.

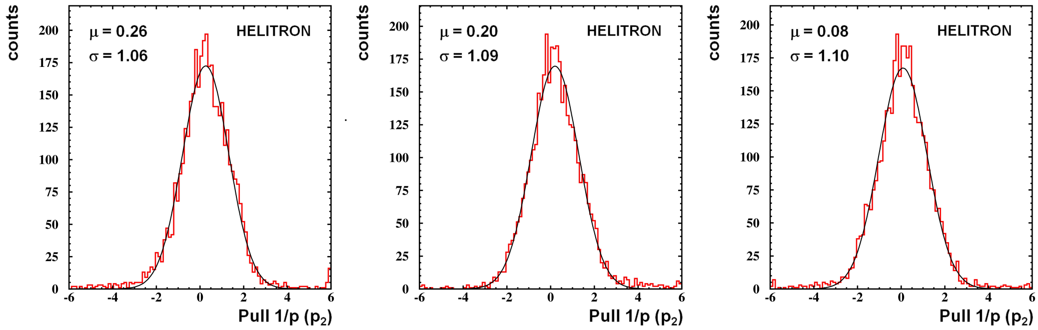

Figure 4.7: Kinematic refit with invariant mass constraint applied to $pK^+\Lambda$ simulations. Shown are the pull distributions for the three momentum parameters of the particle p_2 in the HELITRON. The black curves represent the fitted Gauss functions.

effectively removes background events, which do not fulfill the constraints after the refit. The χ^2 distribution is shown in figure 4.6a, yielding a fitted ndf value of 0.92. The pull distributions (Figure 4.7) have a Gaussian shape and correct variances. However, the pull spectra of the $1/p$ and θ parameters for HELITRON tracks and of the θ parameters for the CDC show a slight shift along the x-axis. This indicates the presence of systematic errors in θ, which can propagate to the momentum parameters (equation 2.9). These errors are observed for both, CDC and HELITRON tracks.

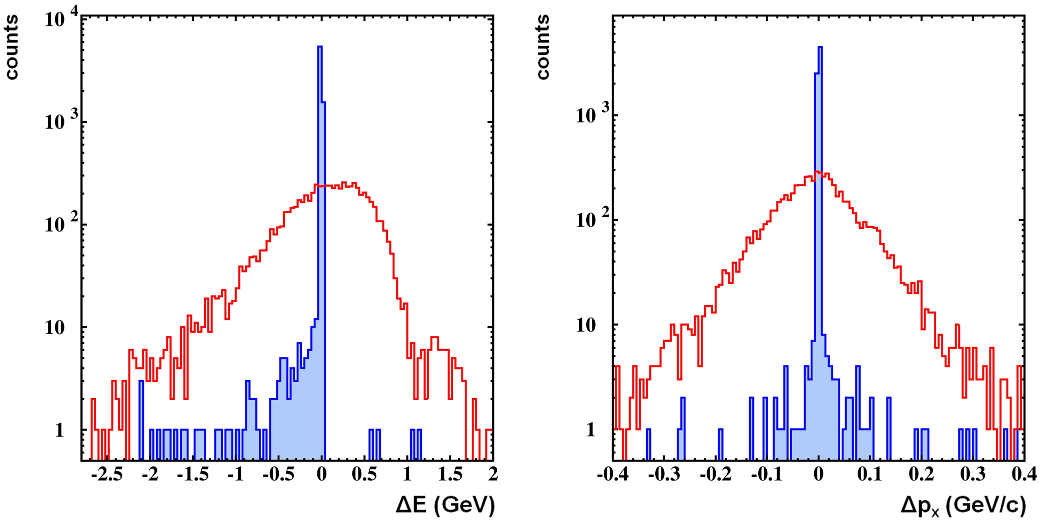

(a) (b)

Figure 4.8: Kinematic refit with energy and momentum conservation constraint applied to $pK^+\Lambda$ simulations. (a): The difference of initial and final energy is illustrated for raw (red) and refitted (blue) events. (b): The plot shows the difference of initial and final x component of the momentum for raw (red) and refitted (blue) particles.

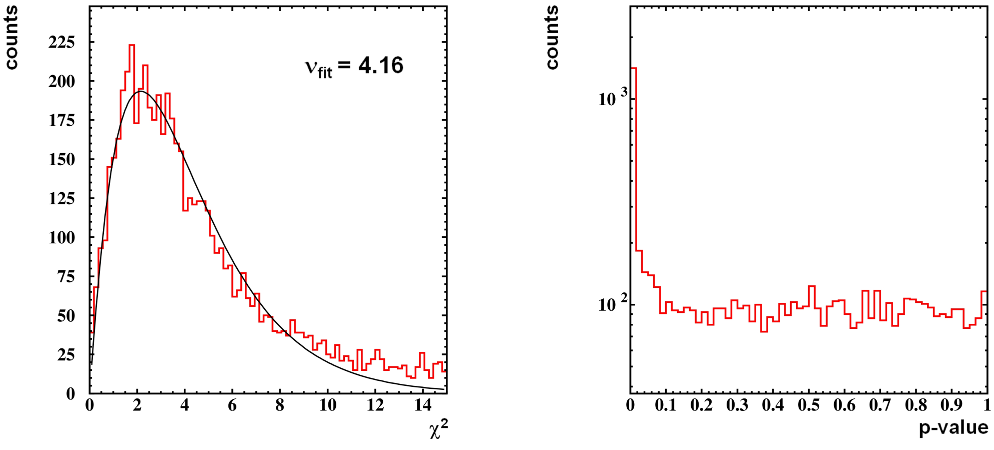

(a) (b)

Figure 4.9: Kinematic refit with energy and momentum conservation constraint applied to $pK^+\Lambda$ simulations. (a): χ^2 distribution with $ndf = 4$ (b): p-value distribution. The black curve indicates the fit to the red χ^2 spectrum.

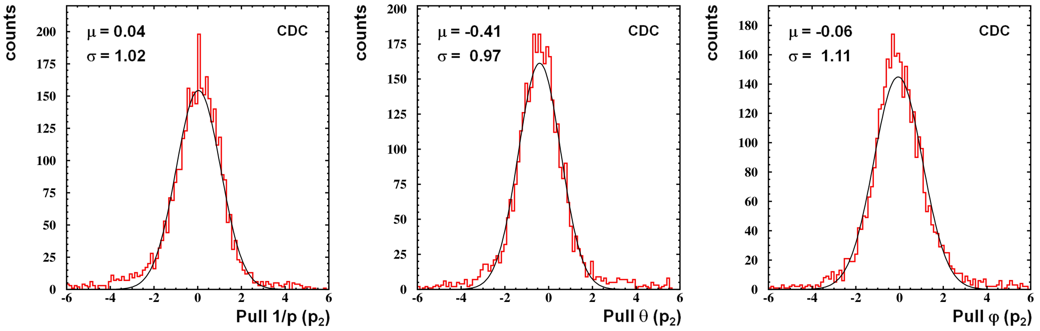

Figure 4.10: Kinematic refit with energy and momentum conservation constraint applied to $pK^+\Lambda$ simulations. Shown are the pull distributions for the three momentum parameters of the particle p_2 in the CDC. The black curves represent the fitted Gauss functions.

Energy and momentum conservation constraint

By far the most important and effective constraint condition of the kinematic refit is the energy and momentum conservation. It improves the parameters of all final state particles coincidently and exploits the most fundamental physical laws.

Figure 4.8 shows the missing energy (a) and the x-component of the missing momentum (b) for raw (red) and refitted (blue) events. Again, the spectra show small tails containing events, that do not exactly fulfill the constraints after the refit. In this case, these tails cannot be removed by cutting on low p-values, even though the corresponding spectrum (Figure 4.9b) has an excess at low values. The χ^2 distribution

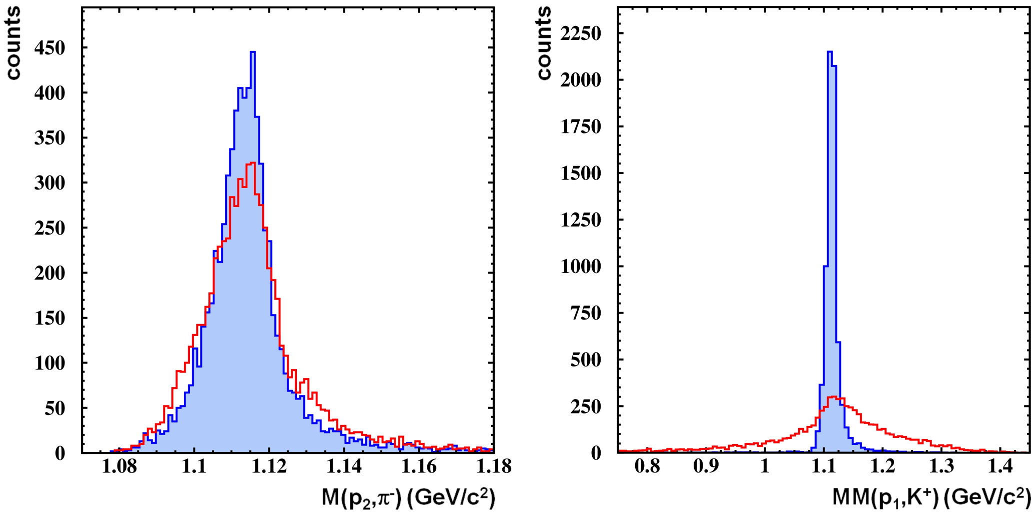

(a) (b)

Figure 4.11: Invariant mass of p_2 and π^- (a) and missing mass of p_1 and K^+ (b) before (red spectrum) and after (blue spectrum) the kinematic refit with energy and momentum conservation constraint applied to $pK^+\Lambda$ simulations.

of the refit with a fitted ndf value of 4.16 is illustrated in figure 4.9a. Obviously, background is not expected to appear by applying this constraint, since only one reaction (R.6) is contained in the simulations. In contrast to the invariant mass constraint, which requires the correct assignment of the proton originating from the Λ decay, the energy and momentum conservation constraint acts on all particles, independent of the particular proton ID. Therefore, the peak at low p-values only contains correct $pK^+\Lambda$ events and a cut has no further consequence on the other spectra besides the reduction of statistics. One fraction of this peak contains the previously discussed local minima, which are always present. The other fraction could emerge from the existence of systematic errors, which can be observed by looking at the pull distributions (Figure 4.10). Analog to the invariant mass constraint, the spectra show systematic shifts in the θ and $1/p$ parameters for HELITRON and in the θ parameters for CDC tracks. As explained in section 3.3.3, the Gauss-Markov theorem is no longer valid in the presence of systematic errors. Therefore, the kinematic refit does not inevitably deliver new parameters which are unbiased and have

Observable	σ_{raw}	σ_{refit}	$\Delta\sigma$
$M(p_2,\pi^-)$	9.3 MeV/c^2	7.3 MeV/c^2	22%
$MM(p_1,K^+)$	57 MeV/c^2	7.3 MeV/c^2	87%

Table 4.3: Resolutions of raw and refitted mass spectra for the kinematic refit with energy and momentum conservation constraint applied to $pK\Lambda$ simulations.

Nr.	Reaction $p + p \rightarrow$	σ (mb)	$B_{channel}/S$	Remaining after cut
Strangeness channels				
1	$p + K^+ + \Lambda$	$4.3 \cdot 10^{-2}$	1	63.3%
2	$p + K^+ + \Sigma^0(\rightarrow \Lambda + \gamma)$	$1.8 \cdot 10^{-2}$	$356 \cdot 10^{-3}$	16.9%
3	$n + K^+ + \Sigma^+$	$3.2 \cdot 10^{-2}$	$2.82 \cdot 10^{-3}$	0.00%
Non-strangeness channels				
4	$p + p$	9.7	$18.6 \cdot 10^{-3}$	0.00%
5	$p + n + \pi^+$	9.4	$16.9 \cdot 10^{-3}$	0.00%
6	$p + n + \pi^+ + \pi^0$	4.2	$15.8 \cdot 10^{-3}$	0.00%
7	$p + p + \pi^0$	3.8	$6.77 \cdot 10^{-3}$	0.00%
8	$p + p + \pi^+ + \pi^-$	2.7	$327 \cdot 10^{-3}$	0.34%
9	$p + n + \pi^+ + \pi^+ + \pi^-$	1.5	$12.4 \cdot 10^{-3}$	0.00%
10	$n + n + \pi^+ + \pi^+$	n.a.	$2.26 \cdot 10^{-3}$	0.00%

Table 4.4: Simulated pp reaction channels, which are identified as $pK^+\Lambda$ events (channel 1). The values for the cross sections are determined for a beam energy of 3 GeV. The value $B_{channel}/S$ is defined as the number of events belonging to the respective background channel after the event selection divided by the number of channel 1 events. The right column quotes the fractions of these single channels, which remain after the p-value cut with a significance of $\alpha = 0.05$. For the kinematic refit, the energy and momentum conservation constraint is used.

minimum variance. Moreover, the refit tries to compensate the systematic errors by a statistical procedure. In principle, the kinematic refit can be used to estimate these systematic errors by the systematic study of the effect of manually imposed errors on the pull distributions.

Nevertheless, the mass resolution of the Λ is still improved, which is demonstrated by figure 4.11. Panel (a) shows the invariant mass spectrum of p_2 and π^- for raw (red) and refitted (blue) events. The kinematic refit improves the invariant mass resolution by 22 % (see table 4.3). The raw missing mass (p_1, K^+) spectrum is broader than the invariant mass (p_2, π^-) distribution, since the different particles are measured by various detectors with different probabilities, according to the kinematics of the reaction. Therefore, the measurements of the different particles have varying uncertainties. After the refit, as a consequence of energy and momentum conservation, the missing and invariant mass spectra have equal shape and width. This leads to an improvement of the missing mass resolution of about 87 %.

4.2.2 Simulation of the pp reaction

In order to investigate the behavior of the kinematic refit when applied to background reactions, the pp reaction at 3.1 GeV is simulated with $9.5 \cdot 10^5$ events with the UrQMD (Ultrarelativistic Quantum Molecular Dynamics) transport model, which includes the most common reaction channels [UrQ]. The channels, which are present as background after the event selection due to misidentification, are listed in table 4.4

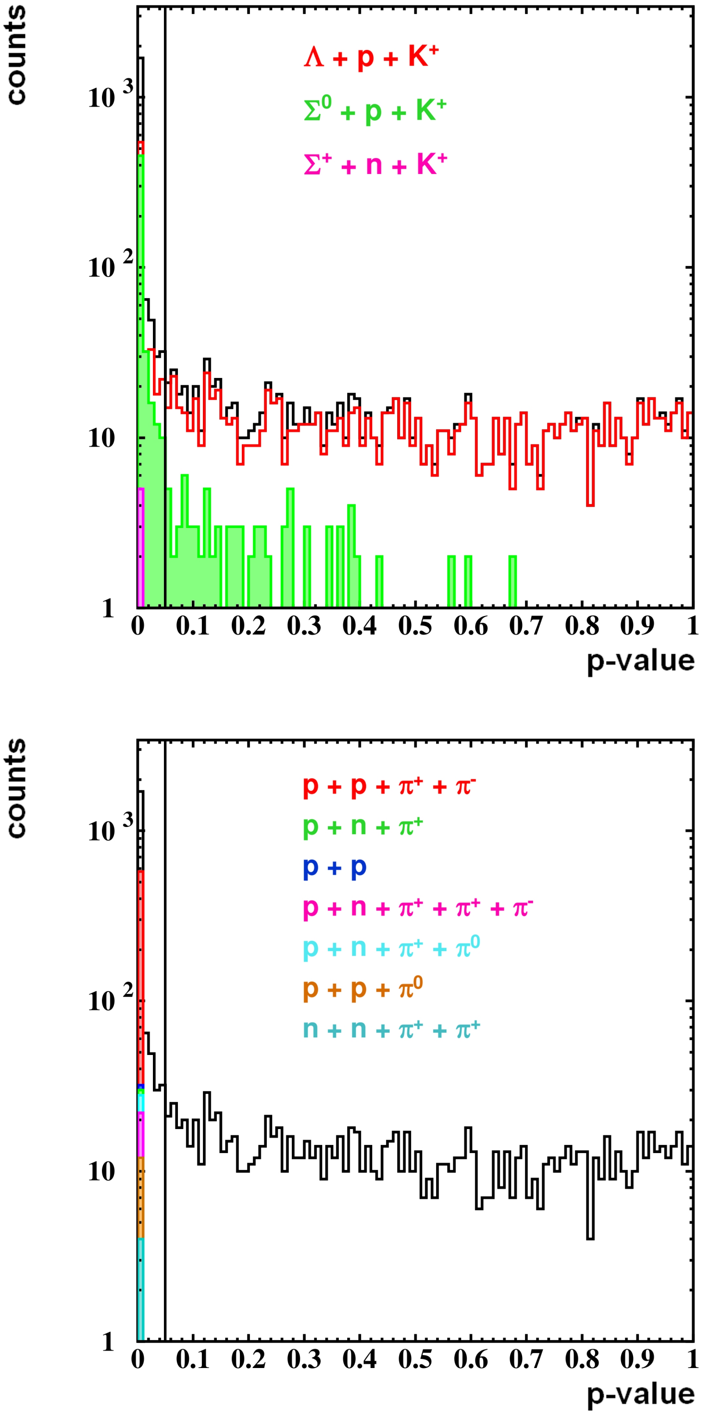

Figure 4.12: Kinematic refit with energy and momentum conservation constraint applied to pp simulations. The p-value distributions of the different strangeness (upper panel) and non-strangeness (lower panel) channels are shown as colored curves. The total p-value distribution is represented by the black curves. The black lines illustrate the position of the p-value cut, defined by the significance $\alpha = 0.05$, which is determined by maximizing $\pi \cdot \varepsilon$.

together with the respective cross sections. Since the two channels 1 and 2 only differ by the photon which is produced in the Σ^0 decay of the latter, they result in the same final state due to the incapability of the FOPI spectrometer of measuring γ's. Therefore, the misidentification of reaction 2 as channel 1 is expected to yield the biggest contribution to the background. Another strong contribution is associated with channel 8, where the π^+ can be misidentified as a K^+, since the corresponding p/q vs. v curves in figure 4.2b partially overlap. The other reactions can be mistaked for $pK^+\Lambda$ events in combination with fake-tracks, which do not correspond to any real process. Since the probability for these incidents is rather small, the corresponding channels have a minor contribution to the background compared to reactions 2 and 8. The S/B ratio, taking all background channels into account, is 1.319.

In order to study the behavior of background, which is subject to the kinematic fitting procedure, the refit with energy and momentum conservation constraint is applied to the simulated pp events. The upper panel of figure 4.12 shows the p-value distribution of the fit (black), where the single contributions of the three strangeness channels (reactions 1-3 in table 4.4) are indicated in different colors. As discussed in section 3.3.4, the kinematic refit has to shift tracks belonging to background events by a larger distance in order to fulfill the constraint, compared to true $pK^+\Lambda$ events. Hence, these background events result in low p-values. As expected, the biggest contribution to the background originates from channel 2 (green), which has the same final state as channel 1 (red). Since the violation of energy and momentum conservation is only caused by the photon, which is not detected, the deviation from the constraint is smaller than for other background channels, such as reaction 3 (violet). Therefore, even though the channel 2 events accumulate at low p-values, the distribution also reaches higher values. In contrast, channel 3 events, which inevitably contain at least one fake track (due to the undetected neutron), are located at the very left end of the p-value distribution. The different non-strangeness channels (reactions 4-10 in table 4.4) and their p-value distributions are shown in the lower panel of figure 4.12. Due to the respective event topologies, which substantially differ from reaction 1, the background events are located at p-values around zero.

By defining a significance α, a cut on low p-values rejecting events with $p-value < \alpha$ reduces the amount of background. In order to estimate the best value for α, the product of cut purity π and efficiency ε as a function of α is maximized. The two quantities are defined in the following way [Mün12].

$$\pi(\alpha) = \frac{B_{p-value \leq \alpha}}{B_{tot}} \qquad\qquad \varepsilon(\alpha) = \frac{S_{p-value > \alpha}}{S_{tot}} \tag{4.1}$$

S denotes the number of signal events belonging to channel 1 and B is the number of background events. For the maximization, only channel 2 is considered as background, since the other channels have p-values very close to zero. According to this procedure, the best value for the significance in case of using the energy and momentum conservation constraint is $\alpha = 0.05$. The position of the p-value cut is illustrated by the black lines in figure 4.12. According to this significance, the p-value cut removes nearly all non-strangeness channel events. Also a large fraction

	No non-vertex	Invariant mass	Conservation	All non-vertex
No vertex	-	0.40	0.05	0.03
Intersection p_2 & π^-	0.60	0.60	0.04	0.03
Secondary vertex	0.30	0.20	0.02	0.007

Table 4.5: Significances for the different constraint combinations, obtained by maximizing $\pi \cdot \varepsilon$ for pp simulations.

	No non-vertex	Invariant mass	Conservation	All non-vertex
No vertex	-	2.562	9.686	11.73
Intersection p_2 & π^-	1.166	2.721	12.28	14.67
Secondary vertex	1.864	3.092	10.83	10.91

Table 4.6: S/B ratios for the different constraint combinations, obtained by maximizing $\pi \cdot \varepsilon$ for pp simulations. The S/B ratio without p-value cut is 1.319.

of channel 2 is rejected, however, due to the broad distribution a certain amount of background still remains. The last column of table 4.4 contains the fractions of events for each single channel, which remain after applying the p-value cut. Only the background channels 2 (16.9%) and 8 (0.34%) partially remain after the cut. Since the number of events belonging to reaction 1 is only reduced by 36.7%, the signal to background ratio, which calculates to $S/B_{cut} = 9.686$, is improved by a factor of 7. This procedure is repeated for all possible combinations of constraint conditions, which are available for the kinematic refit. The respective quantities $\pi \cdot \varepsilon$ are maximized, yielding the corresponding values for the best significance α and the new signal to background ratios. The values for the different constraint combinations are listed in tables 4.5 and 4.6. The corresponding p-value distributions for the different background channels are shown in appendix C.

The values listed in the table 4.5 reveal the trend of a decreasing significance for an increasing number of constraint conditions applied to the simulations. This implies, that the accumulation of background events at low p-values is stronger for a higher number of constraints. The reason for this tendency is, that the differences between true and misidentified $pK^+\Lambda$ events, when modified by the kinematic refit, increase, if the tracks have to fulfill a larger number of constraint conditions. Moreover, the distributions shown in appendix C clearly indicate, that the constraints involving only two particle tracks (invariant mass (p_2,π^-) and intersection (p_2,π^-)) are not able to properly distinct between signal and background events, especially concerning channel 2. This behavior is expected, since the additional photon, produced in channel 2, does not affect the invariant mass or the vertex of the p_2 and π^- tracks. The best separation between signal and background events in terms of the p-values is achieved by application of all non-vertex constraints together with the secondary vertex constraint. The corresponding significance is $\alpha = 0.007$. However, since the large number of constraint conditions causes the fit distributions to slightly deviate from the expected behavior (see section 3.3.2), the p-value and pull distributions are

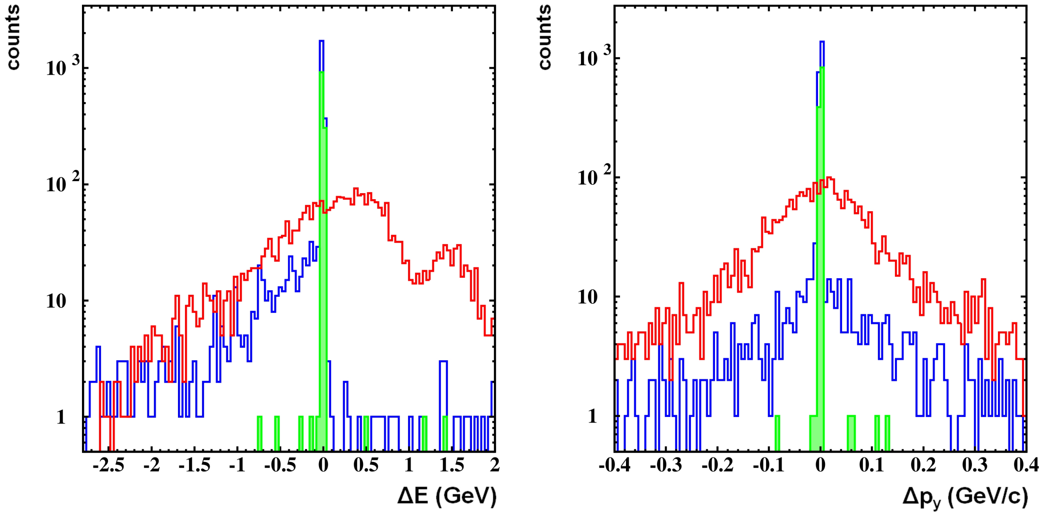

(a) (b)

Figure 4.13: Kinematic refit with energy and momentum conservation constraint applied to pp simulations. (a): The difference of initial and final energy is illustrated for raw (red) and refitted (blue) events. (b): The plot shows the difference of initial and final y component of the momentum for raw (red) and refitted (blue) particles. The distributions after the p-value cut ($\alpha = 0.05$) are shown in green.

less meaningful with respect to the correct error input and the presence of systematic errors. Therefore, this constraint combination is not used in the further analysis.
The discussed trend of the significances for different constraint combinations is not fully reflected by the corresponding S/B ratios (see table 4.6). This originates from the fact, that maximizing $\pi \cdot \varepsilon$ yields different results than maximizing the S/B or S^2/B ratios.
Returning to the discussion of the kinematic refit with energy and momentum conservation constraint applied to pp simulations, the distributions for the missing energy and the y component of the missing momentum are illustrated by figure 4.13. The raw spectra are shown in red, the refitted distributions without and with p-value cut are represented by the blue and green curves, respectively. The refitted spectra without p-value cut show clear constraint peaks at zero, however, broad tails are observed

Observable	σ_{raw}	σ_{refit}	$\sigma_{refit,cut}$	$\Delta\sigma$	$\Delta\sigma_{refit}$
$M(p_2,\pi^-)$	9.85 MeV/c^2	8.64 MeV/c^2	8.47 MeV/c^2	12.3%	1.97%
$MM(p_1,K^+)$	83.9 MeV/c^2	8.64 MeV/c^2	8.47 MeV/c^2	83.9%	1.97%

Table 4.7: Resolutions of raw and refitted mass spectra, with and without p-value cut for the kinematic refit with energy and momentum conservation constraint applied to pp simulations. $\Delta\sigma$ is the difference of raw and refitted mass resolutions. $\Delta\sigma_{refit}$ denotes the difference of the refitted mass resolutions with and without p-value cut.

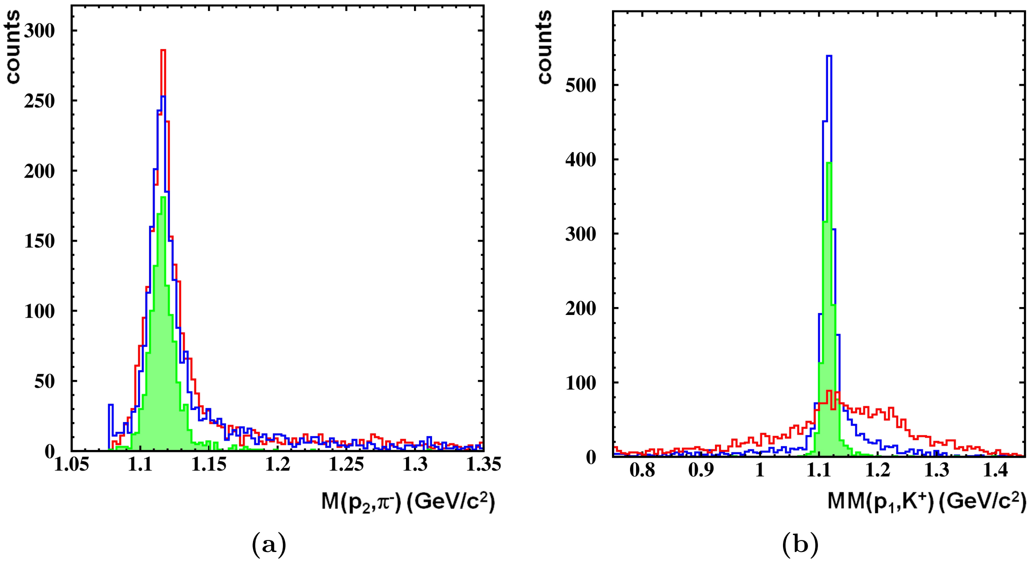

(a) (b)

Figure 4.14: Invariant mass of p_2 and π^- (a) and missing mass of p_1 and K^+ (b) before (red) and after (blue) the kinematic refit with energy and momentum conservation constraint, applied to pp simulations. The distributions after the p-value cut ($\alpha = 0.05$) are shown in green.

even for the refitted events. These tails originate from refitted background events, which is demonstrated by the green curves, showing the corresponding spectra after applying the p-value cut, where the tails are suppressed. The rejection of background events due to the cut almost completely removes the tails. However, since the cut also reduces the signal events, the constraint peaks slightly shrink in their magnitude. Figure 4.14 shows the the invariant mass (p_2,π^-) and missing mass (p_1,K^+) distributions for the fit. The values for the respective resolutions are listed in table 4.7. Again, the unconstrained spectra are shown in red, the refitted distributions without and with p-value cut are illustrated by the blue and green curves, respectively. Clearly, the p-value cut removes the broad tails of the refitted mass distributions. This leads, besides the enhancement caused by the kinematic refit itself, to a further improvement of the mass resolutions.

4.3 Application of the kinematic refit to experimental data

The following section describes the application of the kinematic refit with energy and momentum conservation constraint to the experimental data. Altogether $72 \cdot 10^6$ events are analyzed, accepting all possible trigger combinations.

Analog to the previous section, the errors for the refit are estimated via the pull distributions of the fit. The values are listed in table 4.8. In case of analyzed data, a large amount of background is present. In order to reduce the number of refitted background events, a cut on the invariant mass (p_2,π^-) around the nominal Λ mass

Particle	$\sigma(1/p)$	$\sigma(\theta)$	$\sigma(\varphi)$	$\sigma(x)$	$\sigma(y)$	$\sigma(z)$
CDC						
p	31 %	4.01°	29.8°	0.60 cm	0.60 cm	1.6 cm
K^+	40 %	18.3°	5.16°	0.52 cm	0.52 cm	1.8 cm
π^-	52 %	13.8°	29.2°	0.50 cm	0.50 cm	1.6 cm
HELITRON						
p	29 %	1.78°	0.0688°	0.30 cm	0.30 cm	0.20 cm
π^-	56 %	5.10°	0.0745°	0.30 cm	0.30 cm	0.20 cm

Table 4.8: Errors for the kinematic refit applied to experimental data extracted from pull distributions. A possible explanation for the large uncertainties of the $1/p$ parameters are systematic errors, which can be observed in the pull distributions (Figure 4.15)

is performed. The kinematic refit is applied to events, where the invariant mass (p_2,π^-) is smaller than 1.146 GeV/c^2 for CDC and smaller than 1.185 GeV/c^2 for HELITRON tracks. The lower cut boundary is defined by the $p\pi^-$ threshold of 1.078 GeV/c^2. Due to the different resolutions, the cut is performed for the two detectors separately.

Figure 4.15 shows the pull distributions for the momentum parameters of p_1 in the CDC (upper row) and of π^- in the HELITRON (lower row). The non-Gaussian shapes and distinct peaks are a consequence of the refitted background. Besides their peculiar shapes, the spectra show clear indications for the presence of systematic errors in θ and $1/p$, which manifest themselves in shifts of the distributions along the x-axis. These shifts are stronger for the CDC tracks, nevertheless also the HELITRON distributions show systematic errors.

The implications of these systematic errors can be observed in the refitted mass distributions. Figure 4.16a shows the invariant mass (p_2,π^-) distribution for raw (red) and refitted (blue) events. Additionally, the green spectrum illustrates the refitted events after a p-value cut corresponding to a significance of $\alpha = 0.84$ is applied. The estimation of α is discussed at the end of this section. The raw spectrum shows a clear Λ peak on top of a broad background distribution. After the kinematic refit, the blue spectrum is obtained, where the structure of the Λ peak emerges more clearly from the background. The two edges on the right side of the peak originate from the invariant mass cut for the refit around the Λ mass. However, the refitted Λ peak has

Observable	σ_{raw}	σ_{refit}	$\sigma_{refit,cut}$	$\Delta\sigma$	$\Delta\sigma_{refit}$
$M(p_2,\pi^-)$	10.0 MeV/c^2	12.7 MeV/c^2	10.3 MeV/c^2	-21.3%	18.9%
$MM(p_1,K^+)$	n.a.	18.2 MeV/c^2	8.78 MeV/c^2	n.a.	51.8%

Table 4.9: Resolutions of raw and refitted mass spectra, with and without p-value cut for the kinematic refit with energy and momentum conservation constraint applied to experimental data. $\Delta\sigma$ is the difference of raw and refitted mass resolutions. $\Delta\sigma_{refit}$ denotes the difference of the refitted mass resolutions with and without p-value cut.

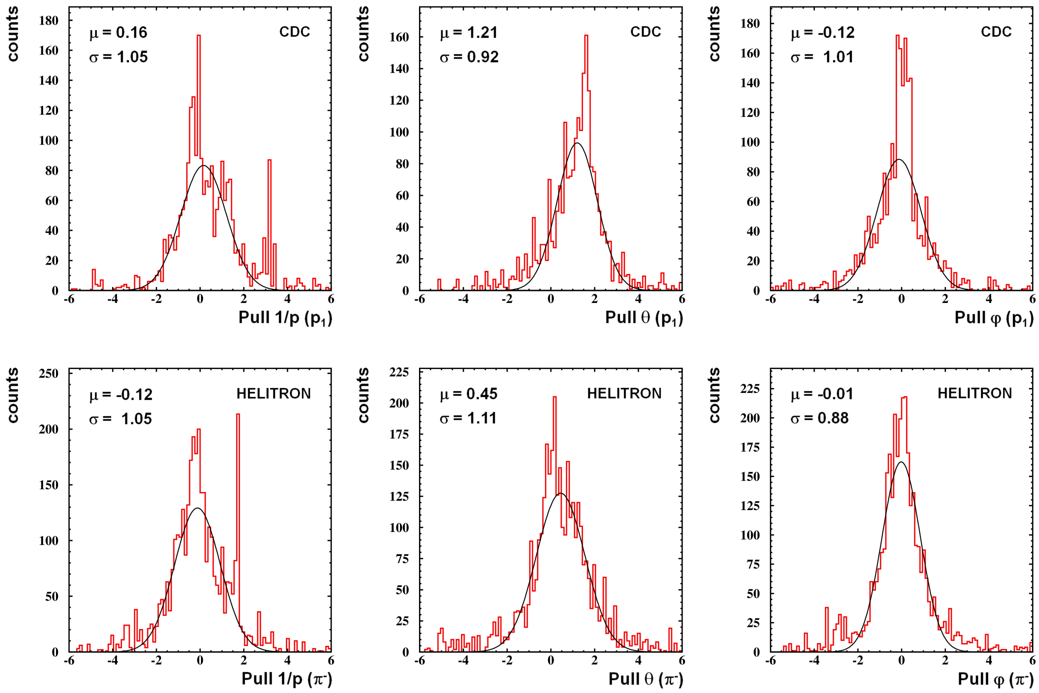

Figure 4.15: Kinematic refit with energy and momentum conservation constraint applied to experimental data. The upper row shows the pull distributions for the momentum parameters of p_1 in the CDC. The lower row shows the pull distributions for the momentum parameters of pions in the HELITRON. The black curves indicate the fitted Gauss functions.

a larger width than the unrefitted peak (see table 4.9), which might be caused by the systematic errors. As discussed in section 4.2.1, the Gauss-Markov theorem is not valid in the presence of systematic errors. Therefore, the kinematic refit does not necessarily calculate the best set of parameters, which could cause the decreasing of the mass resolution. Finally, the green spectrum is obtained by applying a cut on low p-values with a significance of $\alpha = 0.84$ to the refitted events. The p-value cut improves the mass resolution of the refitted spectrum, yielding the original value of the unrefitted Λ peak. Hence, altogether the invariant mass resolution is not improved by the kinematic refit. However, the green distribution shows only a very small fraction of background beneath the Λ peak. Obviously, the p-value cut enables an effective reduction of background events.

The same effect is observed in the missing mass (p_1,K^+) spectrum (Figure 4.16b). The raw spectrum (red) does not show any clear peak signature of the Λ, due to the reduced resolution in the measurement of the involved particles. After applying the kinematic refit, the blue curve is obtained, which shows a clear Λ peak on top of a broad background distribution. Performing a cut on low p-values results in the green spectrum, which is almost background free and has an improved mass resolution by 51.8%.

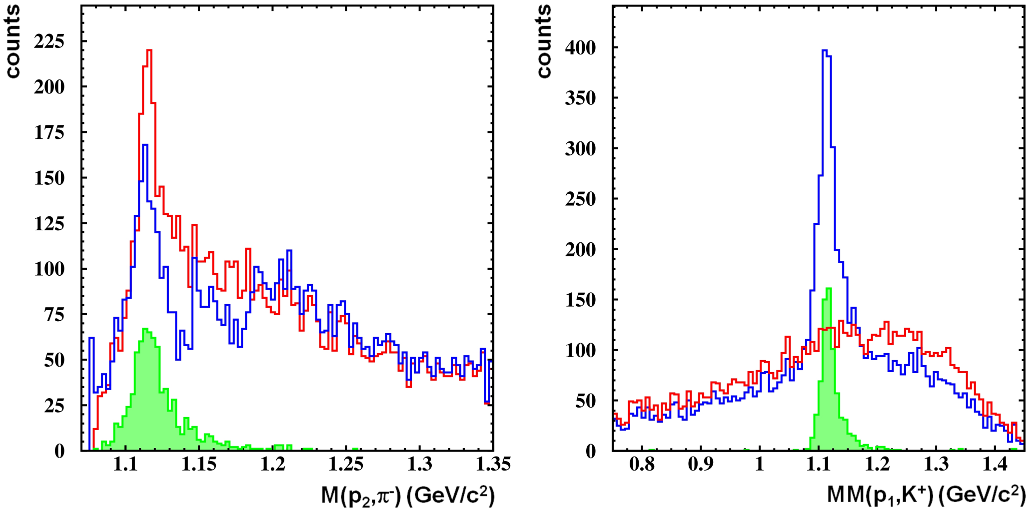

(a) (b)

Figure 4.16: Kinematic refit with energy and momentum conservation constraint applied to experimental data. Invariant mass (p_2,π^-) (a) and missing mass (p_1,K^+) (b) distribution for raw (red) and refitted (blue) events. The green spectrum shows the refitted distribution after the application of the p-value cut ($\alpha = 0.84$).

These spectra show, that the kinematic refit with energy and momentum conservation constraint does not lead to an improvement of the mass resolutions, which is probably caused by the systematic errors. Nevertheless, an effective background reduction is achieved by applying a p-value cut on the refitted events. Therefore, the kinematic refit can be used as a cut procedure for background reduction, where the unconstrained track parameters are used for the further analysis instead of the refitted parameters. In order to systematically study the background reduction for different values of the significance α, the kinematic refit with energy and momentum conservation constraint is applied to all events. For different values of α, the signal times signal to background ratio is calculated, since this quantity is, additionally to the signal to background ratio, sensitive to the number of signal events. For the calculation of the S^2/B, which is defined within 3σ around the maximum of the Λ peak, a polynomial function is fitted to the background distribution, together with a Gauss function fit to the signal. Figure 4.17a illustrates the S^2/B as a function of α. The S^2/B increases with increasing significance and shows a maximum at $\alpha = 0.84$. For larger α, the S^2/B decreases, since in this region, the cut starts to reduce a large amount of signal.

The corresponding p-value distribution is shown in figure 4.17b, where the gray area denotes the events, which are rejected due to the p-value cut with $\alpha = 0.84$. The spectrum shows a large peak at zero, originating from the background events. Additionally, a peak at large p-values is observed. The rather large value for the optimized significance of $\alpha = 0.84$ indicates, that the true $pK^+\Lambda$ events are located at large p-values and can be associated with the peak at the right end of the spectrum.

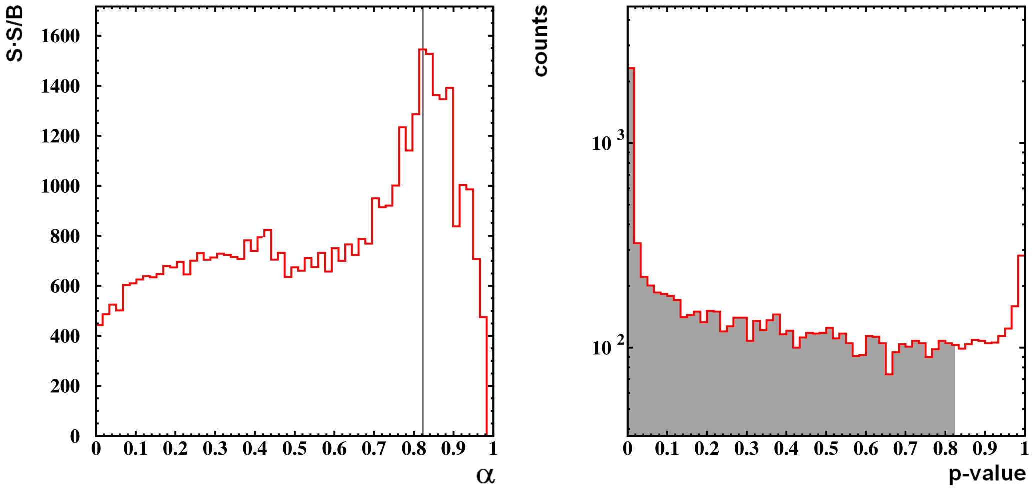

(a) (b)

Figure 4.17: Kinematic refit with energy and momentum conservation constraint applied to experimental data. (a): S^2/B as a function of the significance α. The gray line indicates the maximum value of $\alpha = 0.84$. (b): P-value distribution of the fit. The gray area denotes the events, which are rejected by the p-value cut with a corresponding significance of $\alpha = 0.84$.

An explanation for this effect could again be the systematic errors, which are certainly present in the analysis.
The upper panel of figure 4.18a shows the invariant mass (p_2,π^-) spectrum for unrefitted tracks. The polynomial function, which is fitted to the background, is indicated by the red curve. The lower panel illustrates the background subtracted invariant mass distribution, showing a Gaussian shaped Λ signal. Figure 4.18b shows the same distributions after a p-value cut with $\alpha = 0.84$ is performed, after the kinematic refit with energy and momentum conservation constraint is applied to all events. Table 4.10 collects the corresponding values. The refit is exclusively used to calculate a p-value for each event, which is compared to α. The new parameters $\vec{\alpha}$ are reseted to the unconstrained values after the fit. Clearly, the p-value cut effectively reduces a large amount of background, whereas the resolution of the signal remains unchanged (see table 4.10). As a result of the p-value cut, the S/B is improved by

Cut on α	*Mass*	σ	*Nr. of signal events*	S/B	S^2/B
no	$1.115\,\mathrm{GeV/c^2}$	$7.2\,\mathrm{MeV/c^2}$	854	0.445	380.1
yes	$1.115\,\mathrm{GeV/c^2}$	$7.2\,\mathrm{MeV/c^2}$	507	2.57	1305

Table 4.10: Properties of the unrefitted invariant mass (p_2,π^-) spectra with and without p-value cut ($\alpha = 0.84$).

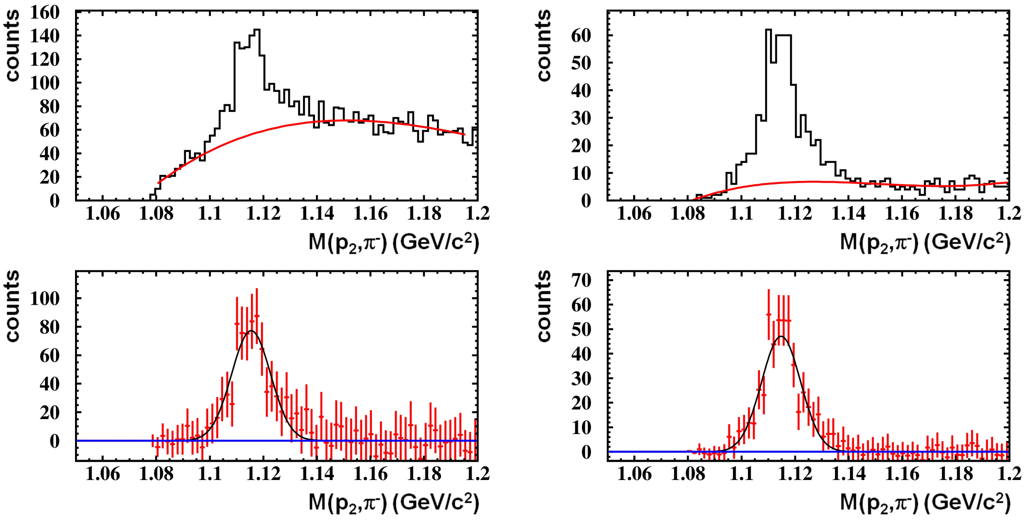

(a) (b)

Figure 4.18: Kinematic refit with energy and momentum conservation constraint applied to experimental data. The upper panels show the unrefitted invariant mass (p_2,π^-) distributions without (a) and with (b) p-value cut corresponding to a significance of $\alpha = 0.84$. The red curves indicate the polynomial fits to the background. The lower panels show the respective background subtracted distributions. The Gauss fits to the signals are denoted by the black curves.

a factor of 5.8 and an enhancement factor of 3.4 is achieved for the S^2/B. This illustrates that even in the presence of systematic errors, the kinematic refit is an important tool for the exclusive analysis of the experimental data, as it allows for an effective reduction of background.

5 Analysis of the elastic pp channel

This chapter describes the analysis of the elastic reaction $pp \rightarrow pp$ at a beam energy of 3.1 GeV, which is performed in parallel to the exclusive analysis of the reaction $pp \rightarrow pK^+\Lambda$. The goal of this analysis is the quantification of the CDC-RPC matching efficiency and the relative HELITRON efficiency. Besides the characterization of these detector properties, the elastics channel is used to investigate the characteristics of the kinematic refit and to test the correct alignment of the beam.

5.1 Motivation

The pp elastics channel is a frequently used tool to study various detector properties, such as the alignment, tracking capability and matching efficiency between different sub-detectors [Sch08; Spa05]. These characteristics can only be studied, if the event topology and kinematics is well-understood. Especially for the investigation of the detector efficiencies, it is essential to reduce the number of fake-tracks to a minimum. These tracks can appear, if e.g. hitpoints from different reactions are combined into one track, which obviously does not correspond to any real process. It is evident, that the fake-tracks are confined to the single sub-detectors. Consequently, in most of the cases, they cannot be matched with other detectors, reducing the relative number of matched tracks and hence diminishing the matching efficiency. Of course, if the kinematics of the processes is known, the fake-tracks can be rejected by the application of cuts on different kinematics properties. Since the elastic reaction has the most fundamental kinematics, it is perfectly suited for this characterization.

5.2 Kinematics of elastic reactions

The kinematics of two-body collisions, like the pp elastic reaction, is fixed. Figure 5.1a shows the elastic scattering process of a beam and a target proton with momenta $\vec{p}_b$ and $\vec{p}_t$ in the center of mass (CMS) reference frame. Due to momentum conservation, the outgoing protons are emitted back-to-back, with momenta $\vec{p}_1$ and $\vec{p}_2$. This defines the following relation for the azimuthal angles.

$$\Delta\varphi = |\varphi_1 - \varphi_2| = 180^\circ \tag{5.1}$$

Since the two protons are indistinguishable after the reaction, they cannot be uniquely associated to the beam or target particle, respectively.
Figure 5.1b illustrates the same scattering process in the laboratory (LAB) reference frame. Via a Lorentz transformation, the momenta of the protons are boosted in forward direction, obtaining an opening angle $\theta_{op} = \theta_1 + \theta_2$, where θ_1 and θ_2 are the

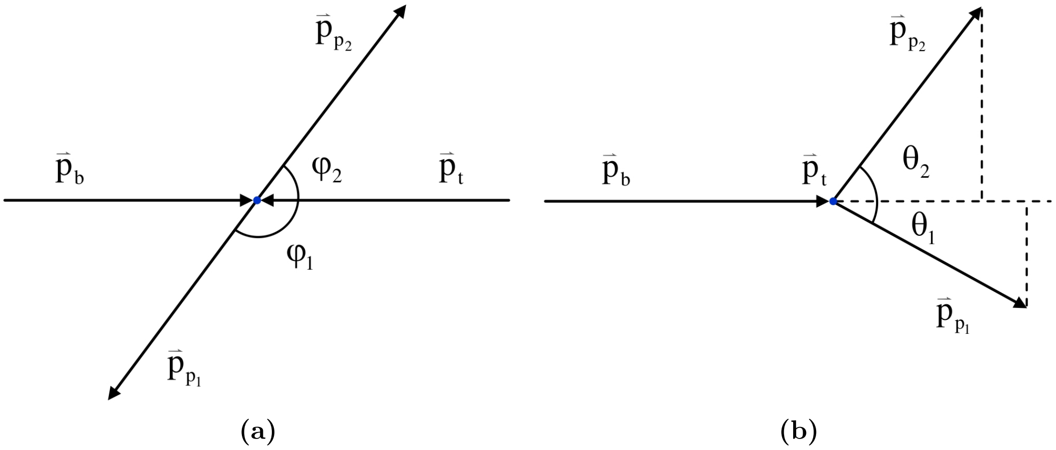

Figure 5.1: (a) Kinematics of elastic scattering processes in the CMS frame (b) and in the LAB frame.

polar angles of the protons. Also in the LAB system, the two outgoing protons lay on the same reaction plane (equation 5.1).

After the Lorentz transformation, the total energy and momentum still have to be conserved, yielding the following relation between the two polar angles[1].

$$tan\theta_1 \cdot tan\theta_2 = \frac{1}{\gamma_{CMS}^2} \tag{5.2}$$

where $\gamma_{CMS} = \frac{1}{\sqrt{1-\beta_{CMS}^2}}$ is the Lorentz factor of the CMS frame with a corresponding velocity of β_{CMS}. Given the kinetic beam energy E_{kin} and the rest mass of the protons $m_p = 938.27\,\mathrm{GeV/c^2}$, the velocity of the CMS system can be calculated with the following formula.

$$\beta_{CMS} = \frac{\sqrt{E_{kin} + 2E_{kin}m_p}}{E_{kin} + 2m_p} \tag{5.3}$$

The kinematical values for the underlying pp experiment are collected in table 5.1. Equation 5.2 implies, that the broadening of the opening angle between the two protons depends on the one hand on the kinetic energy of the beam projectile. On the other hand, it depends on the values of the single polar angles. The minimum value $\theta_{op,min} = 63°$ is obtained when the two protons have the same polar angle $\theta_1 = \theta_2 = 31.5°$[2]. In the limit of $\theta_i = 0°$, the maximum opening angle $\theta_{op,max} = 90°$ is achieved. However, since the HELITRON is not capable of detecting particles with

---

[1] In the non-relativistic limit $\gamma_{CMS} \to 1$, equation 5.2 signifies that the opening angle between the elastic scattered particles is always 90°.

[2] This value is obtained by minimizing the function $\theta_{op} = \theta + atan\left(\frac{1}{\gamma^2 tan\theta}\right)$ with respect to θ, where $\theta \in [0,\pi/2]$.

E_{kin}	p_{beam}	β_{CMS}	γ_{CMS}	θ_{op}	$M(p_1,p_2)$
3.10 GeV	3.93 GeV/c	0.79 c	1.63	[63°,83°]	3.06 GeV/c^2

Table 5.1: Summary of the kinematical properties of the analyzed elastic $pp \rightarrow pp$ reaction.

polar angles smaller than $\theta = 4.5°$, the maximum opening angle of the elastic protons at this energy is $\theta_{op,max} = 83°$.

According to equation 5.2, the polar angle of an elastic proton can be predicted if the angle of the other proton track is measured. This allows to define tight cuts based on the elastics kinematics, enabling an effective selection of elastics events. These cuts will be used in the following analysis to reduce the amount of fake tracks for the calculation of the detector efficiencies.

Momentum conservation in the LAB system implies the following equations for the transverse and longitudinal momentum components p_t and p_l.

$$p_{t,1} - p_{t,2} = p_1 sin\theta_1 - p_2 sin\theta_2 = 0 \tag{5.4}$$

$$p_{l,1} + p_{l,2} = p_1 cos\theta_1 + p_2 cos\theta_2 = p_{beam} \tag{5.5}$$

Together with equation 5.2, another relation can be derived, which correlates the momentum of an elastic proton with its polar angle.

$$p_i = \frac{p_{beam}}{cos\theta_i + \gamma^2_{CMS} sin\theta_i tan\theta_i} \tag{5.6}$$

Subject to this formula, by measuring the polar angle of an elastic proton, its momentum can be estimated and compared to the value reconstructed by the tracking algorithms. This allows for a quantification of the tracking system's momentum resolution.

More detailed calculations concerning elastic reactions can be found in [Spa05] and [Rus06].

5.3 Identification of elastics

The first step in the analysis of the reaction $p + p \rightarrow p + p$ is the identification and separation of the protons. Only events containing two protons are accepted and the particle ID is selected, using the graphical cuts introduced in section 4.1. These 2-proton events yield the desired elastics as well as background events, which have to be removed. For this purpose, a set of cuts is defined, based on the kinematics of elastic reactions, which was introduced in the previous section.

In the underlying analysis, the convention is chosen, that the proton with subscript 2 is always measured by the CDC. Since the opening angle is always larger than 63° (see table 5.1) at least one of the protons generally falls within the CDC acceptance ($27° < \theta < 113°$). In 90 % of the cases, the proton p_1 is measured by the HELITRON,

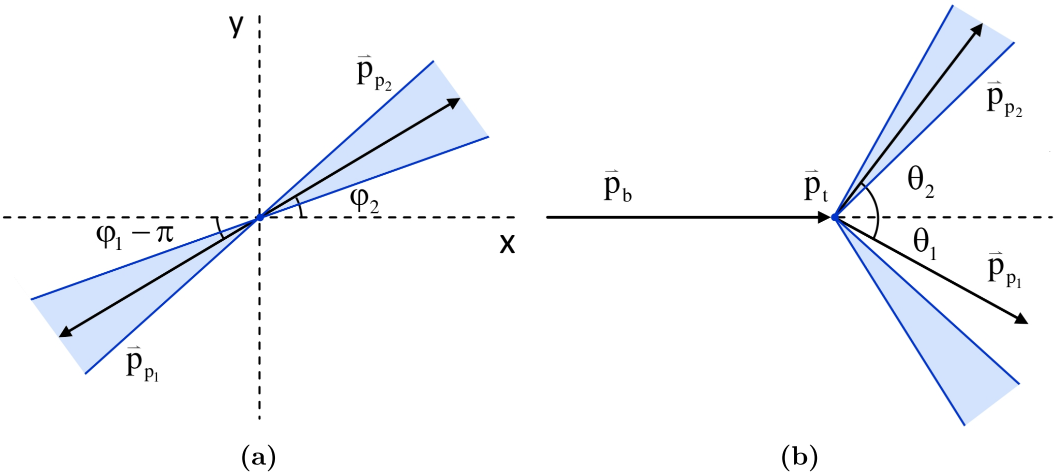

Figure 5.2: Cuts on the angular relations for elastic events. The blue areas indicate the allowed angles. (a): Cut on the difference of the azimuthal angles $\varDelta\varphi$. (b): Cut on the difference $\varDelta\theta$ of measured and predicted polar angle of the proton p_2. In combination with the cut on $\varDelta\varphi$, two valid angular regions are remaining. The unphysical angle (empty blue area beneath the beam axis) violates momentum conservation and can be rejected.

whereas the other elastics particle p_2 is detected by the CDC. Only around 10 % of the events have both protons emitted in the CDC acceptance.

The first selection is based on equation 5.1, performing a cut on the difference of the azimuthal angles $\varDelta\varphi$ (Figure 5.2a).

$$\varDelta\varphi = |\varphi_1 - \varphi_2| \tag{5.7}$$

Corresponding to relation 5.2, the polar angle of one elastic proton is determined by the other particle. This allows to define a cut on the difference of the predicted and the measured polar angle $\varDelta\theta$, which is depicted by figure 5.2b. The cut is applied to the second proton.

$$\varDelta\theta = \theta_2 - atan\left(\frac{1}{\gamma^2 tan\theta_1}\right) \tag{5.8}$$

The polar angle cut principally constitutes a spherical segment of validity around the beam axis, which reduces to two allowed θ-regions in combination with the cut on $\varDelta\varphi$. The wrong polar angle is unphysical because it violates conservation of the transversal momentum components (equation 5.4) and can therefore be rejected.

The third cut is performed on the invariant mass of the two protons, which depends on the beam energy. The different cut values are listed in table 5.2.

The effect of applying these cuts to the pp data is demonstrated by figure 5.3. For the spectra in the following subsections, the whole statistics with all possible trigger combinations (see section 2.6) is analyzed ($\approx 72 \cdot 10^6$ events). Picture (a) shows

Cut on	*Lower bound*	*Upper bound*
$M(p_1,p_2)$	$2.50\,\mathrm{GeV/c^2}$	$3.50\,\mathrm{GeV/c^2}$
$\varDelta\varphi$	176°	186°
$\varDelta\theta$	-8°	5°
p-value	0.05	1

Table 5.2: Cut boundaries for the selection of elastic pp events.

a two-dimensional histogram of all events containing 2 protons, where the the two polar angles θ_1 and θ_2 are plotted against each other. The black lines indicate the different detector acceptances in θ (see chapter 2).

- HELITRON: $4.5^\circ < \theta < 27^\circ$
- CDC - RPC: $27^\circ < \theta < 50^\circ$
- CDC - Plastic Barrel: $\theta > 50^\circ$

In the elastics analysis, the HELITRON tracks are always matched with the Si$\varLambda$Vio detector.

Since no cuts are applied (besides the cut on the proton mass), a large amount of background is present, especially at small polar angles, and no clear elastic structure is visible. Panel (c) of figure 5.3 shows the corresponding distribution of $\varDelta\theta$. The large peak at negative values corresponds to the yield enhancement in the lower left corner of picture (a), where both tracks lie in the HELITRON acceptance. However, even a small bump at zero is visible, originating from elastic events.

Figure 5.3b presents the θ_2 vs. θ_1 distribution, where the cuts on $\varDelta\varphi$ and $M(p_1,p_2)$ were applied. A large fraction of background can be removed this way, revealing a clear elastic structure which nicely follows the theoretical curve indicated by the black dashed line. For the calculation of the CDC-RPC matching efficiency, the second proton should cross the RPC (following the index convention of this analysis). The respective area in picture (b) is denoted by the bold black frame. Due to the large opening angle of the elastic particles, most of the CDC protons have polar angles larger than 50°, which is evidenced by the peak structure at large θ_2. Hence, only a certain fraction of the total number of elastics can be used for the determination of the CDC-RPC matching efficiency.

Even after applying the $\varDelta\varphi$ and $M(p_1,p_2)$ cuts, some background is remaining. It can be further reduced by the cut on $\varDelta\theta$, indicated by the two red lines. They correspond to the red area below spectrum 5.3d, which results from the left hand picture (c) after using the cuts on $\varDelta\varphi$ and $M(p_1,p_2)$. A distinct and symmetric elastic peak centered around zero is visible.

Finally, the kinematic refit with energy and momentum conservation constraint (see section 3.3) is applied to the selected events, which are located inside the $\varDelta\theta$ cut. Since even after the kinematical cuts still some background is left, the kinematic refit is also applied on these wrongly identified elastics.

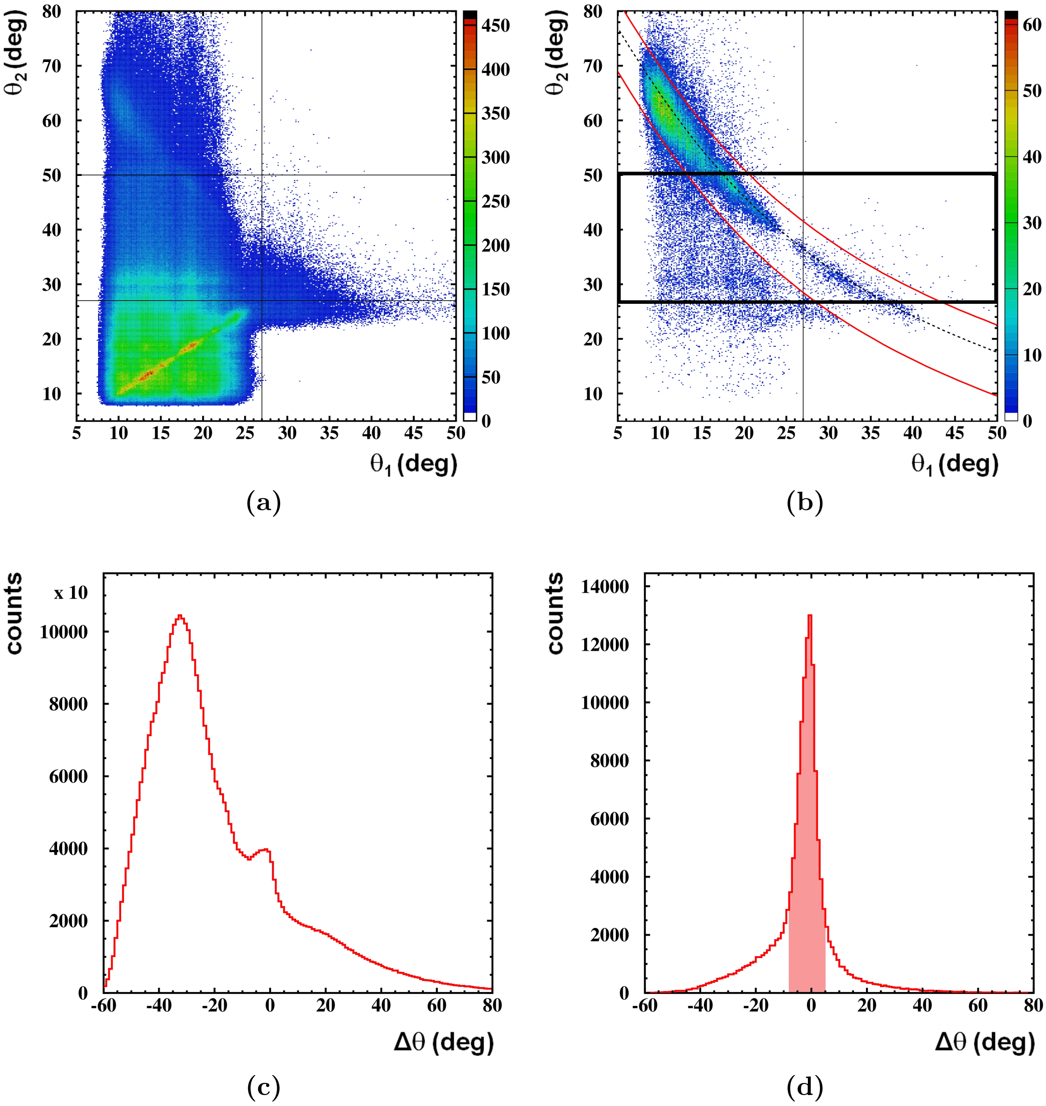

(a)

(b)

(c)

(d)

Figure 5.3: Background reduction with cuts on elastic events. Panels (a) and (c) show the raw spectra, while the distributions shown in panels (b) and (d) are obtained by cutting on $\Delta\varphi$ and $M(p_1,p_2)$. The black lines in panels (a) and (b) represent the different detector acceptances. The location of elastic protons, which can be used for the estimation of the CDC-RPC matching efficiency, is indicated by the black box in figure (b). The red lines in (b) and the red shaded area in (d) signify the cut on $\Delta\theta$. Finally, the kinematic refit is applied to the remaining, falling within the red lines in (b). A cut on the p-value of the fit further reduces background.

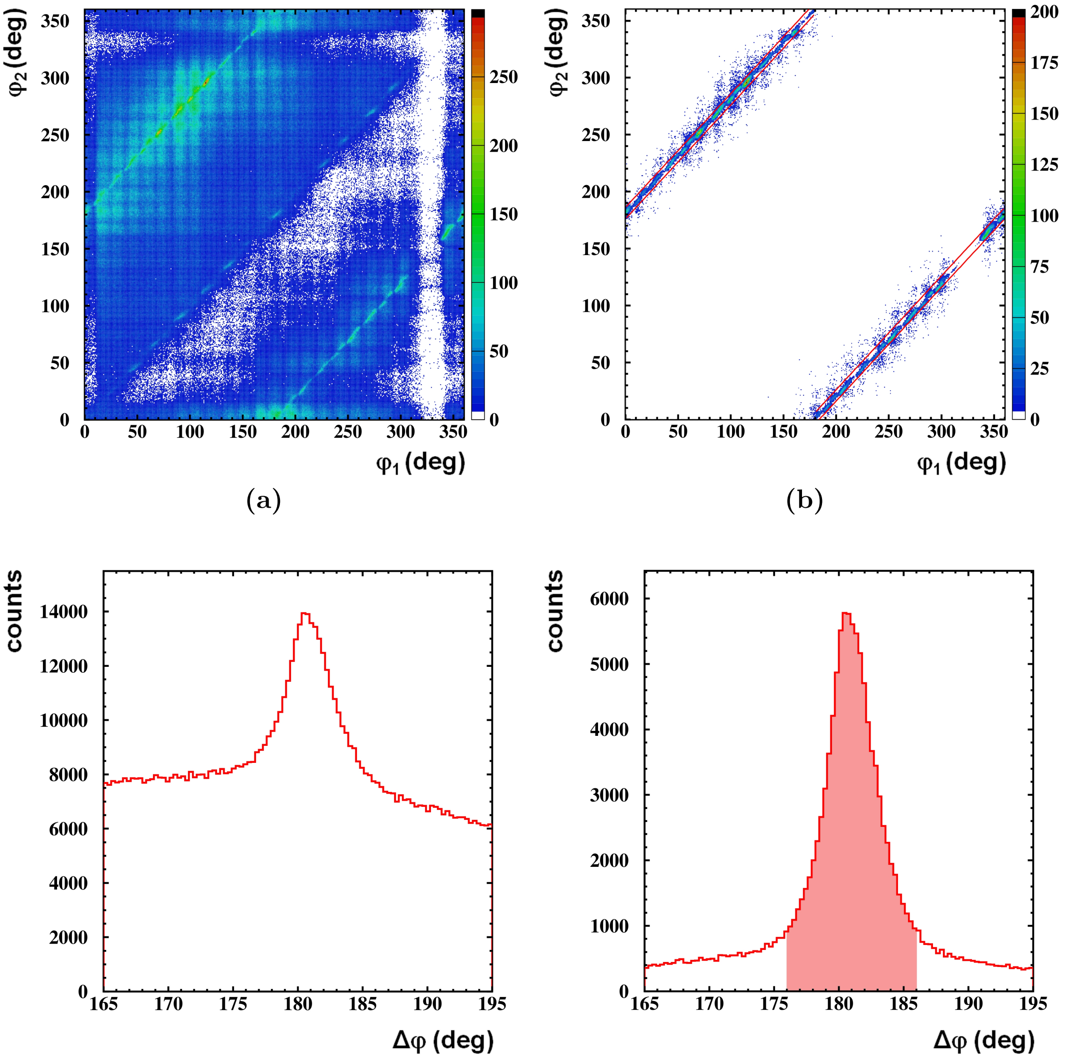

(a) (b)

(c) (d)

Figure 5.4: Background reduction with cuts on elastic events. Panels (a) and (c) show the raw spectra, while the distributions shown in panels (b) and (d) are obtained by cutting on $\Delta\theta$ and $M(p_1,p_2)$. The red lines in (b) and the red shaded area in (d) denote the cut on $\Delta\varphi$. The events within the $\Delta\varphi$ cut boundaries are finally refitted. Consequently, a cut on the p-value is applied.

This results in a peak at low values in the corresponding p-value distribution (see section 5.5). Cutting on the p-value by defining a significance of 0.05 leads to a further reduction of misidentified events, which can be seen by the sharp edge in the background at the red cut boundaries in figure 5.3b. The resulting elastic structure is broader for combinations containing one proton in the HELITRON, due to the smaller momentum resolution. However, the kinematic refit is used for cutting on the p-value only. In the further analysis, the unrefitted parameters are used.

The analog spectra for the azimuthal angles are shown in figure 5.4. Again, the pictures in panels (a) and (c) show the distributions obtained without applying any cuts, whereas the spectra in panels (b) and (d) are obtained after applying the cuts on $\varDelta\theta$ and $M(p_1,p_2)$. Picture 5.4b shows two diagonals corresponding to elastic events, which are clearly visible and almost background free. The final cut on $\varDelta\varphi$ is indicated by the red lines. After refitting the remaining events with the energy and momentum conservation constraint, a cut on low p-values is applied. The lower row shows the distributions of the cut variable $\varDelta\varphi$, left (c) without and right (d) with cuts. Again, the red shaded area corresponds to the $\varDelta\varphi$ cut boundaries in panel (b). Figure 5.4a reveals some interesting structures which are worthwhile to be discussed briefly. First, even without cuts, the two diagonals corresponding to elastic events are clearly visible. Moreover, a rectangular sub-pattern seems to be superimposed on the plot. This regular structure reflects the boundaries of the 24 radial sectors of the HELITRON drift chamber (see section 2.1.2). Furthermore, a clear asymmetry between the upper left and the lower right triangular region is recognizable. This effect originates from the fact, that the $\varLambda$ Trigger Si$\varLambda$Vio was slightly misaligned in the vertical direction and was hanging downwards with respect to the beam axis. This small misalignment during the experiment lead to an increased fraction of particles flying through the upper hemisphere of the second silicon layer Si$\varLambda$Vio-B, causing a bias in the $\varLambda$ trigger (see section 2.5). Since in the underlying elastics analysis, the hits occurring on Si$\varLambda$Vio-B are matched with the HELITRON hits, the asymmetry propagates to the HELITRON tracks. Last, the poorly populated strips at $\varphi_i \approx 330°$ stem from an acceptance hole in the HELITRON, caused by two sectors, that were defect during the experiment.

5.4 Characterization of the drift chambers

The elastic events, that were selected via the cuts introduced in the previous section, contain only a small fraction of background and fake-tracks. Therefore, they are well-suited for the characterization of different detector properties.

5.4.1 CDC-RPC matching efficiency

In order to analyze the experimental data, the information of the different sub-detectors has to be combined. For the ppK^- analysis, especially the matching between CDC and RPC tracks is important, since the produced kaons can only be identified via the TOF measurement in the RPC. In order to be able to compare the experimental data to simulations, the CDC-RPC matching efficiency has to be known. It is defined as the number of CDC tracks which could be matched with the RPC and therefore are associated to a RPC mass[3], divided by the total number of

---

[3] i.e. the mass is determined by the combination of velocity and momentum in contrast to the CDC mass which is calculated via the energy loss in the drift chamber (see section 2.7).

CDC tracks. This number generally depends on the momentum and polar angle of the particles, whereas it should be independent of φ.

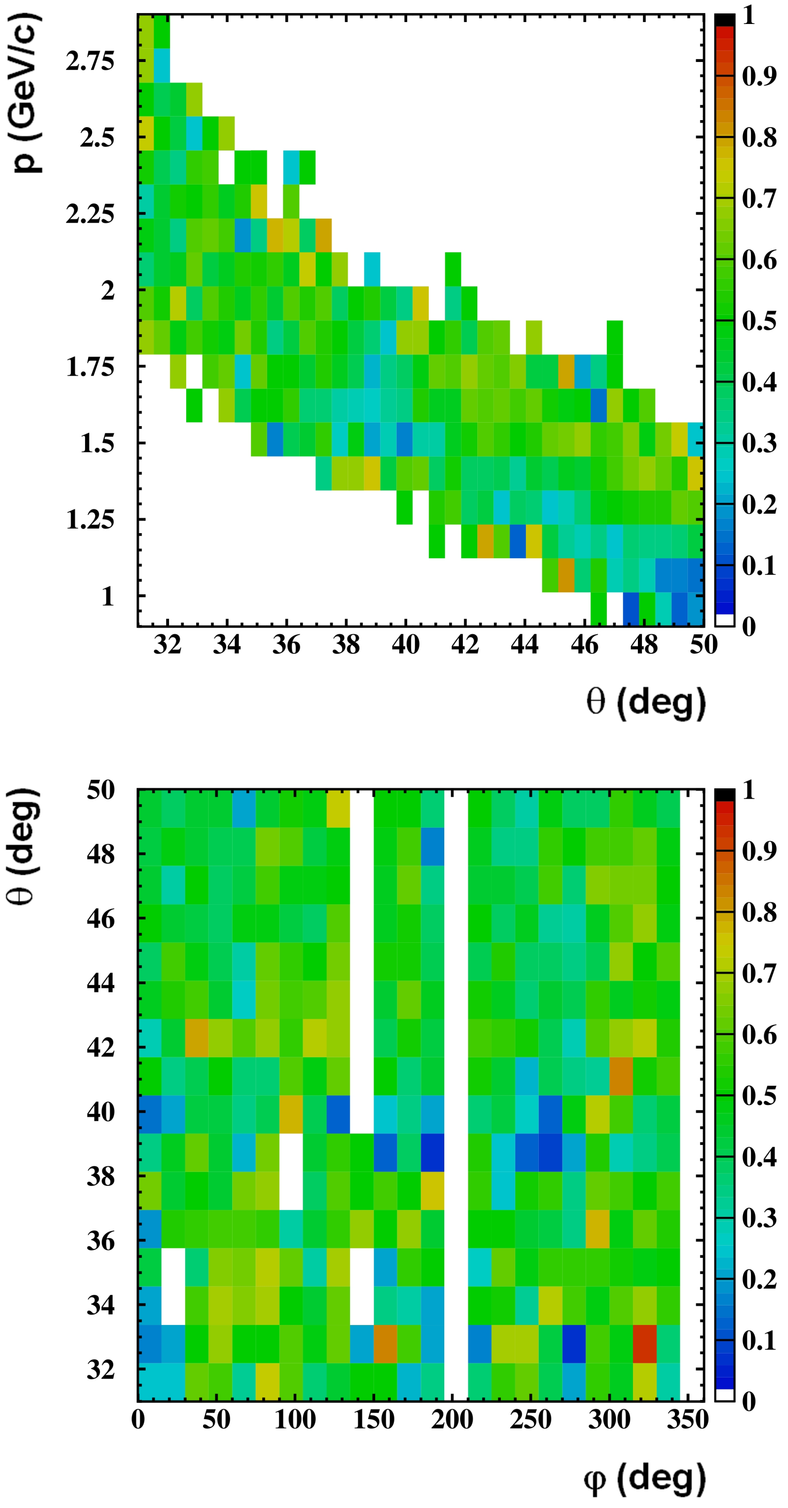

Figure 5.5: CDC-RPC matching efficiency as a function of the momentum p and the polar angle θ (upper picture) and as a function of θ and φ (lower picture).

The upper panel in figure 5.5 shows the CDC-RPC matching efficiency as a function of the momentum p and the polar angle θ of the elastic particle p_2. The course of the distribution follows the $p(\theta)$ relation given by equation 5.6. The matching efficiency roughly varies between 40 % and 70 %, tending to lower values for larger polar angles and smaller momenta. The CDC-RPC matching efficiency as a function of θ and φ is illustrated in the lower panel of figure 5.5 and shows three acceptance holes in φ. The left hole at $\varphi = 150°$ originates from the broken HELITRON sectors. It corresponds to the poorly populated strips at $\varphi = 330°$ in picture 5.4. Since the two elastic protons always have a difference in φ of 180°, the acceptance hole in the HELITRON propagates to the CDC: 150° = 300° - 180°. The two holes at $\varphi = 200°$ and $\varphi = 350°$ result from two acceptance holes in the RPC. Again, the matching efficiency varies between 40 % and 70 %. Since various corrections (e.g. electric field distortions) are not yet included in the underlying RPC calibration, the CDC-RPC matching efficiency is expected to increase if further iterations of the calibrations are employed.

5.4.2 Relative HELITRON efficiency

The selected elastic events can be used to study different detector properties in comparison with simulations, since both, data and simulation refer to the same reaction.

In about 90 % of the cases, the elastic proton p_1 is measured by the HELITRON. By comparing the distribution of all p_1 as a function of the momentum p and the angles θ and φ in the data to the same distribution resulting from full scale simulations, the relative HELITRON efficiency is determined (Figure 5.6). It is calculated for each bin as the number of p_1 hits in the data divided by the number of entries in the simulation. Both values are normalized to the number of LVL1 trigger events respectively in order to render the distributions comparable. For the simulation of the pp reaction, the UrQMD transport model is used, including the most common reaction channels [UrQ].

In figure 5.6, also tracks are included, which are not matched with the SiΛVio detector in order to increase the available statistics. In the lower panel, the φ angle is divided into 24 bins, adjusted to the 24 sectors of the HELITRON. The empty strip at $\varphi = 330°$ belongs to the acceptance hole caused by the broken sectors, which also appears in figures 5.4a and 5.5. The second acceptance hole at $\varphi = 170°$ results from the RPC.

The pictures can be used as efficiency matrices for the later analysis in order to scale down the simulated distributions to fit the experimental ones. This will be essential for a systematic investigation of the different reaction channels contained in the data.

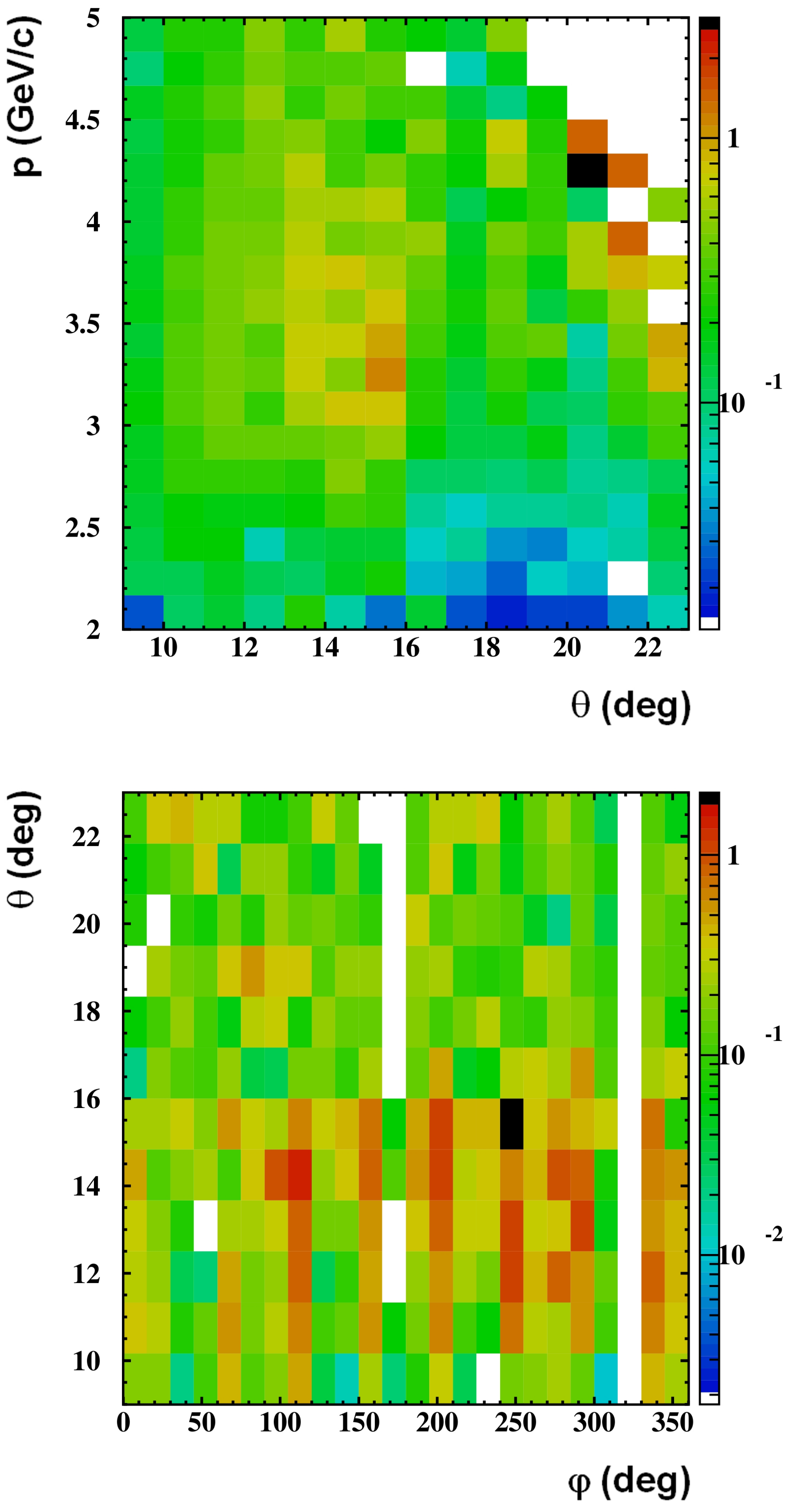

Figure 5.6: Relative HELITRON efficiency normalized to LVL1 trigger events as a function of the momentum p and θ (upper picture) and as a function of θ and φ (lower picture). Two acceptance holes are visible in the θ vs. φ picture, at $\varphi = 170°$ originating from the RPC and at $\varphi = 330°$, resulting from the broken HELITRON sectors. The empty area in the upper right corner of the upper panel originates from the kinematics.

5.5 Application of the kinematic refit

The application of the kinematic refit to the elastic events provides a useful tool to reduce the background, which cannot be removed with the cuts on the elastic kinematics. Due to the nature of the kinematics, the possible constraint conditions that can be used with the refit are limited to the energy and momentum conservation constraint (which in this case equals the constraint to set the invariant mass $M(p_1,p_2)$ to 3.06 GeV/c^2) and the intersection constraint. However, the latter is not used, since its effect is negligible.

Figure 5.7 shows the missing energy and the y-component of the missing momentum for raw (red) and refitted (blue) elastic events. The used errors, which are estimated with the help of the pull distributions, are listed in table 5.3. The energy and momentum conservation constraint is clearly fulfilled after the kinematic refit. Moreover, the refit exactly shifts all distributions (e.g. p vs. θ, θ_2 vs. θ_1, etc.) onto the theoretical curves, following the equations, explained in section 5.2.

The corresponding χ^2 and p-value distributions are illustrated in figure 5.8. The presence of background reflects in the deviation of the χ^2 distribution from the theoretical curve. The fitted ndf value is 4.32, compared to the true value of 4. This deviation appears as a peak at low p-values in figure 5.8b. By defining a significance of $\alpha = 0.05$, all p-values, which are located within the gray shaded area, are rejected. As shown in section 5.3, this leads to a considerable reduction of background. The respective pull distributions (Figure 5.9) show a clear deviation from the Gaussian shape for the $1/p$ and φ parameters. Besides the obvious effect of the refitted background, the translation of the pull spectra indicate the presence of systematic errors.

According to equation 5.6, the theoretical momentum p_{theo} can be predicted by the measurement of the polar angle θ. By comparing the theoretical to the measured momentum p_{exp}, this enables the determination of the momentum resolution for the different drift chambers. The red curves in figure 5.10 represent the momentum resolutions $p^{raw}_{theo} - p^{raw}_{exp}$ for the HELITRON (a) and the CDC (b) for unrefitted events. Due to the higher momentum reconstruction capability, the resolution of the CDC is much better. Again, the shift of the momentum resolution to higher values for

Proton in	$\sigma(1/p)$	$\sigma(\theta)$	$\sigma(\varphi)$
UrQMD pp simulations			
CDC	8.0 %	2.29°	0.57°
HELITRON	18 %	5.73°	6.88°
experimental data			
CDC	7.0 %	2.86°	2.30°
HELITRON	18 %	0.86°	0.06°

Table 5.3: Errors for the kinematic refit applied to measured and simulated elastic proton reactions $pp \rightarrow pp$.

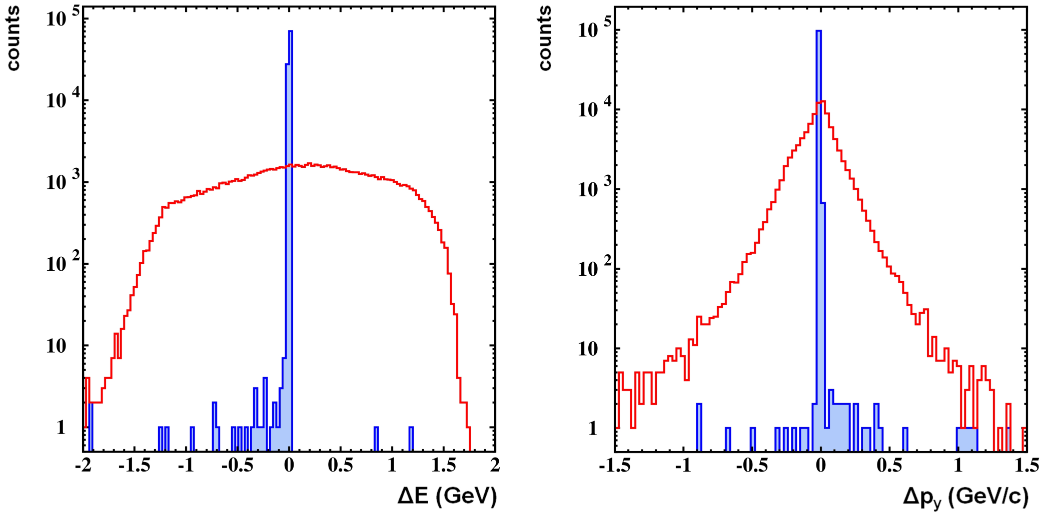

(a) (b)

Figure 5.7: (a): Energy conservation for raw (red) and refitted (blue) events. (b): Momentum conservation in y-direction before (red) and after (blue) the application of the kinematic refit with energy and momentum conservation constraint.

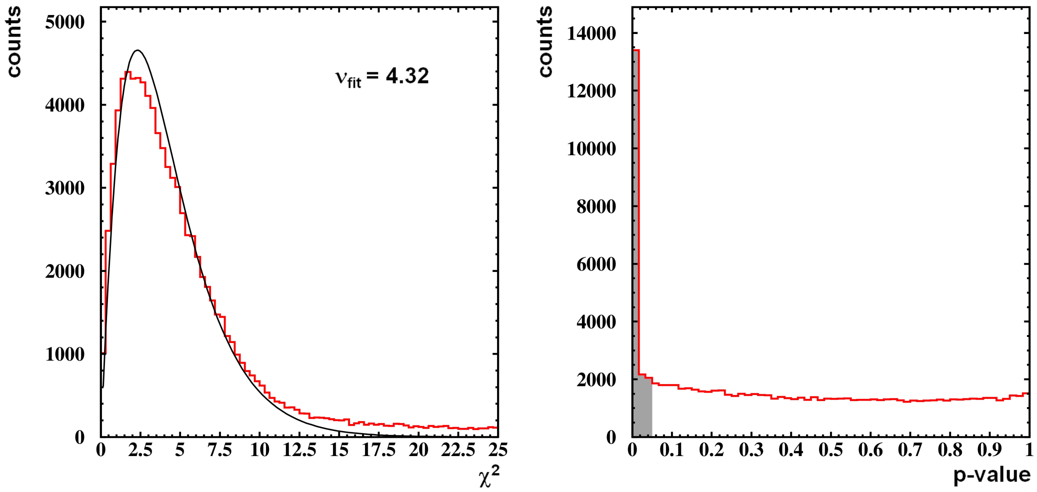

(a) (b)

Figure 5.8: χ^2 distribution with $ndf = 4$ (a) and p-value distribution (b) of the kinematic refit with energy and momentum conservation constraint. The Grey area beneath the p-value distribution indicates the significance of $\alpha = 0.05$ which is used as a cut on low p-values. The black line in (a) indicates the fitted χ^2 curve to the spectrum.

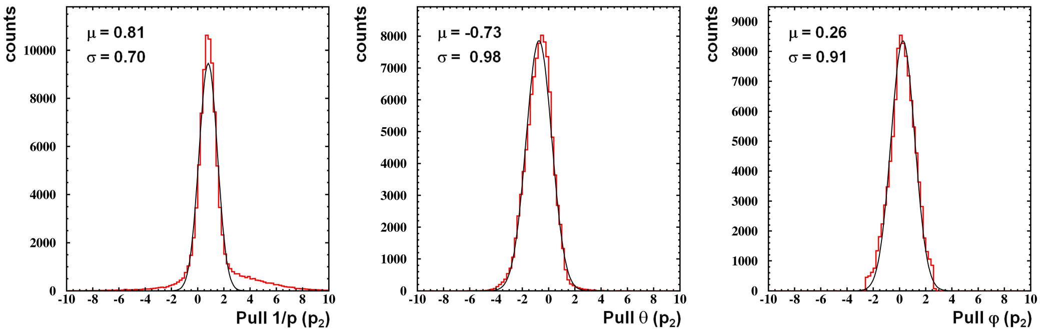

Figure 5.9: Kinematic refit with energy and momentum conservation constraint. Shown are the pull distributions for the 3 momentum parameters of the elastic proton p_2 in the CDC. The black lines represent the fitted Gauss functions corresponding to the values in the upper left corners. The tails of the pull distribution in the first panel originate from refitted background.

the CDC is a hint for possible systematic errors, which could in a further step be estimated with the kinematic refit via the pull distributions. After the kinematic refit with energy and momentum conservation constraint, the respective resolutions are sharp peaks at zero. Since the particles afterwards exactly satisfy relation 5.6, the refitted resolutions $p_{theo}^{refit} - p_{exp}^{refit}$ are not meaningful. Instead, the blue curves in Figure 5.10 show the difference of the theoretical momentum predicted by the raw polar angle θ and the refitted measured momentum $p_{theo}^{raw} - p_{exp}^{refit}$. The values for the different resolutions are listed in table 5.4. For the HELITRON (panel (a), figure 5.10), the resolution drastically enhances by 96 %. The improvement reflects the fact, that the kinematic refit shifts the momentum to the value, which is predicted before the refit. This arises from the more precise measurement of the polar angle compared to the momentum. In case of the CDC (b), the resolution improves by 12 % and its mean value is shifted towards zero. Clearly, in the presence of systematic errors, the kinematic refit fails to further improve the resolution, since it tries to compensate the systematic errors by a statistical procedure. Nevertheless, a noticeable effect is visible.

Particle	σ_{raw}	σ_{refit}	$\Delta\sigma$
p_1	630 MeV/c	25 MeV/c	96%
p_2	108 MeV/c	95 MeV/c	12%

Table 5.4: Resolutions of the raw and refitted differences of theoretical and measured momenta.

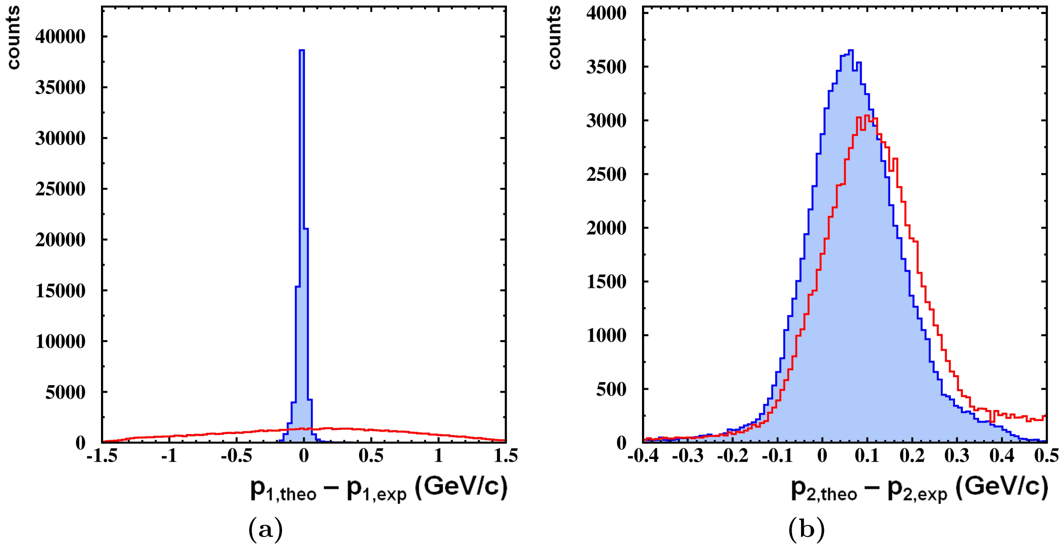

(a) (b)

Figure 5.10: Theoretical momentum resolution for the HELITRON (a) and the CDC (b). The red curves represent the difference of predicted and measured raw momenta $p^{raw}_{theo} - p^{raw}_{exp}$. The blue spectra are obtained by comparing the raw predicted momenta to the refitted measured ones $p^{raw}_{theo} - p^{refit}_{exp}$.

5.6 Coplanarity of elastics and beam alignment

According to equation 5.1 the momentum vectors of the two elastic protons lie in one common plane together with the momentum of the beam proton. The three vectors are referred to as being coplanar. This relation can be used to check, whether the direction of the incoming beam was really exactly parallel to the z-axis during the experiment.

Since the beam particles are not explicitly measured, it is assumed, that their momentum vector only has a z-component, which is determined by the beam energy: $p_z = \sqrt{(E_{kin} + m_p)^2 - m_p^2}$. If this hypothesis is true, the vector product $\vec{p_1} \times \vec{p_2}$ of the two elastic proton momenta is always orthogonal to the beam momentum. However, if the real beam is inclined by an angle θ_b with respect to the z-axis, the emission plane of the elastic protons is tilted as well. Therefore, the elastics and the hypothetic beam direction along the z-axis are not coplanar anymore.

This situation is illustrated by figure 5.11. The vector product of the elastic momenta, which is represented by the blue arrow, is still orthogonal to the real beam momentum $\vec{p_b}$. Though, the angle to the z-axis θ_{co}, which is assumed to be the direction of the beam, is different from 90°. Hence, by investigating the angle θ_{co} as a function of the azimuthal angle φ, a possible inclination of the original beam direction can be determined and corrected.

Figure 5.12a shows the coplanarity angle θ_{co} of the elastics as a function of φ for full scale UrQMD pp simulations. In the lower row, the φ range is sub-divided into

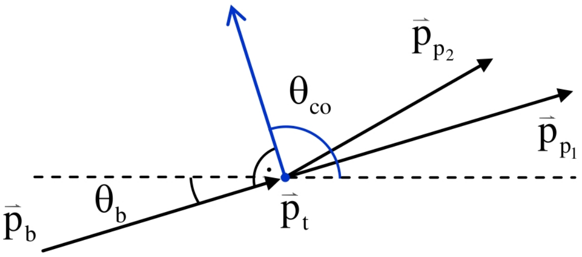

Figure 5.11: Scheme of the coplanarity of elastics and beam momenta. The blue arrow is the vector product of the two elastics momenta $\vec{p_1} \times \vec{p_2}$, which is always orthogonal to the beam direction. The angle $\theta_{co} = \frac{\pi}{2} + \theta_b$ is a direct measure of the tilt angle of the beam θ_b.

12 bins. Each bin is fitted with a Gauss function, the standard deviation of which is represented by the vertical lines. The mean values of the θ_{co} distributions are scattered around 90° with deviations less than 0.05°. This proves, that incident beam was indeed parallel to the z-axis during the experiment. A tilt of the beam can therefore be excluded as a source of systematic errors.

The effect of a non-parallel beam on the spectra is shown in figure 5.12b. For this test, a x-component $p_{b,x}$ of 10 MeV/c is added manually to the beam momentum.

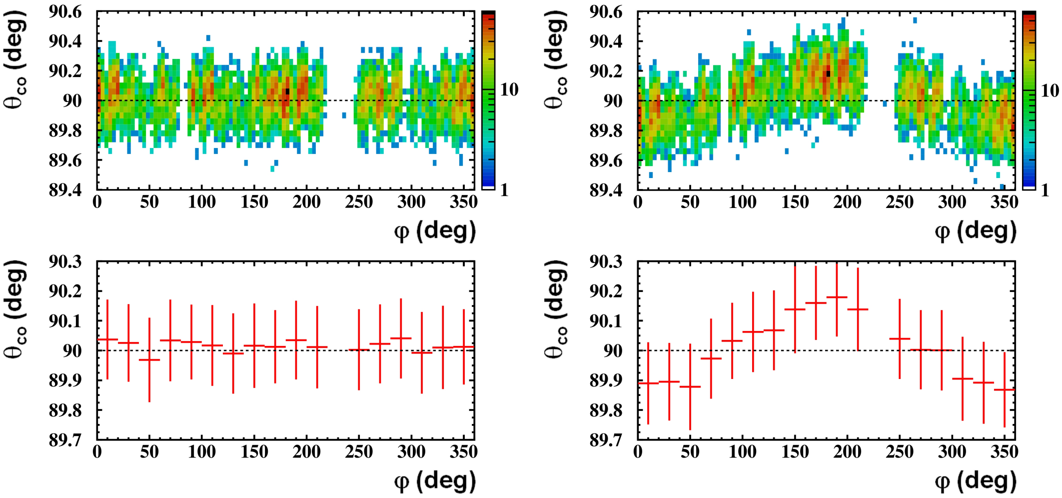

(a) (b)

Figure 5.12: Coplanarity of elastics and beam momenta for full scale pp simulations. (a): Distribution of the angle θ_{co} as a function of φ. (b): Effect of a tilted beam momentum by $\theta_b = 0.15°$. The lower row shows the distributions of the upper pictures, where the φ axis is divided into 12 bins. The vertical red lines represent the widths of the fitted Gaussian functions of each bin.

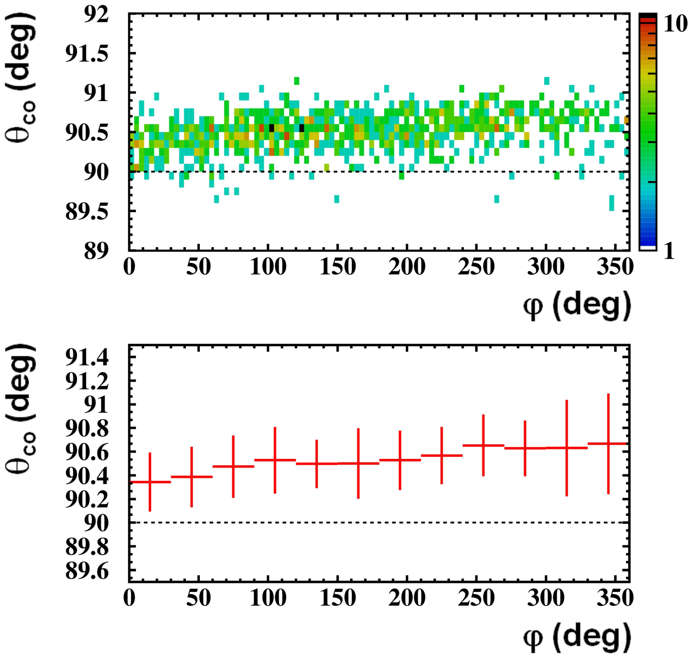

Figure 5.13: Coplanarity of elastics and beam momenta for the experimental data. The systematic shift of θ_{co} indicates systematic errors in the measurement of $\vec{p_1}$ and $\vec{p_2}$. This requires at least a systematic error in φ, in order to affect the coplanarity.

This results in a tilt angle of

$$\theta_b = atan\left(\frac{p_{b,x}}{p_{b,z}}\right) = atan\left(\frac{0.01GeV/c}{3.93GeV/c}\right) = 0.15^\circ \tag{5.9}$$

The course of the θ_{co} distribution reflects this tilt by showing a minimum at $\varphi = 0^\circ$ and a maximum at $\varphi = 180^\circ$, corresponding to the angle obtained in equation 5.9. The positions of the extrema belong to a tilt in positive x direction, since at $\varphi = 180^\circ$ the vector $\vec{p_1} \times \vec{p_2}$ points along the x-axis. The tilt angle can directly be extracted from the maximum deviation of

$$\theta_{co} = \frac{\pi}{2} + \theta_b \tag{5.10}$$

The θ_{co} distribution for the data is shown in figure 5.13. It follows an almost flat curve, indicating that no tilt of the beam axis was present during the experiment. However, a systematic θ_{co} shift of 0.4°-0.6° is observed. Confirming the results of the kinematic refit in the previous section, this signifies the presence of systematic errors in the measurement of the elastic protons, which also affects the θ_{co} angle. The precondition for this shift in θ_{co} is a systematic error in the φ angle. Otherwise, a change in θ or $1/p$ would not alter the coplanarity of the elastics and the beam.

As recently as a shift in φ rotates the momenta of the protons out of the common emission plane, also changes in the other parameters affect the error of θ_{co}. Hence, a quantitative estimation of the corresponding systematic errors is difficult. In principle, the effect of manually imposed systematic errors in θ and φ on the coplanarity could be investigated. However, since the errors of this two parameters are correlated, the determination of the explicit error values is complicated.

6 Conclusions and outlook

Conclusions

Within the framework of this thesis, the kinematic refit developed for the exclusive analysis of the $pK^+\Lambda$ reaction was presented, as well as the underlying mathematical principles were explained. Before applying the kinematic refit to the experimental data, it was tested with various simulations in order to systematically investigate the behavior of the different constraints and the effect of systematic errors and background.
Finally, the analysis of elastic $p + p$ reactions was presented, where different detector efficiencies and the beam alignment were determined. The application of the kinematic refit reduced the background and enabled a better separation of elastic events.

The most important steps and results of this work are listed in the following.

- The kinematic refit, which was developed for the exclusive analysis of the reaction $pp \to pK^+\Lambda$, is constructed in a modular and general way. It includes the following constraint conditions, which can be applied in all possible combinations (see section 3.3).
  - invariant or missing mass constraint
  - energy and momentum conservation constraint
  - intersection constraint for 2 or 2x2 particle tracks
  - secondary vertex constraint

  An arbitrary number of particles and iteration steps can be used, together with three different track representations.

- In order to validate the correct functioning and to study its basic behavior, the kinematic refit with the single constraint conditions was applied to PLUTO simulations of the $pK^+\Lambda$ reaction, where the parameters of the tracks were manually smeared around the simulated values. It was shown that only the energy and momentum conservation constraint has an impact on the momentum and angular resolutions of the different particles. The intersection constraint did not cause any noticeably improvement of the vertex (p_2,π^-) resolution. In contrast, the secondary vertex constraint improved the primary vertex (p_1,K^+,Λ) resolution noticeably.

- The pull, χ^2 and p-value distributions of the refit are sensitive to the correct error input and to the presence of systematic errors and background (see section

3.3.3). Hence, the covariance matrix $\mathbf{V}_{\vec{\alpha}_0}$ could be estimated by adjusting the pull distributions of the fit.

- The kinematic refit with invariant mass (p_2,π^-) constraint is sensitive to the correct combination of p and π^- to stem from the Λ decay. This feature was exploited in a pre-selection process which assigned the correct IDs to the two protons, that appear in the final state (see section 4.1).

- Applied to full scale $pK^+\Lambda$ simulations, the kinematic refit with energy and momentum conservation constraint lead to an improvement of the mass resolutions of the reconstructed Λ (see section 4.2.1). The pull distributions indicated the influence of systematic errors.

- The refit was applied to full scale simulations of the pp reaction in order to study its effect on background events (see section 4.2.2). Via a cut on low p-values, the refit reduced a large amount of background, provided that the particular constraint combination acted on all four charged particles. A systematic analysis of all constraint combinations was performed, showing that the cut efficiency increased with an increased number of constraint conditions. This trend was also followed by the S/B ratios of the single fits.

- Finally, the kinematic refit with energy and momentum conservation constraint was applied to experimental data (see section 4.3). The pull distributions showed clear indications for systematic errors in the θ and $1/p$ parameters. The refit did not improve the invariant mass (p_2,π^-) but drastically reduced the background. It was demonstrated, that the kinematic refit can be used to efficiently reduce a large amount of background via a cut on the p-value. Since the refitted tracks did not show an improved mass resolution, the unconstrained parameters were used for the further analysis. In this case, the kinematic refit exclusively acted as a cut procedure.

- In the last chapter, the analysis of elastic pp reactions was presented. It was pointed out, that elastic events are a well-suited tool for the determination of detector efficiencies. Due to the fixed kinematics, tight cuts efficiently select elastic events and reduce the amount of fake tracks. The kinematic refit with energy and momentum conservation constraint was used to further reduce the background by cutting on the p-value of the fit. Again, indications for systematic errors were observed in the pull distributions. The CDC-RPC matching efficiency and the relative HELITRON efficiency as a function of the momentum and the angles were determined and discussed. Furthermore, the alignment of the beam was investigated via the coplanarity of elastic and beam protons. A systematic shift was observed which pointed to the presence of systematic errors.

Outlook

The kinematic refit is a powerful tool for the exclusive analysis of the $pK^+\Lambda$ reaction. For the future analysis, the following steps involving the kinematic refit are planned.

- Different results of this work clearly indicate the presence of systematic errors. The next step in the exclusive analysis is the localization and quantification of these uncertainties together with a subsequent correction. The kinematic refit can be used to localize the systematic errors by manually imposing systematic shifts on the different parameters. The investigation of the resulting effects on the pull distributions could help to understand the origin of the observed uncertainties.
  Currently, a re-calibration of the detectors is ongoing. In course of these corrections, the systematic errors are expected to diminish.

- Analog to the pre-selection procedure presented in section 4.1, the kinematic refit can be used to select exclusive $pK^+\Lambda$ events without the necessity of graphical cuts. If the appropriate combination of constraints is used, the refit is sensitive to the correct event topology. The advantage of such an event identification method is the possibility to accept also events with more than 4 reconstructed track candidates. In case of an event selection with graphical cuts (see section 4.1), all exclusive events that occur together with fake tracks are rejected by the condition of exactly 4 reconstructed particle tracks. The refit based event selection would keep those events. According to the particular charges of the different particles, all possible event hypothesis are made, where the different particles are assigned to the $pK^+\Lambda$ final state particles (e.g. in the case of one negatively and three positively charged particles, 6 possible combinations exist). Consequently, the procedure selects the combination which results in the smallest χ^2 value.
  Moreover, this procedure would enable an exclusive event selection without the requirement of a direct K^+ identification in the RPC, which would lead to an increased acceptance for exclusive $pK^+\Lambda$ events [Mün12].

- As explained in section 1.4, N^* resonances play an important role in the production mechanisms of the $pK^+\Lambda$ reaction. Since a large fraction of the analyzed exclusive events belong to the direct $pK^+\Lambda$ production without the formation of an intermediate ppK^-, the signatures of different N^* resonances could be discovered in the data. According to figure 1.14, the contribution of heavier N^* like $N(1710)$ or $N(1720)$ should be dominant at the FOPI beam energy of 3.1 GeV. Indeed, the kinematic refit could intensify possible N^* structures contained in the data. Figure 6.1 shows the missing mass (p_1) distribution for raw (red) and refitted (blue) events. The refitted spectrum shows a structure, which could emerge from an intermediate $N(1900)$ resonance. Subsequently, this effect has to be investigated with UrQMD pp simulations, which also contain reactions with intermediate N^* resonances.

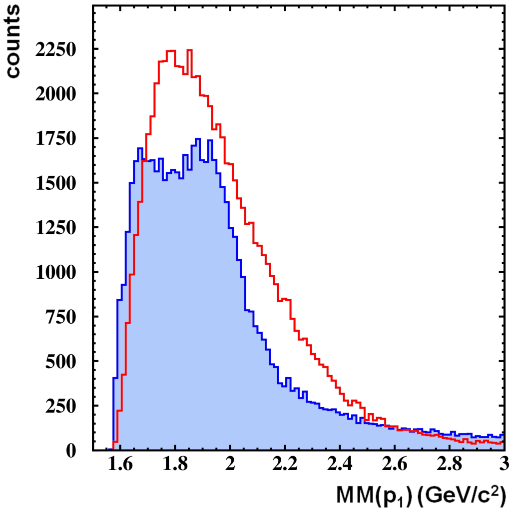

Figure 6.1: Missing mass (p_1) distribution for raw (red) and refitted (blue) tracks, where the kinematic refit with energy and momentum conservation constraint is applied to experimental data. The refitted spectrum shows a structure, which could emerge from a intermediate $N(1900)$ resonance [Mün12].

A D- and E-matrix elements and constraint equations

Definitions

Momentum parameters:

$$\vec{p}_i = \begin{pmatrix} p_{x,i} \\ p_{y,i} \\ p_{z,i} \end{pmatrix} \overset{sph}{=} \quad p_i \begin{pmatrix} sin\theta_i \, cos\varphi_i \\ sin\theta_i \, sin\varphi_i \\ cos\theta_i \end{pmatrix}$$

Emission point parameters:

$$\vec{x}_i = \begin{pmatrix} x_{x,i} \\ x_{y,i} \\ x_{z,i} \end{pmatrix} \overset{sph}{=} R_{\vec{x},i} \begin{pmatrix} sin\theta_{\vec{x},i} \, cos\varphi_{\vec{x},i} \\ sin\theta_{\vec{x},i} \, sin\varphi_{\vec{x},i} \\ cos\theta_{\vec{x},i} \end{pmatrix}$$

$\varLambda$ vertex parameters:

$$\vec{z}_\varLambda = \begin{pmatrix} z_{\varLambda,x} \\ z_{\varLambda,y} \\ z_{\varLambda,z} \end{pmatrix} \overset{sph}{=} R_{\vec{z}} \begin{pmatrix} sin\theta_{\vec{z}} \, cos\varphi_{\vec{z}} \\ sin\theta_{\vec{z}} \, sin\varphi_{\vec{z}} \\ cos\theta_{\vec{z}} \end{pmatrix}$$

Primary vertex parameters:

$$\vec{z}_{Prim} = \begin{pmatrix} z_{Prim,x} \\ z_{Prim,y} \\ z_{Prim,z} \end{pmatrix}$$

Momentum:

$$p_i = \sqrt{p_{x,i}^2 + p_{y,i}^2 + p_{z,i}^2} \overset{sph}{=} \sqrt{p_i^2 sin^2\theta_i cos^2\varphi_i + p_i^2 sin^2\theta_i sin^2\varphi_i + p_i^2 cos^2\theta_i}$$

Energy:

$$E_i = \sqrt{\vec{p}_i^2 + M_i^2} \overset{sph}{=} \sqrt{p_i^2 sin^2\theta_i cos^2\varphi_i + p_i^2 sin^2\theta_i sin^2\varphi_i + p_i^2 cos^2\theta_i + M_i^2}$$

Invariant mass constraint

In the following expressions, the subscript “i” stands for the particles p_2 and π^-.

Constraint equation*

$$H(\vec{\alpha}) = 0 = (E_{p_2} + E_{\pi^-})^2 - (\vec{p}_{p_2} + \vec{p}_{\pi^-})^2 - M_\Lambda^2$$

D-matrix elements in spherical coordinates

$$\frac{\partial H(\vec{\alpha})}{\partial (1/p)_i} = -2(E_{p_2} + E_{\pi^-})\,\frac{p_i^3}{E_i} + 2(p_{x,p_2} + p_{x,\pi^-})\,p_i p_{x,i} \tag{A.1}$$

$$+2(p_{y,p_2} + p_{y,\pi^-})\,p_i p_{y,i} + 2(p_{z,p_2} + p_{z,\pi^-})\,p_i p_{z,i} \tag{A.2}$$

$$\frac{\partial H(\vec{\alpha})}{\partial \theta_i} = \quad 2(E_{p_2} + E_{\pi^-})\,\frac{p_i}{E_i}\,(p_{x,i} cos\theta_i cos\varphi_i + p_{y,i} cos\theta_i sin\varphi_i - p_{z,i} sin\theta_i) \tag{A.3}$$

$$-2(p_{x,p_2} + p_{x,\pi^-})\,p_i cos\theta_i cos\varphi_i - 2(p_{y,p_2} + p_{y,\pi^-})\,p_i cos\theta_i sin\varphi_i \tag{A.4}$$

$$+2(p_{z,p_2} + p_{z,\pi^-})\,p_i sin\theta_i \tag{A.5}$$

$$\frac{\partial H(\vec{\alpha})}{\partial \varphi_i} = 2(p_{x,p_2} + p_{x,\pi^-})\,p_{y,i} - 2(p_{y,p_2} + p_{y,\pi^-})\,p_{x,i}$$

D-matrix elements in Cartesian coordinates

$$\frac{\partial H(\vec{\alpha})}{\partial p_{x,i}} = 2(E_{p_2} + E_{\pi^-})\,\frac{p_{x,i}}{E_i} - 2(p_{x,p_2} + p_{x,\pi^-})$$

$$\frac{\partial H(\vec{\alpha})}{\partial p_{y,i}} = 2(E_{p_2} + E_{\pi^-})\,\frac{p_{y,i}}{E_i} - 2(p_{y,p_2} + p_{y,\pi^-})$$

$$\frac{\partial H(\vec{\alpha})}{\partial p_{z,i}} = 2(E_{p_2} + E_{\pi^-})\,\frac{p_{z,i}}{E_i} - 2(p_{z,p_2} + p_{z,\pi^-})$$

Missing mass constraint

In the following expressions, the subscript “i” stands for the particles p_1 and K^+.

Constraint equation*

$$H(\vec{\alpha}) = 0 = (E_{p_b} + E_{p_t} - E_{p_1} - E_{K^+})^2 - (\vec{p}_{p_b} + \vec{p}_{p_t} - \vec{p}_{p_1} - \vec{p}_{K^+})^2 - M_\Lambda^2$$

D-matrix elements in spherical coordinates

$$\begin{aligned}
\frac{\partial H(\vec{\alpha})}{\partial (1/p)_i} = \quad & 2(E_{p_b} + E_{p_t} - E_{p_1} - E_{K^+})\,\frac{p_i^3}{E_i} && \text{(A.6)}\\
& -2(p_{x,p_b} + p_{x,p_t} - p_{x,p_1} - p_{x,K^+})\,p_i p_{x,i} && \text{(A.7)}\\
& -2(p_{y,p_b} + p_{y,p_t} - p_{y,p_1} - p_{y,K^+})\,p_i p_{y,i} && \text{(A.8)}\\
& -2(p_{z,p_b} + p_{z,p_t} - p_{z,p_1} - p_{z,K^+})\,p_i p_{z,i} && \text{(A.9)}
\end{aligned}$$

$$\begin{aligned}
\frac{\partial H(\vec{\alpha})}{\partial \theta_i} = & -2(E_{p_b} + E_{p_t} - E_{p_1} - E_{K^+})\,\frac{p_i}{E_i}\,(p_{x,i}cos\theta_i cos\varphi_i + p_{y,i}cos\theta_i sin\varphi_i - p_{z,i}sin\theta_i) && \text{(A.10)}\\
& 2(p_{x,p_b} + p_{x,p_t} - p_{x,p_1} - p_{x,K^+})\,p_i cos\theta_i cos\varphi_i && \text{(A.11)}\\
& 2(p_{y,p_b} + p_{y,p_t} - p_{y,p_1} - p_{y,K^+})\,p_i cos\theta_i sin\varphi_i && \text{(A.12)}\\
& -2(p_{z,p_b} + p_{z,p_t} - p_{z,p_1} - p_{z,K^+})\,p_i sin\theta_i && \text{(A.13)}
\end{aligned}$$

$$\begin{aligned}
\frac{\partial H(\vec{\alpha})}{\partial \varphi_i} = & -2(p_{x,p_b} + p_{x,p_t} - p_{x,p_1} - p_{x,K^+})\,p_{y,i} && \text{(A.14)}\\
& +2(p_{y,p_b} + p_{y,p_t} - p_{y,p_1} - p_{y,K^+})\,p_{x,i} && \text{(A.15)}
\end{aligned}$$

D-matrix elements in Cartesian coordinates

$$\frac{\partial H(\vec{\alpha})}{\partial p_{x,i}} = -2(E_{p_b} + E_{p_t} - E_{p_1} - E_{K^+})\,\frac{p_{x,i}}{E_i} + 2(p_{x,p_b} + p_{x,p_t} - p_{x,p_1} - p_{x,K^+})$$

$$\frac{\partial H(\vec{\alpha})}{\partial p_{y,i}} = -2(E_{p_b} + E_{p_t} - E_{p_1} - E_{K^+})\,\frac{p_{y,i}}{E_i} + 2(p_{y,p_b} + p_{y,p_t} - p_{y,p_1} - p_{y,K^+})$$

$$\frac{\partial H(\vec{\alpha})}{\partial p_{z,i}} = -2(E_{p_b} + E_{p_t} - E_{p_1} - E_{K^+})\,\frac{p_{z,i}}{E_i} + 2(p_{z,p_b} + p_{z,p_t} - p_{z,p_1} - p_{z,K^+})$$

Energy and momentum conservation constraint

In the following expressions, the subscript “i” refers to all 4 particles (p_1, K^+, p_2, π^-).

Constraint equation*s

$$H_1(\vec{\alpha}) = 0 = E_{p_b} + E_{p_t} - E_{p_1} - E_{K^+} - E_{p_2} - E_{\pi^-} \tag{A.16}$$

$$H_2(\vec{\alpha}) = 0 = p_{x,p_b} + p_{x,p_t} - p_{x,p_1} - p_{x,K^+} - p_{x,p_2} - p_{x,\pi^-} \tag{A.17}$$

$$H_3(\vec{\alpha}) = 0 = p_{y,p_b} + p_{y,p_t} - p_{y,p_1} - p_{y,K^+} - p_{y,p_2} - p_{y,\pi^-} \tag{A.18}$$

$$H_4(\vec{\alpha}) = 0 = p_{z,p_b} + p_{z,p_t} - p_{z,p_1} - p_{z,K^+} - p_{z,p_2} - p_{z,\pi^-} \tag{A.19}$$

D-matrix elements in spherical coordinates

$$\frac{\partial H_1(\vec{\alpha})}{\partial(1/p)_i} = \frac{p_i^3}{E_i}$$

$$\frac{\partial H_1(\vec{\alpha})}{\partial\theta_i} = -\frac{p_i}{E_i}\left(p_{x,i}cos\theta_i cos\varphi_i + p_{y,i}cos\theta_i sin\varphi_i - p_{z,i}sin\theta_i\right)$$

$$\frac{\partial H_1(\vec{\alpha})}{\partial\varphi_i} = 0$$

$$\frac{\partial H_2(\vec{\alpha})}{\partial(1/p)_i} = p_i^2 sin\theta_i cos\varphi_i = p_i p_{x,i}$$

$$\frac{\partial H_2(\vec{\alpha})}{\partial\theta_i} = -p_i cos\theta_i cos\varphi_i$$

$$\frac{\partial H_2(\vec{\alpha})}{\partial\varphi_i} = p_i sin\theta_i sin\varphi_i = p_{y,i}$$

$$\frac{\partial H_3(\vec{\alpha})}{\partial(1/p)_i} = p_i^2 sin\theta_i sin\varphi_i = p_i p_{y,i}$$

$$\frac{\partial H_3(\vec{\alpha})}{\partial\theta_i} = -p_i cos\theta_i sin\varphi_i$$

$$\frac{\partial H_3(\vec{\alpha})}{\partial\varphi_i} = -p_i sin\theta_i cos\varphi_i = -p_{x,i}$$

$$\frac{\partial H_4(\vec{\alpha})}{\partial(1/p)_i} = p_i^2 cos\theta_i = p_i p_{z,i}$$

$$\frac{\partial H_4(\vec{\alpha})}{\partial \theta_i} = p_i sin\theta_i$$

$$\frac{\partial H_4(\vec{\alpha})}{\partial \varphi_i} = 0$$

D-matrix elements in Cartesian coordinates

$$\begin{array}{lll}
\frac{\partial H_1(\vec{\alpha})}{\partial p_{x,i}} = -\frac{p_{x,i}}{E_i} & \frac{\partial H_1(\vec{\alpha})}{\partial p_{y,i}} = -\frac{p_{y,i}}{E_i} & \frac{\partial H_1(\vec{\alpha})}{\partial p_{z,i}} = -\frac{p_{z,i}}{E_i} \\
\frac{\partial H_2(\vec{\alpha})}{\partial p_{x,i}} = -1 & \frac{\partial H_2(\vec{\alpha})}{\partial p_{y,i}} = \quad 0 & \frac{\partial H_2(\vec{\alpha})}{\partial p_{z,i}} = \quad 0 \\
\frac{\partial H_3(\vec{\alpha})}{\partial p_{x,i}} = \quad 0 & \frac{\partial H_3(\vec{\alpha})}{\partial p_{y,i}} = -1 & \frac{\partial H_3(\vec{\alpha})}{\partial p_{z,i}} = \quad 0 \\
\frac{\partial H_4(\vec{\alpha})}{\partial p_{x,i}} = \quad 0 & \frac{\partial H_4(\vec{\alpha})}{\partial p_{y,i}} = \quad 0 & \frac{\partial H_4(\vec{\alpha})}{\partial p_{z,i}} = -1
\end{array}$$

Intersection constraint

In the following expressions, the subscript “i” stands for the particles p_2 and π^-.

Constraint equation*s

$$H_1(\vec{\alpha},\vec{z}_\Lambda) = 0 = x_{x,p_2} - x_{x,\pi^-} + C_{p_2}\frac{d_{p_2}}{p_{p_2}}p_{x,p_2} - C_{\pi^-}\frac{d_{\pi^-}}{p_{\pi^-}}p_{x,\pi^-} \tag{A.20}$$

$$H_2(\vec{\alpha},\vec{z}_\Lambda) = 0 = x_{y,p_2} - x_{y,\pi^-} + C_{p_2}\frac{d_{p_2}}{p_{p_2}}p_{y,p_2} - C_{\pi^-}\frac{d_{\pi^-}}{p_{\pi^-}}p_{y,\pi^-} \tag{A.21}$$

$$H_3(\vec{\alpha},\vec{z}_\Lambda) = 0 = x_{z,p_2} - x_{z,\pi^-} + C_{p_2}\frac{d_{p_2}}{p_{p_2}}p_{z,p_2} - C_{\pi^-}\frac{d_{\pi^-}}{p_{\pi^-}}p_{z,\pi^-} \tag{A.22}$$

with

$$d_i = |\vec{z}_\Lambda - \vec{x}_i| = \sqrt{(z_{\Lambda,x} - x_{x,i})^2 + (z_{\Lambda,y} - x_{y,i})^2 + (z_{\Lambda,z} - x_{z,i})^2} \tag{A.23}$$

$$= \Big[(R_{\vec{z}} sin\theta_{\vec{z}} cos\varphi_{\vec{z}} - R_{\vec{x},i} sin\theta_{\vec{x},i} cos\varphi_{\vec{x},i})^2 \tag{A.24}$$

$$+\ (R_{\vec{z}} sin\theta_{\vec{z}} sin\varphi_{\vec{z}} - R_{\vec{x},i} sin\theta_{\vec{x},i} sin\varphi_{\vec{x},i})^2 \tag{A.25}$$

$$+\ (R_{\vec{z}} cos\theta_{\vec{z}} - R_{\vec{x},i} cos\theta_{\vec{x},i})^2\Big]^{1/2} \tag{A.26}$$

and

$$C_i = \frac{z_{\Lambda,z} - x_{z,i}}{\sqrt{(z_{\Lambda,z} - x_{z,i})^2}} = \begin{cases} +1 & \text{if } x_{z,i} < z_{\Lambda,z} \\ -1 & \text{if } x_{z,i} > z_{\Lambda,z} \end{cases}$$

D-matrix elements in spherical coordinates

The leading signs of the following D-matrix elements depend on the signs in front of the respective parameters in the constraint equations (i.e. “±” refers to “+” for $i = p_2$ and to “−” for $i = \pi^-$).

$$\frac{\partial H_1(\vec{\alpha},\vec{z}_\Lambda)}{\partial(1/p)_i} = \quad 0$$

$$\frac{\partial H_1(\vec{\alpha},\vec{z}_\Lambda)}{\partial\theta_i} = \pm\, C_i d_i cos\theta_i \left[cos\varphi_i - \frac{p_{x,i}}{p_i^2}(p_{x,i}cos\varphi_i + p_{y,i}sin\varphi_i - p_{z,i}tan\theta_i)\right]$$

$$\frac{\partial H_1(\vec{\alpha},\vec{z}_\Lambda)}{\partial\varphi_i} = \mp\, C_i d_i \frac{p_{y,i}}{p_i}$$

$$\frac{\partial H_1(\vec{\alpha},\vec{z}_\Lambda)}{\partial R_{\vec{x},i}} = \pm\ sin\theta_{\vec{x},i}cos\varphi_{\vec{x},i}\ \mp\ C_i\frac{p_{x,i}}{p_id_i}\,[(z_{\Lambda,x}-x_{x,i})sin\theta_{\vec{x},i}cos\varphi_{\vec{x},i} \tag{A.27}$$

$$+\ (z_{\Lambda,y}-x_{y,i})sin\theta_{\vec{x},i}sin\varphi_{\vec{x},i}+(z_{\Lambda,z}-x_{z,i})cos\theta_{\vec{x},i}] \tag{A.28}$$

$$\frac{\partial H_1(\vec{\alpha},\vec{z}_\Lambda)}{\partial \theta_{\vec{x},i}} = \pm\ R_{\vec{x},i}cos\theta_{\vec{x},i}cos\varphi_{\vec{x},i}\ \mp\ C_i\frac{R_{\vec{x},i}p_{x,i}}{p_id_i}\,[(z_{\Lambda,x}-x_{x,i})cos\theta_{\vec{x},i}cos\varphi_{\vec{x},i} \tag{A.29}$$

$$+\ (z_{\Lambda,y}-x_{y,i})cos\theta_{\vec{x},i}sin\varphi_{\vec{x},i}-(z_{\Lambda,z}-x_{z,i})sin\theta_{\vec{x},i}] \tag{A.30}$$

$$\frac{\partial H_1(\vec{\alpha},\vec{z}_\Lambda)}{\partial \varphi_{\vec{x},i}} = \mp\, x_{y,i}\pm\ C_i\frac{p_{x,i}}{p_id_i}\,[(z_{\Lambda,x}-x_{x,i})x_{y,i}\ -\ (z_{\Lambda,y}-x_{y,i})x_{x,i}]$$

$$\frac{\partial H_2(\vec{\alpha},\vec{z}_\Lambda)}{\partial (1/p)_i} = \quad 0$$

$$\frac{\partial H_2(\vec{\alpha},\vec{z}_\Lambda)}{\partial \theta_i} = \pm\, C_id_icos\theta_i\left[sin\varphi_i-\frac{p_{y,i}}{p_i^2}(p_{x,i}cos\varphi_i+p_{y,i}sin\varphi_i-p_{z,i}tan\theta_i)\right]$$

$$\frac{\partial H_2(\vec{\alpha},\vec{z}_\Lambda)}{\partial \varphi_i} = \pm\, C_id_i\frac{p_{x,i}}{p_i}$$

$$\frac{\partial H_2(\vec{\alpha},\vec{z}_\Lambda)}{\partial R_{\vec{x},i}} = \pm\ sin\theta_{\vec{x},i}sin\varphi_{\vec{x},i}\ \mp\ C_i\frac{p_{y,i}}{p_id_i}\,[(z_{\Lambda,x}-x_{x,i})sin\theta_{\vec{x},i}cos\varphi_{\vec{x},i} \tag{A.31}$$

$$+\ (z_{\Lambda,y}-x_{y,i})sin\theta_{\vec{x},i}sin\varphi_{\vec{x},i}+(z_{\Lambda,z}-x_{z,i})cos\theta_{\vec{x},i}] \tag{A.32}$$

$$\frac{\partial H_2(\vec{\alpha},\vec{z}_\Lambda)}{\partial \theta_{\vec{x},i}} = \pm\ R_{\vec{x},i}cos\theta_{\vec{x},i}sin\varphi_{\vec{x},i}\ \mp\ C_i\frac{R_{\vec{x},i}p_{y,i}}{p_id_i}\,[(z_{\Lambda,x}-x_{x,i})cos\theta_{\vec{x},i}cos\varphi_{\vec{x},i} \tag{A.33}$$

$$+\ (z_{\Lambda,y}-x_{y,i})cos\theta_{\vec{x},i}sin\varphi_{\vec{x},i}-(z_{\Lambda,z}-x_{z,i})sin\theta_{\vec{x},i}] \tag{A.34}$$

$$\frac{\partial H_2(\vec{\alpha},\vec{z}_\Lambda)}{\partial \varphi_{\vec{x},i}} = \pm\, x_{x,i}\pm\ C_i\frac{p_{y,i}}{p_id_i}\,[(z_{\Lambda,x}-x_{x,i})x_{y,i}\ -\ (z_{\Lambda,y}-x_{y,i})x_{x,i}]$$

$$\frac{\partial H_3(\vec{\alpha},\vec{z}_\Lambda)}{\partial (1/p)_i} = \quad 0$$

$$\frac{\partial H_3(\vec{\alpha},\vec{z}_\Lambda)}{\partial \theta_i} = \mp\, C_id_icos\theta_i\left[tan\theta_i+\frac{p_{z,i}}{p_i^2}(p_{x,i}cos\varphi_i+p_{y,i}sin\varphi_i-p_{z,i}tan\theta_i)\right]$$

$$\frac{\partial H_3(\vec{\alpha},\vec{z}_\varLambda)}{\partial \varphi_i} = \quad 0$$

$$\frac{\partial H_3(\vec{\alpha},\vec{z}_\varLambda)}{\partial R_{\vec{x},i}} = \pm\ cos\theta_{\vec{x},i}\ \mp\ C_i\frac{p_{z,i}}{p_i d_i}\left[(z_{\varLambda,x}-x_{x,i})sin\theta_{\vec{x},i}cos\varphi_{\vec{x},i}\right. \tag{A.35}$$

$$\left.+\ (z_{\varLambda,y}-x_{y,i})sin\theta_{\vec{x},i}sin\varphi_{\vec{x},i}+(z_{\varLambda,z}-x_{z,i})cos\theta_{\vec{x},i}\right] \tag{A.36}$$

$$\frac{\partial H_3(\vec{\alpha},\vec{z}_\varLambda)}{\partial \theta_{\vec{x},i}} = \mp\ R_{\vec{x},i}sin\theta_{\vec{x},i}\ \mp\ C_i\frac{R_{\vec{x},i}p_{z,i}}{p_i d_i}\left[(z_{\varLambda,x}-x_{x,i})cos\theta_{\vec{x},i}cos\varphi_{\vec{x},i}\right. \tag{A.37}$$

$$\left.+\ (z_{\varLambda,y}-x_{y,i})cos\theta_{\vec{x},i}sin\varphi_{\vec{x},i}-(z_{\varLambda,z}-x_{z,i})sin\theta_{\vec{x},i}\right] \tag{A.38}$$

$$\frac{\partial H_3(\vec{\alpha},\vec{z}_\varLambda)}{\partial \varphi_{\vec{x},i}} = \pm\, C_i\frac{p_{z,i}}{p_i d_i}\left[(z_{\varLambda,x}-x_{x,i})x_{y,i}\ -\ (z_{\varLambda,y}-x_{y,i})x_{x,i}\right]$$

E-matrix elements in spherical coordinates

$$\frac{\partial H_1(\vec{\alpha},\vec{z}_\varLambda)}{\partial R_{\vec{z}}} = C_{p_2}\frac{p_{x,p_2}}{p_{p_2}d_{p_2}}\left[(z_{\varLambda,x}-x_{x,p_2})sin\theta_{\vec{z}}cos\varphi_{\vec{z}}\right. \tag{A.39}$$

$$\left.+\ (z_{\varLambda,y}-x_{y,p_2})sin\theta_{\vec{z}}sin\varphi_{\vec{z}}+(z_{\varLambda,z}-x_{z,p_2})cos\theta_{\vec{z}}\right] \tag{A.40}$$

$$-\ C_{\pi^-}\frac{p_{x,\pi^-}}{p_{\pi^-}d_{\pi^-}}\left[(z_{\varLambda,x}-x_{x,\pi^-})sin\theta_{\vec{z}}cos\varphi_{\vec{z}}\right. \tag{A.41}$$

$$\left.+\ (z_{\varLambda,y}-x_{y,\pi^-})sin\theta_{\vec{z}}sin\varphi_{\vec{z}}+(z_{\varLambda,z}-x_{z,\pi^-})cos\theta_{\vec{z}}\right] \tag{A.42}$$

$$\frac{\partial H_1(\vec{\alpha},\vec{z}_\varLambda)}{\partial \theta_{\vec{z}}} = C_{p_2}\frac{R_{\vec{z}}p_{x,p_2}}{p_{p_2}d_{p_2}}\left[(z_{\varLambda,x}-x_{x,p_2})cos\theta_{\vec{z}}cos\varphi_{\vec{z}}\right. \tag{A.43}$$

$$\left.+\ (z_{\varLambda,y}-x_{y,p_2})cos\theta_{\vec{z}}sin\varphi_{\vec{z}}-(z_{\varLambda,z}-x_{z,p_2})sin\theta_{\vec{z}}\right] \tag{A.44}$$

$$-\ C_{\pi^-}\frac{R_{\vec{z}}p_{x,\pi^-}}{p_{\pi^-}d_{\pi^-}}\left[(z_{\varLambda,x}-x_{x,\pi^-})cos\theta_{\vec{z}}cos\varphi_{\vec{z}}\right. \tag{A.45}$$

$$\left.+\ (z_{\varLambda,y}-x_{y,\pi^-})cos\theta_{\vec{z}}sin\varphi_{\vec{z}}-(z_{\varLambda,z}-x_{z,\pi^-})sin\theta_{\vec{z}}\right] \tag{A.46}$$

$$\frac{\partial H_1(\vec{\alpha},\vec{z}_\varLambda)}{\partial \varphi_{\vec{z}}} = C_{p_2}\frac{p_{x,p_2}}{p_{p_2}d_{p_2}}\left[(z_{\varLambda,y}-x_{y,p_2})z_{\varLambda,x}-(z_{\varLambda,x}-x_{x,p_2})z_{\varLambda,y}\right] \tag{A.47}$$

$$-\ C_{\pi^-}\frac{p_{x,\pi^-}}{p_{\pi^-}d_{\pi^-}}\left[(z_{\varLambda,y}-x_{y,\pi^-})z_{\varLambda,x}-(z_{\varLambda,x}-x_{x,\pi^-})z_{\varLambda,y}\right] \tag{A.48}$$

$$\frac{\partial H_2(\vec{\alpha},\vec{z}_\Lambda)}{\partial R_{\vec{z}}} = C_{p2}\frac{p_{y,p2}}{p_{p2}d_{p2}}\left[(z_{\Lambda,x} - x_{x,p_2})sin\theta_{\vec{z}}cos\varphi_{\vec{z}}\right. \tag{A.49}$$

$$\left. + \ (z_{\Lambda,y} - x_{y,p_2})sin\theta_{\vec{z}}sin\varphi_{\vec{z}} + (z_{\Lambda,z} - x_{z,p_2})cos\theta_{\vec{z}}\right] \tag{A.50}$$

$$- \ C_{\pi^-}\frac{p_{y,\pi^-}}{p_{\pi^-}d_{\pi^-}}\left[(z_{\Lambda,x} - x_{x,\pi^-})sin\theta_{\vec{z}}cos\varphi_{\vec{z}}\right. \tag{A.51}$$

$$\left. + \ (z_{\Lambda,y} - x_{y,\pi^-})sin\theta_{\vec{z}}sin\varphi_{\vec{z}} + (z_{\Lambda,z} - x_{z,\pi^-})cos\theta_{\vec{z}}\right] \tag{A.52}$$

$$\frac{\partial H_2(\vec{\alpha},\vec{z}_\Lambda)}{\partial \theta_{\vec{z}}} = C_{p2}\frac{R_{\vec{z}}p_{y,p2}}{p_{p2}d_{p2}}\left[(z_{\Lambda,x} - x_{x,p_2})cos\theta_{\vec{z}}cos\varphi_{\vec{z}}\right. \tag{A.53}$$

$$\left. + \ (z_{\Lambda,y} - x_{y,p_2})cos\theta_{\vec{z}}sin\varphi_{\vec{z}} - (z_{\Lambda,z} - x_{z,p_2})sin\theta_{\vec{z}}\right] \tag{A.54}$$

$$- \ C_{\pi^-}\frac{R_{\vec{z}}p_{y,\pi^-}}{p_{\pi^-}d_{\pi^-}}\left[(z_{\Lambda,x} - x_{x,\pi^-})cos\theta_{\vec{z}}cos\varphi_{\vec{z}}\right. \tag{A.55}$$

$$\left. + \ (z_{\Lambda,y} - x_{y,\pi^-})cos\theta_{\vec{z}}sin\varphi_{\vec{z}} - (z_{\Lambda,z} - x_{z,\pi^-})sin\theta_{\vec{z}}\right] \tag{A.56}$$

$$\frac{\partial H_2(\vec{\alpha},\vec{z}_\Lambda)}{\partial \varphi_{\vec{z}}} = C_{p2}\frac{p_{y,p2}}{p_{p2}d_{p2}}\left[(z_{\Lambda,y} - x_{y,p_2})z_{\Lambda,x} - (z_{\Lambda,x} - x_{x,p_2})z_{\Lambda,y}\right] \tag{A.57}$$

$$- \ C_{\pi^-}\frac{p_{y,\pi^-}}{p_{\pi^-}d_{\pi^-}}\left[(z_{\Lambda,y} - x_{y,\pi^-})z_{\Lambda,x} - (z_{\Lambda,x} - x_{x,\pi^-})z_{\Lambda,y}\right] \tag{A.58}$$

$$\frac{\partial H_3(\vec{\alpha},\vec{z}_\Lambda)}{\partial R_{\vec{z}}} = C_{p2}\frac{p_{z,p2}}{p_{p2}d_{p2}}\left[(z_{\Lambda,x} - x_{x,p_2})sin\theta_{\vec{z}}cos\varphi_{\vec{z}}\right. \tag{A.59}$$

$$\left. + \ (z_{\Lambda,y} - x_{y,p_2})sin\theta_{\vec{z}}sin\varphi_{\vec{z}} + (z_{\Lambda,z} - x_{z,p_2})cos\theta_{\vec{z}}\right] \tag{A.60}$$

$$- \ C_{\pi^-}\frac{p_{z,\pi^-}}{p_{\pi^-}d_{\pi^-}}\left[(z_{\Lambda,x} - x_{x,\pi^-})sin\theta_{\vec{z}}cos\varphi_{\vec{z}}\right. \tag{A.61}$$

$$\left. + \ (z_{\Lambda,y} - x_{y,\pi^-})sin\theta_{\vec{z}}sin\varphi_{\vec{z}} + (z_{\Lambda,z} - x_{z,\pi^-})cos\theta_{\vec{z}}\right] \tag{A.62}$$

$$\frac{\partial H_3(\vec{\alpha},\vec{z}_\Lambda)}{\partial \theta_{\vec{z}}} = C_{p2}\frac{R_{\vec{z}}p_{z,p2}}{p_{p2}d_{p2}}\left[(z_{\Lambda,x} - x_{x,p_2})cos\theta_{\vec{z}}cos\varphi_{\vec{z}}\right. \tag{A.63}$$

$$\left. + \ (z_{\Lambda,y} - x_{y,p_2})cos\theta_{\vec{z}}sin\varphi_{\vec{z}} - (z_{\Lambda,z} - x_{z,p_2})sin\theta_{\vec{z}}\right] \tag{A.64}$$

$$- \ C_{\pi^-}\frac{R_{\vec{z}}p_{z,\pi^-}}{p_{\pi^-}d_{\pi^-}}\left[(z_{\Lambda,x} - x_{x,\pi^-})cos\theta_{\vec{z}}cos\varphi_{\vec{z}}\right. \tag{A.65}$$

$$\left. + \ (z_{\Lambda,y} - x_{y,\pi^-})cos\theta_{\vec{z}}sin\varphi_{\vec{z}} - (z_{\Lambda,z} - x_{z,\pi^-})sin\theta_{\vec{z}}\right] \tag{A.66}$$

$$\frac{\partial H_3(\vec{\alpha},\vec{z}_\Lambda)}{\partial \varphi_{\vec{z}}} = C_{p2}\frac{p_{z,p2}}{p_{p2}d_{p2}}\left[(z_{\Lambda,y} - x_{y,p_2})z_{\Lambda,x} - (z_{\Lambda,x} - x_{x,p_2})z_{\Lambda,y}\right] \tag{A.67}$$

$$- \ C_{\pi^-}\frac{p_{z,\pi^-}}{p_{\pi^-}d_{\pi^-}}\left[(z_{\Lambda,y} - x_{y,\pi^-})z_{\Lambda,x} - (z_{\Lambda,x} - x_{x,\pi^-})z_{\Lambda,y}\right] \tag{A.68}$$

D-matrix elements in Cartesian coordinates

The leading signs of the following D-matrix elements depend on the signs in front of the respective parameters in the constraint equations (i.e. “$\pm$” refers to “$+$” for $i = p_2$ and to “$-$” for $i = \pi^-$).

$$\frac{\partial H_1(\vec{\alpha},\vec{z}_\Lambda)}{\partial p_{x,i}} = \pm\, C_i \frac{d_i}{p_i}\left(1 - \frac{p_{x,i}^2}{p_i^2}\right)$$

$$\frac{\partial H_1(\vec{\alpha},\vec{z}_\Lambda)}{\partial p_{y,i}} = \mp\, C_i d_i \frac{p_{x,i} p_{y,i}}{p_i^3}$$

$$\frac{\partial H_1(\vec{\alpha},\vec{z}_\Lambda)}{\partial p_{z,i}} = \mp\, C_i d_i \frac{p_{x,i} p_{z,i}}{p_i^3}$$

$$\frac{\partial H_1(\vec{\alpha},\vec{z}_\Lambda)}{\partial x_{x,i}} = \pm\,\left(1 - C_i \frac{p_{x,i}}{p_i}\frac{(z_{\Lambda,x} - x_{x,i})}{d_i}\right)$$

$$\frac{\partial H_1(\vec{\alpha},\vec{z}_\Lambda)}{\partial x_{y,i}} = \mp\, C_i \frac{p_{x,i}}{p_i}\frac{(z_{\Lambda,y} - x_{y,i})}{d_i}$$

$$\frac{\partial H_1(\vec{\alpha},\vec{z}_\Lambda)}{\partial x_{z,i}} = \mp\, C_i \frac{p_{x,i}}{p_i}\frac{(z_{\Lambda,z} - x_{z,i})}{d_i}$$

$$\frac{\partial H_2(\vec{\alpha},\vec{z}_\Lambda)}{\partial p_{x,i}} = \mp\, C_i d_i \frac{p_{y,i} p_{x,i}}{p_i^3}$$

$$\frac{\partial H_2(\vec{\alpha},\vec{z}_\Lambda)}{\partial p_{y,i}} = \pm\, C_i \frac{d_i}{p_i}\left(1 - \frac{p_{y,i}^2}{p_i^2}\right)$$

$$\frac{\partial H_2(\vec{\alpha},\vec{z}_\Lambda)}{\partial p_{z,i}} = \mp\, C_i d_i \frac{p_{y,i} p_{z,i}}{p_i^3}$$

$$\frac{\partial H_2(\vec{\alpha},\vec{z}_\Lambda)}{\partial x_{x,i}} = \mp\, C_i \frac{p_{y,i}}{p_i}\frac{(z_{\Lambda,x} - x_{x,i})}{d_i}$$

$$\frac{\partial H_2(\vec{\alpha},\vec{z}_\Lambda)}{\partial x_{y,i}} = \pm\,\left(1 - C_i \frac{p_{y,i}}{p_i}\frac{(z_{\Lambda,y} - x_{y,i})}{d_i}\right)$$

$$\frac{\partial H_2(\vec{\alpha},\vec{z}_\Lambda)}{\partial x_{z,i}} = \mp\, C_i \frac{p_{y,i}}{p_i}\frac{(z_{\Lambda,z} - x_{z,i})}{d_i}$$

$$\frac{\partial H_3(\vec{\alpha},\vec{z}_\Lambda)}{\partial p_{x,i}} = \mp\, C_i d_i \frac{p_{z,i} p_{x,i}}{p_i^3}$$

$$\frac{\partial H_3(\vec{\alpha},\vec{z}_\Lambda)}{\partial p_{y,i}} = \mp\, C_i d_i \frac{p_{z,i} p_{y,i}}{p_i^3}$$

$$\frac{\partial H_3(\vec{\alpha},\vec{z}_\Lambda)}{\partial p_{z,i}} = \mp\, C_i \frac{d_i}{p_i}\left(1-\frac{p_{z,i}^2}{p_i^2}\right)$$

$$\frac{\partial H_3(\vec{\alpha},\vec{z}_\Lambda)}{\partial x_{x,i}} = \mp\, C_i \frac{p_{z,i}}{p_i}\frac{(z_{\Lambda,x}-x_{x,i})}{d_i}$$

$$\frac{\partial H_3(\vec{\alpha},\vec{z}_\Lambda)}{\partial x_{y,i}} = \mp\, C_i \frac{p_{z,i}}{p_i}\frac{(z_{\Lambda,y}-x_{y,i})}{d_i}$$

$$\frac{\partial H_3(\vec{\alpha},\vec{z}_\Lambda)}{\partial x_{z,i}} = \pm\,\left(1-C_i \frac{p_{z,i}}{p_i}\frac{(z_{\Lambda,z}-x_{z,i})}{d_i}\right)$$

E-matrix elements in Cartesian coordinates

$$\frac{\partial H_1(\vec{\alpha},\vec{z}_\Lambda)}{\partial z_{\Lambda,x}} = C_{p_2}\frac{p_{x,p_2}}{p_{p_2}}\frac{(z_{\Lambda,x}-x_{x,p_2})}{d_{p_2}} - C_{\pi^-}\frac{p_{x,\pi^-}}{p_{\pi^-}}\frac{(z_{\Lambda,x}-x_{x,\pi^-})}{d_{\pi^-}}$$

$$\frac{\partial H_1(\vec{\alpha},\vec{z}_\Lambda)}{\partial z_{\Lambda,y}} = C_{p_2}\frac{p_{x,p_2}}{p_{p_2}}\frac{(z_{\Lambda,y}-x_{y,p_2})}{d_{p_2}} - C_{\pi^-}\frac{p_{x,\pi^-}}{p_{\pi^-}}\frac{(z_{\Lambda,y}-x_{y,\pi^-})}{d_{\pi^-}}$$

$$\frac{\partial H_1(\vec{\alpha},\vec{z}_\Lambda)}{\partial z_{\Lambda,z}} = C_{p_2}\frac{p_{x,p_2}}{p_{p_2}}\frac{(z_{\Lambda,z}-x_{z,p_2})}{d_{p_2}} - C_{\pi^-}\frac{p_{x,\pi^-}}{p_{\pi^-}}\frac{(z_{\Lambda,z}-x_{z,\pi^-})}{d_{\pi^-}}$$

$$\frac{\partial H_2(\vec{\alpha},\vec{z}_\Lambda)}{\partial z_{\Lambda,x}} = C_{p_2}\frac{p_{y,p_2}}{p_{p_2}}\frac{(z_{\Lambda,x}-x_{x,p_2})}{d_{p_2}} - C_{\pi^-}\frac{p_{y,\pi^-}}{p_{\pi^-}}\frac{(z_{\Lambda,x}-x_{x,\pi^-})}{d_{\pi^-}}$$

$$\frac{\partial H_2(\vec{\alpha},\vec{z}_\Lambda)}{\partial z_{\Lambda,y}} = C_{p_2}\frac{p_{y,p_2}}{p_{p_2}}\frac{(z_{\Lambda,y}-x_{y,p_2})}{d_{p_2}} - C_{\pi^-}\frac{p_{y,\pi^-}}{p_{\pi^-}}\frac{(z_{\Lambda,y}-x_{y,\pi^-})}{d_{\pi^-}}$$

$$\frac{\partial H_2(\vec{\alpha},\vec{z}_\Lambda)}{\partial z_{\Lambda,z}} = C_{p_2}\frac{p_{y,p_2}}{p_{p_2}}\frac{(z_{\Lambda,z}-x_{z,p_2})}{d_{p_2}} - C_{\pi^-}\frac{p_{y,\pi^-}}{p_{\pi^-}}\frac{(z_{\Lambda,z}-x_{z,\pi^-})}{d_{\pi^-}}$$

$$\frac{\partial H_3(\vec{\alpha},\vec{z}_\Lambda)}{\partial z_{\Lambda,x}} = C_{p_2}\frac{p_{z,p_2}}{p_{p_2}}\frac{(z_{\Lambda,x}-x_{x,p_2})}{d_{p_2}} - C_{\pi^-}\frac{p_{z,\pi^-}}{p_{\pi^-}}\frac{(z_{\Lambda,x}-x_{x,\pi^-})}{d_{\pi^-}}$$

$$\frac{\partial H_3(\vec{\alpha},\vec{z}_\Lambda)}{\partial z_{\Lambda,y}} = C_{p_2}\frac{p_{z,p_2}}{p_{p_2}}\frac{(z_{\Lambda,y}-x_{y,p_2})}{d_{p_2}} - C_{\pi^-}\frac{p_{z,\pi^-}}{p_{\pi^-}}\frac{(z_{\Lambda,y}-x_{y,\pi^-})}{d_{\pi^-}}$$

$$\frac{\partial H_3(\vec{\alpha},\vec{z}_\Lambda)}{\partial z_{\Lambda,z}} = C_{p_2}\frac{p_{z,p_2}}{p_{p_2}}\frac{(z_{\Lambda,z}-x_{z,p_2})}{d_{p_2}} - C_{\pi^-}\frac{p_{z,\pi^-}}{p_{\pi^-}}\frac{(z_{\Lambda,z}-x_{z,\pi^-})}{d_{\pi^-}}$$

Secondary vertex constraint

Constraint equation*s

Intersection of p_2 and π^- in $\vec{z}_\Lambda$:

$$H_1(\vec{\alpha},\vec{z}_\Lambda,\vec{z}_{Prim}) = 0 = x_{x,p_2} - x_{x,\pi^-} + C_{p_2}\frac{d_{p_2}}{p_{p_2}}p_{x,p_2} - C_{\pi^-}\frac{d_{\pi^-}}{p_{\pi^-}}p_{x,\pi^-} \tag{A.69}$$

$$H_2(\vec{\alpha},\vec{z}_\Lambda,\vec{z}_{Prim}) = 0 = x_{y,p_2} - x_{y,\pi^-} + C_{p_2}\frac{d_{p_2}}{p_{p_2}}p_{y,p_2} - C_{\pi^-}\frac{d_{\pi^-}}{p_{\pi^-}}p_{y,\pi^-} \tag{A.70}$$

$$H_3(\vec{\alpha},\vec{z}_\Lambda,\vec{z}_{Prim}) = 0 = x_{z,p_2} - x_{z,\pi^-} + C_{p_2}\frac{d_{p_2}}{p_{p_2}}p_{z,p_2} - C_{\pi^-}\frac{d_{\pi^-}}{p_{\pi^-}}p_{z,\pi^-} \tag{A.71}$$

Intersection of p_1 and Λ in $\vec{z}_{Prim}$:

$$H_4(\vec{\alpha},\vec{z}_\Lambda,\vec{z}_{Prim}) = 0 = x_{x,p_1} - z_{\Lambda,x} + C_{p_1}\frac{d_{p_1}}{p_{p_1}}p_{x,p_1} - C_\Lambda\frac{d_\Lambda}{|\vec{p}_{p_2} + \vec{p}_{\pi^-}|}(p_{x,p_2} + p_{x,\pi^-}) \tag{A.72}$$

$$H_5(\vec{\alpha},\vec{z}_\Lambda,\vec{z}_{Prim}) = 0 = x_{y,p_1} - z_{\Lambda,y} + C_{p_1}\frac{d_{p_1}}{p_{p_1}}p_{y,p_1} - C_\Lambda\frac{d_\Lambda}{|\vec{p}_{p_2} + \vec{p}_{\pi^-}|}(p_{y,p_2} + p_{y,\pi^-}) \tag{A.73}$$

$$H_6(\vec{\alpha},\vec{z}_\Lambda,\vec{z}_{Prim}) = 0 = x_{z,p_1} - z_{\Lambda,z} + C_{p_1}\frac{d_{p_1}}{p_{p_1}}p_{z,p_1} - C_\Lambda\frac{d_\Lambda}{|\vec{p}_{p_2} + \vec{p}_{\pi^-}|}(p_{z,p_2} + p_{z,\pi^-}) \tag{A.74}$$

Intersection of K^+ and Λ in $\vec{z}_{Prim}$:

$$H_7(\vec{\alpha},\vec{z}_\Lambda,\vec{z}_{Prim}) = 0 = x_{x,K^+} - z_{\Lambda,x} + C_{K^+}\frac{d_{K^+}}{p_{K^+}}p_{x,K^+} - C_\Lambda\frac{d_\Lambda}{|\vec{p}_{p_2} + \vec{p}_{\pi^-}|}(p_{x,p_2} + p_{x,\pi^-}) \tag{A.75}$$

$$H_8(\vec{\alpha},\vec{z}_\Lambda,\vec{z}_{Prim}) = 0 = x_{y,K^+} - z_{\Lambda,y} + C_{K^+}\frac{d_{K^+}}{p_{K^+}}p_{y,K^+} - C_\Lambda\frac{d_\Lambda}{|\vec{p}_{p_2} + \vec{p}_{\pi^-}|}(p_{y,p_2} + p_{y,\pi^-}) \tag{A.76}$$

$$H_9(\vec{\alpha},\vec{z}_\Lambda,\vec{z}_{Prim}) = 0 = x_{z,K^+} - z_{\Lambda,z} + C_{K^+}\frac{d_{K^+}}{p_{K^+}}p_{z,K^+} - C_\Lambda\frac{d_\Lambda}{|\vec{p}_{p_2} + \vec{p}_{\pi^-}|}(p_{z,p_2} + p_{z,\pi^-}) \tag{A.77}$$

with

$$d_i = |\vec{z}_\Lambda - \vec{x}_i| = \sqrt{(z_{\Lambda,x} - x_{x,i})^2 + (z_{\Lambda,y} - x_{y,i})^2 + (z_{\Lambda,z} - x_{z,i})^2}$$

and

$$d_\Lambda = |\vec{z}_{Prim} - \vec{z}_\Lambda| = \sqrt{(z_{Prim,x} - z_{\Lambda,x})^2 + (z_{Prim,y} - z_{\Lambda,y})^2 + (z_{prim,z} - z_{\Lambda,z})^2}$$

The coefficients C_i and C_Λ are defined in the following way.

$$C_i = \frac{z_{Prim,z} - x_{z,i}}{\sqrt{(z_{Prim,z} - x_{z,i})^2}} = \begin{cases} +1 & \text{if } x_{z,i} < z_{Prim,z} \\ -1 & \text{if } x_{z,i} > z_{Prim,z} \end{cases}$$

$$C_\Lambda = \frac{z_{\Lambda,z} - z_{Prim,z}}{\sqrt{(z_{\Lambda,z} - z_{Prim,z})^2}} = \begin{cases} +1 & \text{if } z_{Prim,z} < z_{\Lambda,z} \\ -1 & \text{if } z_{Prim,z} > z_{\Lambda,z} \end{cases}$$

D-matrix elements in spherical coordinates

The D-matrix elements of the momentum parameters are shown for both coordinate systems, the derivatives of the emission point parameters are calculated in Cartesian coordinates only, since in the pp analysis, the mixed track representation $\vec{\alpha}_{mix}$ is used.
The derivatives of the constraint equations 1-3 with respect to the parameters of p_2 and π^- are equivalent to the expressions of the single intersection constraint. Therefore, they are not explicitly listed again.

Derivatives with respect to p_1 and K^+

In the following expressions, the subscript "i" stands for the particles p_1 and K^+.

$$\frac{\partial H_{4,7}(\vec{\alpha},\vec{z}_\Lambda,\vec{z}_{Prim})}{\partial(1/p)_i} = 0$$

$$\frac{\partial H_{4,7}(\vec{\alpha},\vec{z}_\Lambda,\vec{z}_{Prim})}{\partial\theta_i} = C_i d_i cos\theta_i \left[cos\varphi_i - \frac{p_{x,i}}{p_i^2}(p_{x,i}cos\varphi_i + p_{y,i}sin\varphi_i - p_{z,i}tan\theta_i) \right]$$

$$\frac{\partial H_{4,7}(\vec{\alpha},\vec{z}_\Lambda,\vec{z}_{Prim})}{\partial\varphi_i} = -C_i \frac{d_i p_{y,i}}{p_i}$$

$$\frac{\partial H_{5,8}(\vec{\alpha},\vec{z}_\Lambda,\vec{z}_{Prim})}{\partial(1/p)_i} = 0$$

$$\frac{\partial H_{5,8}(\vec{\alpha},\vec{z}_\Lambda,\vec{z}_{Prim})}{\partial\theta_i} = C_i d_i cos\theta_i \left[sin\varphi_i - \frac{p_{y,i}}{p_i^2}(p_{x,i}cos\varphi_i + p_{y,i}sin\varphi_i - p_{z,i}tan\theta_i) \right]$$

$$\frac{\partial H_{5,8}(\vec{\alpha},\vec{z}_\Lambda,\vec{z}_{Prim})}{\partial\varphi_i} = C_i \frac{d_i p_{x,i}}{p_i}$$

$$\frac{\partial H_{6,9}(\vec{\alpha},\vec{z}_\Lambda,\vec{z}_{Prim})}{\partial(1/p)_i} = 0$$

$$\frac{\partial H_{6,9}(\vec{\alpha},\vec{z}_{\Lambda},\vec{z}_{Prim})}{\partial \theta_i} = -C_i d_i cos\theta_i \left[tan\theta_i + \frac{p_{z,i}}{p_i^2}(p_{x,i}cos\varphi_i + p_{y,i}sin\varphi_i - p_{z,i}tan\theta_i) \right]$$

$$\frac{\partial H_{6,9}(\vec{\alpha},\vec{z}_{\Lambda},\vec{z}_{Prim})}{\partial \varphi_i} = 0$$

Derivatives with respect to p_2 and π^-

In the following expressions, the subscript “i” stands for the particles p_2 and π^-. The Λ momentum vector is defined as $\vec{p}_{\Lambda} = \vec{p}_{p_2} + \vec{p}_{\pi^-}$.

$$\frac{\partial H_{4,7}(\vec{\alpha},\vec{z}_{\Lambda},\vec{z}_{Prim})}{\partial (1/p)_i} = 0$$

$$\frac{\partial H_{4,7}(\vec{\alpha},\vec{z}_{\Lambda},\vec{z}_{Prim})}{\partial \theta_i} = -\, C_{\Lambda}\frac{d_{\Lambda}}{p_{\Lambda}} p_i cos\theta_i \left[cos\varphi_i \right. \tag{A.78}$$

$$\left. - \frac{p_{\Lambda,x}}{p_{\Lambda}^2}(p_{\Lambda,x}cos\varphi_i + p_{\Lambda,y}sin\varphi_i - p_{\Lambda,z}tan\theta_i) \right] \tag{A.79}$$

$$\frac{\partial H_{4,7}(\vec{\alpha},\vec{z}_{\Lambda},\vec{z}_{Prim})}{\partial \varphi_i} = C_{\Lambda}\frac{d_{\Lambda}}{p_{\Lambda}} p_{y,i} \left[1 + \frac{p_{\Lambda,x}}{p_{\Lambda}^2}(p_{\Lambda,y}artan\varphi_i - p_{\Lambda,x}) \right]$$

$$\frac{\partial H_{5,8}(\vec{\alpha},\vec{z}_{\Lambda},\vec{z}_{Prim})}{\partial (1/p)_i} = 0$$

$$\frac{\partial H_{5,8}(\vec{\alpha},\vec{z}_{\Lambda},\vec{z}_{Prim})}{\partial \theta_i} = -\, C_{\Lambda}\frac{d_{\Lambda}}{p_{\Lambda}} p_i cos\theta_i \left[sin\varphi_i \right. \tag{A.80}$$

$$\left. - \frac{p_{\Lambda,y}}{p_{\Lambda}^2}(p_{\Lambda,x}cos\varphi_i + p_{\Lambda,y}sin\varphi_i - p_{\Lambda,z}tan\theta_i) \right] \tag{A.81}$$

$$\frac{\partial H_{5,8}(\vec{\alpha},\vec{z}_{\Lambda},\vec{z}_{Prim})}{\partial \varphi_i} = C_{\Lambda}\frac{d_{\Lambda}}{p_{\Lambda}} p_{x,i} \left[1 + \frac{p_{\Lambda,y}}{p_{\Lambda}^2}(p_{\Lambda,y} - p_{\Lambda,x}tan\varphi_i) \right]$$

$$\frac{\partial H_{6,9}(\vec{\alpha},\vec{z}_{\Lambda},\vec{z}_{Prim})}{\partial (1/p)_i} = 0$$

$$\frac{\partial H_{6,9}(\vec{\alpha},\vec{z}_{\Lambda},\vec{z}_{Prim})}{\partial \theta_i} = C_{\Lambda}\frac{d_{\Lambda}}{p_{\Lambda}} p_i cos\theta_i \left[tan\theta_i \right. \tag{A.82}$$

$$\left. + \frac{p_{\Lambda,z}}{p_{\Lambda}^2}(p_{\Lambda,x}cos\varphi_i + p_{\Lambda,y}sin\varphi_i - p_{\Lambda,z}tan\theta_i) \right] \tag{A.83}$$

$$\frac{\partial H_{6,9}(\vec{\alpha},\vec{z}_\Lambda,\vec{z}_{Prim})}{\partial \varphi_i} = C_\Lambda \frac{d_\Lambda}{p_\Lambda^3} p_{z,i}(p_{\Lambda,y}p_{x,i} - p_{\Lambda,x}p_{y,i})$$

D-matrix elements in Cartesian coordinates

Derivatives with respect to p_1 and K^+

In the following expressions, the subscript "i" stands for the particles p_1 and K^+.

$$\frac{\partial H_{4,7}(\vec{\alpha},\vec{z}_\Lambda,\vec{z}_{Prim})}{\partial p_{x,i}} = C_i \frac{d_i}{p_i}\left(1 - \frac{p_{x,i}^2}{p_i^2}\right)$$

$$\frac{\partial H_{4,7}(\vec{\alpha},\vec{z}_\Lambda,\vec{z}_{Prim})}{\partial p_{y,i}} = -C_i d_i \frac{p_{x,i}p_{y,i}}{p_i^3}$$

$$\frac{\partial H_{4,7}(\vec{\alpha},\vec{z}_\Lambda,\vec{z}_{Prim})}{\partial p_{z,i}} = -C_i d_i \frac{p_{x,i}p_{z,i}}{p_i^3}$$

$$\frac{\partial H_{4,7}(\vec{\alpha},\vec{z}_\Lambda,\vec{z}_{Prim})}{\partial x_{x,i}} = 1 - C_i \frac{p_{x,i}}{p_i}\frac{(z_{Prim,x} - x_{x,i})}{d_i}$$

$$\frac{\partial H_{4,7}(\vec{\alpha},\vec{z}_\Lambda,\vec{z}_{Prim})}{\partial x_{y,i}} = -C_i \frac{p_{x,i}}{p_i}\frac{(z_{Prim,y} - x_{y,i})}{d_i}$$

$$\frac{\partial H_{4,7}(\vec{\alpha},\vec{z}_\Lambda,\vec{z}_{Prim})}{\partial x_{z,i}} = -C_i \frac{p_{x,i}}{p_i}\frac{(z_{Prim,z} - x_{z,i})}{d_i}$$

$$\frac{\partial H_{5,8}(\vec{\alpha},\vec{z}_\Lambda,\vec{z}_{Prim})}{\partial p_{x,i}} = -C_i d_i \frac{p_{y,i}p_{x,i}}{p_i^3}$$

$$\frac{\partial H_{5,8}(\vec{\alpha},\vec{z}_\Lambda,\vec{z}_{Prim})}{\partial p_{y,i}} = C_i \frac{d_i}{p_i}\left(1 - \frac{p_{y,i}^2}{p_i^2}\right)$$

$$\frac{\partial H_{5,8}(\vec{\alpha},\vec{z}_\Lambda,\vec{z}_{Prim})}{\partial p_{z,i}} = -C_i d_i \frac{p_{y,i}p_{z,i}}{p_i^3}$$

$$\frac{\partial H_{5,8}(\vec{\alpha},\vec{z}_\Lambda,\vec{z}_{Prim})}{\partial x_{x,i}} = -C_i \frac{p_{y,i}}{p_i}\frac{(z_{Prim,x} - x_{x,i})}{d_i}$$

$$\frac{\partial H_{5,8}(\vec{\alpha},\vec{z}_\Lambda,\vec{z}_{Prim})}{\partial x_{y,i}} = 1 - C_i \frac{p_{y,i}}{p_i}\frac{(z_{Prim,y} - x_{y,i})}{d_i}$$

$$\frac{\partial H_{5,8}(\vec{\alpha},\vec{z}_\Lambda,\vec{z}_{Prim})}{\partial x_{z,i}} = -C_i \frac{p_{y,i}}{p_i}\frac{(z_{Prim,z} - x_{z,i})}{d_i}$$

$$\frac{\partial H_{6,9}(\vec{\alpha},\vec{z}_\Lambda,\vec{z}_{Prim})}{\partial p_{x,i}} = -C_i d_i \frac{p_{z,i}p_{x,i}}{p_i^3}$$

$$\frac{\partial H_{6,9}(\vec{\alpha},\vec{z}_{\Lambda},\vec{z}_{Prim})}{\partial p_{y,i}} = -C_i d_i \frac{p_{z,i}p_{y,i}}{p_i^3}$$

$$\frac{\partial H_{6,9}(\vec{\alpha},\vec{z}_{\Lambda},\vec{z}_{Prim})}{\partial p_{z,i}} = C_i \frac{d_i}{p_i}\left(1-\frac{p_{z,i}^2}{p_i^2}\right)$$

$$\frac{\partial H_{6,9}(\vec{\alpha},\vec{z}_{\Lambda},\vec{z}_{Prim})}{\partial x_{x,i}} = -C_i \frac{p_{z,i}}{p_i}\frac{(z_{Prim,x}-x_{x,i})}{d_i}$$

$$\frac{\partial H_{6,9}(\vec{\alpha},\vec{z}_{\Lambda},\vec{z}_{Prim})}{\partial x_{y,i}} = -C_i \frac{p_{z,i}}{p_i}\frac{(z_{Prim,y}-x_{y,i})}{d_i}$$

$$\frac{\partial H_{6,9}(\vec{\alpha},\vec{z}_{\Lambda},\vec{z}_{Prim})}{\partial x_{z,i}} = 1-C_i \frac{p_{z,i}}{p_i}\frac{(z_{Prim,z}-x_{z,i})}{d_i}$$

Derivatives with respect to p_2 and π^-

In the following expressions, the subscript “i” stands for the particles p_2 and π^-.

$$\frac{\partial H_{4,7}(\vec{\alpha},\vec{z}_{\Lambda},\vec{z}_{Prim})}{\partial p_{x,i}} = -C_{\Lambda}\frac{d_{\Lambda}}{p_{\Lambda}}\left(1-\frac{p_{\Lambda,x}^2}{p_{\Lambda}^2}\right)$$

$$\frac{\partial H_{4,7}(\vec{\alpha},\vec{z}_{\Lambda},\vec{z}_{Prim})}{\partial p_{y,i}} = C_{\Lambda}d_{\Lambda}\frac{p_{\Lambda,x}p_{\Lambda,y}}{p_{\Lambda}^3}$$

$$\frac{\partial H_{4,7}(\vec{\alpha},\vec{z}_{\Lambda},\vec{z}_{Prim})}{\partial p_{z,i}} = C_{\Lambda}d_{\Lambda}\frac{p_{\Lambda,x}p_{\Lambda,z}}{p_{\Lambda}^3}$$

$$\frac{\partial H_{5,8}(\vec{\alpha},\vec{z}_{\Lambda},\vec{z}_{Prim})}{\partial p_{x,i}} = C_{\Lambda}d_{\Lambda}\frac{p_{\Lambda,y}p_{\Lambda,x}}{p_{\Lambda}^3}$$

$$\frac{\partial H_{5,8}(\vec{\alpha},\vec{z}_{\Lambda},\vec{z}_{Prim})}{\partial p_{y,i}} = -C_{\Lambda}\frac{d_{\Lambda}}{p_{\Lambda}}\left(1-\frac{p_{\Lambda,y}^2}{p_{\Lambda}^2}\right)$$

$$\frac{\partial H_{5,8}(\vec{\alpha},\vec{z}_{\Lambda},\vec{z}_{Prim})}{\partial p_{z,i}} = C_{\Lambda}d_{\Lambda}\frac{p_{\Lambda,y}p_{\Lambda,z}}{p_{\Lambda}^3}$$

$$\frac{\partial H_{6,9}(\vec{\alpha},\vec{z}_{\Lambda},\vec{z}_{Prim})}{\partial p_{x,i}} = C_{\Lambda}d_{\Lambda}\frac{p_{\Lambda,z}p_{\Lambda,x}}{p_{\Lambda}^3}$$

$$\frac{\partial H_{6,9}(\vec{\alpha},\vec{z}_{\Lambda},\vec{z}_{Prim})}{\partial p_{y,i}} = C_{\Lambda}d_{\Lambda}\frac{p_{\Lambda,z}p_{\Lambda,y}}{p_{\Lambda}^3}$$

$$\frac{\partial H_{6,9}(\vec{\alpha},\vec{z}_{\Lambda},\vec{z}_{Prim})}{\partial p_{z,i}} = -C_{\Lambda}\frac{d_{\Lambda}}{p_{\Lambda}}\left(1-\frac{p_{\Lambda,z}^2}{p_{\Lambda}^2}\right)$$

E-matrix elements in Cartesian coordinates

Derivatives with respect to p_2 and π^-

In the following expressions, the subscript “i” stands for the particles p_1 and K^+.

$$\frac{\partial H_{4,7}(\vec{\alpha},\vec{z}_\Lambda)}{\partial z_{Prim,x}} = C_i \frac{p_{x,i}}{p_i}\frac{(z_{Prim,x}-x_{x,i})}{d_i} - C_\Lambda \frac{p_{\Lambda,x}}{p_\Lambda}\frac{(z_{Prim,x}-x_{\Lambda,x})}{d_\Lambda}$$

$$\frac{\partial H_{4,7}(\vec{\alpha},\vec{z}_\Lambda)}{\partial z_{Prim,y}} = C_i \frac{p_{x,i}}{p_i}\frac{(z_{Prim,y}-x_{y,i})}{d_i} - C_\Lambda \frac{p_{\Lambda,x}}{p_\Lambda}\frac{(z_{Prim,y}-x_{\Lambda,y})}{d_\Lambda}$$

$$\frac{\partial H_{4,7}(\vec{\alpha},\vec{z}_\Lambda)}{\partial z_{Prim,z}} = C_i \frac{p_{x,i}}{p_i}\frac{(z_{Prim,z}-x_{z,i})}{d_i} - C_\Lambda \frac{p_{\Lambda,x}}{p_\Lambda}\frac{(z_{Prim,z}-x_{\Lambda,z})}{d_\Lambda}$$

$$\frac{\partial H_{5,8}(\vec{\alpha},\vec{z}_\Lambda)}{\partial z_{Prim,x}} = C_i \frac{p_{y,i}}{p_i}\frac{(z_{Prim,x}-x_{x,i})}{d_i} - C_\Lambda \frac{p_{\Lambda,y}}{p_\Lambda}\frac{(z_{Prim,x}-x_{\Lambda,x})}{d_\Lambda}$$

$$\frac{\partial H_{5,8}(\vec{\alpha},\vec{z}_\Lambda)}{\partial z_{Prim,y}} = C_i \frac{p_{y,i}}{p_i}\frac{(z_{Prim,y}-x_{y,i})}{d_i} - C_\Lambda \frac{p_{\Lambda,y}}{p_\Lambda}\frac{(z_{Prim,y}-x_{\Lambda,y})}{d_\Lambda}$$

$$\frac{\partial H_{5,8}(\vec{\alpha},\vec{z}_\Lambda)}{\partial z_{Prim,z}} = C_i \frac{p_{y,i}}{p_i}\frac{(z_{Prim,z}-x_{z,i})}{d_i} - C_\Lambda \frac{p_{\Lambda,y}}{p_\Lambda}\frac{(z_{Prim,z}-x_{\Lambda,z})}{d_\Lambda}$$

$$\frac{\partial H_{6,9}(\vec{\alpha},\vec{z}_\Lambda)}{\partial z_{Prim,x}} = C_i \frac{p_{z,i}}{p_i}\frac{(z_{Prim,x}-x_{x,i})}{d_i} - C_\Lambda \frac{p_{\Lambda,z}}{p_\Lambda}\frac{(z_{Prim,x}-x_{\Lambda,x})}{d_\Lambda}$$

$$\frac{\partial H_{6,9}(\vec{\alpha},\vec{z}_\Lambda)}{\partial z_{Prim,y}} = C_i \frac{p_{z,i}}{p_i}\frac{(z_{Prim,y}-x_{y,i})}{d_i} - C_\Lambda \frac{p_{\Lambda,z}}{p_\Lambda}\frac{(z_{Prim,y}-x_{\Lambda,y})}{d_\Lambda}$$

$$\frac{\partial H_{6,9}(\vec{\alpha},\vec{z}_\Lambda)}{\partial z_{Prim,z}} = C_i \frac{p_{z,i}}{p_i}\frac{(z_{Prim,z}-x_{z,i})}{d_i} - C_\Lambda \frac{p_{\Lambda,z}}{p_\Lambda}\frac{(z_{Prim,z}-x_{\Lambda,z})}{d_\Lambda}$$

Derivatives with respect to the secondary vertex parameters

$$\frac{\partial H_{4,7}(\vec{\alpha},\vec{z}_\Lambda)}{\partial z_{\Lambda,x}} = C_\Lambda \frac{p_{\Lambda,x}}{p_\Lambda}\frac{(z_{Prim,x}-x_{\Lambda,x})}{d_\Lambda} - 1$$

$$\frac{\partial H_{4,7}(\vec{\alpha},\vec{z}_\Lambda)}{\partial z_{\Lambda,y}} = C_\Lambda \frac{p_{\Lambda,x}}{p_\Lambda}\frac{(z_{Prim,y}-x_{\Lambda,y})}{d_\Lambda}$$

$$\frac{\partial H_{4,7}(\vec{\alpha},\vec{z}_\Lambda)}{\partial z_{\Lambda,z}} = C_\Lambda \frac{p_{\Lambda,x}}{p_\Lambda}\frac{(z_{Prim,z}-x_{\Lambda,z})}{d_\Lambda}$$

$$\frac{\partial H_{5,8}(\vec{\alpha},\vec{z}_\Lambda)}{\partial z_{\Lambda,x}} = C_\Lambda \frac{p_{\Lambda,y}}{p_\Lambda}\frac{(z_{Prim,x}-x_{\Lambda,x})}{d_\Lambda}$$

$$\frac{\partial H_{5,8}(\vec{\alpha},\vec{z}_{\Lambda})}{\partial z_{\Lambda,y}} = C_{\Lambda}\frac{p_{\Lambda,y}}{p_{\Lambda}}\frac{(z_{Prim,y} - x_{\Lambda,y})}{d_{\Lambda}} - 1$$

$$\frac{\partial H_{5,8}(\vec{\alpha},\vec{z}_{\Lambda})}{\partial z_{\Lambda,z}} = C_{\Lambda}\frac{p_{\Lambda,y}}{p_{\Lambda}}\frac{(z_{Prim,z} - x_{\Lambda,z})}{d_{\Lambda}}$$

$$\frac{\partial H_{6,9}(\vec{\alpha},\vec{z}_{\Lambda})}{\partial z_{\Lambda,x}} = C_{\Lambda}\frac{p_{\Lambda,z}}{p_{\Lambda}}\frac{(z_{Prim,x} - x_{\Lambda,x})}{d_{\Lambda}}$$

$$\frac{\partial H_{6,9}(\vec{\alpha},\vec{z}_{\Lambda})}{\partial z_{\Lambda,y}} = C_{\Lambda}\frac{p_{\Lambda,z}}{p_{\Lambda}}\frac{(z_{Prim,y} - x_{\Lambda,y})}{d_{\Lambda}}$$

$$\frac{\partial H_{6,9}(\vec{\alpha},\vec{z}_{\Lambda})}{\partial z_{\Lambda,z}} = C_{\Lambda}\frac{p_{\Lambda,z}}{p_{\Lambda}}\frac{(z_{Prim,z} - x_{\Lambda,z})}{d_{\Lambda}} - 1$$

B Initial vertex of two non-intersecting lines

In general, two particle tracks that originally stem from a common vertex do not intersect because of the measurement uncertainties. The kinematic refit with intersection constraint forces the particles to really intersect in a new vertex $\vec{z}$. However, for the calculations an initial vertex position $\vec{z}_0$ has to be determined. Since the tracks probably do not intersect in the first place, the initial vertex has to be calculated as the mean intersection point, which is the center of the minimum distance between the two lines.
The particles are represented by straight lines

$$\vec{r}_i = \vec{x}_i + \tau_i \, \vec{p}_i \tag{B.1}$$

where $\vec{p}_i$ is the momentum of the particles and $\vec{x}_i$ a point at which it is evaluated, the so called emission point. τ_i is a scalar, which determines the length of the momentum vector $\vec{p}_i$, that is necessary in order to reach the arbitrary point $\vec{r}_i$ on the line. For the following calculations, the two particles are chosen to be p_2 and π^-.
The general difference vector of two arbitrary points on the two lines $\vec{d}$ is given by the following expression.

$$\vec{d} = \vec{r}_{\pi^-} - \vec{r}_{p_2} = \vec{x}_{\pi^-} + \tau_{\pi^-} \, \vec{p}_{\pi^-} - \vec{x}_{p_2} - \tau_{p_2} \, \vec{p}_{p_2} \tag{B.2}$$

The coefficients τ_{π^-} and τ_{p_2} determine the positions of the points on the respective lines. The task is now, to find expressions for these two coefficients, so that the difference vector $\vec{d}$ is orthogonal to both lines. In this case, the magnitude of $\vec{d}$ represents the minimum distance between the tracks of p_2 and π^-. The initial mean vertex of the two particle tracks is located at the center of the minimum distance.

$$\vec{z}_0 = \vec{r}_{p_2} + \frac{1}{2}\vec{d} = \frac{1}{2}(\vec{r}_{p_2} + \vec{r}_{\pi^-}) \tag{B.3}$$

The first condition, that $\vec{d}$ is orthogonal to the π^- track, reads

$$\vec{d} \cdot \vec{r}_{\pi^-} = 0 \tag{B.4}$$

yielding the following equation

$$\tau_{\pi^-} p_{\pi^-}^2 - \tau_{p_2} C + D_{\pi^-} = 0 \tag{B.5}$$

with

$$p_i^2 = p_{x,i}^2 + p_{y,i}^2 + p_{z,i}^2 \tag{B.6}$$

$$D_i = p_{x,i}(x_{x,\pi^-} - x_{x,p_2}) + p_{y,i}(x_{y,\pi^-} - x_{y,p_2}) + p_{z,i}(x_{z,\pi^-} - x_{z,p_2}) \tag{B.7}$$

$$C = (p_{x,\pi^-}p_{x,p_2} + p_{y,\pi^-}p_{y,p_2} + p_{z,\pi^-}p_{z,p_2}) \tag{B.8}$$

The second condition is the orthogonality of the p_2 track and $\vec{d}$.

$$\vec{d} \cdot \vec{r}_{p_2} = 0 \tag{B.9}$$

which leads to

$$\tau_{\pi^-}C - \tau_{p_2}p_{p_2}^2 + D_{p_2} = 0 \tag{B.10}$$

Solving the two equations B.5 and B.10 for the coefficients, yields

$$\tau_{p_2} = \frac{D_{\pi^-}C - D_{p_2}p_{\pi^-}^2}{C^2 - p_{p_2}^2 p_{\pi^-}^2} \tag{B.11}$$

$$\tau_{\pi^-} = \frac{D_{\pi^-}C - D_{p_2}p_{\pi^-}^2}{C^2 - p_{p_2}^2 p_{\pi^-}^2}\,\frac{C}{p_{\pi^-}^2} - \frac{D_{\pi^-}}{p_{\pi^-}^2} \tag{B.12}$$

The initial mean vertex is now given by the following equation.

$$\vec{z}_0 = \frac{1}{2}(\vec{x}_{p_2} + \vec{x}_{\pi^-} + \tau_{p_2}\,\vec{p}_{p_2} + \tau_{\pi^-}\,\vec{p}_{\pi^-}) \tag{B.13}$$

C P-value distributions for pp simulations

This appendix shows the p-value distributions for the different constraint combinations of the kinematic refit applied to full scale pp simulations. The black lines indicate the significance of the respective combination, which is determined by maximizing the product of purity and efficiency. The different channels are written in the pictures, the fractions of the single channels, which remain after the p-value cuts, are quoted in brackets behind the respective channels.

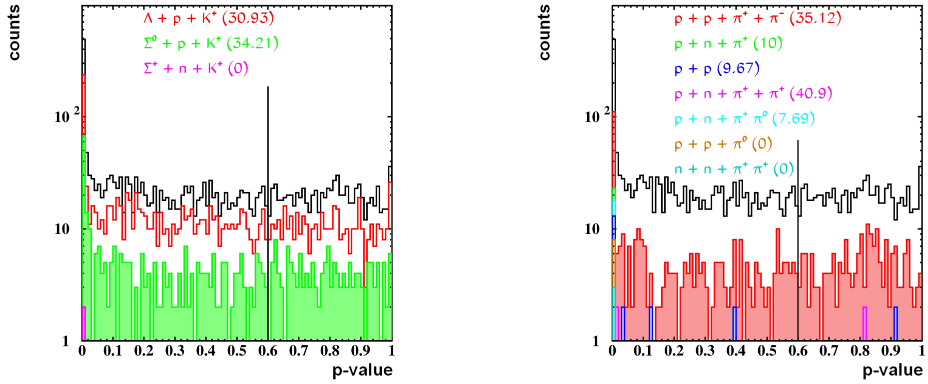

Figure C.1: Kinematic refit with intersection (p_2,π^-) constraint. Significance for this fit: $\alpha = 0.6$.

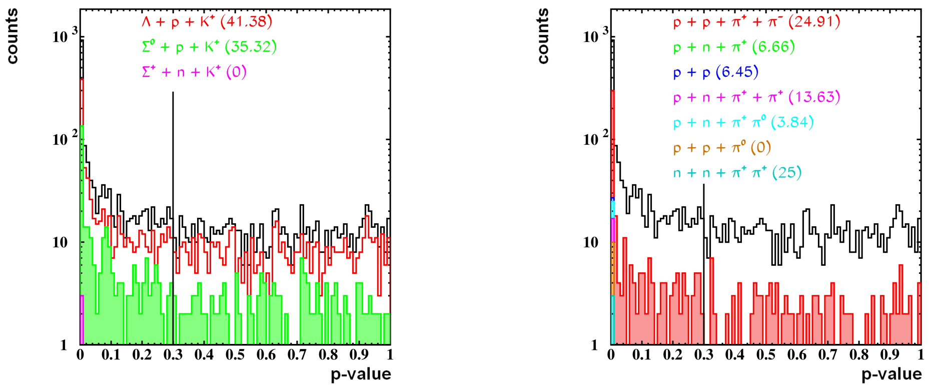

Figure C.2: Kinematic refit with secondary vertex constraint. Significance for this fit: $\alpha = 0.3$.

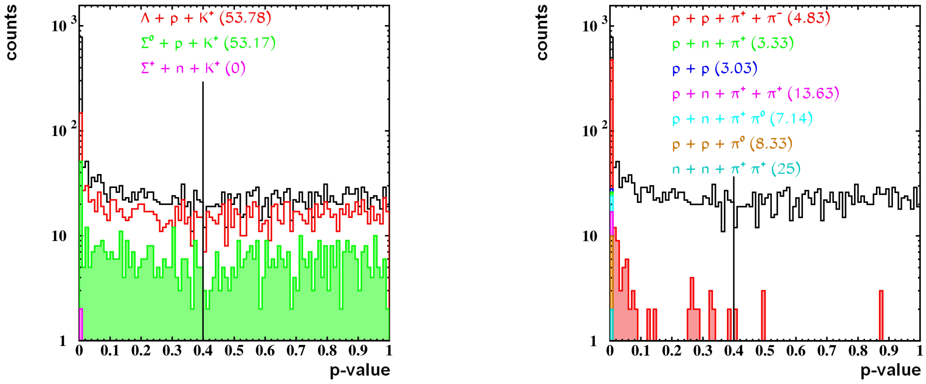

Figure C.3: Kinematic refit with invariant mass constraint. Significance for this fit: $\alpha = 0.4$.

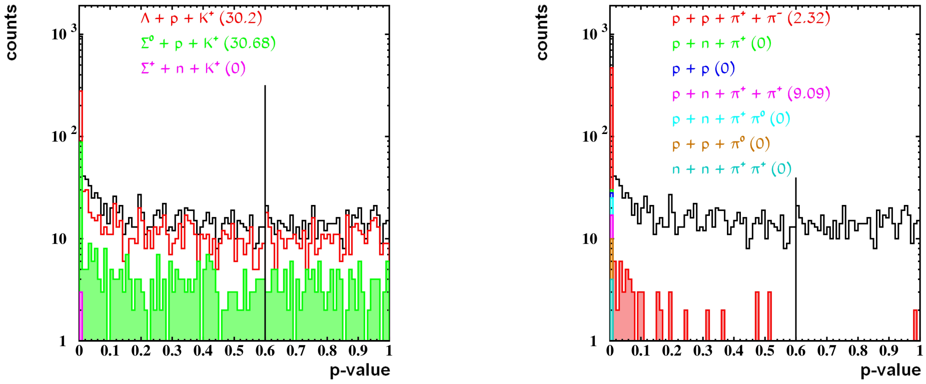

Figure C.4: Kinematic refit with invariant mass and intersection (p_2,π^-) constraint. Significance for this fit: $\alpha = 0.6$.

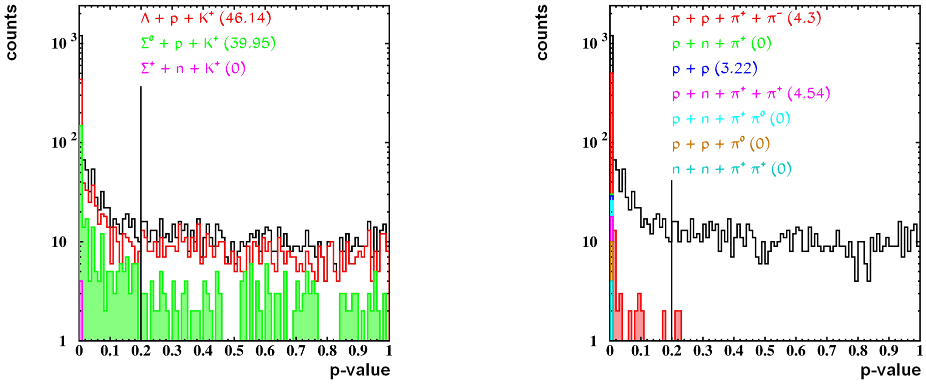

Figure C.5: Kinematic refit with invariant mass and secondary vertex constraint. Significance for this fit: $\alpha = 0.2$.

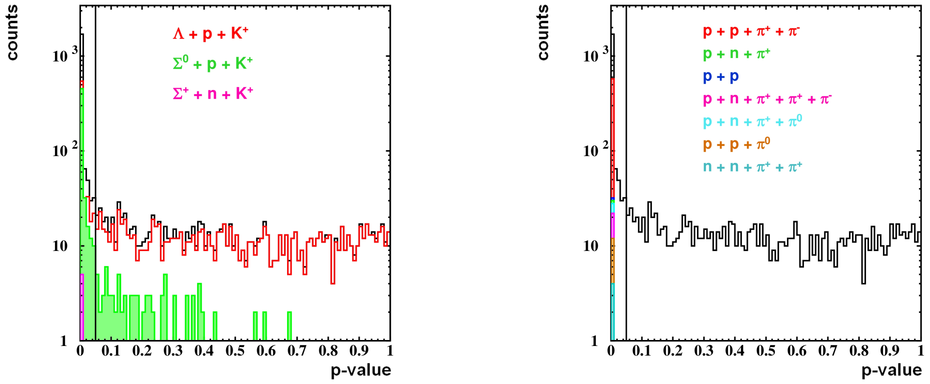

Figure C.6: Kinematic refit with conservation constraint. Significance for this fit: $\alpha = 0.5$.

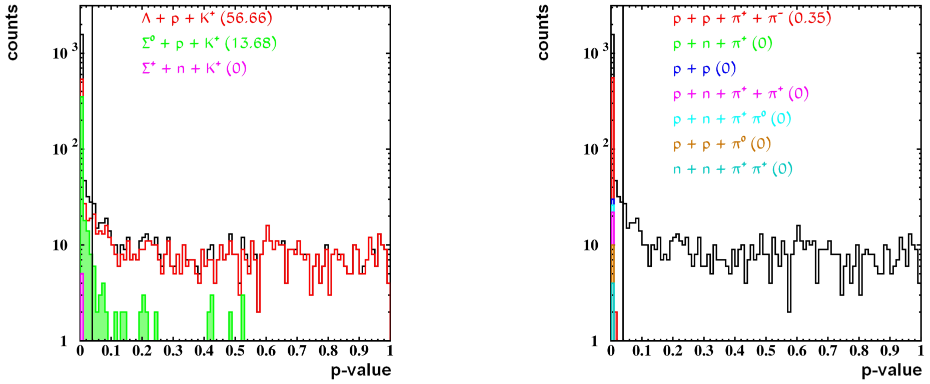

Figure C.7: Kinematic refit with conservation and intersection (p_2,π^-) constraint. Significance for this fit: $\alpha = 0.04$.

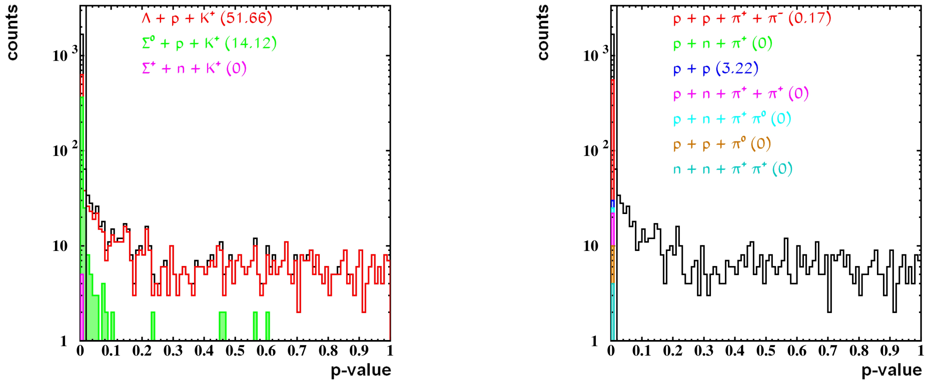

Figure C.8: Kinematic refit with conservation and secondary vertex constraint. Significance for this fit: $\alpha = 0.02$.

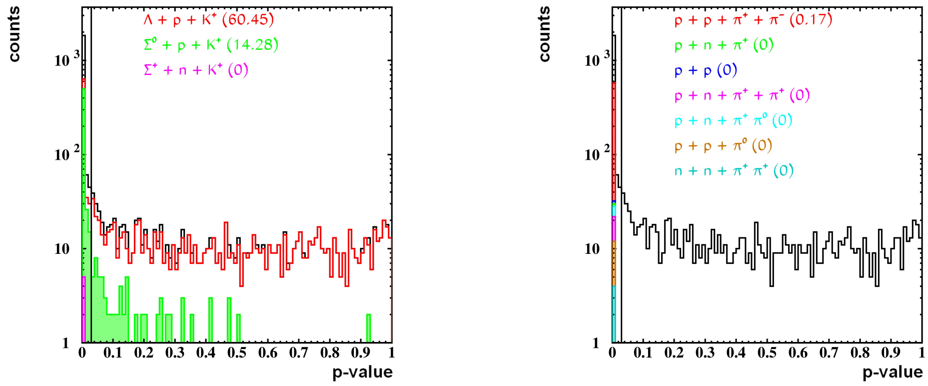

Figure C.9: Kinematic refit with invariant mass and conservation constraint. Significance for this fit: $\alpha = 0.03$.

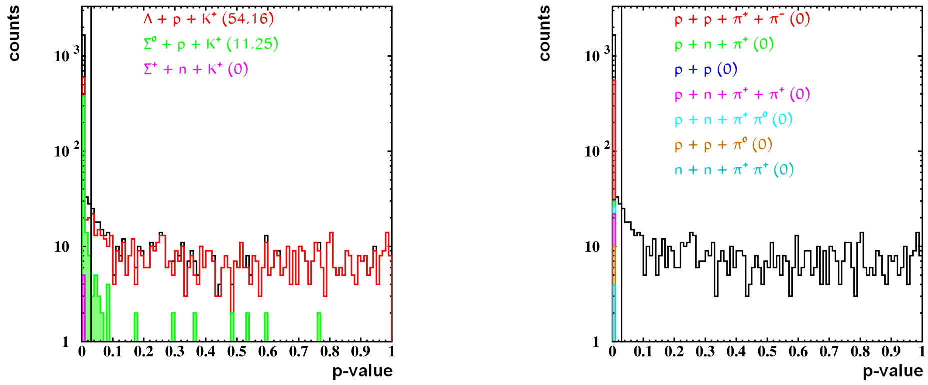

Figure C.10: Kinematic refit with invariant mass, conservation and intersection (p_2,π^-) constraint. Significance for this fit: $\alpha = 0.03$.

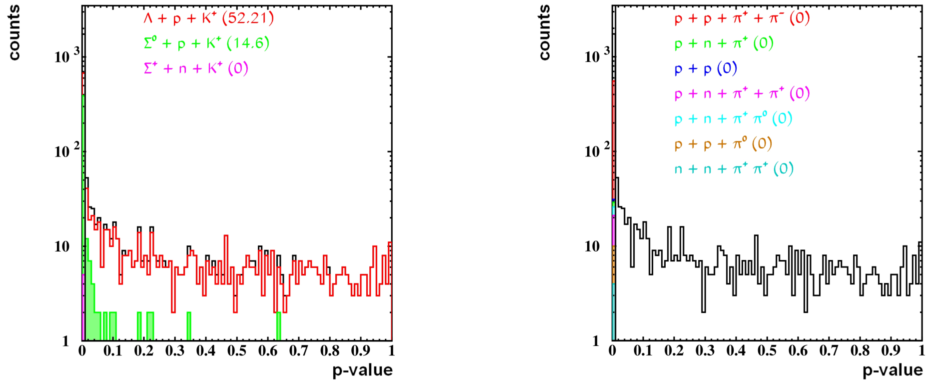

Figure C.11: Kinematic refit with invariant mass, conservation and secondary vertex constraint. Significance for this fit: $\alpha = 0.007$.

Index

Bibliography

[Ave98] Avery, P.: *Fitting Theory Writeups and References.* 1998. – `http://www.phys.ufl.edu/~avery/fitting.html`, accessed at March 21, 2012

[Bau00] Bauer, J. M.: Kinematic Fit for the Radiative Bhabha Calibration of BaBar's Electromagnetic Calorimeter. In: *arXiv:0011019v1 hep-ex* (2000)

[Ben07] Benabderrahmane, M. L.: *Measurement of the K^0 Inclusive Cross Section in Pion-Induced Reactions at* 1.15 GeV/c, Universität Heidelberg, Dissertation., 2007

[Ber09] Berger, M.: *SiΛViO: Entwicklung eines auf Silizium basierenden Trigger und Tracking Systems*, Technische Universität München, Master's thesis, 2009

[BGL12] Barnea, N. ; Gal, A. ; Liverts, E. Z.: Realistic calculations of $\bar{K}NN$, $\bar{K}NNN$, and $\bar{K}\bar{K}NN$ quasibound states. In: *arXiv:1203.5234v2 [nucl-th]* (2012)

[BHS+09] Bühler, P. ; Hartmann, O. ; Schafhauser, M. ; Suzuki, K. ; Zmeskal, J.: Start counter and target system for the FOPI S349 experiment. In: *GSI scientific report, NQMA-Experiments-05* (2009), S. 233

[BLL10] Beckmann, M. ; List, B. ; List, J.: Treatment of Photon Radiation in Kinematic Fits at Future $e^+ e^-$ Colliders. In: *NIM A 624* (2010), S. 184–191

[BNW05] Borasoy, B. ; Nissler, R. ; Weise, W.: Chiral dynamics of kaon-nucleon interactions, revisited. In: *Phys. Rev. Lett. 66* 25 (2005), S. 79–96

[BR91] Brown, G. E. ; Rho, M.: Scaling effective Lagrangians in a dense medium. In: *Phys. Rev. Lett. 66* (1991), S. 2720–2723

[Cha01] Chanfray, G.: Hadrons in dense and hot matter: implications of chiral symmetry restoration. In: *Nucl. Phys. A* 685 (2001), S. 328–345

[Cro98] Crochet, P.: K^+ Flow in Heavy Ion Collisions at SIS Energies. In: *Act. Phys. Pol. B* 29 (1998)

[CRW96] Chanfray, G. ; Rapp, R. ; Wambach, J.: Medium Modifications of the Rho Meson at CERN Super Proton Synchrotron Energies (200 GeV/nucleon). In: *Phys. Rev. Lett. 76* (1996), S. 368–371

[D$^+$07] Damjanovic, S. et al.: NA60 results on the ρ spectral function in In – In collisions. In: *Nucl. Phys. B* 783 (2007), S. 327–334

[DPR$^+$10] Demorest, P. B. ; Pennucci, T. ; Ransom, S. M. ; Roberts, M. S. E. ; Hessels, J. W. T.: A two-solar-mass neutron star measured using Shapiro delay. In: *Nature 467* (2010), S. 1081–1083

[E$^+$10] Eyrich, W. et al.: Influence of N^*-resonances on hyperon production in the channel $pp \rightarrow K^+ \Lambda p$ at 2.95, 3.20 and 3.30 GeV/c beam momentum. In: *Phys. Lett. B* 688 (2010), S. 142–149

[Epp09] Epple, E.: *The $\Lambda(1405)$-Resonance measured via its decay into $\Sigma^0\pi^0$ in proton proton collisions with the HADES spectrometer*, Technische Universität München, Master's thesis, 2009

[F$^+$10] Fröhlich, I. et al.: Design of the pluto event generator. In: *J. Phys.: Conf.* (2010)

[Fab10] Fabbietti, L.: Search for ppK^- with proton induced reactions at GSI. In: *Int. J. Mod. Phys. E* 19 (2010), S. 2606–2611

[FE10] Fabbietti, L. ; Epple, E.: Study of the $\Lambda(1405)$ Resonance in $p+p$ at 3.5 AGeV. In: *Nucl. Phys. A* 835 (2010), S. 333–336

[FH11] Fukushima, K. ; Hatsuda, T: The phase diagram of dense QCD. In: *Rep. Prog. Phys.* 74 (2011)

[FIN05] FINUDA Collaboration: Evidence for a Kaon-Bound State K^-pp Produced in K Absorption Reactions at Rest. In: *Phys. Rev. Lett.* 94 (2005)

[FRB$^+$00] Frühwirth, R. ; Regler, M. ; Bock, R. K. ; Grote, H. ; Notz, D.: *Data Analysis Techniques for High-Energy Physics*. 2. Cambridge University Press, 2000

[FS$^+$09] Fabbietti, L. ; Schmah, A. et al.: Φ decay: A relevant source for K^- production at energies available at the GSI Schwerionen-Synchrotron (SIS)? In: *Phys. Rev. C* 80 (2009)

[G$^+$02] Geissel, H. et al.: Deeply Bound 1s and 2p Pionic States in ^{205}Pb and Determination of the s-Wave Part of the Pion-Nucleus Interaction. In: *Phys. Lett. B 465* 88 (2002)

[GEA] GEANT: *The GEANT Collaboration*. – http://geant4.web.cern.ch/geant4/, accessed at April 13, 2012

[Gru93] Grupen, C.: *Teilchendetektoren.* BI-Wissenschaftsverlag, 1993

[Har03] Hartmann, O.: *Experimentelle Untersuchungen der asymmetrischen Schwerionenreaktionen* Ca + Au *und* Au + Ca *bei* 1.5 GeV/u *Projektilenergie*, Technische Universität Darmstadt, Dissertation., 2003

[Hem84] Hemingway, R. J.: Production of $\Lambda(1405)$ in K^-p reactions at 4.2 AGeV/c. In: *Nucl. Phys. B* 253 (1984)

[HJ12] Hyodo, T. ; Jido, D.: The nature of the $\Lambda(1405)$ resonance in chiral dynamics. In: *Prog. Part. Nucl. Phys.* 67 (2012), S. 55–98

[HL92] Hatsuda, T. ; Lee, S. H.: QCD sum rules for vector mesons in the nuclear medium. In: *Phys. Rev. C* 29 (1992)

[HOA03] Hartnack, C. ; Oeschler, H. ; Aichelin, J.: What Determines the K^- Multiplicity at Energies Around $1-2$ AGeV? In: *Phys. Rev. Lett. 90* (2003)

[HW08] Hyodo, T. ; Weise, W.: Effective $\bar{K}N$ interaction based on chiral $SU(3)$ dynamics. In: *Phys. Rev. C* 77 (2008)

[I^+00] Itahashi, K. et al.: Deeply bound π^- states in ^{207}Pb formed in the ^{208}Pb(d,^{3}He) reaction. II. Deduced binding energies and widths and the pion-nucleus interaction. In: *Phys. Rev. C* 62 (2000)

[IKMW08] Ivanov, A. N. ; Kienle, P. ; Marton, J. ; Widmann, J.: Phenomenological model of the Kaonic Nuclear Cluster K^-pp in the ground state. In: *arXiv:nucl-th/0512037v2* (2008)

[Jam06] James, F.: *Statistical Methods in Experimental Physics.* 2. World Scientific Printers, 2006

[JOO^+03] Jido, D. ; Oller, J. A. ; Oset, E. ; Ramos, A. ; Meißner, U.: Chiral dynamics of the two $\Lambda(1405)$ states. In: *Nucl. Phys. A* 62 (2003), S. 181–200

[JSI^+10] Jido, D. ; Sekihara, T. ; Ikeda, Y. ; Hyodo, T. ; Kanada-Enyo, Y. ; Oset, E.: The nature of $\Lambda(1405)$ hyperon resonance in chiral dynamics. In: *Nucl. Phys. A* 835 (2010), S. 59–66

[Ket10] Ketzer, B.: *Moderne Teilchendetektoren-Theorie und Praxis.* Vorlesungsskript, TU München, 2010

[Kim04] Kim, J. Y.: *Study of the Nuclear Stopping in Isospin Asymmetric Nuclear Collisions at* 0.4 A *and* 1.5 AGeV, Korea University, Dissertation., 2004

[Kiš10] Kiš, M.: *FOPI MMRPC ToF Barrel.* Darmstadt, feb 2010. – FOPI Collaboration Meeting

[Koc96] Koch, V.: Aspects of Chiral Symmetry. In: *Int. J. Mod. Phys. E* (1996)

[Kre97] Kress, T.: *Ein universelles Monitorsystem zur Überwachung des Betriebszustands der Driftkammern des FOPI-Detektors*, Technische Universität Darmstadt, Master's thesis, 1997

[KSW95] Kaiser, N. ; Siegel, P. B. ; Weise, W.: Chiral dynamics and the low-energy kaon-nucleon interaction. In: *Nucl. Phys. A* 594 (1995), S. 325–345

[Kut99] Kutsche, R.: *Untersuchungen der In-Medium-Eigenschaften von K^0_S-Mesonen und Λ-Hyperonen an der Produktionsschwelle*, Technische Universität Darmstadt, Dissertation., 1999

[Leo94] Leo, W. R.: *Techniques for Nuclear and Particle Physics Experiments.* 2. Springer Verlag, 1994

[LKW92] Lutz, M. ; Klimt, S. ; Weise, W.: Meson properties at finite temperature and baryon density. In: *Nucl. Phys. A* 542 (1992), S. 521–558

[Lor08] Lorentz, M.: *Geladene Kaonen Produktion in* $\mathrm{Ar}+\mathrm{KCl}$ *Reaktionen bei* 1.756 AGeV, Universität Frankfurt, Master's thesis, 2008

[MFBH10] Münzer, R. ; Fabbietti, L. ; Berger, M. ; Hartmann, O.: SiΛVio: A trigger for Λ-Hyperons. In: *NIM A 617* (2010), S. 300–302

[Mic06] Michalski, S.: *Chiral Symmetry Restoration in Quantum Field Theories at Finite Temperature*, Universität Dortmund, Dissertation., 2006

[MORT06] Magas, V. K. ; Oset, E. ; Ramos, A. ; Toki, H.: Critical view on the deeply bound K^-pp system. In: *Phys. Rev. C* 74 (2006)

[Mün08] Münzer, R.: *SiΛViO: Ein Trigger für Lambda Hyperonen*, Technische Universität München, Master's thesis, 2008

[Mün12] Münzer, R.: *private communication.* 2012

[NA609] NA60 Collaboration: NA60 results on thermal dimuons. In: *Europ. Phys. J. C 4* 61 (2009), S. 711–120

[Nöh98] Nöhrenberg, W.: Restoration of Chiral Symmetry in Nucleus-Nucleus Collisions around 10 GeV/u. In: *Act. Phys. Pol. A* 29 (1998)

[O$^+$12] Okada, S. et al.: Kaonic hydrogen X-ray measurement in SIDDHARTA. In: *Nucl. Phys. A* (2012)

[OM01] Oller, J. A. ; Meißner, U.: Chiral dynamics in the presence of bound states: kaon-nucleon interactions revisited. In: *Phys. Lett. B* 500 (2001), S. 263–272

[OR98] Oset, E. ; Ramos, A.: Non-perturbative chiral approach to S-wave $\bar{K}N$ interactions. In: *Nucl. Phys. A* 635 (1998), S. 99–120

[Par10] Particle Data Group: Review of Particle Physics. In: *J. Phys. G Nucl. Part.* 37 (2010)

[Ple99] Plettner, C. L.: *Strangenesspoduktion bei kleinen transversalen Impulsen und mittleren Rapiditäten in der Reaktion* $^{96}\mathrm{Ru} + {}^{96}\mathrm{Ru}$ *at* 1.69 AGeV, Technische Universität Dresden, Dissertation., 1999

[PRCZ09] Povh, B. ; Rith, K. ; C., Scholz ; Zetsche, F.: *Teilchen und Kerne.* 8. Springer Verlag, 2009

[PS95] Peskin, M. E. ; Schröder, D. V.: *An Introduction to Quantum Field Theory.* Westview Press, 1995

[PSSG99] Pal, S. ; Song, G. ; Stöcker, H. ; Greiner, W.: Meson mass modification in strange hadronic matter. In: *Phys. Lett. B 465* (1999), S. 282–290

[RHK11] Ryu, M. S. ; Hong, B. ; Kang, T. I.: FOPI Detector for Heavy-ion Collision Experiment at SIS/GSI. In: *Journal of the Korean Physical Society* 59 (2011), Nr. 2, S. 1605–1608

[Rit95] Ritman, J.: The FOPI Detector at SIS/GSI. In: *Nucl. Phys. B Proc. Suppl.* 44 (1995), S. 708–715

[Röt11] Röttgers, B.: *Dense Baryonic Matter: new constraints from neutron stars*, Technische Universität München, Bachelor Thesis, 2011

[Rus06] Rustamov, A.: *Exclusive Eta Meson Reconstruction in Proton-Proton Collisions at* 2.2 GeV *with the HADES Spectrometer and High Resolution Tracking*, Universität Darmstadt, Dissertation., 2006

[Ryu09] Ryu, M. S.: *Production of the proton and light fragments in* ${}^{96}_{44}\mathrm{Ru} + {}^{96}_{44}\mathrm{Ru}$ *collisions at SIS18 energies and the multigap Resistive Plate Chamber*, Korea University, Dissertation., 2009

[S^{+}11] Siebenson, J. et al.: Strange baryon resonances in pp collisions measured with HADES. In: *Hyperfine Interact.* (2011)

[SB12] Solaguren-Bescoa, A.: *Strange Multibaryon Systems: Predictions and Experiments*, Technische Universität München, Master's thesis, 2012

[SBMJ97] Schaffner-Bielich, J. ; Mishustin, I. ; J., Bondorf: In-medium kaon production at the mean-field level. In: *Nucl. Phys. A 625* (1997), S. 325–346

[Sch04] Schüttauf, A.: Timing RPCs in FOPI. In: *NIM A 533* (2004), S. 65–68

[Sch08] Schmah, A.: *Produktion von Seltsamkeit in* Ar + KCl *Reaktionen bei* 1.756 AGeV *mit HADES*, Technische Universität Darmstadt, Dissertation., 2008

[SGM07] Shevchenko, N. V. ; Gal, A. ; Mares, J: Faddeev Calculation of a $K^{-}pp$ Quasibound State. In: *Phys. Rev. Lett. 98* (2007)

[She07] Shende, S. V.: *Strangeness Photoproduction on the Deuterium Target*, University of Groningen, Dissertation., 2007

[Sie10] Siebenson, J.: *Exclusive analysis of the* $\Lambda(1405)$ *resonance in the charged* $\Sigma\pi$ *decay channels*, Technische Universität München, Master's thesis, 2010

[Spa05] Spataro, S.: *Characterization of the HADES Spectrometer in pp Collisions at* 2.2 GeV*: Elastic Scattering and Exclusive Eta Reconstruction*, University of Catania, Dissertation., 2005

[SPM08] Shyam, R. ; Penner, G. ; Mosel, U.: Role of $N^{*}(1650)$ in the near threshold $pp \to p\Lambda K^{+}$ and $pp \to p\Sigma^{0}K^{+}$ reactions. In: *Phys. Rev. C* 63 (2008)

[Stu01] Sturm, C.: *K^{+}-Produktion in Schwerionenreaktionen als Sonde für die Inkompressibilität von Kernmaterie*, Universität Darmstadt, Dissertation., 2001

[SW^{+}10] Schulte-Wissermann, M. et al.: Production of Λ and Σ^{0} hyperons in proton-proton collisions. In: *Europ. Phys. Journ. A* 46 (2010), S. 27–44

[Uhl03] Uhlig, F.: *Systematische Untersuchung der Emission geladener Teilchen in* Ni + Ni*-Reaktionen bei SIS-Energien*, Universität Darmstadt, Dissertation., 2003

[UrQ] UrQMD: *The UrQMD Group.* – http://urqmd.org/, accessed at April 13, 2012

[WBW97] Waas, T. ; Brockmann, R. ; Weise, W.: Deeply bound pionic states and the effective pion mass in nuclear systems. In: *Nucl. Phys. A* 405 (1997), S. 215–218

[Win74] Wind, H.: Momentum Analysis by using a Quintic Spline Model for the Track. In: *NIM 115* (1974), S. 431–434

[Y^{+}96] Yamazaki, T. et al.: Discovery of deeply bound π^{-} states in the ^{208}Pb(d,^{3}He) reaction. In: *Z. Phys. A* 355 (1996), S. 219–221

[Y^{+}98] Yamazaki, T. et al.: Effective pion mass in the nuclear medium deduced from deeply bound pionic states in ^{207}Pb. In: *Phys. Let. B* 418 (1998), S. 246–251

[Y^+10] Yamazaki, T. et al.: Indication of a Deeply Bound and Compact K^-pp State Formed in the $pp \to pK^+\Lambda$ Reaction at 2.85 GeV. In: *Phys. Rev. Lett. 104* (2010)

[Y^+11] Yamazaki, T. et al.: Role of the $\Lambda(1405)$ in the Formation of the $X = K^-pp$ Deeply Bound States Revealed in the $pp \to X + K^+$ Reaction at 2.50 GeV and 2.85 GeV. In: *arXiv:1102.0482v1 [nucl-ex]* (2011)

[YA99] Yamazaki, T. ; Akaishi, Y.: Nuclear medium effects on invariant mass spectra of hadrons decaying in nuclei. In: *Phys. Let. B* 453 (1999), S. 1–6

[YA02] Yamazaki, T. ; Akaishi, Y.: Nuclear K^- bound states in light nuclei. In: *Phys. Rev. C* 65 (2002), S. 1–9

[YA07] Yamazaki, T. ; Akaishi, Y.: Basic K nuclear cluster, K^-pp, and its enhanced formation in the $p + p \to K^+ + X$ reaction. In: *Phys. Rev. C* 76 (2007)

[YAOW10] Yamazaki, T. ; Akaishi, Y. ; Obu, M. ; Wada, M.: Single-pole nature of $\Lambda(1405)$ and structure of K^-pp. In: *arXiv:1002.2560v1 [nucl-th]* (2010)

[Z^+05] Zmeskal, J. et al.: The DEAR experiment - first results on kaonic hydrogen. In: *Nucl. Phys. A* 754 (2005), S. 369–374

[ZCH^+96] Zeballos, E. C. ; Crotty, I. ; Hatzifotiadou, D. ; Valverde, J. L. ; Neupane, S. ; Williams, M. C. S. ; Zichichi, A.: A new type of resitive plate chambers: The multigap RPC. In: *NIM A 374* (1996), S. 132–135

List of Figures

List of Tables

Danksagung

Zu Beginn möchte ich mich bei Prof. Dr. Laura Fabbietti bedanken, dass sie mich so früh in diese tolle Gruppe geholt hat. Sie hat mich stets gefördert, geleitet und mir die Freiheit gegeben, meine Aufgaben eigenständig und -verantwortlich zu verwirklichen. Für dieses Vertrauen, welches sie in mich gesetzt hat, bin ich sehr dankbar.
Ganz allgemein gilt mein Dank allen “Clusties” für die ausgelassene und unglaublich kollegiale Atmosphäre in der Gruppe. Im Speziellen danke ich Francesco, dass er immer ein offenes Ohr hatte, Rafal für seine Hilfe, wenn mein bescheidenes Linux-Wissen einmal wieder an seine Grenzen stieß, Kirill, dessen unübertroffen trockener Humor so manches Meeting bereicherte und Eliane, der besten Frauenbeauftragten der TUM, für ihre Hilfsbereitschaft. Für ihre unvergleichliche Art und Kreativität, mich zu beschimpfen und sich von mir beleidigen zu lassen, möchte ich besonders Martin und Johannes danken. Vor allem für die vielen schönen Stunden in den Hotels während verschiedener Konferenzen und für die “inteluellen” Gespräche abseits der Arbeit danke ich Johannes. Speziell Martin danke ich für das freundschaftliche Verhältnis und dafür, dass er mir immer mit Rat und Tat zur Seite stand. Natürlich möchte ich mich ganz besonders bei Chii bedanken, meiner tollen Zimmergenossin. Sie war und ist mir nicht nur eine gute Freundin, sondern sorgte mit ihrer besonnenen und hilfsbereiten Art stets für einen angenehmen Ausgleich. Auch für ihre konstante Versorgung mit leckeren asiatischen Kleinigkeiten danke ich ihr herzlich.
Ganz besonderer Dank gilt meinem großartigen Betreuer und Kollegen Robert. Für seine Geduld und Hilfsbereitschaft, meine Fragen zu beantworten und mir bei Problemen zur Seite zu stehen. Dank seiner positiven und lebensbejahenden Sicht auf die Dinge weiß ich nun die Notwendigkeit von Glücksbärchi-Tagen zu schätzen. Vom ihm habe ich sehr viel gelernt.
Ich möchte meiner gesamten Familie danken, dass sie mich während meines Studiums in allen Belangen stets unterstützt hat. Ich hatte immer eine offene Tür und konnte zu jeder Zeit mit meinen Sorgen zu ihnen kommen. Danke.

Mein größter Dank gilt meiner Freundin Leila. Ohne dich, Leila, wäre diese Arbeit in dieser Form nicht zustande gekommen, sie ist zur Hälfte auch dein Verdienst. Du hast mich während der letzten 4,5 Jahre meines Studiums unglaublich unterstützt, hast enorm viel zurückgesteckt und bist mehr als nur ein paar mal für mich selbst an deine Grenzen gegangen. Selbst wenn der Tag noch so anstrengend und ich noch so frustriert war, du hast es immer geschafft, mich zu stützen und wieder aufzubauen. Für diese bewundernswerte Aufopferung werde ich dir immer dankbar sein. Ich freue mich sehr darauf, dich morgen zu heiraten.


Martin stinkt